EFFECTS OF WELDING PARAMETERS ON THE INTEGRITY AND STRUCTURE OF HDPE PIPE BUTT FUSION WELDS

Muhammad Shaheer

College of Engineering, Design, and Physical Sciences

Brunel University London

A thesis submitted for the degree of

Doctor of Philosophy

September 2017

"Read! In the name of

your Lord who created."

اِقۡرَأۡ بِاسۡمِ رَبِّكَ الَّذِى خَلَقَ ۝١

The Holy Quran

[Chapter 96: Al-'Alaq, 1]

Abstract

Butt fusion welding process is an extensively used method of joining for high density polyethylene (HDPE) pipe. With the increasing number of HDPE resin and pipe manufacturers and the diversity of industries utilising HDPE pipes, a wide range of different standards have evolved to specify the butt fusion welding parameters with inspection and testing methods, to maintain quality and structural integrity of welds. There is a lack of understanding and cohesion in these standards for the selection of welding parameters; effectiveness, accuracy, and selection of the test methods and; correlation of the mechanical properties to the micro and macro joint structure.

The common standards (WIS 4-32-08, DVS 2207-1, ASTM F2620, and ISO 21307) for butt fusion welding were used to derive the six welding procedures. A total of 48 welds were produced using 180 mm outer diameter SDR 11 HDPE pipe manufactured from BorSafe™ HE3490-LS black bimodal PE100 resin.

Three short term coupon mechanical tests were conducted. The waisted tensile test was able to differentiate the quality of welds using the energy to break parameter. The tensile impact test due to specimen geometry caused the failure to occur in the parent material. The guided side bend specimen geometry proved to be too ductile to be able to cause failures. A statistical t-test was used to analyse the results of the short term mechanical tests. The circumferential positon of the test specimen had no impact on their performance. Finite element analysis (FEA) study was conducted for the long term whole pipe tensile creep rupture (WPTCR) test to find the minimum length of pipe required for testing based on pipe geometry parameters of outer diameter and SDR.

Macrographs of the weld beads supplemented with heat treatment were used to derive several weld bead parameters. The FEA modelling of the weld bead parameters identified the length to be a key parameter and provided insight into the relationship between the geometry of the weld beads and the stresses in the weld region. The realistic bead geometry digitised using the macrographs contributed a 30% increase in pipe wall stress due to the stress concentration effect of the notches formed between the weld beads and the pipe wall. The circumferential position of the weld bead had no impact on the pipe wall stresses in a similar manner to the results of the different mechanical tests.

Nanoindentation (NI) and differential scanning calorimetry (DSC) techniques were used to study the weld microstructure and variation of mechanical properties across the weld at the resolutions of 100 and 50 microns, respectively. NI revealed signature 'twin-peaks and a valley' distribution of hardness and elastic modulus across the weld. The degrees of crystallinity obtained from DSC followed the NI pattern as crystallinity positively correlates with the material properties. Both techniques confirm annealing of the heat affected zone (HAZ) material towards the MZ from the parent material. The transmission light microscopy (TLM) was used to provide dimensions of the melt zone (MZ) which displays an hour glass figure widening to the size of the weld bead root length towards the pipe surfaces. Thermal FEA modelling was validated using both NI and TLM data to predict the HAZ size. The HAZ-parent boundary temperature was calculated to be 105 ^{0}C.

The 1st contribution of the study is to prove the existence of a positive correlation between the heat input calculated from FEA and the energy to break values obtained from the waisted tensile test. The 2nd contribution providing the minimum length of pipe for WPTCR based on the pipe dimensions. The 3rd contribution is the recommendation for the waisted tensile test with the test using the geometry designed to minimise deformation of the loading pin holes. The 4th contribution related the weld bead parameters to pipe wall stresses and the effect of notches as stress concentrators. The 5th contribution is a new method of visualising a welding procedure that can be used to not only compare the welding procedures but also predict the size of the MZ and the HAZ. The 6th contribution of the study is the proposal of new weld bead geometry that consist of the MZ bounded by the HAZ, for butt fusion welded joints of HDPE pipes.

Acknowledgement

Table of Contents

List of Tables

List of Figures

XVI

List of Equations

Abbreviations and Nomenclature

Abbreviation	Nomenclature
^{0}	A unit of measurement of angles
^0C	Degree centigrade, a SI Celsius scale for temperature
2D	Two dimensional
3D	Three dimensional
A	Thickness of the test specimen
A_0	Pipe wall thickness
ASM	ASM International, a material science society
ASTM	American Society for Testing and Materials
B	Width of the test specimen shoulder
B_0	Calibrated and parallel width of the test specimen
Bar	A unit of pressure
BD	Brittle-ductile
BS	British Standards
B_w	Maximum width of the weld bead
CAD	Computer aided design
CD	Design coefficient
CL	Chemiluminescence
DIN	German Institute for Standardisation
DMA	Dynamic mechanical analysis
DSC	Differential scanning calorimetry
DVS	German Welding Society
EAA	Acrylic acid
EEA	Ethyl acrylate
EMA	Methyl acrylate
EN	European Standards
ESCR	Environmental stress crack resistance
EVA	Vinyl acetate
EVOH	Vinyl alcohol
FEA	Finite element analysis
f_l	Long-term tensile weld factor
f_s	Short-term tensile weld factor
FTIR	Fourier transformed infrared spectroscopy
GPa	Giga-pascal
GUI	Graphical user interface
h	Hour, a unit of time

Abbreviation	Nomenclature
HAZ	Heat affected zone
HDPE	High density polyethylene
HDS	Hydrostatic design stress
HMWPE	High molecular weight polyethylene
Hz	Hertz, SI unit of frequency
ICI	Imperial Chemical Company
ID	Diameter of the pipe
IIW	International Institute of Welding
ISO	International Organisation for Standardisation
J	Joule, derived SI unit of energy
kg	Kilogram, SI unit of weight
L	Total length of the test specimen
L_0	Calibrated and parallel length of the test specimen
L_c	Minimum distance between the test specimen clamps/grips/pins
LDPE	Low density polyethylene
LED	Light emitting diode
LLDPE	Linear low density polyethylene
m	Metre, SI unit of length
MDPE	Medium density polyethylene
MFR	Melt flow rate
MI	Melt index
min	Minute, a unit of time
MPa	Mega-pascal
MRS	Minimum required strength
MWD	Molecular weight distribution
MZ	Melt zone
N	Newton, SI unit of force
NAFEMS	National Agency for Finite Element Methods and Standards
NI	Nanoindentation
nm	Nanometre, m^{-9}
Ø	Hole diameter for clamping bolts and traction pins
OD	Outer diameter of the pipe
ρ	Density
Pa	Pascal, SI unit of pressure
PC	Polycarbonate
PE	Polyethylene

Abbreviation	Nomenclature
PEEK	Polyether ether ketone
PE-RT	Polyethylene of raised temperature resistance
PET	Polyethylene terephthalate
PEX	Cross-linked polyethylene
PF	Phenol formaldehyde
PMMA	Polymethyl methacrylate
PP	Polypropylene
PPI	Plastic Pipe Institute
PS	Polystyrene
psi	Pounds per square inch, Imperial unit of pressure
PTFE	Polytetrafluorethylene
PVC	Polyvinylchloride
P_W	Working pressure
R	Radius of the test specimen shoulder or specified notches
s	Second, a SI unit of time
SCG	Slow crack growth
SDR	Standard dimension ratio
SI	International System of Units
t	Pipe wall thickness
TC	Tungsten carbide
T_g	Glass transition temperature
TLM	Transmission light microscopy
UHMWPE	Ultra-high molecular weight polyethylene
µm	Micrometre, 10^{-6}
UV	Ultra-violet radiation
V	Volt, SI unit of voltage
VCCT	Virtual crack closing technique
VLDPE	Very low density polyethylene
WIS	Water Industry Specification
WP	Welding procedure
WPTCR	Whole pipe tensile creep rupture
XRD	X-ray diffraction

1 Introduction

1.1 Background

Polyethylene (PE) was first practically synthesised on an industrial scale in 1933 by Imperial Chemical Company (ICI) using high-pressure (96-305 MPa) and high temperature (93-316 ºC) auto-clave reactors. The early process was dangerous and expensive, spurring the development of safer and more economical processes (PPI, 2014). The monomer ethylene for industrial production was originally obtained from molasses but now it is primarily obtained from petroleum sources (Brydson, 1999). Now, PE has the largest market share among the common commodity polymers: PVC, PP, PS, and PMMA (Piringer & Baner, 2008). One of the most popular applications of PE is in the form of pipes. PE pipes are most widely used in pressurised piping systems and in applications where large diameter pipes are required Polyethylene (PE) pipes in variety of diameters and wall thicknesses have found widespread applications in many industries, particularly in water and gas industries. Construction of gas and water supply networks require consistent high quality joining of pipes as joint failures can be both costly and detrimental.

The first low density polyethylene (LDPE) pipes were produced in 1945 followed by: expensive high density polyethylene (HDPE) pipes in 1955; medium density polyethylene (MDPE) pipes in 1971; and linear low density polyethylene (LLDPE) pipes in 1986 (Janson, 1989). Through advancements in polymerisation, process, and pipe technology, LDPE was displaced by MDPE which in turn was replaced by HDPE when it became economical. PE pipes and fittings are primarily manufactured out of HDPE, superseding the use of MDPE in pipes and fittings. This is due to HDPE offering improved material properties such as creep resistance, stiffness and strength. Therefore, thinner HDPE parts can be used for equivalent MDPE pressure ratings (TWI, 2006).

The PE resin is polymerised from ethylene with the processing conditions dictating the end product and applications. With the increasing number of HDPE resin and pipe manufacturers and the diversity of industries utilising HDPE pipes, a wide range of different standards have evolved to specify the butt fusion welding parameters

with inspection and testing methods, to maintain quality and structural integrity of welds. There is a lack of understanding and cohesion in these standards for: the variety of welding parameters; effectiveness, accuracy, and selection of the test methods; and correlation of the mechanical properties to the micro and macro joint structure.

It is the close molecular packing induced by crystallisation provides the strength of PE. The low cost coupled with good corrosion resistance, lightweight, flexible, toughness, and processability ensured PE material swiftly replaced traditional pipe materials such as lead and copper in the gas and the water industries (Stevens, 1995). For HDPE pipe applications enhanced toughness, strength, and crack resistance can be obtained by using high molecular weight PE, at the cost of processability. This has led to the development of bimodal molecular weight distribution (MWD) by combining low MWD fraction for ease of processability and high MWD fraction for its good mechanical properties, using two reactors in series or phased polymerisation. Today pipes made from bimodal resins offer resistance against slow crack growth (SCG) and rapid crack growth (RCG) while available in sizes up to 2 metres in diameter and with wall thickness of over 100 mm (Beech, et al., 2008; Beech, et al., 2010; Beech, et al., 2012).

There are several joining methods that are available for joining PE pipes but electrofusion welding and butt fusion welding are the most common ones. Electrofusion welding uses a plastic coupler that forms part of each weld (Bowman, 1997). Pipes are shaved to remove thin layer of oxidised material before being inserted into the coupler. The heating wires integrated into the inner wall melt and expand the surrounding material when energised, causing the pipes to fuse to the coupler. The added wall thickness from the coupler does provide reinforcement to the pipeline. However, the additional cost of the coupler and difficulty in production of couplers with good dimensional tolerance especially for large diameter pipes make electrofusion welding less competitive than butt fusion welding (Rashid, 1997).

Butt fusion welding is a well-established, efficient, and cost effective method requiring no additional material that forms part of the weld. Alternatively, it is also known as mirror, hot plate or heated tool welding. The butt fusion process involves the use of clamps, a trimmer, a heater plate, and a control box depending on the

level of automation of the process. The clamps can make use of mechanical leverage or hydraulic power to allow firm gripping of the pipes. Depending on the type of equipment, the process can be manual, semi-automatic or fully automatic. The preference in the industry is towards fully automatic machines to minimise human error. Out of the several joining methods, butt fusion welding is the only method applicable in joining of thick-wall and large diameter HDPE pipes.

The pipes are loaded in a clamping system which prevents longitudinal slippage and minimises the misalignment of the pipe. The pipe ends are squared using a trimmer and brought together to check for any misalignment. The heater plate is then placed in the machine and pipe ends under sufficient pressure to make intimate contact with the heater plate to allow adequate and even heat penetration; this is known as the bead-up phase. The heater plate remains in contact for a set time appropriate for the pipe's material, size, and welding procedure; this phase is known as the heat soak phase. The heater plate is removed quickly, the pipe ends are briefly exposed, and the heated pipe ends are then brought together to be welded under pressure. The cooling rate of the exposed areas of pipe ends is exponential therefore it is crucial to keep the dwell time as short as possible. The pipe remains clamped under pressure until cooled sufficiently for removal, in the cooling phase. The welding is achieved by molecular segments diffusing across the contact surfaces and forming bonds. There are several theories that attempt to explain the welding of polymers; they will be discussed in the literature review Chapter, Section 2.4.3.

The world market for plastic pipes is expected to grow by 22 million tonnes per year (Ceresana, 2012) in 2011 and is expected to reach 32.5 million tonnes per year by 2019, at an average rate of 5% per annum. PE pipes contributed 6.5 million tonnes towards the plastics pipes market share in 2011. HDPE variations in form of crosslinked polyethylene (PE-X) and polyethylene of raised temperature resistance (PE-RT) are now being increasingly used for PE pipe-production. Furthermore, there are new application based developments using PE in the form of PE blends (Al-Shamrani, 2010), as a matrix in fibre reinforced pipes (Osbourne, 2013), and as a layer in composite pipes (Yu, et al., 2017).

The economics of transferring fluids are the driving force behind piping system design and construction. Studies are carried out to determine the size of pipe

diameter, wall thickness, and material as well as ancillary services such as pumping requirements. The oil, gas, and chemical industries have different needs to the sewage or water industry due to the severity and consequences of leaks. Utility providers for gas and water make use of the same type of PE pipe with the exception of colours and welding standards. The nuclear industry has very rigorous reliability requirements as the severity and consequences of failure are often catastrophic. Hence, for the nuclear industry, one of the additional costs is for the inspection and monitoring of the piping system.

Despite the various standards for butt fusion welding stipulating different welding parameters and test methods for qualification; the PE pipes have demonstrated through both testing and actual usage to not only meet but also to exceed the service life prediction of 50 years for both pressure and drainage applications. For current HDPE pipes systems the service life is expected to exceed 100 years. The various mechanical testing method used to optimise welding parameters are the reason why there are major differences in butt fusion welding standards. Critically previous work by Troughton and Booth (1996), Hinchcliff and Troughton (1998), and Brown and Troughton (2003) has shown a number of standard tests were deficient in differentiating between the welding parameters. Among the current test methods, there was no correlation between short-term and long-term or coupon and whole pipe tests. The nuclear industry highlighted the need for this research by their use of HDPE pipes in safety-critical applications. The national regulatory bodies must be satisfied with proof that the welded pipe systems will last for the design life of the system using an appropriate welding parameters and apt mechanical test methods.

The total cost of the piping system is the sum of installation and operating costs (Mohitpour, 2008). Installation costs are: design, materials, transport, terraforming, welding, and finishing. Some of the costs associated with operation are: pressure generation, cleaning, maintenance, monitoring, and leak detection. Safety critical applications are expected to have larger operating costs due to the need to rigorously monitor the piping system. Having a myriad of standard for both welding and qualification leads to significant resource duplication and compromises safety.

1.2 Aims and Objectives

1.2.1 Aims

This PhD work aims to address the current stratification of welding parameters specified in the standards currently being used worldwide. Existing best practice will be identifiable by running a range of short and long term, coupon and full size tests on the parameters specified in each of the popular standard welding procedures. By optimising the welding parameters, most favourable combination for structural integrity of a butt fusion weld can be specified.

1.2.2 Objectives

- Compare the short-term and long-term mechanical properties, and weld microstructure, of butt fusion joints in PE pipes made according to different national and international welding procedures.
- Determine the effect of the size, geometry and structure of the weld and weld beads on the mechanical properties of the joint.
- Determine the optimal structure of a butt fusion weld in PE pipe to obtain maximum joint integrity.
- Determine the most appropriate method for qualifying butt fusion welding procedures.
- Determine which of the current standard butt fusion welding procedures produces welds with the highest mechanical integrity.

The key aspects of work programme undertaken are organised in 3 key stages as shown in Figure 1-1 and more detailed plan is shown as a Gantt chart in Appendix A: Table A-1.
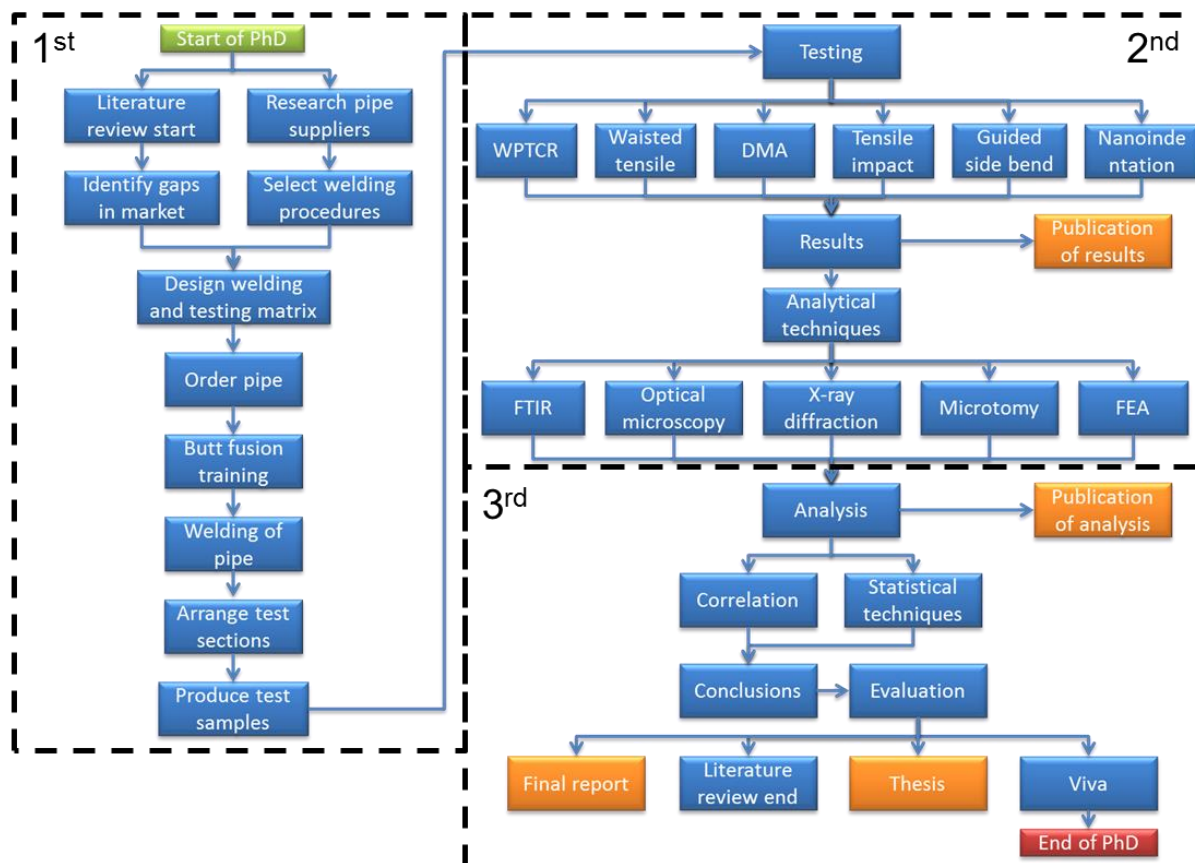
Figure 1-1 Flow chart illustrating key stages for each year of the PhD

Stage 1 hinges on conducting research on the pipe manufacturers, the market, and the standards that define the welding procedures and those that specify testing methods. The pipes were purchased from Agru Austria GmbH and they were joined using butt fusion welding. The stage concludes by allocating and welded pipes and test sample preparation for different mechanical tests and analytical techniques.

Stage 2 encompasses of two major components of mechanical testing and analytical techniques, and one minor component of consolidating results for publication. The mechanical testing component consisted of one whole pipe tests and several coupon tests. The analytical component required trials to be carried out for each of the proposed analytical technique. The techniques that succeeded in producing suitable results in the initial trials were fully utilised for each welding procedure selected in Stage 1.

Stage 3 is focused on critical analysis of the Stage 2 results from the mechanical testing and analytical techniques. It is split into the production of the final thesis and dissemination of the key findings.

1.3 Thesis Structure

There are nine chapters that comprise this thesis. Following Chapter 1 - the introduction of the PhD project, Chapter 2 gives a comprehensive literature review covering aspects of polymer chemistry, polymer properties, polyethylene applications, polyethylene welding and testing. Chapter 3 describes the experiment details in the methodology of welding, welding machines, sampling matrix, and cutting of test specimens. Chapters 4-6 contain the main body of work performed, containing the methodologies and results for the tests and analytical procedures used in this work. The work on mechanical tests and statistical analysis forms Chapter 4. Chapter 5 focused on the structure of the weld beads that are resultant from butt fusion welding using finite element analysis. The work on microstructure of the weld using analytical techniques such as nanoindentation and differential scanning calorimetry is included in Chapter 6. The key findings of the thesis from Chapters 4-6 are discussed in Chapter 7. The PhD project is concluded in Chapter 8. Chapter 9 summarises the recommendations for future work, after which the references are listed and followed by seven appendices that supplement the thesis.

2 Literature Review

2.1 Introduction

Polymers can be classified as thermoplastics that area composed of weakly-bonded long chain-like molecules and as thermosets that are composed of three-dimensional permanent crosslinked network of polymer chains, crosslinked in the final stages of production. Elastomers or rubbers are composed of similar three-dimensional structure to thermosets with less degree of crosslinking and thus the structure is less rigid. This allows elastomers to memorise the original chain structure and recover shape of the components on release of stress due to lower degree of crosslinking. Lastly, fibres can be composed of either thermoplastics or thermosets but they consist of highly aligned bundle of chains. Only thermoplastics can be reprocessed into new products by melting and shaping processes. Some polymers are produced in either thermoplastic and thermoset variety or mixed together and cured to form elastomers of desired properties, (Mills, 2005). Plastic is the general term for polymer-based materials that are used for industrial products and normally contain additives such as processing aids and fillers etc. Polyethylene (PE) is one of the widely used thermoplastics.

This literature review focuses on the topics of PE background, PE pipes, butt fusion welding, and assessment of structural integrity.

The body of the text is loosely structured in 4 parts:

1. PE: ethylene, polymerisation, morphology, compounding, shaping, and general applications.
2. HDPE pipe: extrusion process, pipe manufacture, pipe design, quality control, and service conditions.
3. Welding of HDPE pipes: welding techniques, butt fusion (BF) welding process, theory of welding, BF weld microstructure, BF standards, and defects in BF welds.
4. Assessing performance: weld failure modes, whole pipe tests, coupon tests, test standards, and comparison of the mechanical tests.

2.2 Polyethylene (PE)

Polyethylene (PE) was invented in 1933 by Imperial Chemical Company (ICI) in England using high-pressure (96-305 MPa) and high temperature (93-316 ºC) auto-clave reactors. The early process was dangerous and expensive, spurring the development of safer and more economical processes (PPI, 2014). Now, PE has the largest market share among the common commodity polymers: PVC, PP, PS, and PMMA (Piringer & Baner, 2008). Variants of PE can be categorised as either commodity or engineering materials. LDPE, linear low density polyethylene (LLDPE), medium density polyethylene (MDPE), and high density polyethylene (HDPE) are categorised as commodity industrial polymers, whereas very low density polyethylene (VLDPE), high molecular weight polyethylene (HMWPE), and ultra-high molecular weight polyethylene (UHMWPE) are considered to be engineering polymer materials (Ulrich , 1993).

Commonly there are three processing stages before polymers can be used as plastics in products. Polymerisation is the first stage where a polymer is made from its base ingredients. This stage is followed by compounding which involves mixing stabilisers, dyes, and fillers with the polymer to produce plastic. The final stage is shaping the now compounded polymer in useful plastics shapes such as pipes or as plastic products. The nature of certain polymers or products may require these stages to be combined as a single process.

2.2.1 Ethylene

The constituent for the polymerisation are hydrocarbons that are distilled or decomposed from crude oil, natural gas, coal, biomass, and waste streams. Heat is used to crack or decompose larger hydrocarbons into smaller ones. Steam cracking is the dominant process used to produce ethylene. The hydrocarbons from fossil fuels are cracked in tubular reactors suspended over gas-fired furnaces at elevated temperatures (Amghizar, et al., 2017).

From coal, the reaction between coke and lime produces calcium carbide which is decomposed by cracking. Hydrolysis of calcium carbide produces the simplest alkyne, acetylene (also known as ethyne) and calcium hydroxide, this reaction was discovered by Friedrich Wohler (Wohler, 1862).

Ethylene is the simplest monomer unit, which is the building block of polyethylene as shown in Figure 2-1. Each ethylene monomer consists of two carbon atoms connected with a double covalent bond with each carbon atom being connected to hydrogen atoms via single covalent bonds. When forming a chain the carbon atoms lose the double bond between them and form a bond with a carbon atom from the next monomer. A molecule with a double or a triple bond is said to be unsaturated or active while a molecule with only single bonds is a saturated molecule. Most polymers are made from unsaturated monomers (Callister, 2003).
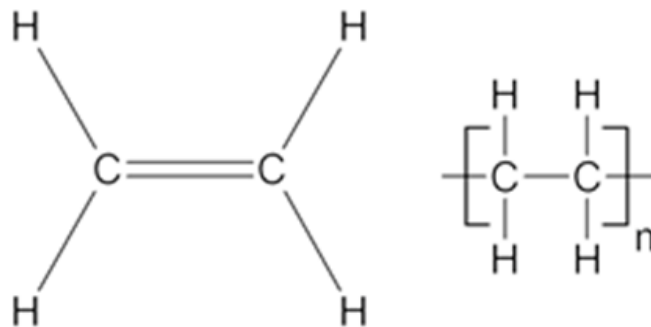
Figure 2-1 Unsaturated monomer and the corresponding polymer forms for ethylene

2.2.2 Polymerisation

Monomers can be joined together using a process called polymerisation to form a polymer chain. An essential feature of a monomer is polyfunctionality, i.e. the ability to form chemical bonds to at least two other monomer molecules. The process of polymerisation has three stages: initiation, propagation, and termination. During the initiation stage the rate of polymerisation accelerates; through propagation stage the rate reaches a steady-state; and in the termination stage the rate declines and the end product can be extracted. Bifunctional monomers such as those in polyethylene have two active bonds to interact with two other monomers. Bifunctional monomers can only form linear chains of polymers. Depending on the bond angles a polymer chain can form a regular zigzag or an irregular random pattern. However, some complex monomers can feature tri-functional or multi-functional bonds, and can form other types of polymer chains and structures (Crawford, 1998, p. 415).

Polymerisation has two types of reactions kinematics, chain-growth and step-growth and two types of reaction mechanisms, addition and condensation. The chain-growth polymerisation reaction initiates from using free radicals, ions, and catalysts, to form long chains. The step-growth polymerisation reaction initiates from using the

functional groups of monomer units, to form many small chains followed by assimilation of the small chains to form larger molecules. Table 2-1 compares the kinematics of chain-growth and step-growth polymerisation.

Table 2-1 Comparison of polymerisation kinematics routes, (Ram, 1997, p. 14)

Chain-growth polymerisation	Step-growth polymerisation
1. Long polymer chains form in the early stage	1. Small polymer chains form in the early stage
2. Number of monomers decrease steadily as chain length increases	2. Significant decrease in number of monomers in the early stage
3. No elimination of molecules or atoms such as free radicals in the solution as they become end groups of polymer chains	3. Elimination of small molecules and atoms such as free radicals in the solution by formation of small molecules known as condensate, usually water
4. High molecular weight ($10^5 - 2 \times 10^6$)	4. Low to medium molecular weight (<50000)
5. Continuation of polymerisation increases monomer conversion into chains	5. Continuation of polymerisation increases monomer conversation and the molecular weights by assimilation of small chains

The addition polymerisation reaction mechanism produces polymer by requiring both an initiator and a monomer. The process proceeds by addition of one monomer to the chain at a time. The condensation polymerisation reaction mechanism requires the presence of reactive functional groups at each end of the monomer that during the polymerisation process will react with functional groups in other monomers, producing the polymer and by-products such as water or ammonia.

Both types of polymerisation reactions kinematics can use either reaction mechanism depending on the ability and the behaviour of the initiating substance and the desired end product. Polymerisation of the ethylene monomer is usually a chain-growth polymerisation reaction that today uses a variation of addition polymerisation reaction mechanism called stereospecific polymerisation.

A chain consisting of more than one monomer type is referred as a copolymer chain and it is created by a process of copolymerisation. Monomer units are selected and copolymerised based on required properties for specific application: some of the commonly used monomer units used as copolymers with PE are shown in Table 2-2. Following copolymerisation, the polyethylene chain may have different arrangements between the monomers based on the copolymer as shown in Figure 2-2.

Table 2-2 Ethylene copolymers (Ulrich , 1993)

Comonomer	Name	Copolymer content (%)
Vinyl acetate	EVA	5~50*
Vinyl alcohol	EVOH	27-48
Methyl acrylate	EMA	20-40
Ethyl acrylate	EEA	15-30
Acrylic acid	EAA	3-20
*if Vinyl acetate content exceeds 50%, the copolymer is named VAE.		
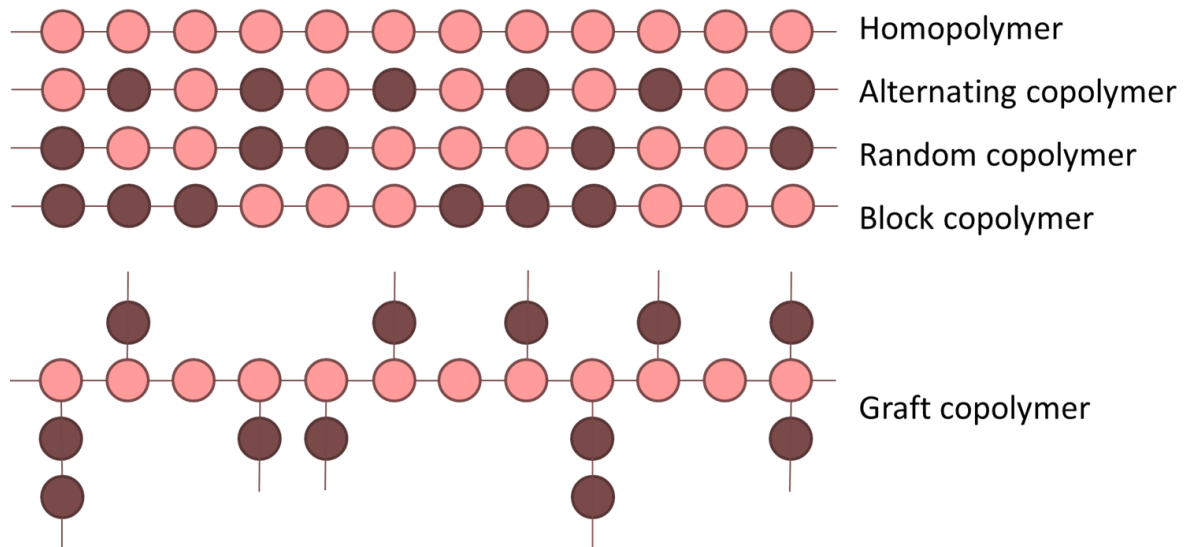
Figure 2-2 Monomer arrangements in polymer and copolymer chains (Crawford, 1998)

Chains of different molecular weight (MW) may be produced depending on the type monomer, comonomer, and polymerisation process used. MW has an effect on a number of important mechanical and thermal properties as the length of polymer chains affect the material properties. Material properties such as toughness, hardness, creep resistance, softening temperature, stiffness, and yield strength are improved by increasing the MW (PPI, 2014). For example, candle wax has approximately 40 ethylene monomers per chain compared to polyethylene which has several thousands of monomers per chain. Both materials feel similar to touch yet polyethylene is harder than candle wax based on the magnitude of their respective MW.

The MW is simply the weight of the sample divided by the number of moles in a sample, if all the chains are the same length in a polymer. The numerous chains of different MW typically form a bell curve distribution, as seen in Figure 2-3 for broad and narrows curves. This distribution of chains can be described by average MW:

the number-average emphasises the smaller chains and the weight-average emphasises the larger chains. Molecular weight distribution (MWD) or dispersity is an indication of how uniform is the distribution of polymers' chain lengths. It is calculated by dividing the weight-average MW by the number-average MW. MWD will approach unity when molecules are of the same length i.e. uniform state. Techniques such as end group analysis, gel permeation or size exclusion chromatography, membrane osmometry, static light scattering, and viscometry can be used to obtain MWD of a polymer.
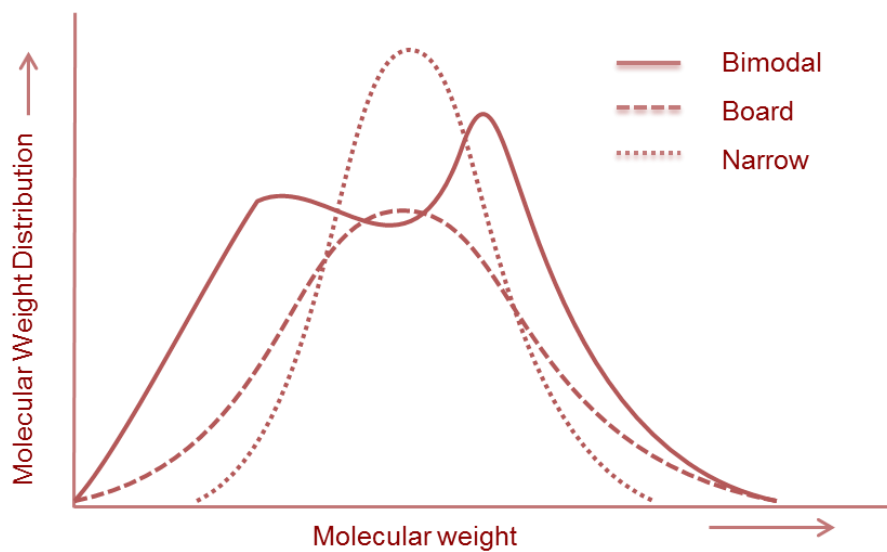
Figure 2-3 Bimodal, broad, and narrow molecular weight distributions curves (PPI, 2014)

MWD that is broad will have a large difference in chain length of small and large molecules while a narrow MWD will have large number of molecules with a similar chain length (Rosen, 1993, p. 53). Broad MWD have versatile properties and flow easily while narrow MWD tends to crystallise at a uniform rate. It is possible to have a bimodal MWD with peaks at both short and long end of MW. Bimodal offers superior properties while maintaining good processability. A high MW is desirable but becomes difficult to process during manufacturing. High MW molecules have high viscosity because they flow slowly due to their long chain length. The viscosity of the polymer is incorporated into a measurement known as the melt index (MI).

Industrial polymerisation has four major production processes as shown in Figure 2-4. Control of process variables such as thermal control and process support mechanisms such as mixing are necessary to avoid process issues. Each individual

industrial polymerisation process is comprised of several batch stages, though certain large scale implementations of these stages if operated simultaneously and frequently can be considered to be continuous process. The efficiency of each process can be increased by removal of polymer products which reduce viscosity, and efficiently extracting heat produced in the polymerisation process (Chekal, 2002; Frank, 2001; Otaigbe, 1996).
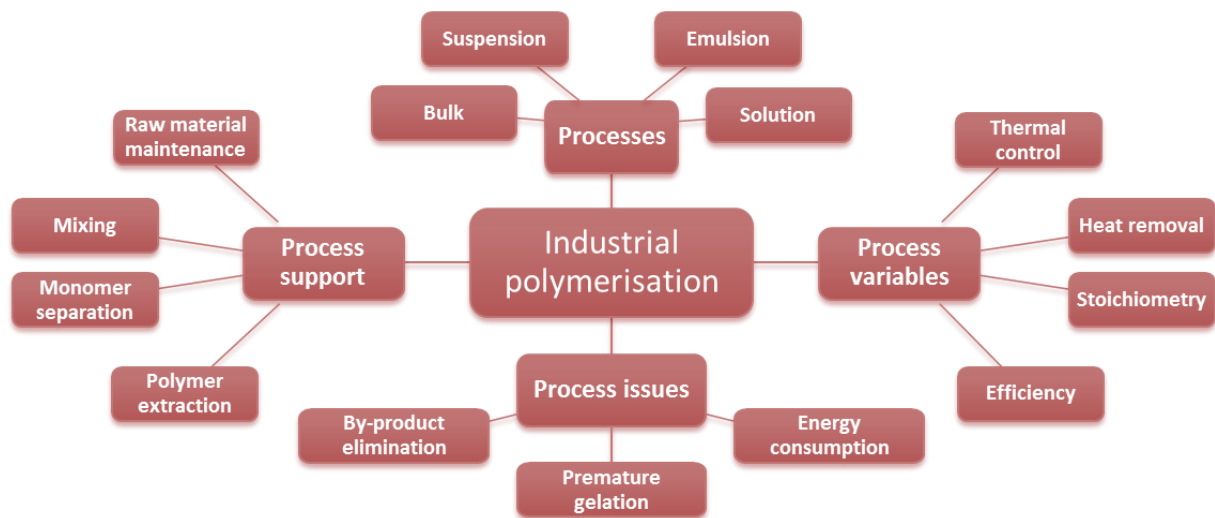
Figure 2-4 Parameters of industrial polymerisation (Chekal, 2002)

There are five polymerisation processes for PE:

1. High-pressure processes
2. Ziegler processes
3. The Phillips process
4. The Standard Oil (Indiana) process
5. Metallocene processes

These five processes can be divided into three polymerisation processes for ethylene (Halary, et al., 2011): radical, Ziegler-Natta catalysed, and Metallocene-catalysed. During free-radical polymerisation transfer reactions take place CH_2 groups which give rise to short branches (20 per 1000 main chain carbon atoms) if the groups are few bonds from the terminal radical or long branches (2-8 per 1000 main chain carbon atoms) if the transfer reaction takes place on preformed chains. The extensive branching off the main chain hinders crystallisation leading to LDPE.

For Ziegler-Natta catalysis, surfaces of titanium chloride crystals are used which are multi-site leading to broad molecular weight distribution (MWD) due to their heterogeneous activity. Without any transfer reactions, very linear chains are produced that crystallise easily leading to HDPE. The process can incorporate comonomers such as butane, hexene, and octane while keeping the main chain linear. Since the comonomers cannot form part of crystalline cell yet the chains can crystallise easily, few percent of comonomer content leads to LLDPE.

Metallocene catalysis uses well-defined single-site catalysts leading to very narrow MWD when compared to Ziegler-Natta catalysis. The process produced extremely long linear chains due to absence of transfer reactions which led to high viscosity material that was difficult to use with the current industrial processes. Comonomer content in metallocene catalysis is incorporated in the the main chain. The second generation metallocene catalysis allows undergoing of transfer reactions to produce long branches (few per 10000 carbon atoms) while maintain homogeneity of MWD and comonomer distribution.

These catalysts orient each monomer joining the polymer chain in a highly ordered configuration. PE forms linear chains with reduced number of branches that fold efficiently increasing density and crystallinity. These catalysts are derived from metallic elements from groups' I-III and halogen elements from groups' IV-VIII (Ram, 1997). Besides polymerisation temperature, other factors that affect MW and branching are the concentrations of monomers, catalysts, co-catalysts, and transfer agents.

2.2.3 Morphology

Polymer morphology is subject to isomerism of molecules which dictates the folding behaviour of polymer chains in formation of structures consisting of amorphous and crystalline phases. Isomerism refers to the arrangement of the atoms inside a molecule and in turn, the arrangement of molecules inside a chain. A small change in such molecular characteristics is sufficient to affect the broader material properties of a polymer.

The molecular characteristics of a polymer stem from a combination of chemistry, shape, size, and structure, as illustrated in Figure 2-5 (Callister, 2003). The chemistry refers to the composition of the monomer and functional group used in the

polymerisation process. The shape of the chains derives from configuration where the atoms are fixed in space by covalent bonds and conformation where it is possible for intramolecular rotation to occur. The size of the chain is proportional to the number of repeat unit joined together and the average molecular weight. The structure of the polymer chains can often be categorised as one of the following: linear, branched, crosslinked, and networked. However, not all polymer structures fall neatly between these categories.
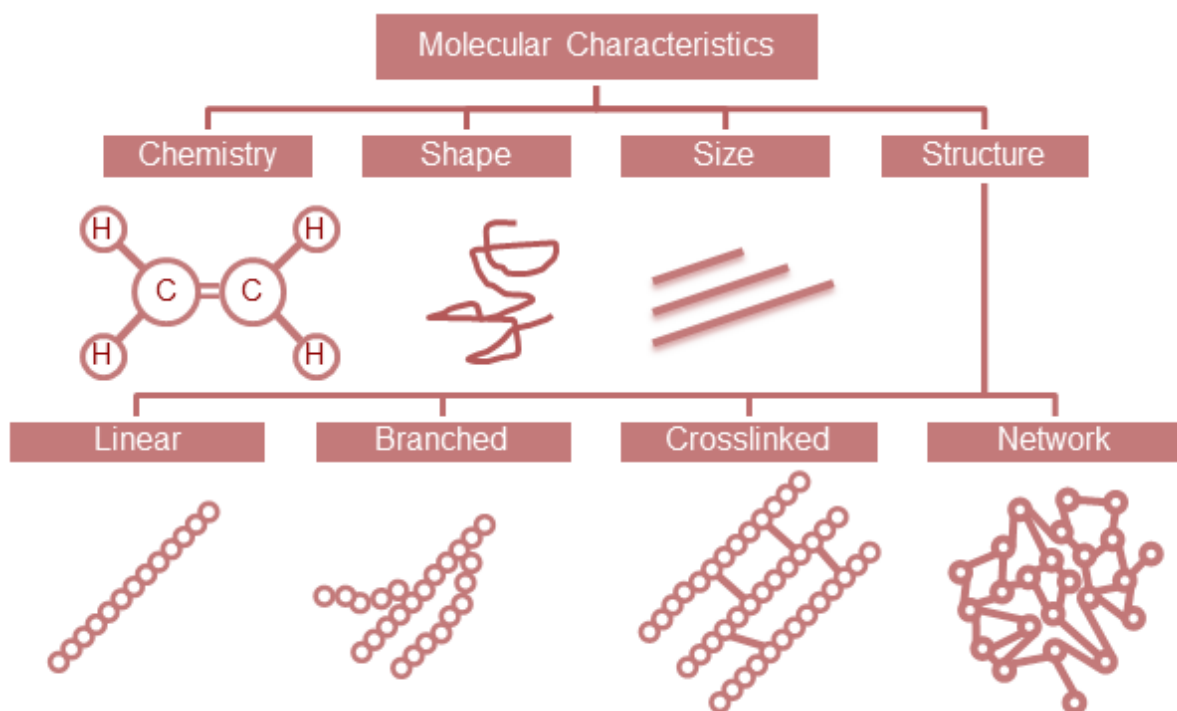
Figure 2-5 Polymer molecule characteristics classification flow chart, (Callister, 2003, p. 467)

Polymers that have both amorphous and crystalline phases are called semi-crystalline. The degree of crystallinity in polymers varies from fully amorphous to almost fully crystalline, up to 95% when using polyethylene for example (Callister, 2003; Bolton, 2013). PS, ABS, and PVC are examples of amorphous polymers while PE, PEEK, and PET are examples of semi-crystalline polymers.

The formation of crystal structures does not only rely on the chain structure of polymer but also sampling and conformation. The most stable conformation for tight packing of polyethylene chains are zigzag shapes. The isotactic molecules in a chain increase the likelihood of the chain forming a crystalline region rather than an amorphous one but the type of region forming is also strongly dependent on the

conditions of processing. The rate of cooling is a major factor that affects the formation of crystalline regions and their size. Polymer melt that is rapidly cooled will mostly be amorphous due to orientation and position of its molecules being frozen while disordered. At a slower rate of cooling, polymer chains in the melt take orderly configuration forming plate-like structures called crystalline lamellae. These lamellae grow in the direction of the temperature gradient. Thinner lamellae have higher probability of sharing chains. The thickness of the lamellae is dependent on the degree of branching and chemical structure.

The lamellae are separated by amorphous regions that consist of disordered chains referred to as tie molecules. Termination of the lamellae growth due to the bends and kinks in molecules produces these disordered regions. The crystalline regions tend to be dense and hard due to their ordered structure and stronger intermolecular forces stemming from the proximity of the molecules while the amorphous regions provide ductility and impact resistance.

Branched polymers form structure called fringe-micelles which are groups of lamellae linked together with inter-lamellae chains called tie molecules as seen in Figure 2-6. Linear non-branched polymers tend to form spherulites, these are spherical semi-crystalline regions composed of ordered lamellae that have assembled radially around a nucleus seed, Figure 2-7. These nucleating seeds can be induced by impurities or additives in the polymer melt. A larger number of nucleation seeds and a fast rate of cooling will produce numerous small spherulites. In the case of opposite conditions, a few larger spherulites are grown. The size of the spherulites ranges from few micrometres, up to one centimetre. Spherulites grow until they reach adjacent spherulites, forming planar boundaries between them.
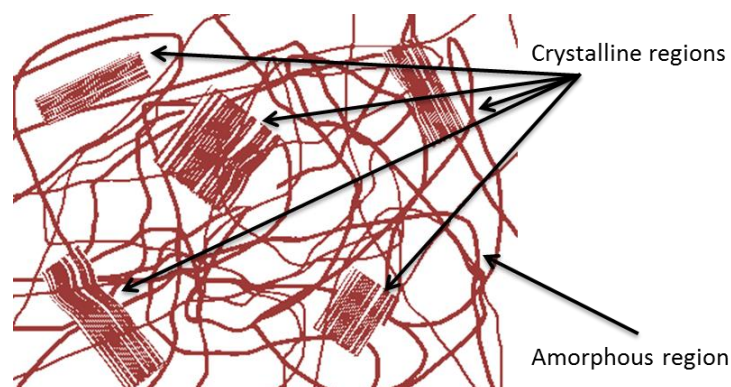
Figure 2-6 Semi crystalline material structure showing exaggerated amorphous and crystalline regions
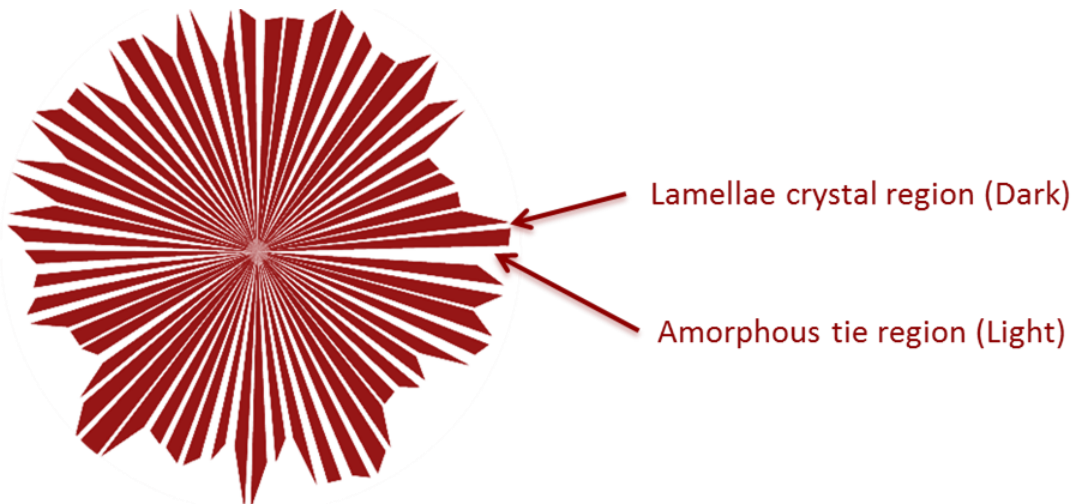
Figure 2-7 A planar 2D cross-section of a spherulite showing lamellar crystals separated by amorphous region

The alignment of the polymer molecules in the lamellae results in birefringence which is responsible for producing a variety of coloured patterns including the Maltese cross. These patterns are visible when the spherulites are viewed between cross polarizers in an optical microscope, Figure 2-8. A micrograph shows a characteristic Maltese cross pattern when produced using cross-polarised light in each spherulites (Callister, 2003).
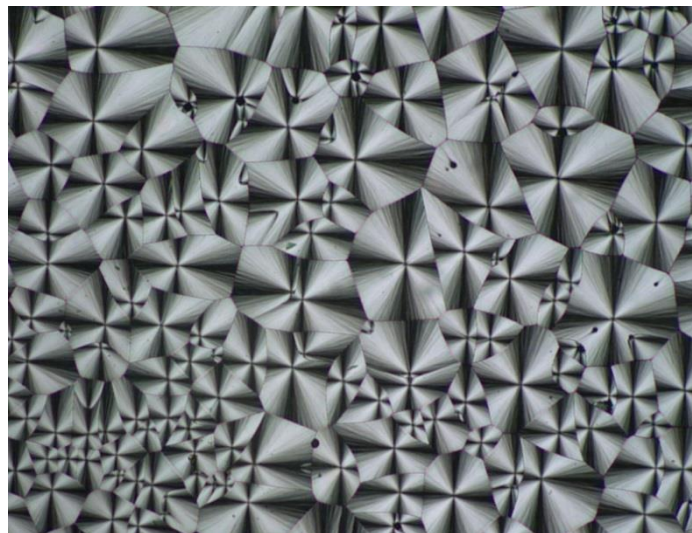
Figure 2-8 Maltese cross patterns produced by spherulites seen using polarised optical microscopy

Crystallinity and its distribution (Van Krevelen, 1997) influence the optical properties of polymers. An amorphous polymer will consist of single phase therefore appear transparent. The crystalline phase of the polymer has higher refractive index due to their uniform nature than the amorphous phase. Additives, discontinuities, fillers,

impurities and material phases in the internal structure scatter light. The refractive indices of spherulites are based on size, orientation, position and separation, of crystalline phases and amorphous phases. The variation in density and the orientation of spherulites exhibit scattering of light, polarisation and birefringence.

The density of PE is proportional to its crystallinity. The crystalline regions are denser than the amorphous regions. The densities of different regions can be used to calculate the degree of crystallinity using Equation 2-1 where: ρ_c, ρ_s and ρ_a are densities of perfectly crystalline PE, density of PE specimen to be established, and density of fully amorphous PE (Callister, 2003).

Equation 2-1

$$\% \ of \ crystallinity = \frac{\rho_c(\rho_s - \rho_a)}{\rho_s(\rho_c - \rho_a)} \times 100$$

Increasing the degree of crystallinity in PE improves its strength by making it less amorphous. This is due to disorganised polymer chains aligning themselves in orderly structures that contribute towards increased degree of crystallinity by forming secondary bonds or intermolecular forces such as hydrogen bonds and the molecules moving closer by reducing bond length. The amount of side branching from the main polymer chain determines the density as branching reduces the efficiency of chain packing and degree of crystallisation. Organised structures can be packed more tightly and have higher density, which affects a number of material properties.

The material properties of a PE are dependent on the density, melt index (MI) and molecular weight distribution (MWD). The melt index and MWD are also interdependent, more so than density which also relies on crystallinity and branching behaviour of chains. These three important properties are proportional to most of the other properties and they are affected by: the bond strength of the monomer constitutes; the bond strength between the two monomer molecules; chain length; and arrangement of chain structure to allow secondary bonds to supplement the primary bonds. PE can be further strengthened by cross-linking to increase the number of bonds using radiation or crosslinking agent to form PEX. By varying these three properties PE can be optimised to be suitable for its different applications.

2.2.4 Compounding

A plastic consists of polymer resin which has been compounded with additives such as: thermal, ultraviolet and fire-retardant stabilisers; antioxidants; reinforcement fibres; fillers; colorants; and plasticisers. Compounding is used to achieve the desired properties of plastic that a polymer alone cannot provide. A large amount of recipes exist for diverse applications therefore compounding is often done at a facility where final product is to be produced.

Stabilisers are the most important additive and can be the only additive during compounding. Compatibility of stabiliser used with the polymer resin is paramount. Thermal stabilisers aim to reduce decomposition through heat where most polymers start to degrade above 200 ºC. Some stabilisers are used to guard against decomposition during the processing stages. Antioxidant stabilisers guard against oxidation of polymer. Polymers with lower degree of crystallinity such as LDPE featuring branching with tertiary carbons bonds are more susceptible to oxidation. The recommended concentration of antioxidants is 0.1-0.3 weight percentage, lower amounts in polymers with higher degree of crystallinity.

Sunlight causes photo-oxidation in forms of UV light which breaks down atomic bonds by providing activation energy, leading to creation of free radicals. This process is called photolysis and the molecules that break free from the macromolecule are known as free radicals which are highly reactive uncharged molecules. These react with oxygen in the air to form peroxy radicals, which contribute to increase in the rate of free radical reactions. Formation of free radicals can be inhibited by using anti-oxidant additives. Ionising radiation can either cause crosslinking or bond scission which lowers the molecular weight of the polymer. Hindered amine light stabiliser (HALS) additives are used in PE; they work via trapping free radicals by reacting with them (Nicholson, 1991, p. 135).

Ultraviolet absorbers (UVA) are used to prevent environmental damage from UV light which acts in the range of 230-290 nm. UVA act as energy absorbers such as benzophenones, converting the incident energy into heat. Useful UVA concentration ranges between 0.10-1 weight percentages, the amount adjusted according to the intensity of predicted solar radiance. UVA that migrate to the surface while adhering to the polymer and have low diffusivity to the atmosphere, offer greater protection.

The ionising effects of radiation can be reduced by absorbing or reflecting UV light using pigments such as carbon black and titanium dioxide.

Fire retardant stabilisers form really strong bond which require a large amount of energy to break, this makes the polymer more resilient to burning especially if the stabiliser forms part of polymer chain. The retardant mechanism is preventing the formation of free radicals, construction of protective char or releasing water. The three main types of fire retardant stabilisers are: organic compounds that include bromine; inorganic compounds that include antimony salts; and patented reactive compounds. Inorganic compounds are preferable for use due to lower toxicity while a combination of stabilisers is usually more effective. Fire retardant stabiliser should activate below the decomposition temperature of the polymer to be effective.

Fillers can compose up to 50% concentration in some applications to reduce cost. Limestone, quartz and natural fillers such as jute, wood flour and sawdust are common fillers. Coupling agents such as titanates increase chemical affinity of polymer and filler material. Distribution of the filler and the filler particle size are extremely important to achieve material homogeneity. Fillers may be used to alter the properties and to increase dimensional stability.

Reinforcement fillers consist of fibres, the length to diameter ratio of which exceeds 100. Glass, aramid and carbon fibres are some of the common fibres used to increase the strength and stiffness of polymers. Fibres should ideally be coated with coupling agent to encourage adhesion to the polymer. Fibres, if introduced in controlled manner may produce polymers that exhibit anisotropic behaviour, this behaviour is exuberated if the fibres are longer. Short fibres are preferable if forming stages are complex as they flow better.

Plasticisers such as camphor, esters and oils are used to reduce the viscosity of the polymer (Ram, 1997). Increasing the percentage of plasticizer will increase the flexibility of the plastic. Plasticisers have very low glass transition temperatures; therefore, they are subject to compatibility with the polymer which may require using specific blends. Migration of plasticiser to surface reduces polymer ductility in addition to carrying a contamination risk (Földes & Szigeti-Erdei, 1997).

21

Colorants can be divided into two groups: pigments and dyes. Dyes are soluble whereas pigments are insoluble in the polymer. Mixing of colorants to achieve an uniform colour is a challenging task and the colour must remain stable during the compounding process. Best colorants resist diffusion or bleeding in the polymer once dispersed. Cadmium, iron oxides and titanium dioxides are some of the popular colorants. Certain pigments such as titanium dioxide are subject to chalking in the presence of moisture which chemically alters the binding compounds of pigments.

Some additives can be used to control degradation for planned obsolescence of used products. Extender additives such as chlorinated hydrocarbons are used to extend the effects of plasticiser and reduce cost by reducing the amount of plasticiser required. Other additives that may appear in very small quantities during compounding are: surface active, blocking, impact modifiers, coupling, blowing and cross-linking agents, catalysts, and hardeners. It is important that the additives contribute to only a small percentage of the polymer mass and they are compatible with the resin; otherwise they might migrate towards the surface weakening the local material properties. Additives do not contributing structural strength as they are unlikely to be part of main polymer chains.

2.2.5 Shaping

Shaping is the next stage after compounding of polymerised polymer with additives. Figure 2-9 illustrates various shaping methods available for manufacturing of products or useful product requisites.
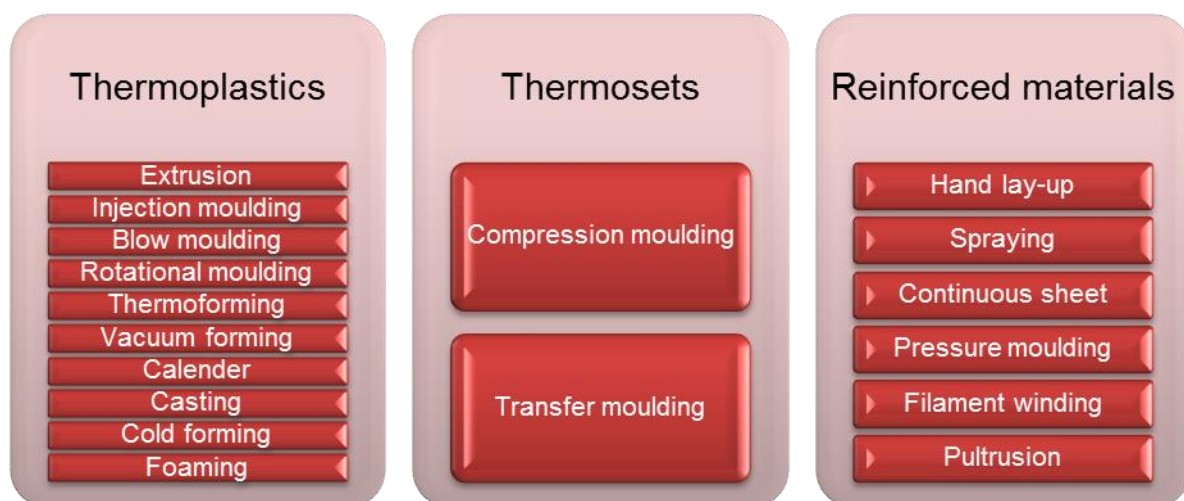
Figure 2-9 Shaping methods available for thermoplastics, thermosets and reinforced materials

Calender, cold-forming, foaming, and extrusion processes produce polymers in shapes where one axis is significantly longer than other such as fibres, pipes, rods, sponges, and sheets (Calender). The moulding or casting processes utilise forces arising from gravity, gas pressure, centrifugal force, and mechanical compression to fill the mould or the cast. Injection moulding and transfer moulding use mechanical force. Blow moulding uses compressed air to inflate the extruded cylinder into the mould shape while foaming uses gases to create bubble structures. Vacuum forming and thermoforming both use a vacuum to draw the heated polymer sheet over the mould; the latter uses compressed air in addition to the vacuum to force the sheet to conform tightly to the mould. The moulds may be actively heated to ensure the mould is properly filled and they may also be actively cooled to increase cycle times.

Most of the shaping processes for reinforced materials vary from the previous processes only by the addition of the reinforcement materials such as fibres. The processes of hand lay-up and spraying apply fibre and resin material over the mould layer-by-layer. In the case of filament winding, a mandrel is used to pattern commonly used fibres such as glass or carbon that are impregnated in a resin bath. The products made from reinforced material require curing to ensure that the fibres have a good interface with the polymer resin matrix.

2.2.6 Applications

The applications of PE are quite broad and make use of different types of PE, which can be classified according to the density and molecular weight. There are also industry specific standards to categorise PE for defined applications for example, ISO 4437-1 (2014a) for the gas and ISO 4427-1 (2007a) for water. The classification of PE pipe by density as stated in ASTM D1248 (2016a) is shown in Table 2-3.

Table 2-3 PE type classification as stated in ASTM D1248 (2016a)

Type	Density (kgm^3)	Example
I	0.910-0.925 (low)	LDPE – Low density polyethylene LLDPE – Linear low density polyethylene VLDPE – Very low density polyethylene
II	0.926-0.940 (medium)	PEX – Cross-linked polyethylene MDPE – Medium density polyethylene
III	0.941-0.959 (high)	HDPE – High density polyethylene
IV	0.945 (high, homopolymer)	UHMWPE – Ultra high molecular weight polyethylene
Butene or hexene are used as comonomer in HDPE to control branching in type III PE, **(PPI, 2014)**.		

LLDPE replaced LDPE for almost all non-clarity film markets in areas such as grocery bags, heavy-duty shipping sacks, diaper liners and agricultural film. The applications that require higher strength than offered by LDPE or LLDPE use HDPE such as pressurised piping systems which were introduced using MDPE. Figure 2-10 and Figure 2-11 for LDPE and HDPE materials respectively illustrate the market share of their common applications. The 1.5 mm LLDPE film thickness is equal to 5 mm of LDPE film thickness in terms of strength (Callister, 2003).

For engineering plastics such as HMWPE and UHMWPE, the applications are: specialised parts for machines handling bulk material, profile extrusion, chemical pump parts and snow plough edges. UHMWPE is also used for the production of high strength fibres which are used as reinforcement material in composites. When compared with commodity PE, the scale of market for engineering PE is several orders of magnitude lower.
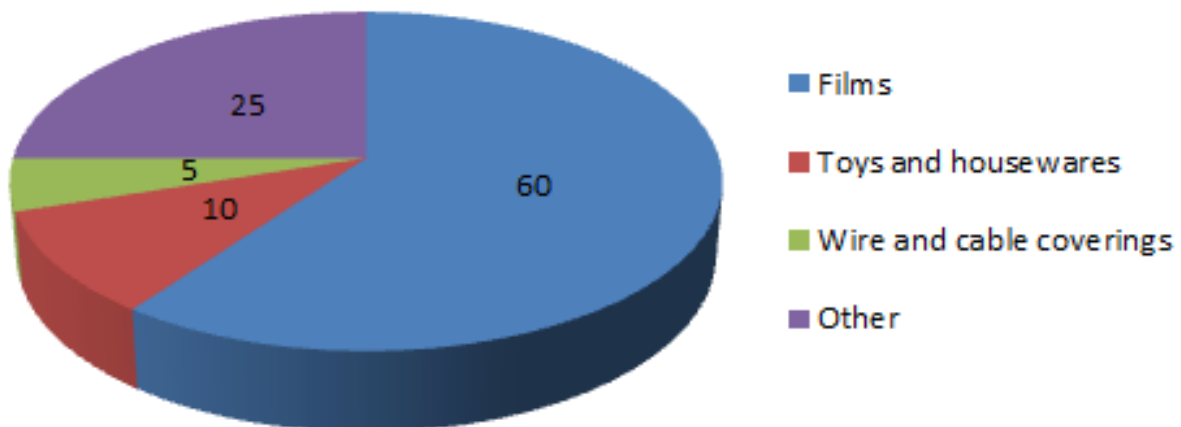
Figure 2-10 The common applications of LDPE including LLDPE and ULDPE (Ceresana, 2012).
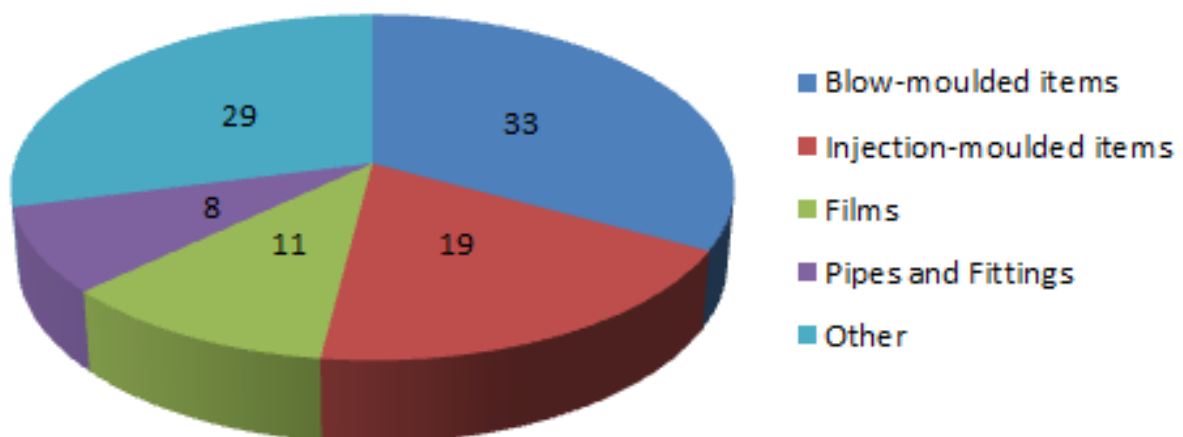
Figure 2-11 The common applications of HDPE (Ceresana, 2012)

24

Typical applications for copolymer enhanced PE polymers include: specialist hose and tubing, films, disposable gloves, balloons, diaper liners, hospital sheeting and hot-melt adhesives. Acrylic and methacrylic acid based PE copolymers have good puncture and low temperature impact resistance. The applications for acrylic acid and methacrylic acid PE copolymers are: sporting goods such as golf ball covers; bumper pads and guards in the automotive industry; and high performance footwear and clothing. Chlorosulfonyl group units used as copolymer enable crosslinking in PE chains. Chlorosulfonyl copolymer can be vulcanised with metal oxides to make the PE product more inert for automotive applications, wire and cable insulation, and as pond liners.

2.3 HDPE Pipe

This section describes briefly the extrusion process before leading on to pipe manufacturing, design, quality control, and service conditions of HDPE pipes.

2.3.1 Extrusion process

Extrusion is a process of transporting material through a die to produce a product known as extrudate with a fixed cross-sectional area. Joseph Bramah patented the process of extruding lead pipes using a hand-plunger to ram molten lead in 1797, the process at the time was known as squirting. Thomas Burr constructed a hydraulic press to mechanise the extrusion process in 1820 (Skinner, 2014). In the same year, Thomas Hancock invented a rubber 'masticator' to shred processed rubber scraps which transports the shredded rubber in a similar manner to an extruder. Edwin Chaffee developed a two-roller machine to add additives to rubber in 1836. The first thermoplastic extruder was invented by Paul Troester and Ashley Gershoff in 1935 (Rauwendaal, 2014); this was followed by the development of a twin-screw extruder by Roberto Colombo of LMP in 1938 in Italy (Plastics Technology, 2005).

There are three categories of extrusion processes defined by the processing temperatures relative to the material being processed: the hot extrusion process is accomplished above the materials' melting temperature; the warm extrusion process is carried out at below materials' melting temperature but above room temperature; and the cold extrusion is done at or just above the room temperature. Plastic extrusion process is usually a hot extrusion process. The delivery method of the material feed determines whether the extrusion process is a batch process which

uses mechanical rams or a continuous process which use Archimedean screws or other rotating devices. There are several types of extrusion processes depicted in Figure 2-12: shape, sheet/film, tubing, blown film, over jacketing, coextrusion and extrusion coating.
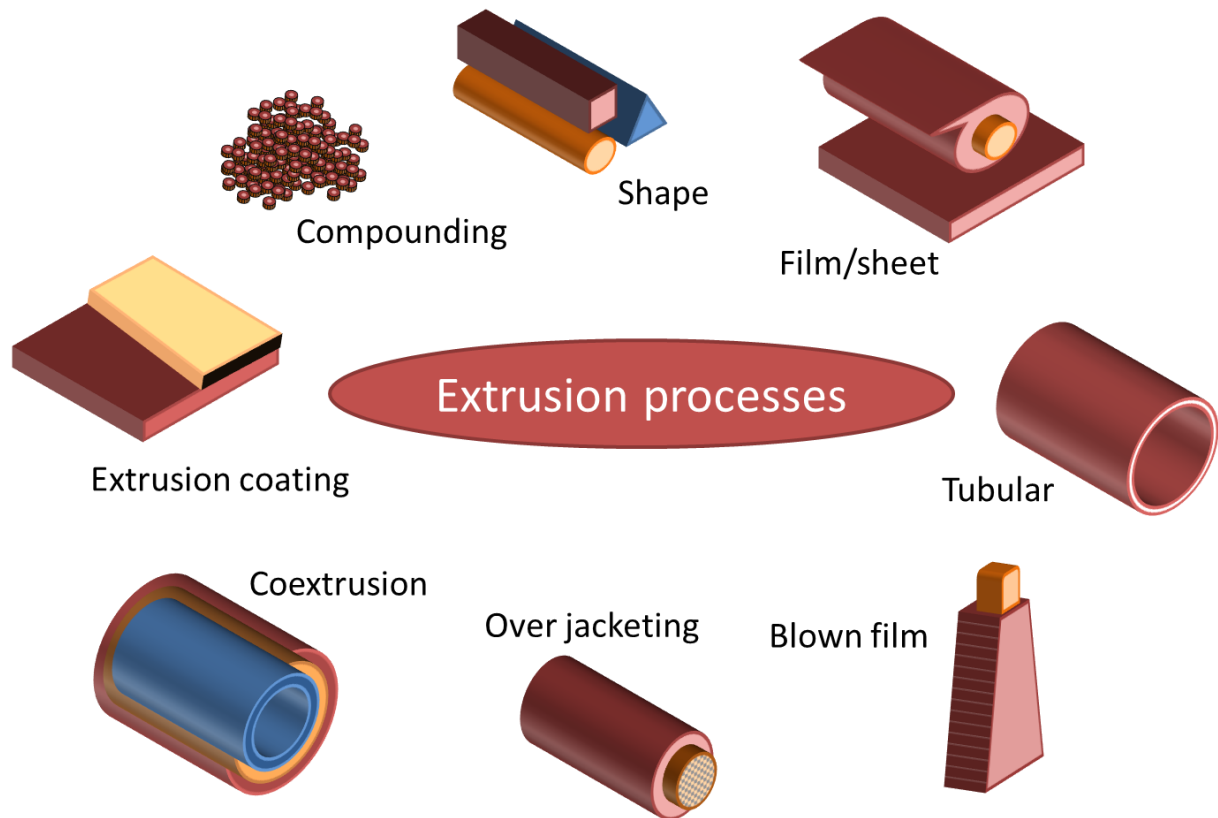
Figure 2-12 Illustration of commercial extrusion processes and their end products

The extrusion process is considered plasticating if the feed is in the solid phase such as powder, pellets or grains. If the feed phase is liquid then the extruder acts purely as a pump and it is considered a melt fed extruder. Compounding extruders melt the polymer feed and mix in additives. The plastic can then be fed into another extrusion process or extruded in the form of strands which are cut and shaped into pellets via a pelletiser. The extruder consists of several components shown in Figure 2-13 with an illustration of a typical extruder.
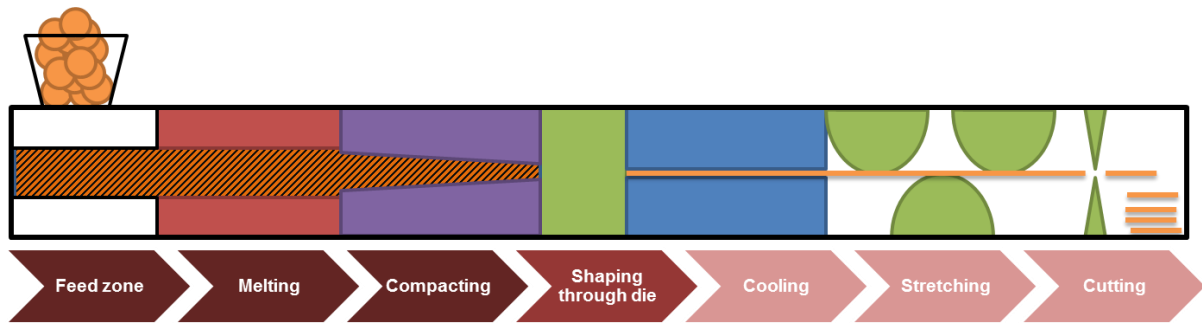
Figure 2-13 A schematic representation of an extrusion process. The first three stages show extrusion process, the fourth stage represents the die that shapes the extruded polymer and the last three stages show common subsequent processes (not to scale)

The volume of contents decreases from the feed zone to the die: this is achieved by reducing the screw pitch and the barrel diameter. The flow of melt is channelled through a helical path between the screw and the barrel, experiencing compression ratios of 2 to 6 typically. Shear heating produced by friction and mixing, by the screw is more effective than external electrical heating elements due to lack of heat conduction exhibited by the polymer. The compacting or the metering zone situated just before the die is typically compromised of 20-50% of the screw length. The rotational speed of the screw is linked with the viscosity and the extrusion pressure, the latter of which may exceed 300 atmospheres. Common screw speeds are between 100-200 rpm but high speed extruders for adiabatic conditions can rotate between 400-500 rpm. Adiabatic conditions reduce energy consumption as no external heat generation or cooling is required to process the material which is solely driven through by the screw; achieving these conditions brings stability to the temperature fluctuations in the extruder. Internal cooling of the screw can be used to prevent degradation of polymer if high rotational speeds are producing unnecessary heat. The efficiency of an extruder is measured in kilograms of extrudate produced per kilowatt of power consumption.

2.3.2 Pipe manufacturing

PE pipes are produced using an extruder as shown in with suitable dies. Pipe fittings such as extension tees, elbow joints, and valves can be made from variety of other production processes such as heated presses, compression moulding, or injection moulding. Pipes can be manufactured using a single extruder, multiple extruders, or extruders using multiple feeds. A flow chart of a pipe production line is shown in Figure 2-14 with each stage numbered. Pipes with multiple layers can be coextruded. The power requirements for the extrusion process are dominated by the

diameter of the extruder barrel, screw geometry, melt viscosity, and the speed of the screw or the rate of extrusion. The length of screw is commonly specified as a length to diameter ratio with values usually in the range of 25-35:1 for thermoplastics. Longer screw lengths ensure the homogeneity of mixture in transit. The diameter of the barrel defines the initial size of extrudate which is later adjusted after passing through the pipe die placed at the end of the extruder barrel.

Figure 2-14 A flow chart of a pipe production line

The pipe die can be a spider die design where the melt directly deposits on a mandrel which is supported by legs shown in Figure 2-15 or a basket die design where the melt is forced though small holes on to a mandrel shown in Figure 2-16. The number of legs in the spider die varies depending on the size of the mandrel that they need to support. The legs need to be streamlined to ensure that the polymer melt is not divided over the mandrel. The basket die design has the advantage as the melt is more evenly split and spaced after going through the die. The melt converges together at the end of die on an area called the land. The land is a typically 15-20 times the annular spacing as a short land length can affect the surface finish of the pipe (PPI, 2014).
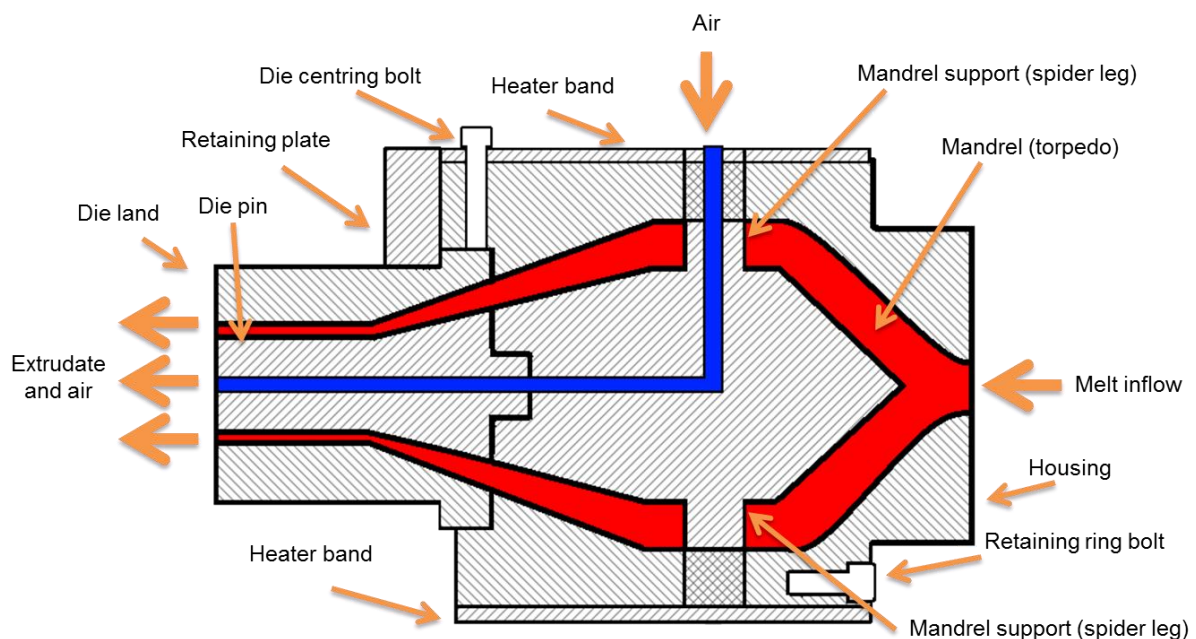
Figure 2-15 Simplified schematic of a spider die design (not to scale) (Kostic & Reifschneider, 2006)

28
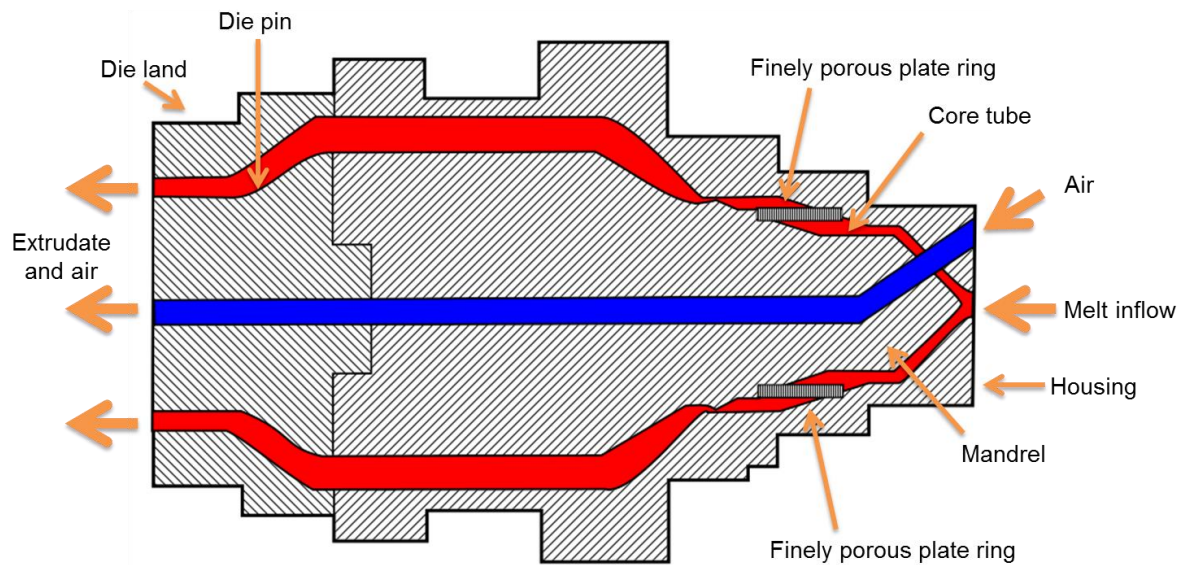
Figure 2-16 Simplified schematic of a basket die design (not to scale) (Kostic & Reifschneider, 2006)

After the die the extrudate proceeds through a sizing sleeve (calibrator) and the cooling tank. In the sizing sleeve, the outer surface of the extrudate is held against a sizing tube or rings using either vacuum or internal pressure, and solidified to retain the shape. Large diameter pipes use adjustable mandrel sizing instead of vacuum or internal pressure. Further cooling of the pipe is achieved through either immersion in water or spray cooling. The length of cooling tank or baths are dependent on the capability of cooling system and the line speed to bring pipe temperature below 70 °C for further handling operations. Spacing between cooling zones is used to enable annealing using heat from the inner pipe wall, annealing is required for reducing the residual stresses generated from the cooling process. In addition to this, annealing also reduces the anisotropy of properties due to extrusion to an extent (PPI, 2014).

Rollers called pullers are adjusted according to the extruder screw speed to provide a constant pulling rate. The speed of the pullers can be varied to adjust the wall thickness of the pipe. The pipe is marked after the cooling stage with details such as pipe size, pipe class, SDR and pressure rating. The marking techniques include ink, hot stamp, and indent. The marking should not vary the thickness of the pipe wall below the minimum value allowed. Majority of the pipes used are not extruded on site using continuous extrusion production process due to the difficulty of setting up production (Tubi Group, 2014).

The pipes are cut or coiled before storage or transportation. Pipe can be supplied in long lengths if they are coiled typically if the diameter is below 150 mm. Manufacturers making use of advance pipe coiling technology can supply pipes in lengths up to 4600 m. However, larger diameter pipes such as those above 150 mm or pipes with thicker walls may prove difficult to coil. Due to the limitations imposed by transport methods available, extruded pipes are cut to accommodating sizes typically in lengths of up to 12 m. Specialist manufacturers can provide pipe with diameters of up to 2500 mm in long lengths up to 600 m, if the pipe is to be transported by sea (PipeLife International GmbH, 2000). Pipes available in long lengths reduce the number of welds required for a pipeline system and in turn the number of potential defects arising from welding processes.

2.3.3 Pipe design

HDPE pipe in use may be under internal and external loads which can be static or dynamic. They are therefore selected to withstand specific loading situations. This section describes the design process to select required parameters of PE pipes such as pipe wall thickness and diameter based on required service conditions such as the service environment and pressure rating.

In order to maintain compatibility between manufacturers, the pipe sizes are standardised (Janson, 1989, p. 65). A standard dimension ratio (SDR), the ratio of external pipe diameter (OD) to the ratio of pipe wall thickness (t) is used by all manufactures, as in Equation 2-2). It is a method of rating the durability of the pipe against pressure where pipes with lower SDR values can withstand higher pressures. Typical SDR values are 7.4, 9 11, 13.6, 17, 21, 26, 33 and 41. However, SDR 11, 17.6 and 26 are most commonly used in the industry (Troughton & Booth, 2000).

Equation 2-2

$$SDR = \frac{OD}{t}$$

A good design will ensure safe operation of pipeline and longevity. Typically a pipeline is designed to last 50 years at a temperature of 20 ºC (Troughton & Booth, 2000), this requirement is now being considered for extension to 100 years if possible in order to save costs incurred in replacing pipelines. The behaviour of the

pipe is affected by load, time, and temperature. Therefore, for long term operation it is necessary to calculate the resistance to internal and external pressures that produce the stresses that the pipe experiences while in service. The results of the long term tests are extrapolated using mathematical techniques to estimate the service life of the pipe.

The most common long term test is the hydrostatic pressure test. Pipes are subjected to internal hydraulic pressure for periods between 120 and 1000 hours depending on the standard used. The time to burst is also recorded and plotted against stress on a log-log scale. This test is often conducted at elevated temperatures up to 80 ºC to accelerate failure. Mathematical techniques such as horizontal and vertical shift functions can be used to produce the shape of 20 ºC curve and extrapolate it to 50 years from the curves produced at elevated temperatures. The values for minimum required strength (MRS) of the pipe material after 50 years are then obtained (Janson, 1989). In practise, a safety factor or a design coefficient (CD) is applied to MRS to calculate the hydrostatic design stress (HDS) using Equation 2-3:

Equation 2-3

$$HDS = \frac{MRS}{CD}$$

HDS is defined as the maximum hoop stress applied continuously using internal hydraulic pressure for long term period. Typical values for the safety factors are between 1.25 (minimum) and 1.66 for water applications. However, in safety critical applications, such as natural gas or super critical carbon dioxide, higher values of 2-3 are used. HDS is used with the working pressure to specify the pipe dimensions (Troughton & Booth, 2000). The equation for hoop stress can be rewritten as Equation 2-4 to include HDS, SDR and working pressure (P_w):

Equation 2-4

$$HDS = \frac{P_w}{2}(SDR - 1)$$

The actual value of allowable working pressure is much lower due to the HDS, and HDS values tend to be higher for larger diameter pipes. Internal or external pressures and the pipe weight are the typical type of sustained loads that are

accounted for in pipe design. This includes dynamic loads that arise in pipes due to rapid change in the mean velocity of the fluid travelling in the pipe. The change in velocity stems from opening or closing of valves, starting or stopping of pumps and failure in pipe.

The HDS also accounts for occasional dynamic loads such as wind and seismic. It is also applicable to the sustained secondary loads not accounted for in design such as settling of pipe supports or failure of pipe support (Janson, 1989, p. 71). Table 2-4 lists the classification of PE pipe by MRS, which is the stress the pipe can sustain at 20 ºC for at least 50 years.

Table 2-4 Pressure classification of pipes (Troughton & Booth, 2000)

Application	MRS/MPa	CD	HDS/MPa	Max allowable working pressure, P_w (bar)		
				SDR11	SDR17.6	SDR26
Water	10	1.25	8.0	16.0	10.0	
	6.3	1.25	5.0	10.0	6.0	4.0
Gas	10	3.0	3.3	7.0	4.0	2.5
	8.0	3.0	2.7	5.5	3.0	2.0
	6.3	3.0	2.1	4.0	2.5	1.5

2.3.4 Quality control

Quality control for PE pipes can be split into 3 phases: material quality control; quality control of pipe processing during manufacturing and that of the finished product, (PPI, 2014, p. Chapter 4). Incoming raw materials can be tested for contamination, density, and the melt flow rate to ensure they meet the specification necessary for production. Long-term strength of the pipe strongly depends on the polymer resin, the additives incorporated during the compounding process, and the manufacturing process of the pipe.

HDPE exhibit lower number of tie molecules due to less branching, hence, they are more susceptible to stress rupture. Therefore it is recommended that HDPE pipes are extruded from bimodal MWD resins that offer some protection against stress rupture. Premature fracture due to stress cracking was a frequent concern in early grades of HDPE. These grades are classified as type 1 by DIN 8075 (1965) standard used in 1970's; the latest revision of this standard is in DIN (2011).

A suitable choice of density, MI and MWD can reduce the likelihood of stress cracking. For long term behaviour prediction it is important that different grades of resins are not blended together. Since the weakest grade in terms of long term material properties will determine the long term performance of the pipe. The extrusion process has several controls built in to monitor the quality of production and control production parameters to achieve production tolerances. The temperatures along the length of the extrusion line are monitored to ensure that polymer melt does not experience thermal degradation and the extrudate is cooled sufficiently when leaving the cooling bath. The gravimetric control ensures that the raw material input matches the pipe output by adjusting the extruder parameter. The thickness of the pipe is monitored using ultrasonic measurement system. In addition to these quality control systems, manufacturers usually perform routine quality control tests on product.

Pipe extrusion can suffer from several types of defects such as foreign particles, gas bubbles, thermal degradation and spider lines if a spider die design is used with insufficient pressure. High screw speeds lead to phenomenon known as shark skin where turbulent flow causes the extrusion to take place in layers. Figure 2-17 shows the windows visible in a microfilm image of a ribbon cut from the pipe wall. These windows are generated due to improper extruder parameters causing uneven mixing to take place.

If pipes experience oxidation during the cooling phase straight after processing, there is a risk of surface degradation due to elevated temperatures. The atmospheric oxygen is absorbed by carbonyl groups at the surface which when oxidised further can break the polymer chains that act as tie molecules. This reduces the molecular weight of the region and encourages crack growth since a smaller number of tie molecules exist to carry the force when they are strained (Janson, 1989, p. 34). Microtomed slices of the surface layer of 0.1 mm thickness or less would be sufficient to determine the extent of the oxidation using analytical methods such as chemiluminescence (CL), differential scanning calorimetry (DSC), and Fourier transform infrared spectroscopy (FTIR) (Ilie, 2009).
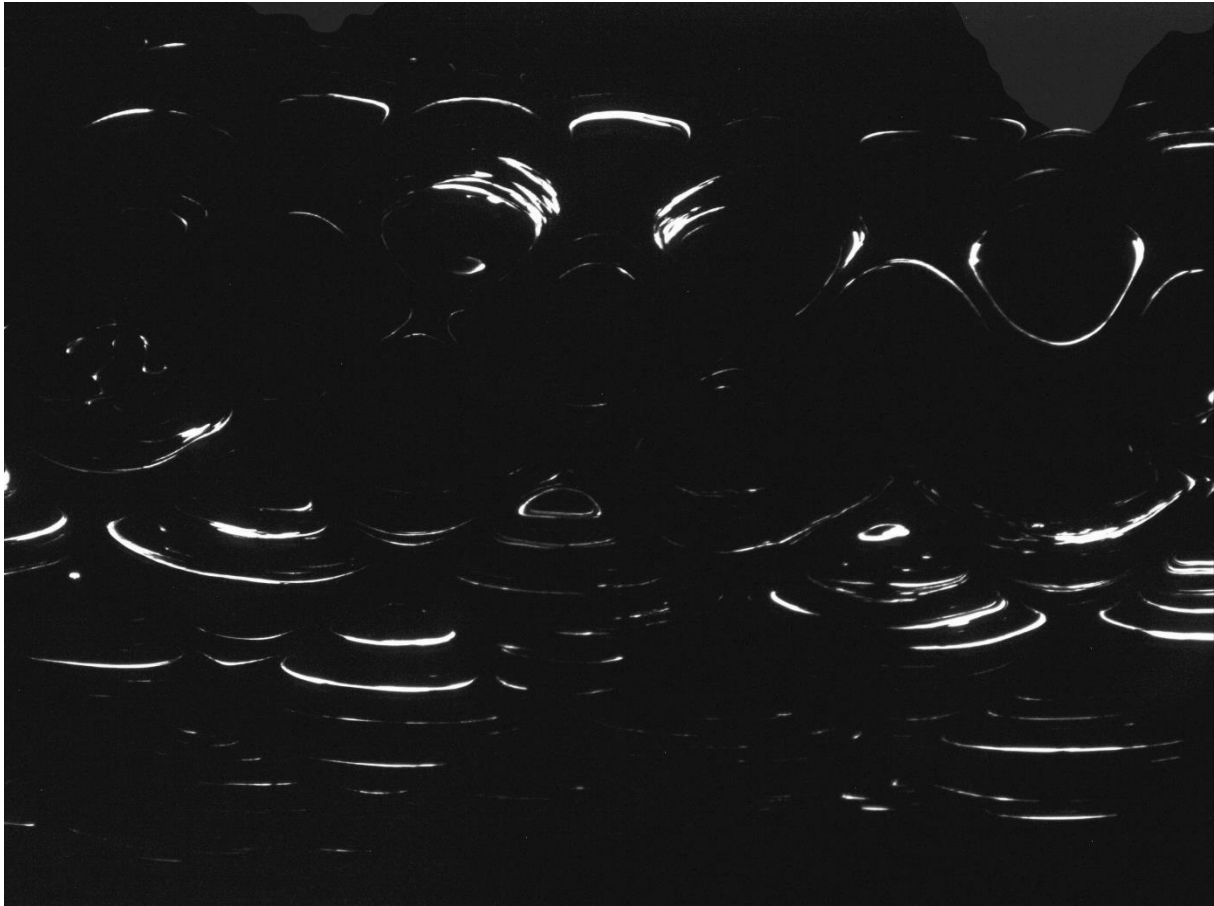
Figure 2-17 Microfilm image of a ribbon cut from the pipe wall showing windows

Depending on cooling process and parameters, the residual stress field may in the pipe wall. For externally cooled pipes, the inner pipe surface will have larger crystalline regions as it is cool slowly while the outer pipe surface is essentially quenched. This causes the residual stresses to building up in the pipe wall with their magnitude matching the pipe wall thickness and temperature difference between the inner and the outer layers. The circumferential residual stresses in this case are compressive in the outer layers and tensile in the inner layers. There are also longitudinal residual stresses that are compressive in nature. They form due to the stress imparted by the pulling mechanism on the cooled pipe being removed from the cooling tanks, freezing in the stresses.

Dimensional tolerance limits are set for pipe diameter, pipe wall thickness, ovality, and length. The service limits are set for pipe content, pressure, and temperature. Both dimensional tolerance and service limits are set by standards such as ASTM D2122-16 (2016b) and ISO 161-1 (1996). Separate standards apply for the gas and water industries. The gas industry uses ASTM D2513-16a (2016c), EN 1555-2 (BS,

34

2010), and ISO 4437-2 (2014b) standards. The water industry uses ASTM D2737-12a (ASTM, 2012a), EN 12201-2 (BS, 2011), and ISO 4427-2 (2007b) standards. Some of the tests used for quality control specified by these standards are listed in the Table 2-5.

Table 2-5 List of some of the characteristic test methods used for the purpose of quality control

Characteristic	Standard	Specimen	Term
Hydrostatic strength	ISO 1167-1 (2006a)	Pipe	Long
Elongation at break	ISO 6259-1 (2015a)	Coupon	Long
Resistance to rapid crack propagation	ISO 13477 (2008a)	Pipe	Short
Resistance to slow crack growth: cone test	ISO 13480 (1997a)	Coupon	Long
Resistance to slow crack growth: notch test	ISO 13479 (2009)	Pipe	Long
Thermal stability	ISO 11357-6 (2008b)	Coupon	Short
Melt flow rate (MFR)	ISO 1133 (2011b)	Coupon	Short
Heat reversion	ISO 2505 (2005)	Pipe	Short
Resistance to gas constituents (as specified in ISO 4437-1 (2014a) Annex A)	ISO 1167-1 (2006a)	Pipe	Long

2.3.5 Service conditions

The majority of the PE pipes in service are either submerged underwater or buried underground. Only a small exception of HDPE pipes has over ground applications such as in the nuclear industry or for use in fire protection systems. Two implications that arise from underground or underwater conditions are the importance of installation and the accessibility difficulties that make maintenance expensive (Janson, 1989).

For soil burial, it is normally necessary to use surrounding filling (backfill) to support the pipe and prevent point loading. It is especially crucial if the pipe is flexible as in case of sewage pipes, otherwise the stability of the circular cross section is compromised. This deviation from the circular cross-section is known as ovality and affects how the pipe handles the buckling stress. It is recommended that the soil is compacted to a specific depth for a given load in order to properly provision for the distance between the pipe supports. In areas where traffic is expected to traverse over the pipe, it is necessary for soil refilling to account for settling and compaction. Nature also plays a role in settling and compaction of surrounding soil via ground water movements, seismic activity, and frost action etc. Compaction of soil around the pipe should be homogenous and well distributed around the pipe. Uneven

settling around the pipe can lead to premature fracture due to uneven distribution of loading forces.

A submerged piping system needs a higher safety factor due to forces arising from seabed floor and through the movement of the surrounding fluid. Concrete weights are designed to counteract the forces acting on the pipe and provide sufficient loading to lower the pipe towards the seabed. Rubber linings are used to interface between pipe and the concrete weights; therefore weights can also function as ring stiffeners for the pipe. Submersion of pipe must account for the maximum strain due to bending as it is being installed. Certain areas that exhibit abnormally high wave forces require the seafloor to have a trench excavated that can provide shelter to the pipeline (Mohitpour, 2008).

Pipes in each environment are exposed to some form of weathering which is defined as the sum of processes of polymer degradation through exposure to natural environment leading to change of material properties, colour, and shape etc. The degradation can be caused by: absorption of moisture; chemicals such as acids, alkalis and salts; photo-oxidation usually in the form of ultraviolet (UV); and variation of temperature extremes where high temperatures accelerate the rate of some reactions and reduce the load carrying capacity.

The primary method of joining PE pipes is welding while joining of PE to dissimilar materials is accomplished using mechanical couplings. Beside the method of joining, the service environment determines the type and performance of the joining methods available.

2.4 Welding of PE Pipes

This section lists the different available welding techniques for plastics before focusing on the butt fusion welding process for PE pipe. An over of the theory of welding for thermoplastics is given followed by a short discussion on the microstructure of butt fusion welds in pipes. The standards that define the butt fusion welding procedures and defects in the butt fusion welding process are conferred before briefly discussing the non-destructive techniques used for detecting the said defects.

2.4.1 Welding techniques for plastics

Joining of thermoplastic pipe is achieved mainly by welding using heat or when required, by mechanical couplings or adhesive bonding (Yousefpour, et al., 2004). The welding techniques can be divided into three categories based on the method of heat is induced. The methods of heat generation and welding techniques that stem from it are shown in Figure 2-18. Regardless of the heating method used, the welding temperature achieved must be above the melt temperature (or glass transition temperature for amorphous plastics) to ensure that the plastic material is softened sufficiently to form a good weld.

Figure 2-18 Overview of thermoplastics welding techniques categorised according to the heat induction mechanism employed, (TWI, 2011)

2.4.2 Butt fusion welding

The butt fusion welding process involves the following steps: the pipes are clamped, trimmed (trim cycle) and checked for alignment (check cycle); next is the bead-up stage where the pipe ends are brought in contact with the heater plate; this is followed by heat soak period for a specified time; the heater plate is removed rapidly (dwell time) and the pipe ends are swiftly brought in contact under fusion pressure and remained clamped until the set cooling time is reached. A manual process requires all stages of the welding cycle to be completed in the set order in the required time. A semi-automatic or an automatic process controls several aspects such as removal of the heater plate and joining of heated pipes in quick steps.

Figure 2-19 shows the change in pressure and temperature during a butt fusion welding cycle. For large diameter pipes dual pressure cycles are sometimes recommended which reduce the amount of material displaced in weld beads, shown in Figure 2-20.
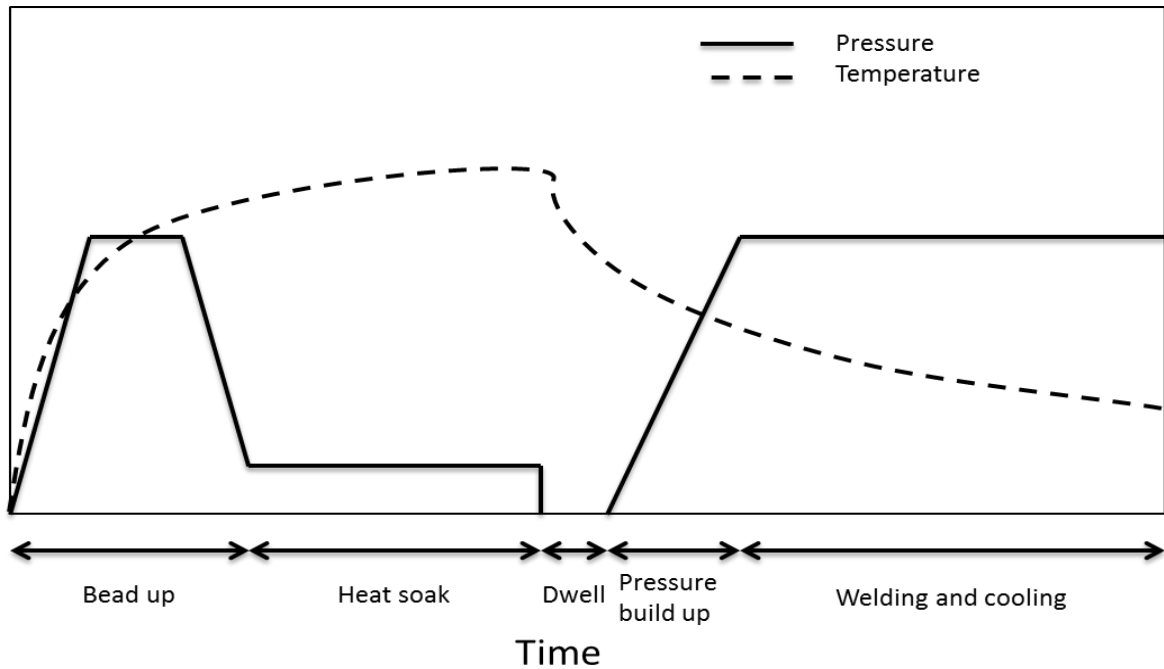
Figure 2-19 Variation of pressure and temperature with time at the interface during a butt fusion welding process cycle (TWI, 2006)
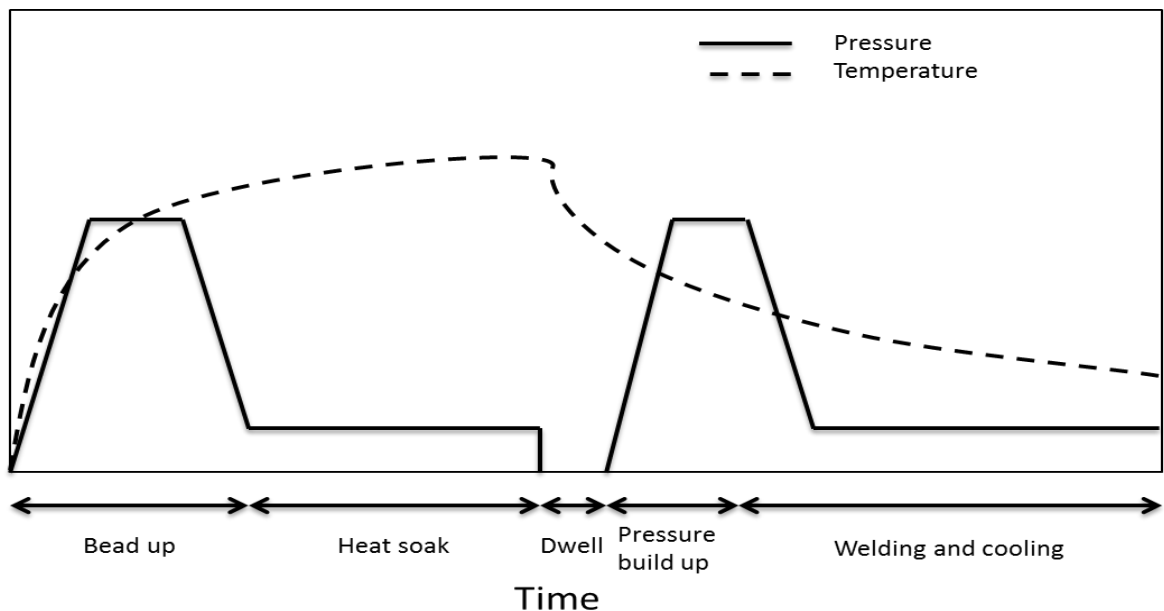
Figure 2-20 Dual pressure butt fusion cycle, (Troughton & Booth, 2000)

The dual pressure cycles differs from the standard cycle by dropping the fusion pressure after a set time, this reduces the amount of molten material being displaced

into weld beads and increases the time the weld interface temperature is above the crystallisation temperature of the material (Troughton & Booth, 2000). The polymer chains diffuse at the weld interface above the crystallisation temperature for a longer period than single pressure cycle. Arbeiter, et al. (2013) shows the impact and fatigue performance of the dual pressure cycle welds to be better than those of single pressure cycle welds. The welding parameters for the butt fusion welding process are summarised in Table 2-6.

Table 2-6 Key butt fusion welding parameters, (TWI, 2006)

Welding parameter	Units
Bead-up pressure	MPa (or N/mm^2)
Heat soak pressure	MPa (or N/mm^2)
Bead size	mm
Heat soak time	S
Dwell time	S
Fusion pressure	MPa (or N/mm^2)
Cooling time	minutes/seconds
Heater plate temperature	^{0}C

2.4.3 Theory of welding of thermoplastics

The application of welding theories relies on the theories of chain dynamics. Small molecules in liquid state undergo translation motions of short diffusion length under applied stress or when under the effect of Brownian motion. For larger molecules like chains the sum of these displacements leads to global conformational change or sliding of the chain relative to its neighbours. The motions of short chains or chain segments with MW lower than MW between entanglements can be accounted for by the use Rouse model while the behaviour of entangled chains is described by de Gennes reptation model (Halary, et al., 2011).

Welding is an interaction at the interface of surfaces of interatomic and intermolecular forces. Discussion of such phenomena is spread across the discipline of surface chemistry, thermodynamics, physics, rheology, polymer chemistry & physics, stress analysis, and fracture mechanics (Awaja, et al., 2009). There are several theories that endeavour to explain the process behind welding of polymers (Brinken, 1982; Brown, 1991):

1. Adhesion theory: ratio of surface energies of the two materials where the maximum adhesion is obtained in the case of identical material where the specific contact surface energy is zero.
2. Viscoelastic contact theory: molecular forces such as Van Der Waals act on the surfaces which deformed under welding pressure, forming a boundary surface as a function of time.
3. Diffusion theory: diffusion of chains or chain segments across the weld interface, provided that the polymers are mutually soluble and the molecules have sufficient mobility achievable by exceeding a certain minimum temperature threshold.
4. Flow process theory: mechanical displacement of chains in the flow field generated by the welding pressure and temperature, forcing mixing to occur as a result of both thermal and mechanical displacement processes.

The adhesion theory does not account for the melt flow index. Brinken (1982) establishes a criterion for compatibility for welding of different PE types based on: surface contact energy; viscoelastic properties; chemical structure in the forms of solubility and melt index; and welding parameters of pressure and temperature.

Parmar (1986), Rashid (1997), and Bonten and Schmachtenberg (2001) have previously reviewed the literature on the theory of welding and summarise the following:

- After reviewing both the diffusion theory discussed in the works of Kinloch (1987) and Voyutskii (1963) and viscoelastic contact theory devised by Anand and Karam (1969). Potente (1977) suggested that both of these mechanisms occurred simultaneously in the butt fusion welding process.
- Malguanera and Earles (1982) investigated the diffusion theory in joining of thermoplastics and its effect of joint quality in their work; they proposed that the joint strength was due to diffusion of chain segments through the weld interface.
- Wool, et al. (1989) like Potente agreed with both viscoelastic contact and diffusion theories. They stated that Van Der Waals forces act on the interface created by the contact of molten surfaces followed by diffusion of chain segments.

- Yuan and Wool (1990) recommended that the mechanical strength at the weld interface can be optimised by controlling the processing thermal history.

- By considering the adhesion theory, Dodin (1981) divided the welding mechanisms in two groups where there are processes which join the parts and processes which enable the conditions for the first group processes to progress. Dodin proposed removal of contact surfaces to enable molecular contact in order to achieve good bonding. As Grimm (1990) states, good bonding is achieved by chain diffusion under applied pressure after polymers have been heated to a viscous state.

- Grandclement (1989) related the diffusion of chains across the weld interface to fusion temperature and heating time in electrofusion welding; where chain diffusion can be promoted by increasing either quantity. Similar conclusion is reached by Maine and Stafford (1985) for butt fusion and electrofusion welding processes for PE that chain diffusion and mixing readily occurs in the molten state.

- Stoke and Hobbs (1989), Watson (1988) and Dodin (1981) established MW as a factor in joint strength as it influences the movement of chains. To improve weld strength the mobility of the chains can be improved by reducing the viscosity of the polymer melt; either by using lower MW polymer or by increasing the welding temperature.

- The dependence of joint strength on the molten flow displaced from the weld interface was studied by Potente and de Zeeuw (1979) and Neubert and Mack (1973); their results suggest that the possible strength increase in the joints is due to intermixing encouraged by shear flow of the molten polymer.

A model proposed by Ezekoye, et al. (1998) proposed to combine the reptation theory with prediction of strength from empirical studies to describe the welding process. The reptation theory assumes a steady state temperature profile while no physical explanation is offered by empirical studies for correlation. The proposed model relates the material properties to the welding parameters by accounting for the temperature dependence of the chain diffusion. After validation by experiment, the model propose that for producing virgin strength welds an ideal range of power densities exists; above which polymers degrade without enough time to sufficient heal and below which there is inadequate energy input into the weld zone. Nonhof

(1996) proposed an optimisation procedure based on full factorial experiment design for hot plate welding which accounts for heating time, temperature, and pressure. The new combined diffusion and geometrical model accounted for interaction between the individual welding parameters.

It is possible for a welded polymer to achieve strength equal to that of the bulk polymer if it is kept above a temperature that allows for molecular motion to occur, for a sufficient amount of time (Grewell & Benatar, 2007). Lack of sufficient molecular motion would lead to failure modes such as chain pull-out or chain fracture in the weld (Bartolai, et al., 2016).

2.4.4 Microstructure of butt fusion welds in pipes

A number of researchers have studied the structure of butt fusion welds using different microscopy techniques. Barber and Atkinson (1972) have performed a study using both electron microscope and transmission light microscope with 6M chromic acid etchant on butt fusion welded polyethylene and polybutene-1. They concluded the microstructure to consistent of five different zones due to a steep temperature gradient that exists in the weld region, as shown in Figure 2-21.

(a)

3. Hottest material
2. Cooler material
1. Remnant of skin
4. Boundary layer
Surface cooling

(b)

4. Boundary nucleation
2. Spherulitic, slightly elongated
1. Remnant of skin
3. Columnar
5. Spherulitic
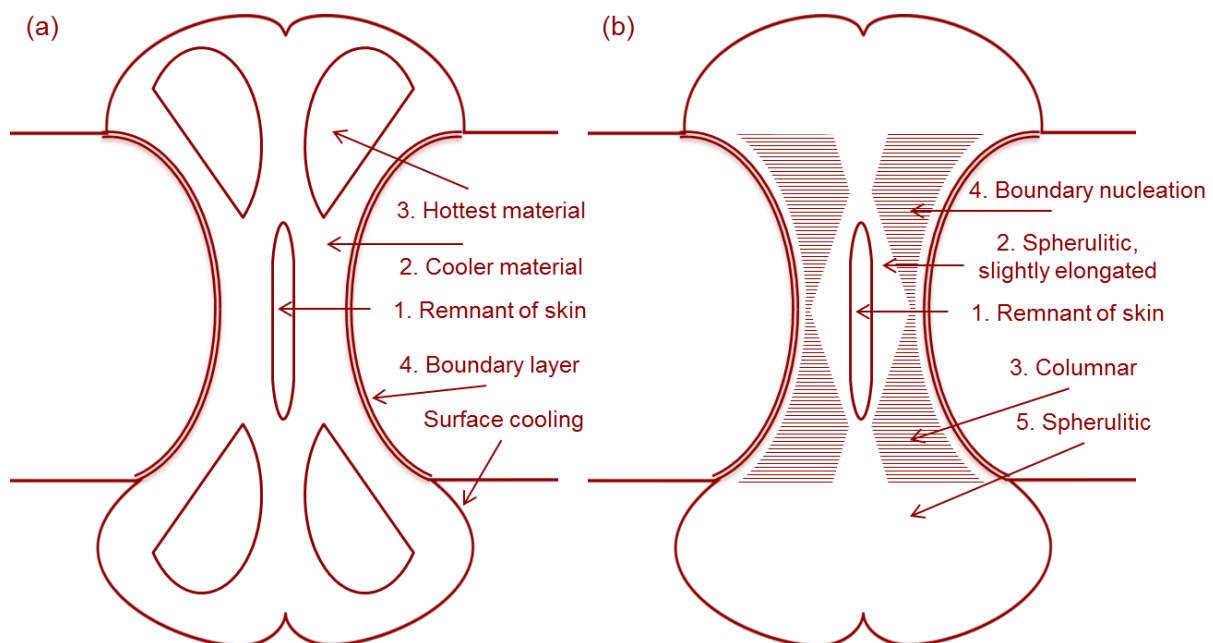
Figure 2-21 Temperature distribution during the final stage of welding (a) and expected microstructure after completion of welding (b), in a section through pipe wall (Barber & Atkinson, 1972)

42

During the final stages of welding the following is expected in the zones:

1. The dwell time will determine the thickness of the central skin. Upon contact of hot pipe ends under pressure the skin is expected to remain stationary due to adhesion while the hotter material flows past it until the skin is melted either partly or fully.
2. The cooler layer is composed of material that is the furthest away from the heater plate. Upon contact of hot pipe ends the cooler layer is expected to be thickest in the centre of the pipe wall as the hotter material is pushed out.
3. The hottest material is expected to be pushed out into the weld beads due to the effect of fusion pressure.
4. The temperature of the boundary layer is expected to be below the melting point but above the softening temperature allowing the layer to deform easily between the hard and cool parent material, and soft and hot weld material.

After the final stage of welding it is expected in the zones:

1. Magnitude of the welding pressure will determine the microstructure and thickness of the skin zone.
2. The amount of material in the region and its temperature will be determined by the welding pressure. At low welding pressure the region will be thick and the material sufficiently hot enough to melt the skin and destroy its nuclei with subsequent slow cooling forming large spherulites. At higher welding pressure the cooler material adjacent to the skin will experience directed growth of spherulite and high welding pressure the material in the skin region will be rapidly cooled forming fine-grained structure of small spherulites.
3. The material near the surfaces of the pipe wall is expected to be hot with a large thermal gradient adequate to induce columnar growth towards interface.
4. All along the boundary it is expected for nucleation to occur.
5. The material in the weld beads will lose heat radially. After solidification of the surface the rate cooling is expected to fall and conventional spherulitic to form in the remaining material.

Later Atkinson and deCourcy (1981) proposed that the columnar structure in zone 3 is due to molecular orientation rather than due to the differences in the crystalline structure after using by chromic acid etchant which is effective on the amorphous

and low MW areas of PE. Galchun, et al. (2015) confirm and conclude: restructuring of the crystalline face due to welding leading to improved local properties.

Stevens (1990) evaluated butt fusion welds in PE and polypropylene using FTIR-microspectroscopy verified by DSC and X-ray diffraction. The crystallinity within the weld zone was found to be lower at the centre of the weld. However, due to the cooling history of the pipe the crystallinity across the pipe wall was higher at the centre than at the surfaces. The welding process reduced the amount of crystalline phase oriented parallel to the pipe axis, changing the orientation to the flow direction of the weld. Stevens (1993) used DSC, scanning electron microscopy (SEM), and transmission light microscopy (TLM) to supplement FTIR work with etching. The welds made using different welding conditions could be distinguished by morphology or microstructure but not always by tensile strength. Both DSC and FTIR showed annealing effects occurring beyond the weld region, the effects of which are not optically visible. SEM analyses of etched samples showed such areas which did not show any visible morphological changes under TLM. Toluene etching was able to reveal the sub-spherulitic details in PE. Lastly, the DSC endotherms confirmed that the morphology of PE was unaffected by the welding process in terms of distribution of lamellae and spherulites, and their thickness and size.

2.4.5 Numerical modelling of the butt fusion welding process

Shillitoe, et al. (1990) proposed one of the first combined decoupled thermal-mechanical models for butt fusion welding as a proof of concept. The heat transfer model calculated the thermal profile which was then used by the mechanical model to implement deformation behaviour while accounting for the temperature dependent material properties, up until the bead up stage. Chang and Teng (2004) use numerical modelling to calculate residual stresses and validated using X-ray diffraction. Modelling by Riahi, et al. (2011) validated experimentally in order to investigate the effect of temperature and pressure on the mechanical characteristics of BF welded PE pipe. It was suggested that impact energy correlated with the welding pressure. The most complete numerical simulation was offered by Yoo, et al. (2017) which included all stages of the butt fusion process including reproduction of flow due to thermal expansion and squeezing and fountain flow in the joining stage. The model was validated experimentally, offering direct observation of flow behaviours during butt fusion welding.

2.4.6 Standardised butt fusion welding procedures

Current standards and procedures such as: ASTM F2620-12 (2012b) revised in 2013 (ASTM), DVS 2207-1 (2005) revised in 2015 (DVS), ISO 21307 (ISO, 2011a), TR-33 (PPI, 2012), and WIS 4-32-08 (2002) revised in 2016 (WIS), provide guidance on butt fusion welding of HDPE pipe. These five standardised procedures are used worldwide and cover the major industry sectors that use PE pipes. Figure 2-22 shows the countries that use one or more of the mentioned standards in the industry. The European standards DVS, ISO and WIS recommend fusion interfacial pressure of 0.15 ± 0.02 MPa and heater plate temperature of 230 ^{0}C (+10 ^{0}C, -5 ^{0}C). ASTM standard recommends the fusion pressure to be 0.41-0.62 MPa and the heater plate temperature to be in the range of 204-232 ^{0}C. The largest discrepancy is in the fusion pressure; where ASTM recommends 2.4-4.8 times the pressure suggested by the European standards. The Plastic Pipe Institute (PPI) produced the TR-33 report which uses the ASTM standard to recommend a criterion for ideal and acceptable range of values for fusion pressure and temperature. The TR-33 report is provided to be used as a generic butt fusion welding procedure.

Figure 2-22 Countries highlighted in red make use of ASTM, DVS, ISO and WIS standards for butt fusion welding of PE pipe.

2.4.7 Defects in butt fusion

There are several sources where defects originate in a butt fusion weld. The defects can be divided into two categories: those that are caused by contaminations and those that are caused by inappropriate welding parameters (Troughton & Booth, 2000). The presence of contamination at the weld interface can be due to contaminations on the hot plate or in the environment such as dust, pollen, or oil

from finger prints. The welding parameters should be adjusted for the given pipe dimensions and material. Investigation by Lai, et al. (2016) on effects of defect on the failure of butt fusion welded PE pipe showed that under different short-term loading conditions the failure of joints was unaffected by a single welding defect provided if the defect size was smaller than 15% of the pipe's wall thickness.

Where possible, the welding should be carried out in a weatherproof shelter. Pipe end plugs are inserts that cover the exposed ends of the pipes, to eliminate drafts through the pipe. An ideal shelter will prevent wind from carrying dust, sand and other contaminants towards the weld interface. The trimmer to plane the pipe ends should have sharp blades that produce continuous swarf of uniform thickness as blunt blade will lead to uneven pipe ends. The trimmer blades should be toughened to prevent particulates of material breaking off and embedding in the pipe ends.

A common practise in the industry is to carry out a dummy weld to clean the hot plate. The hot plate should be placed in its enclosure to prevent surface contamination. The enclosure should be thermally insulated to reduce energy consumption and maintain hot plate temperature. The hot plate surface is coated with polytetrafluoroethylene (PTFE) to prevent sticking of the molten polymer. The PTFE coating should be renewed if damaged or worn to maintain its effectiveness.

Diffusion of polymer chains across the weld interface takes place above the crystallisation temperature of the pipe material. If the crystallisation temperature is reached prior to sufficient molecular diffusion, this will lead to a cold weld due to lack of molecular chain diffusion across the weld interface (Troughton & Booth, 2000; Pokharel, et al., 2016). The conditions leading to cold weld are either due to heater temperature being lower than necessary or the dwell time is prolonged enough to cause cooling of the pipe ends, a combination of insufficient heat and heat soak time (Atkinson & deCourcy, 1981; Bucknall, et al., 1980; deCourcy & Atkinson, 1997). Low fusion pressure will not ensure proper contact of the heated pipe while high fusion pressure is likely to push most of the heated material out into the bead. Cold welds fail in a brittle manner at the weld interface when tested.

Excessive heater plate temperatures will degrade pipe material at the weld interface (Zaitsev, 1972; Zaitsev, 1973). This will cause failure similar to cold welds due to bonds in polymer chain breaking which leads to a lack of diffusion because of the

thermal degradation of the chains. It is recommended to use an external thermocouple to measure hot plate surface temperature on both faces at several points where the pipe ends will make contact.

The weld bead should be even on both sides around the circumference of the pipe. A notch around the circumference is produced as the weld beads roll back in the process of welding. If sharply angled, these notches are stress concentrators which may lead to crack initiation. During the formation of the bead, it is expected that the molten material at the end of the pipe will flow away from centre and due to this movement the contaminants will be carried away from the centre of the pipe weld. Thicker pipe wall leads to larger bead size and the increase in bead size is roughly proportional to the thickness of the pipe wall.

Misalignment of pipes whether axial or angular, is a source of defect that is not related to previous categories (Parmar & Bowman, 1989; Bowman & Parmar, 1989). The causes of misalignment are: the pipes are at the opposite ends of permissible tolerances for their internal or external diameters; misalignment of pipes during the clamping stage; excessive ovality in the pipes; and damaged pipe ends. Misalignment sharpens the notch that exists between the weld bead and the pipe wall. It is recommended that the alignment of pipe ends is checked after the trimming stage. For long length of pipes, it is suggested that the use of pipe supports such as rollers will assist in pipe alignment during clamping and welding (Janson, 1989).

2.4.8 Non-destructive detection of defects

There are a variety of non-destructive techniques available for detecting defects in butt fusion welds, such as radiography, ultrasonic and visual inspection techniques (Troughton & Booth, 2000). Visual inspection of the weld and the weld bead is simple and cost effective. If the bead is insufficient in size for a given pipe wall thickness then it could be an indication of insufficient melting during the heat soak time or large dwell time or insufficient bead-up pressure or fusion pressure. If the bead is not uniform circumferentially around the pipe, this indicates a misalignment of the pipe ends. If the bead is removed then a simple bend back test can reveal the presence of contamination (Troughton & Booth, 2000). Removal of the bead eliminates the notch on the outer side of the joint and removal of the inner beads will lead to less interrupted flow.

Ultrasonic inspection relies on the change in wave speed and intensity of any reflections to detect defects using phased arrays and time of flight diffraction techniques (Crawford, et al., 2008). Radiographic testing using X-ray produces good images of volumetric flaws and weld beads. Low energy X-ray (30 kV rather than the 200 kV used for metals) can be used to penetrate through PE pipes. X-rays are not used for inspecting PE joints on site due to the cost of the detection equipment and safety concerns.

2.5   Assessing Performance of Welds

The performance of a butt fusion weld is normally assessed using destructive techniques. Destructive testing can be split into whole pipe (large scale) and coupon (small scale) tests. The remains from the destructive testing can be analysed using techniques such as SEM or other destructive techniques such as microtomy.

Whole pipe tests are more representative of the service conditions due to stress constraints than the coupon tests which experience release of residual stresses during the cutting and preparation operations. Since the coupon tests are cut from the welded joints they are inexpensive to carry out due to their manageable size that yields multiple test specimens per pipe.

2.5.1   Failure modes

The assessment of the test specimen is based on three types of failure modes: brittle, ductile, and mixed which is a combination of the two modes. The key difference between brittle and ductile failure modes is the amount of energy that is absorbed through deformation before failure, which contributes to changes in the volume of the material around the joint. In the coupon specimens, this volume is known as the gauge volume. The deformation produces an increase in empty volume or cavities in brittle failure mode and no change in volume in ductile failure mode (Deblieck, et al., 2011). Pressure, temperature, and time during welding play an important role in the type of failure mode that is likely to dominate. Some stress-strain curves of ductile and brittle failure modes are shown in Figure 2-23.
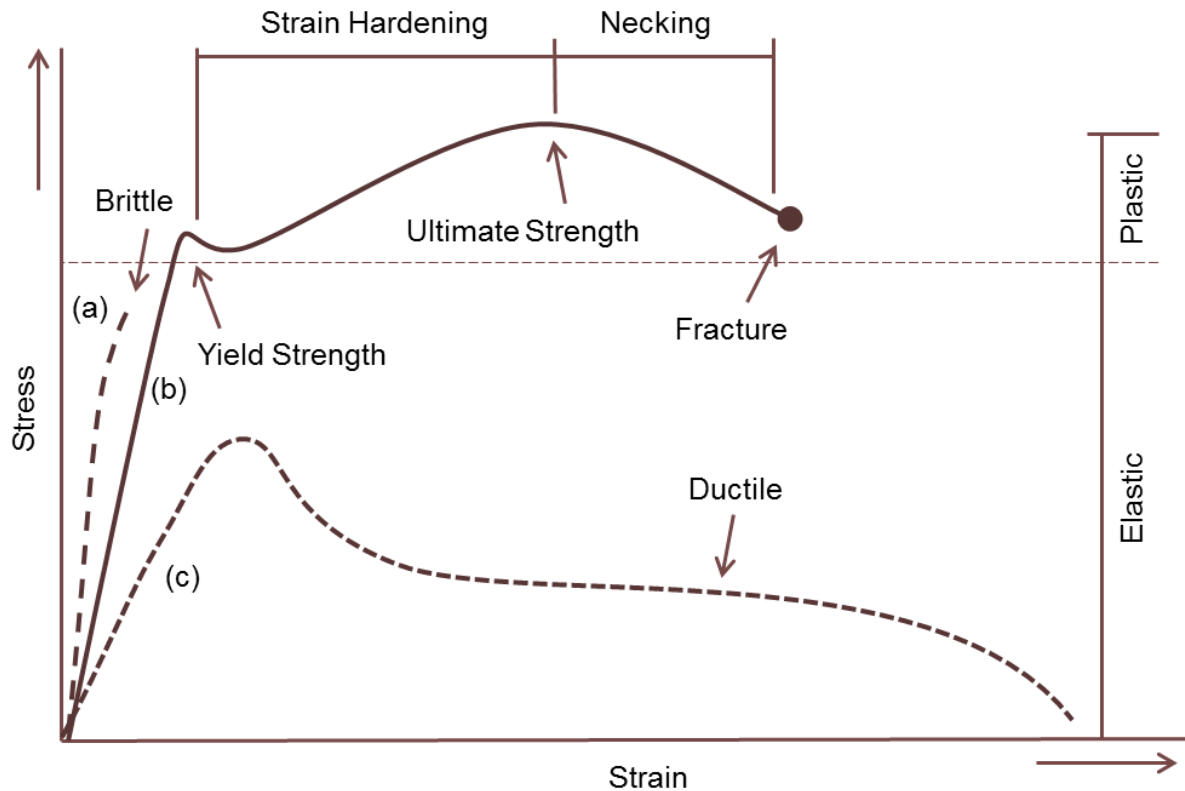
Figure 2-23 Typical tensile stress-strain curves for polymers: brittle polymer (a); ductile polymer with strain hardening (b); and ductile polymer without strain hardening

Depending on type and test temperature of polymers, some polymer show brittle behaviour: they yield very little and fail without large deformations exhibiting very little plasticity (Curve a). Some polymer yield and undergo strain (work) hardening followed by necking under tensile loading and barrelling under compressive loading (Curve b). Other polymers do not exhibit strain hardening (Curve c).

Large deformation in the form of necking in tensile tests results from strain instabilities beyond the yield point in the viscoplastic domain. It is associated with a local stress concentration that results in a non-uniform stress strain field within a sample. Necking propagates in part of the specimen cross-section that is slightly smaller than cross-section of other parts. Deformation in this region is localised due to higher than normal strain where stretching leads to decrease in the cross-section. Necking stabilisation occurs with the beginning of strain hardening without which is the neck is unstable leading to fracture. Further neck propagates through the neighbouring regions, once the stretched chains have reached their extensibility limit or the natural draw ratio. The strain field becomes uniform just before the sample breaks (Halary, et al., 2011).

On a microstructural level the inhomogeneity in the necking behaviour is due to plastic deformation of crystalline lamellae and tie molecules in the amorphous interlamellae regions (Huo, et al., 2013). Lamellae are situated radially in a spherulite. For lamellae there are two deformation mechanisms based on loading conditions and lamellae orientation for the lamellae in spherulites located: at the poles experience interlamellae sliding; and at the equator undergo interlamellae separation. The radial position of the lamellae determines the extent of each mechanism acting on the lamellae at intermediate positions between the poles and the equator of the spherulite (Peterlin, 1971). At low strains the main mechanism is interlamellae sliding followed by plastic deformation due to interlamellae separation which stretches the shape of a spherulite from spherical to ellipsoidal. In the cold drawing regions the high strains break down the spherulites into fibrils, overcoming the plastic instability threshold (Schneider, 2010). The lamellae may undergo strain-induced recrystallization at large deformations in the cold drawing region before failure.

As temperature increases, the molecules receive increasing amount of energy to allow the freedom of movement. There are two characteristic temperatures are important for semicrystalline polymers, the glass transition temperature (T_g) and the melting temperature (T_m). The former is a reversible transition in the amorphous regions of a polymer that as temperature increases changes its behaviour from hard brittle glass state to viscous rubbery state. The MWD controls the width of the temperature around T_g where smaller molecules are affected due to amount of energy required to mobilise the molecules, T_g increase with MW; large cooperative motions of the main chain involving 10-20 bonds. In semicrystalline polymers there are likely to be at least two glass transition values based on the proximity and the interaction of the amorphous chains with the crystalline lamellae. Amorphous chains that are far away from lamellae surface have molecular motions occurring at the same T_g while those near the lamellae surface are constrained as they may form part of short or long folds. Nuclear magnetic resonance technique can be used to investigate the mobility range of chain segments in semicrystalline polymers. T_m defines the point where the crystalline regions of a polymer melt; the value of which depends on the thickness of crystalline lamellae and the MW.

Polymer material is considered to exhibit viscoelastic behaviour where crystalline and amorphous regions have different contributions. The elasticity in both regions is due to local conformations. True elasticity stems from variations of bond angles and bond length observed only at small deformations at preferably low temperatures. The viscous behaviour stems from the conformation of chains as they require energy to move away from their original positions. The plastic behaviour is due to sliding of chain molecules and deformation in the surrounding regions.

The viscoelastic properties of polymers such as creep or stress relaxation are both time and temperature dependent in addition to stress and strain. Creep is an increase in plastic strain under constant stress. Stress relaxation is a decrease in stress under constant strain. The common test methods can be altered to characterise other material properties such as creep, stress relaxation and stress rupture. The factors that affect creep and stress relaxation are stress, strain rate, temperature, and time. For instance, creep increases with elevated temperature relative to the glass transition temperature of the material and decreases with strain rate as seen in Figure 2-24.
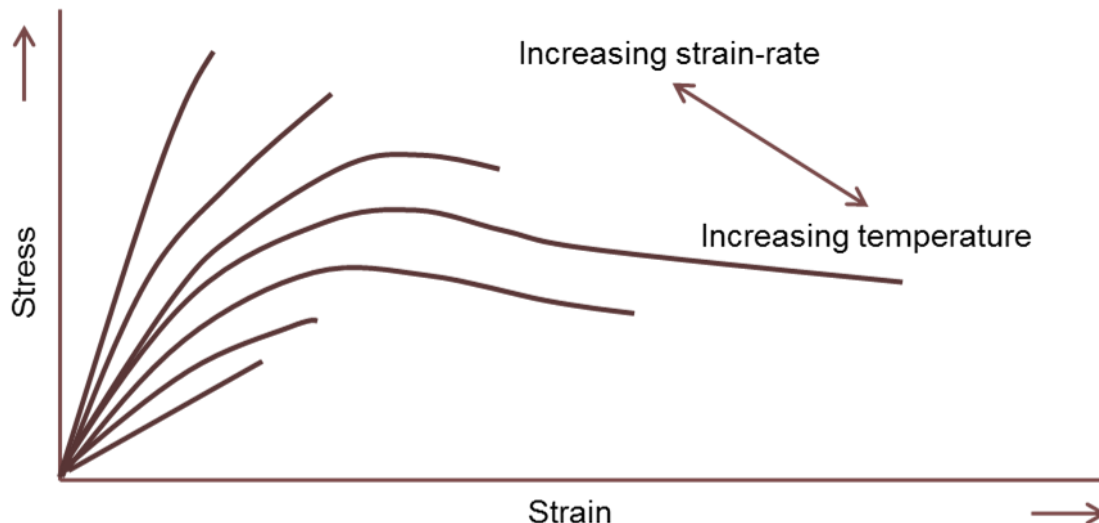
Figure 2-24 Change in creep due to increase in strain-rate and temperature, (PPI, 2014, p. 58)

Creep is a time dependent deformation of a material that is subjected to stress below the yield strength. Creep is expected to occur in polymers operating above their T_g (Udomphol, 2007). Creep has three distinct stages, Figure 2-25. Primary creep is known as transient creep where the creep resistance of the material increases due to material deformation, decreasing the creep rate. Secondary creep is nearly

constant, the average value of which is known as the minimum creep rate. Tertiary creep has a rapid increase in creep rate due to reduced cross-sectional area of the material carrying the load. The shape of the creep curve will change in a similar manner to the stress-strain curve shown in if the rate of creep changes.
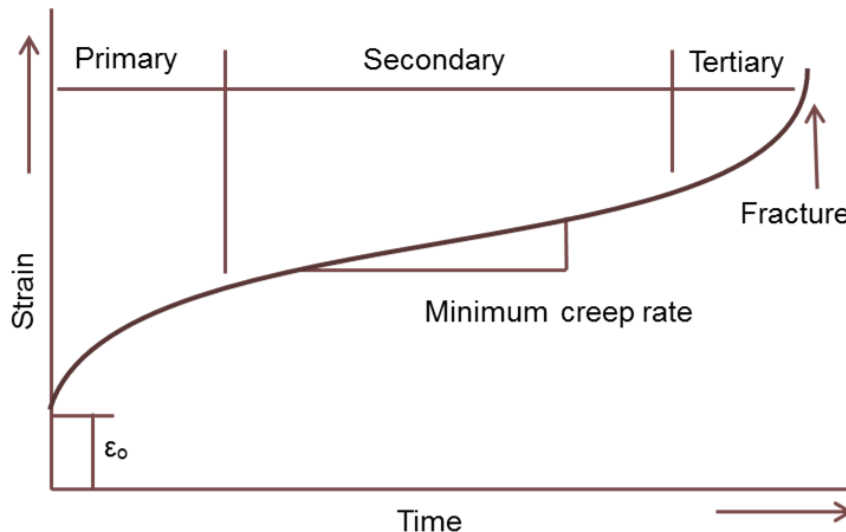
Figure 2-25 Typical creep curve showing three stages of creep

Stress relaxation describes the decrease in stress of a material while the strain remains constant (Inc, 2009). When the material is unloaded it will only partially return to its original shape due to elastic recovery, showing plastic deformation despite the stress value being below the yield strength of the material. Stress relaxation is considered an inverse of creep (Osswald, 2011).

Stress rupture is a complete failure of a material at defined values of stress and temperature, Figure 2-26. The stress rupture test method is similar to a creep test but higher stress levels are used and the test is conducted until the specimen fails. The purpose of this test is to determine the failure mode and the time to failure. The specimens that fail in brittle manner tend to always cluster around the steeper part of the curves in and the specimens that fail in ductile manner cluster around the more flat part of the curves (Janson, 1989, p. 32).
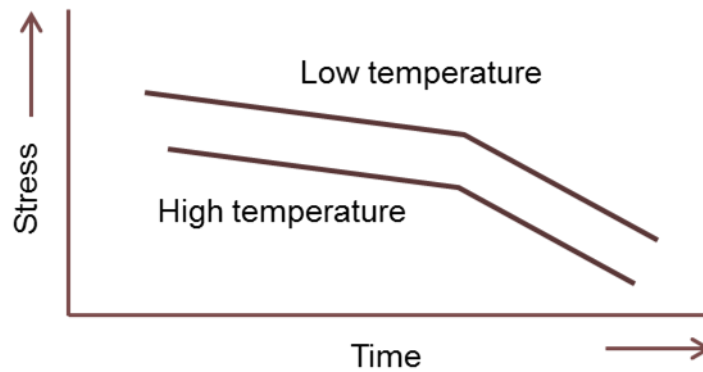
Figure 2-26 Typical hydrostatic stress rupture against time curves on a log-log scale

There are three mechanisms of failure that occur before yielding: brittle failure by chain disentanglement, ductile shear yielding, and brittle failure by chain scission (O'Connell, et al., 2002). There are no morphological differences between the two brittle failure mechanism, both The type of failure mechanism that is dominant will be the one that requires the lowest stress to be active based on the: magnitude of the stress, strain rate, and temperature. Secondary relaxations exist at temperature below T_g denoted by β, γ, and δ, originate from molecular motions with smaller amplitudes and cooperative characters than that of those that occurs at T_g contribute towards the transition between the failure mechanisms (Wu, et al., 2001).

The transition from brittle to ductile or ductile to brittle can be defined using the temperature (T_{bd}) where the fracture occurs at the yield point. The transition temperature increases with the strain rate and damage such as notch or craze. T_{bd} can be determined from the intersection of fracture stress curves of brittle and ductile materials on a stress-temperature diagram. An increase in specimen thickness; sharpening of the notch tip, decrease in temperature or MW, and annealing of the specimen which increase crystallinity, transitions the failure mode from ductile to brittle (Brown, 1982; Boukhili & Gauvin, 1990).

Ductile fractures have a 45^0 between the fracture line and the stretching direction while the brittle fracture are characterised by a fracture line that is perpendicular to the stretching direction. Fracture of the polymer through deformation either without change in volume, known as shear deformation or with change in volume, known as crazing. Eventual failure mechanisms following shearing will be fracture of the plastically yielded zone or craze-crack failure (Deblieck, et al., 2011).

53

The crazing process illustrated in Figure 2-27 shows the growth of microvoids forming under tensile stress. These voids or cavities separated by fibrils introduce empty volume in the area. The fibrils rupture under stress, causing the crack to progress as smaller volumes coalesce. Typical fibril size is reported (Deblieck, et al., 2011) to be coarser in semi-crystalline (200 nm) than amorphous (20 nm) regions. This type of failure normally occurs below the yield stress of the material where after a period of low stress the tie molecules untangle. The remaining tie molecules in the spherulite and between the crystalline regions rupture due to insufficient strength to keep the local region intact.
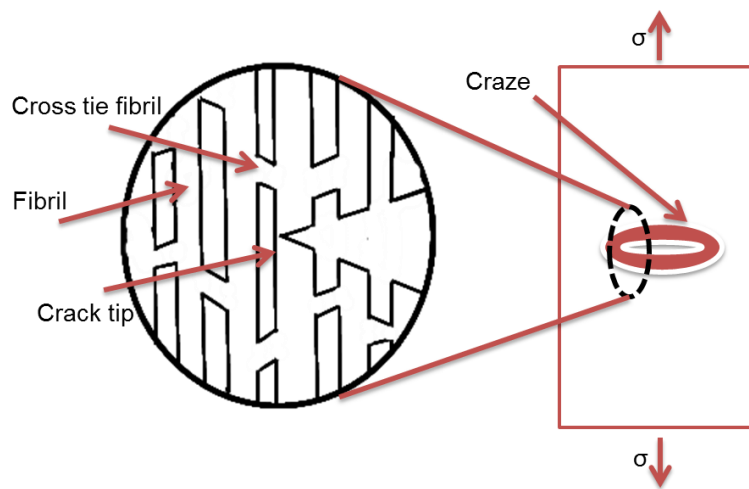
Figure 2-27 Craze-crack tip model showing craze occurring perpendicular to stress at the void edges, (Hui, et al., 1992)

Examples of brittle and ductile failures are shown in Figure 2-28 and Figure 2-29.
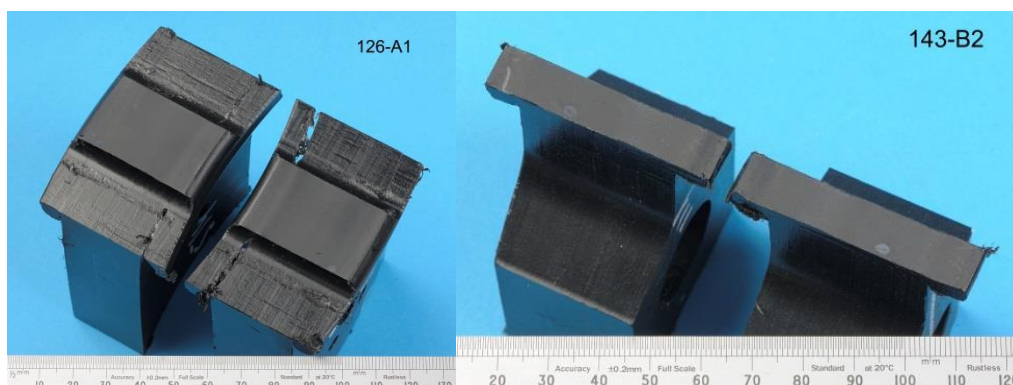
Figure 2-28 A waisted tensile specimen (left) and a tensile impact specimen (right), both showing brittle failure mode
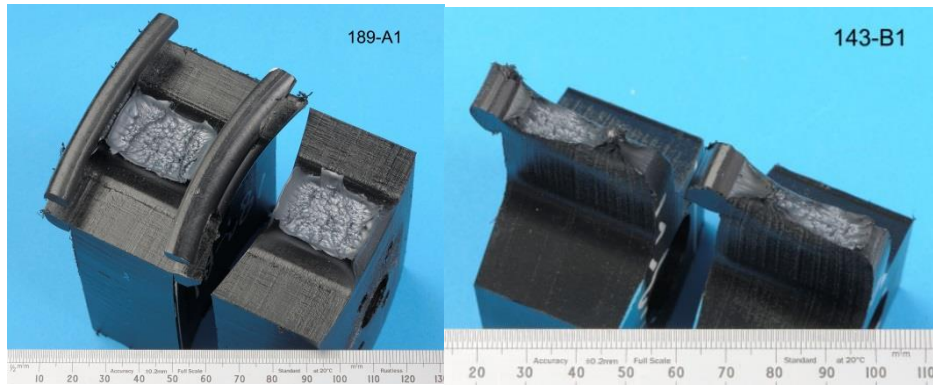
Figure 2-29 A waisted tensile specimen (left) and a ductile tensile impact specimen (right), both showing ductile failure mode

Ductile failure mode as shown in Figure 2-29 is believed to initiate from: the chain slip in crystalline regions of the polymer; unravelling of the folded chains in amorphous regions; or reorientation of chains in the polymer to allow for extension. These lead to extensive shear yielding before failure. The deformation caused by shear yielding dissipates energy in the material which can be observed by increase in the local material temperature. A distinct version of ductile failure occurs in the parent material in the case of a good weld, Figure 2-30. The failure occurring in the parent material implies that the weld has a short-term yield load greater than that of the parent material: this is especially evident in tests where the bead has been left intact, increasing the area carrying the force at the weld joint.
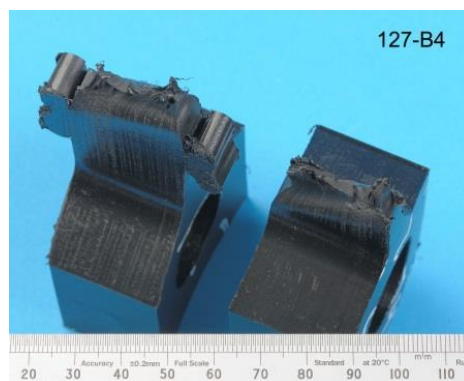
Figure 2-30 A ductile tensile impact specimen where the failure occurred in the parent material

Mixed failure mode occurs where conditions at the time of weld creation only allow small to moderate amount of polymer chains to diffuse through the weld interface to form a joint. The areas where the diffusion of chains is low, fail in a brittle manner. The remaining material carrying the load exhibits micro-ductility and crazing as seen in lighter coloured region of Figure 2-31.

A welded PE pipe under axial and hoop stresses will fail after a certain period of time: the failure in the form of crack will occur perpendicular to the direction of the larger stress. The stress and time period can be plotted on a log-log graph. The stress rupture behaviour (Troughton & Booth, 2000, p. 15) of polymers is due to three types of conditions visible in Figure 2-32 as three distinct regions: short-term high stress, medium-term moderate stress, and long-term low stress.

Failure in the first region will be in a ductile manner due to large localised shear yielding. If the strain rate is high and temperature is low then the pipe may experience a brittle-ductile transition leading to a brittle failure by rapid crack growth (RCG) by chain scission. Failure in the second region will be in a brittle manner due to a process called slow crack growth (SCG) through chain disentanglement without any large deformation from shear yielding. The chain disentanglement mechanism starts by strain hardening and disentangled leading to Rouse retraction and reducing the chain crossing thrice across the interface plane in a critically connected entangled state at the draw ratio (Wool, 2006). SCG most commonly initiated at the site of stress concentration or a defect and crosses through thickness. Failure in the last region will be likely due to environmental stress cracking the mechanism of which is as follows: plastic resin is cracked through contact with a specific chemical agent in corrosive liquids while under stress. The synergetic effect of chemical agents increases the mechanical stresses resulting in cracking. Environments where degradation is accelerated due to corrosive liquids or high service temperatures lay in the latter regions. Chemical agents do not cause direct chemical effect or molecular degradation. Instead, the chemical penetrates into material leading to chain disentanglements, crazing initiation, growth, and propagation which leads to

56

crack. The presence of a chemical accelerates the process of disentanglement. Degradation of the material and increase in the temperature will both move the log-log graph curve towards the origin. This reduces the maximum operating pressure and the time period of allowable pipe life.
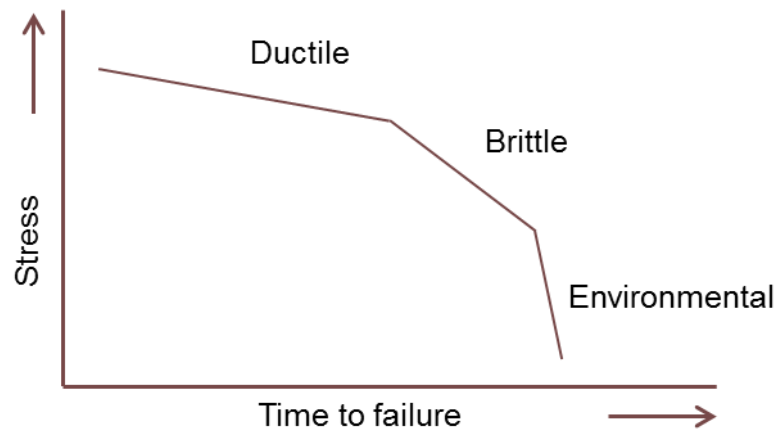
Pipes experiencing fatigue start shifting the region of failure on the time axis from ductile region to brittle region and then the environmental region which is independent of the stress. The fatigue behaviour (Troughton & Booth, 2000, p. 14) of polymers is controlled by several factors such as cyclic load, stress range, and temperature among others. Stress range is the principal controlling variable of fatigue. Cyclic loading also raises the local temperature due to mechanical hysteresis above the ambient temperature due to the viscoelastic nature of polymers. Fatigue failure can be divided in two phases: initiation phase and propagation phase. The latter phase is dominant in the presence of flaws.

A yield criterion is used to define a function of stress components which reach a critical value beyond which plasticity occurs, used to predict the yielding behaviour of material. Tresca yield criterion states that the plastic deformation occurs when the maximum shear stress reaches a critical stress. The maximum shear stress can be determined using Mohr circle. Von Mises stress criterion states that a material yields when the Von Mises stress reaches the yield strength of the material. Von Mises stress is also known as the maximum distortion energy criterion, a scalar value that can be computed from the Cauchy stress tensor. Normally, Von Mises criterion is used for ductile material. Observed in polymer material, hydrostatic pressure has a

significant impact on yield stress; that under identical test conditions of temperature and strain rate, the compression yield stress is larger than the tensile yield stress (Halary, et al., 2011). Hydrostatic pressure can be incorporated in Tresca and Von Mises criterions to obtain Mohr-Coulomb and Drucker-Prager yield criterions.

2.5.2 Whole pipe tests

Pipeline systems are commonly designed for 50 years of service. Internal hydrostatic pressure testing is the specified method of testing in many international specifications and standards. However, TWI developed the whole pipe tensile creep rupture (WPTCR) test to address the deficiencies of a standard hydrostatic pressure test for assessing butt fusion joints.

2.5.2.1 Hydrostatic pressure test

A hydrostatic pressure test pipe sample is typically three times the outer pipe diameter in length. The pipe sample is fitted with pressure-tight end caps, filled with water through the end caps, and immersed unconstrained in temperature controlled water for conditioning which typically lasts for an hour. After the conditioning, hydrostatic pressure is applied through the end caps and the time to failure is measured. The test is conducted at 20 ^{0}C to measure the long-term ductile strength. However, the test is commonly conducted at elevated temperature to produce regression curves of hoop stress against time to failure.

These curves are only applicable for the service life of pipes and not the welds due to hoop stress being twice that of the axial stress in the pressurised pipes with end caps. Henceforth, the hydrostatic tests can only show that the strength of the weld is greater than 50% of the strength of the pipe. This test does not account for the additional axial stresses experienced in service conditions due to bending, thermal expansion, and weld flaws. Variations of hydrostatic pressure tests have been used to investigate misalignment and fatigue for small diameter pipes. Misalignment increases the axial stress but also sharpens the notch between the pipe wall and the weld bead due to the radial offset in the pipe walls at the weld. The hydrostatic pressure test for butt fusion joint is defined by the ISO 1167-4 (2007d) standard.

2.5.2.2 WPTCR test

The aim of WPTCR test is to produce experimental regression curves that predict the service life of PE pipe welds. It requires the failure to occur at the weld and this is

achieved by subjecting the pipe to a constant axial stress at elevated temperature. Pipes are clamped with internal wedge-shaped end caps to prevent the end caps from slipping. The end caps have holes to allow the water to fill the inside of the pipe. The pipes are submerged in a water bath at elevated temperature and undergo a tensile extension in the axial direction.

A WPCTR test has cracks progressing at the weld interface via SCG mechanism which display a typical slip-stick (rippled radiate outward from a central point) fracture surface. It is suggested that removing weld beads eliminates the defects which initiate brittle fractures. WPTCR test tests the weld more rigorously than the standard hydrostatic tests (Troughton & Brown, 2003).

2.5.3 Coupon tests

Several types of tests can be performed using coupons cut-out from the welded pipe such as tensile tests, bend tests, and impact tests. The tensile tests can be further separated into waisted tensile, tensile impact, tensile creep rupture, and low-temperature tensile tests. The common symbols used to illustrate the specimen geometry of these coupon tests are designated in Table 2-7. This is done due to several standards specifying a range of values for these parameters based on the outer pipe diameter and pipe wall thickness. The units used are in millimetres and all other test-specific details will be illustrated or stated in the relevant coupon test subsection. It is highly recommended that the most recent version of the standard is used for specimen preparation and testing.

Table 2-7 List of symbols and designation used in illustrating geometries for coupon tests

Symbol	Designation
A_0	Pipe wall thickness
A	Thickness of the test specimen
B_0	Calibrated and parallel width of the test specimen
B	Width of the test specimen shoulder
B_w	Maximum width of the weld bead
D	Outer diameter of the pipe
L	Total length of the test specimen
L_0	Calibrated and parallel length of the test specimen
L_c	Minimum distance between the test specimen clamps/grips/pins
R	Radius of the test specimen shoulder or specified notches
Ø	Hole diameter for clamping bolts and traction pins

2.5.3.1 Tensile weld factors

There are three tensile weld factors; the short-term defined in EN 12814-2 (BS, 2000a), the long-term defined in EN 12814-3 (BS, 2014), and the low-temperature defined in EN 12814-6 (BS, 2000b). The standard EN 12814-8 (BS, 2001a) lists the recommended range of values for each of the three weld factors for thermoplastic materials. For PE, the recommended value for both short-term and long-term weld factors is 0.8 while the standard advises the value for low-temperature weld factor for PE to be agreed on case by case basis. The calculation method for each welding factor recommends the use of ISO 527-1 (2012) standard where terms such as yield stress and energy to break are defined. The parent material should be tested using the same specimen geometry as the weld specimens to establish a datum. A minimum of five test specimens each for the weld and the parent material are required to establish a good mean.

The short-term tensile weld factor (f_s) is defined as the ratio of the weld strength to the strength of the parent material, it is determined from Equation 2-5 using a dumbbell test specimen:

Equation 2-5

$$f_s = \frac{yield\ stress\ of\ weld}{yield\ stress\ of\ parent\ material}$$

The long-term tensile weld factor (f_l) is a ratio of weld stress and the stress parent material at identical failure times. It is determined from Equation 2-6 using a either a rectangular test specimen or a dumbbell test specimen:

Equation 2-6

$$f_l = \frac{stress\ of\ the\ weld\ at\ time\ t}{stress\ of\ the\ parent\ material\ at\ time\ t}$$

The low temperature tensile weld factor (f_l) is a ratio of fracture stresses of the weld and the parent material determined using Equation 2-7.

Equation 2-7

$$f_l = \frac{fracture\ stress\ of\ the\ weld}{fracture\ stress\ of\ the\ parent\ material}$$

In the case of dumbbell specimen, the weld factor is still insensitive to welding conditions despite the change in specimen geometry since the calculation of the weld area does not account for the size of the weld beads (Troughton & Booth, 2000). It has been suggested that in order to qualify a good weld it should have: the failure mode as ductile and values greater than 50% energy to break per cross-sectional area of the parent material (Troughton & Booth, 2000).

2.5.3.2 Tensile test

The tensile test as described in EN 12814-2 (BS, 2000a), extends the test specimen at 50 mm per minute (the recommended test speed for PE material) until the specimen fails. The load sustained by the specimen is recorded and used to determine the stress sustained. The mean of stresses obtained from welded and parent pipe material test specimens are used to calculate the short-term tensile weld factor. The yield stress is used instead of the fracture stress if the specimen has yielded before fracture.

The test standard recommends three different specimen geometries: a rectangular specimen (Figure 2-33); a dumbbell specimen (Figure 2-34); and a notched specimen (Figure 2-35). The recommendation is to begin with Type 1 specimens; if they consistently fail in clamps then Type 2 specimens should be used instead. The use of notched (waisted) specimen is recommend if the short-term weld factor of one is achieved, to optimise the welding parameters.
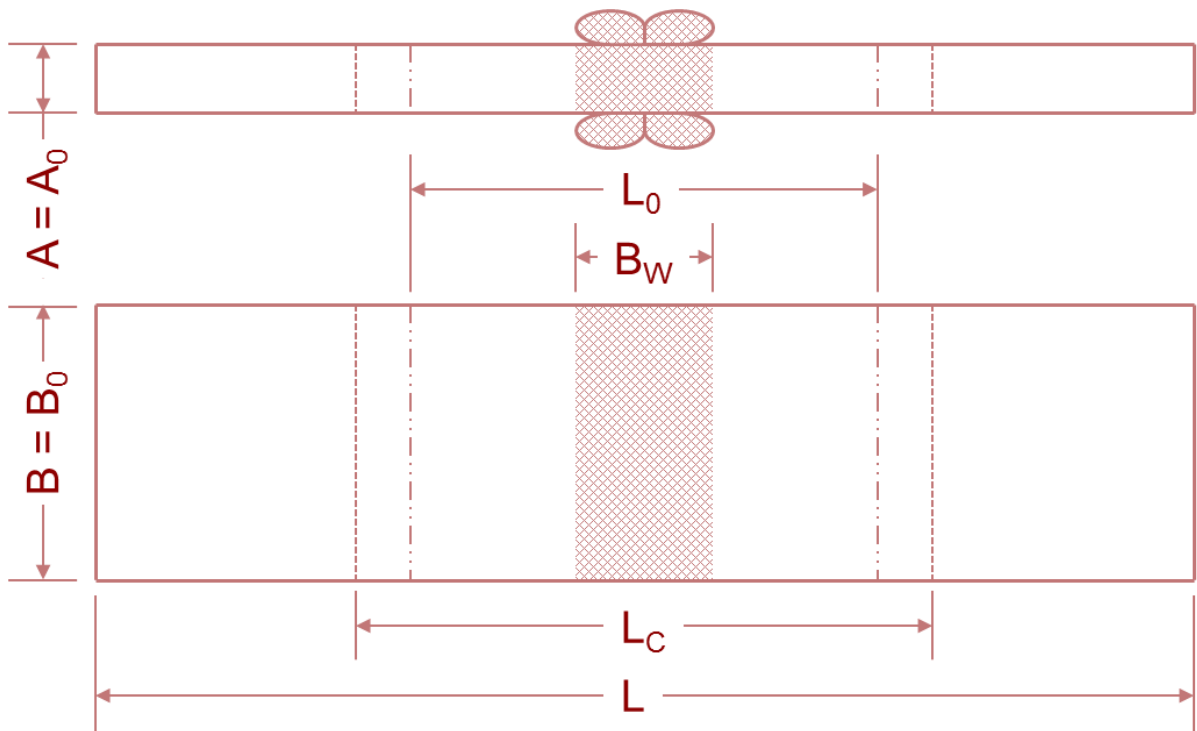
Figure 2-33 Type 1 test specimen for flat sheet and pipe assemblies from EN 12814-2 (BS, 2000a)
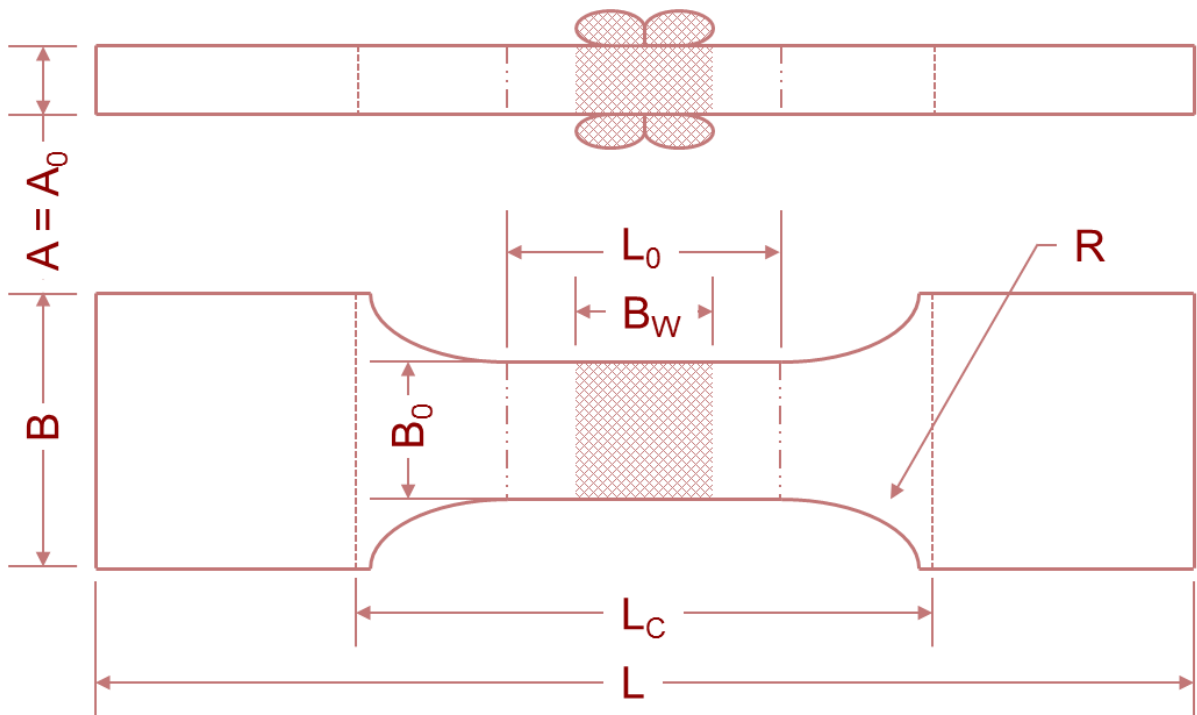
Figure 2-34 Geometry and dimensions of a tensile specimen Type 2 (Troughton, 2010) (BS, 2000a)
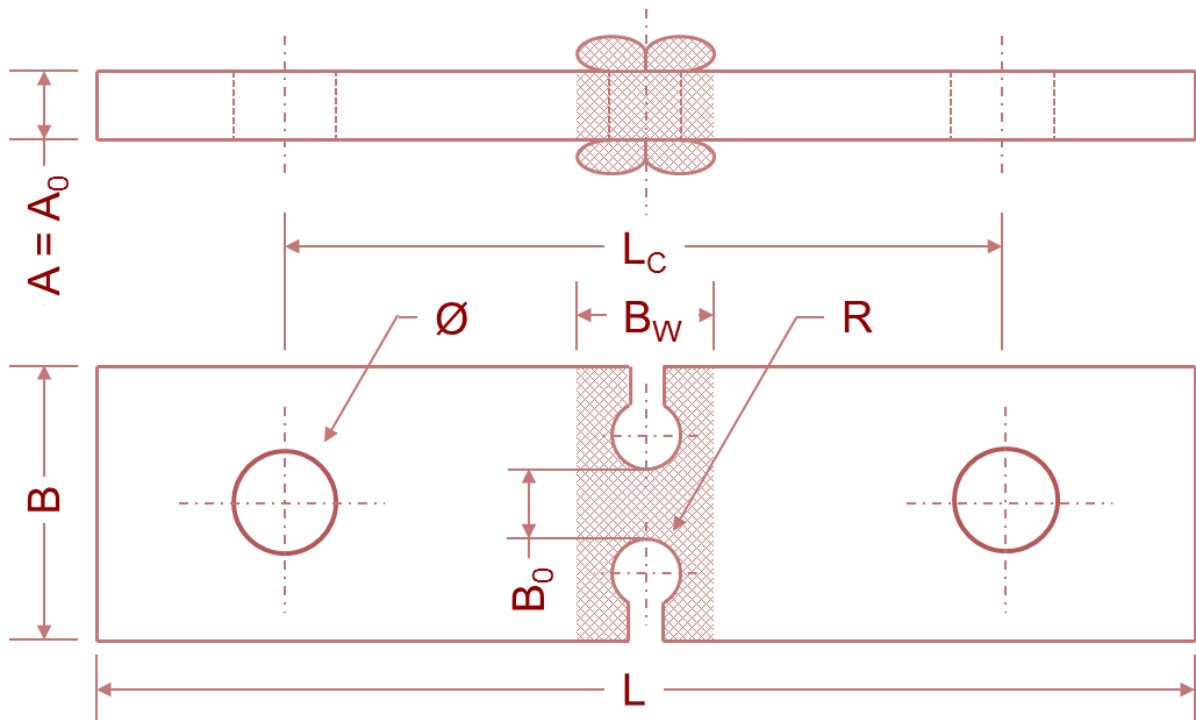
Figure 2-35 Geometry and dimensions of a notched tensile specimen from EN 12814-2 (BS, 2000a) Annex B and a Type A waisted specimen from ISO 13953 (2001)

2.5.3.3 Waisted tensile test

A standard specifying the waisted tensile test is EN 12814-7 (BS, 2002). It recommends the geometry shown in Figure 2-36, which is similar to the notched tensile specimen from the standard EN 12814-2 (BS, 2000a) Annex B and Type A waisted tensile specimen from ISO 13953 (2001), Figure 2-37. The waisted tensile geometry is used to ensure that the failure occurs at the weld. However, the region at the loading pin exhibit deformation in some test cases. The geometry described in EN 12814-7 (BS, 2002) can be improved by ensuring the tensile force is fully directed at the weld. The improved waisted tensile geometry shown in Figure 2-38 when compared to the standard geometry in Figure 2-36 can: minimise the slippage of the specimen; reduce the stress concentration at the loading pin sites; and diminish the deformation of pin sites. These non-standard improvements consist of four smaller holes around the loading pin holes: this allows the use of four bolts to assist the pins at each end to ensure a good distribution of the tensile force by ensuring sufficient tightening of the grips.
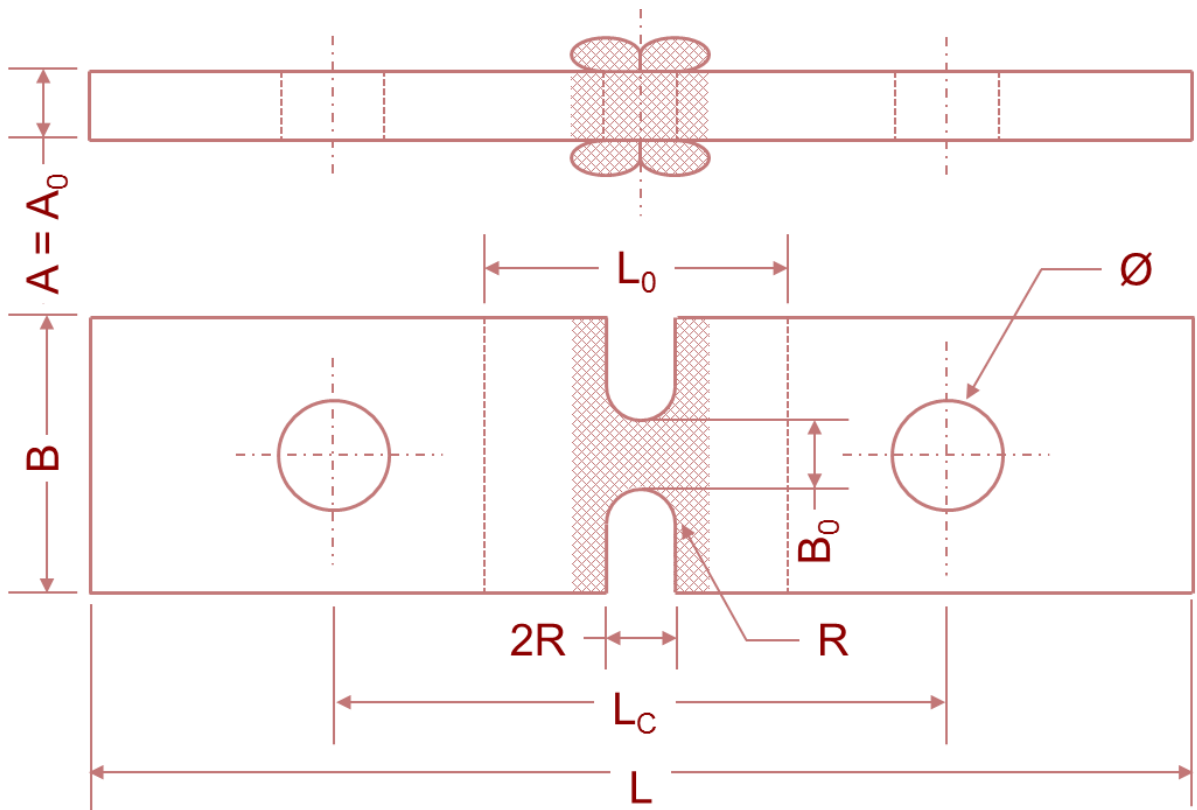
Figure 2-36 Geometry and dimensions of a waisted tensile specimen from EN 12814-7 (BS, 2002)
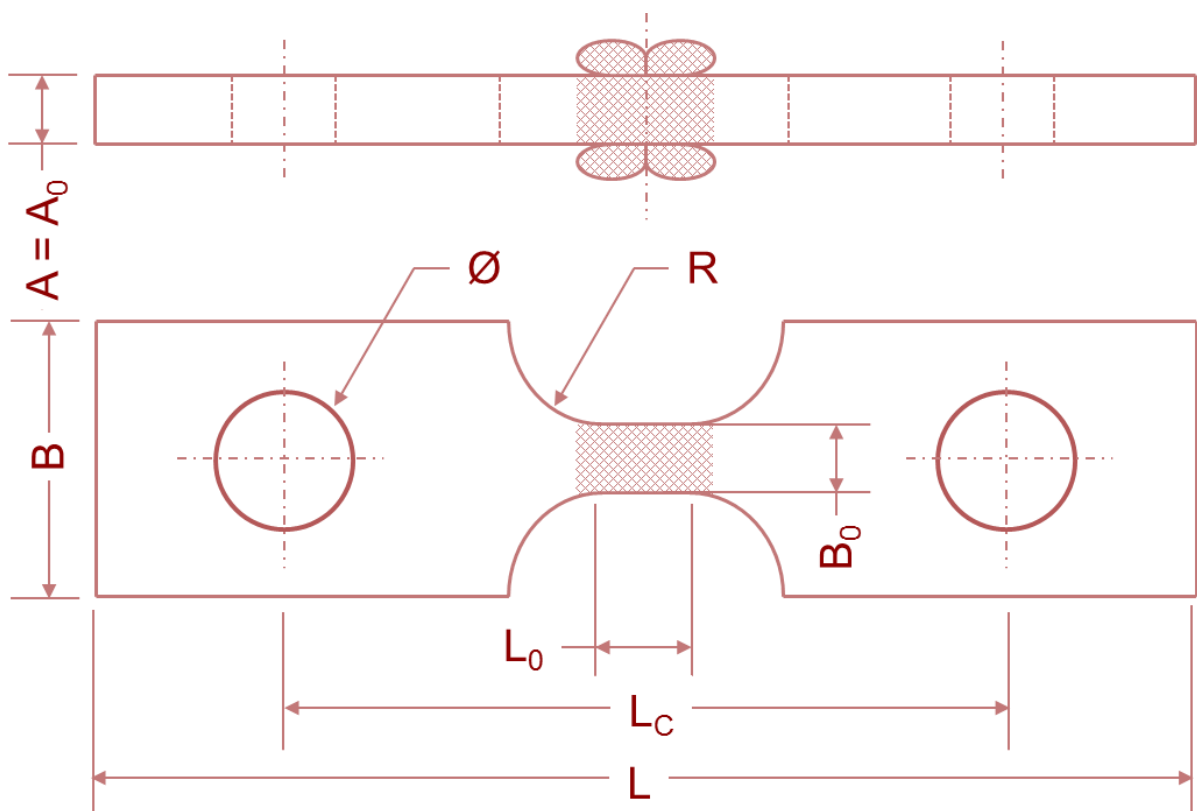
Figure 2-37 Geometry and dimensions of a Type B waisted tensile specimen from ISO 13953 (2001)

64
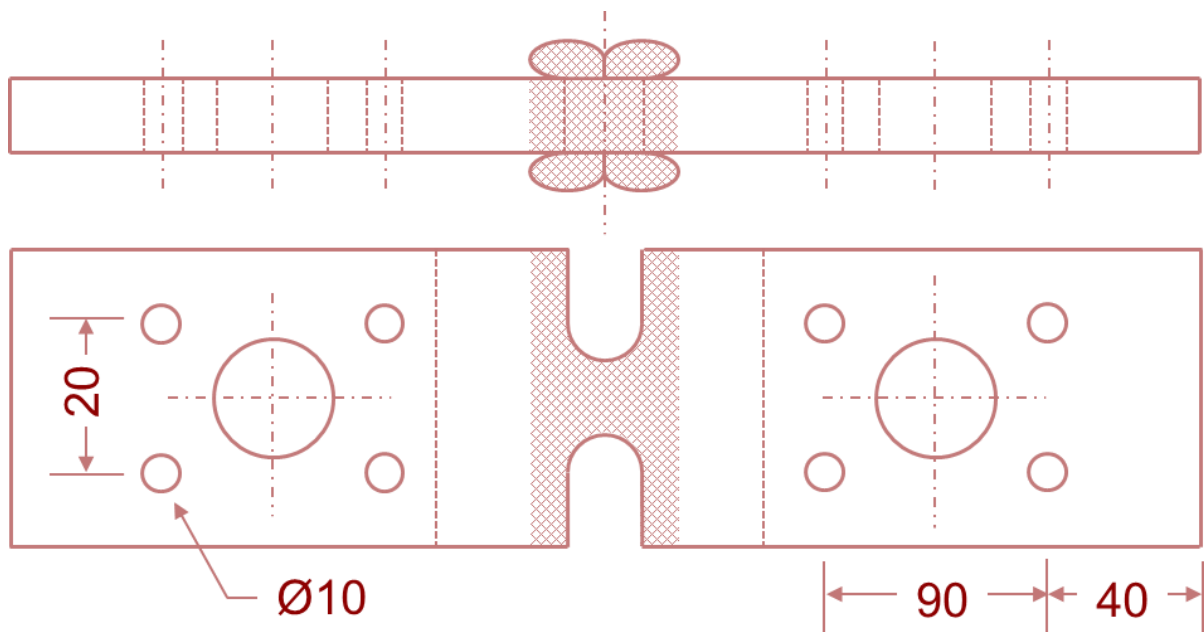
Figure 2-38 Improved geometry of a waisted tensile specimen from EN 12814-7 (BS, 2002; Troughton, 2010)

2.5.3.4 Tensile creep rupture test

The long term tensile testing of a coupon uses specimen geometries similar to those from the tensile test to compare the resistance to SCG of the joint against the parent material. The specimen geometries for the tensile creep rupture test according to EN12814-3 (BS, 2014) test standard are a rectangular specimen (Figure 2-33) and a dumbbell specimen (Figure 2-34). The tensile load, temperature and environmental conditions are defined and maintained in a manner similar to that of hydrostatic pressure or WPTCR testing. Times to failure are recorded on a log-log graph of stress against time and the graph is used with Equation 2-6 to determine the long-term tensile weld factor (f_l). Extensive testing of PE pipe materials and welds made using the same materials have shown that SCG resistance can be significantly lower in welds, despite both the weld and the parent material having similar short-term tensile strength (Troughton & Booth, 2000).

2.5.3.5 Low temperature tensile test

The low temperature test is essentially a tensile test conducted at -40 ºC. The standard EN12814-6 (BS, 2000b) recommends the geometry shown in Figure 2-39 to conduct the test. The results from the test are used in a similar manner to a standard tensile test to determine low-temperature tensile welding factor using Equation 2-7. The aim of the test is to generate brittle fracture. If the test specimen

yields, it is recommended to either increase the test speed or lower the test temperature. A test specimen is disregarded if it yields or the failure occurs in the clamps.
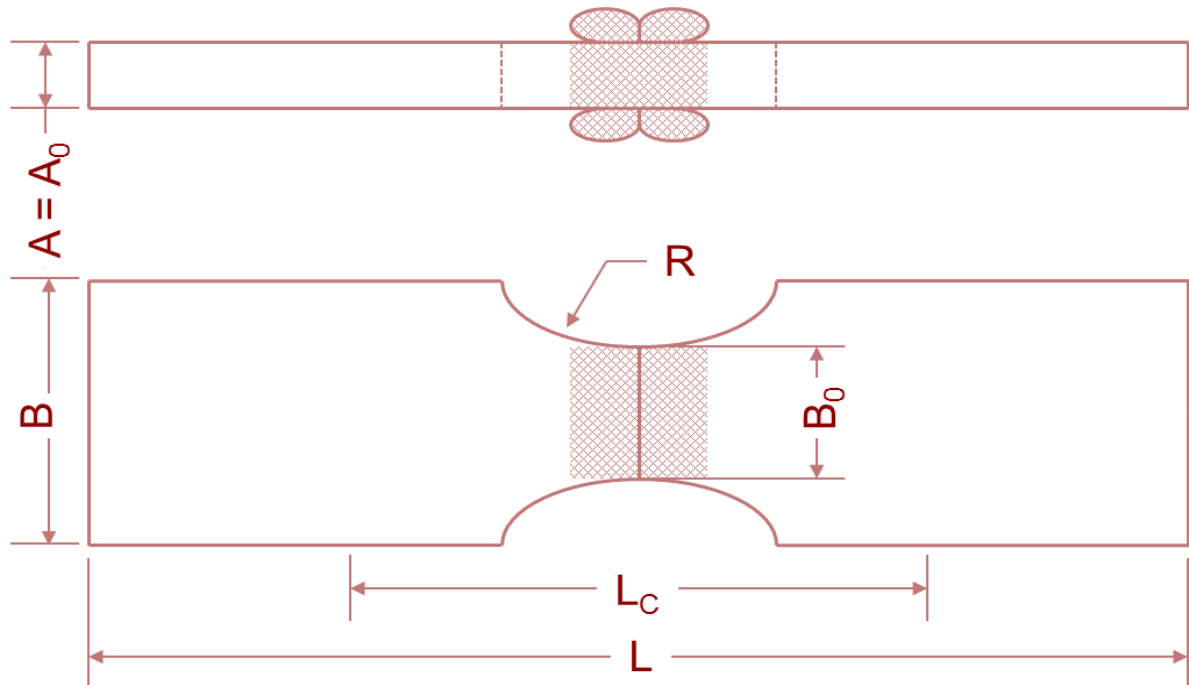
Figure 2-39 Low temperature tensile test specimen geometry from EN 12814-6 (BS, 2000b)

2.5.3.6 Bend test

A standard specifying the specimen geometry and the test procedure is EN 12814-1 (BS, 2000c). The bend test involves a rectangular section cut from across the weld, Figure 2-40. The specimen is subjected to a 3-point bend test. According to EN 12814-1 (BS, 2000c) the test is terminated when the specimen: fractures; a crack initiates; or a bend angle of 160^0 is reached. The angle where the fracture or the crack initiates is measured. For wall thickness values greater than 30 mm, the standard recommends the use of side bend specimen shown in Figure 2-41 or machining down to 30 mm from the side where the weld bead has been removed to accommodate the loading ram.
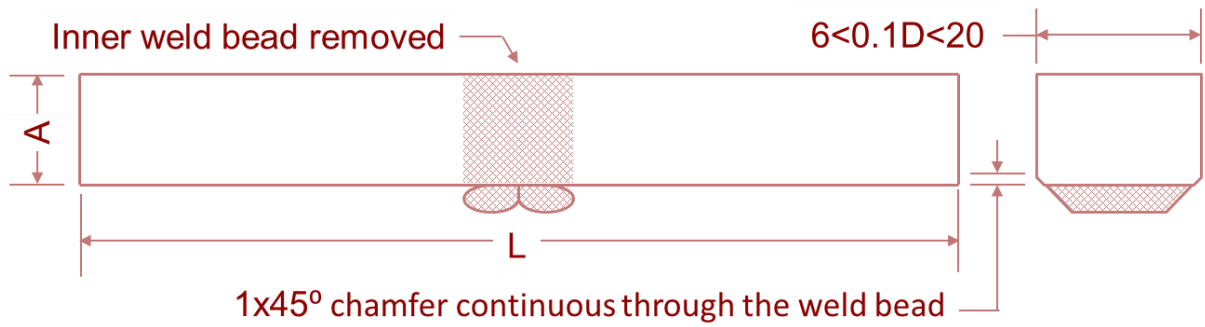
Figure 2-40 Geometry and dimensions of a three point bend specimen from EN 12814-1 (BS, 2000c)
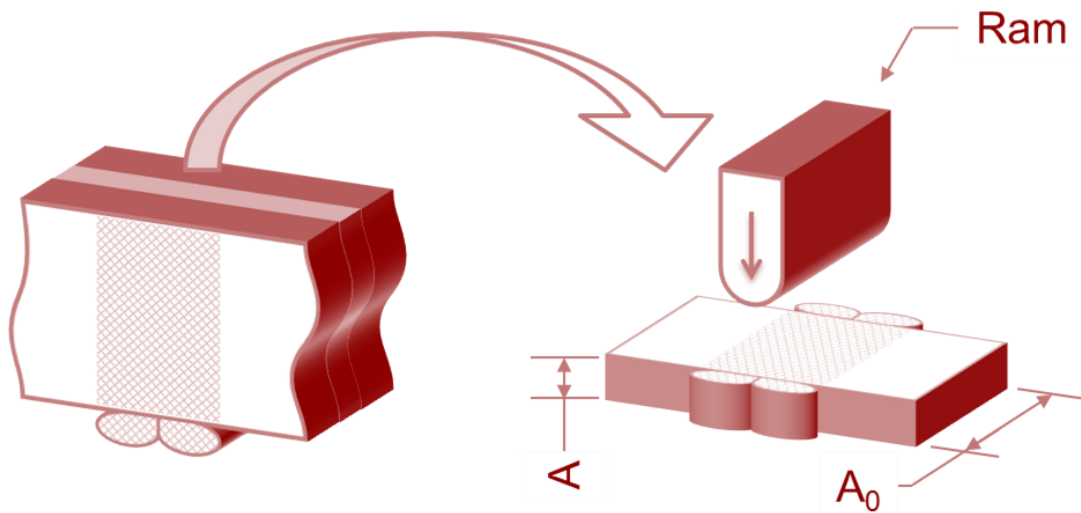
Figure 2-41 Geometry and positioning of the side bend test specimen from EN 12814-1 (BS, 2000c)

The guided side bend test is similar to the 3-point bend test with the exception of the specimen geometry, which is shown in Figure 2-42. The standard specifying the specimen geometry and the test procedure is ASTM F3183-16 (ASTM, 2016d).
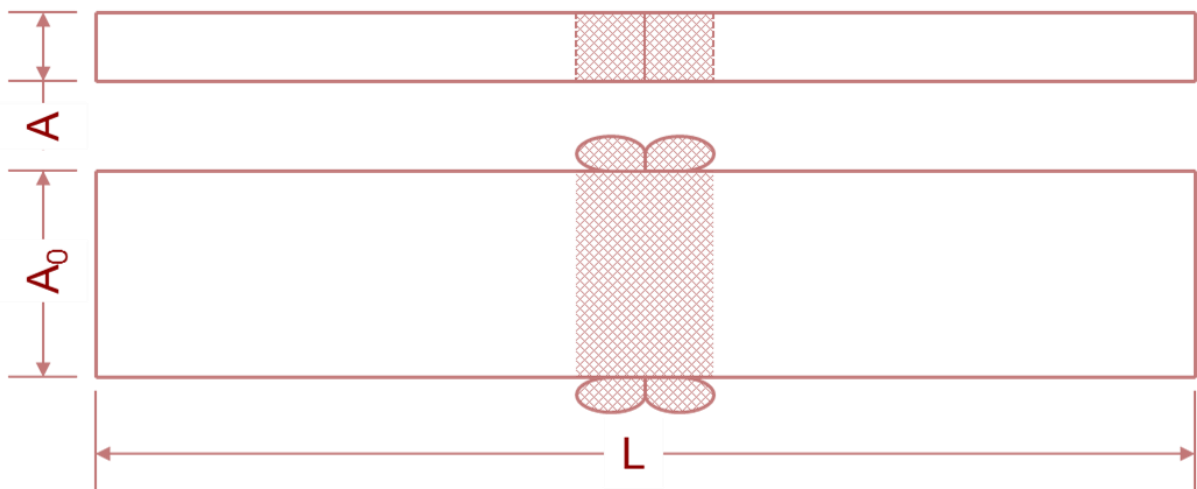
Figure 2-42 Guided side bend specimen geometry from ASTM F3183-16

2.5.3.7 Impact tests

Impact testing is used to estimate the fracture toughness. These tests can be split between flexural tests and tensile impact tests. The three main flexural tests are Charpy (ISO 179-1 (2010), ISO 179-2 (1997b) and ASTM F2231-02 (2002)), Izod (ISO 180 (2000a) and ASTM D256-10e1 (2010)) and falling weight (ISO 6603-1 (2000b), ISO 6603-2 (2000c) and ASTM D2444-99 (1999)). A weighted striker impacts a notched specimen. The standard blunt notch root radii are 0.25 mm (Type A), 1 mm (Type B), and 0.1 mm (Type C), as stated ISO 179-1 (2010). The tests measure total energy absorbed in fracture. An alternative to the blunt notch uses a razor blade to create a sharp notch of 10-20 um size. Several data point of fracture energy can be obtained by varying the depth of the notch. The position of a notch should be at the weld interface and a symmetrical weld bead can be used to position the notch. The notch needs to cause failure at the weld rather than the parent material as it is the weld that needs to be tested. PTFE tape may be used during welding to produce a notch at the weld interface, which addresses the problem of notches in unsymmetrical welds. The current standards define the flexural tests for characterising the parent material properties. Therefore, new tests will have to be adapted from parent material tests in order to qualify the performance of butt fusion welds in PE pipes.

Among the tensile impact test standards, ASTM F2634-15 (2015) is used to determine the quality of butt fusion welds and determine the optimum butt fusion joining parameters in a manner similar to those specified in EN12814-2 (BS, 2000a) using waisted specimen geometry. In addition to the specimen geometry, the tensile impact test differs significantly in testing speed from other tensile tests. The tensile impact test is used with the dumbbell form which is different from the EN12814-2 (BS, 2000a) Type 2 specimen geometry. The new form with loading pins is shown in Figure 2-43. The removal of the weld beads improves the consistency of the tensile impact results as the stress distribution and deformation will not be affected by the bead geometry.
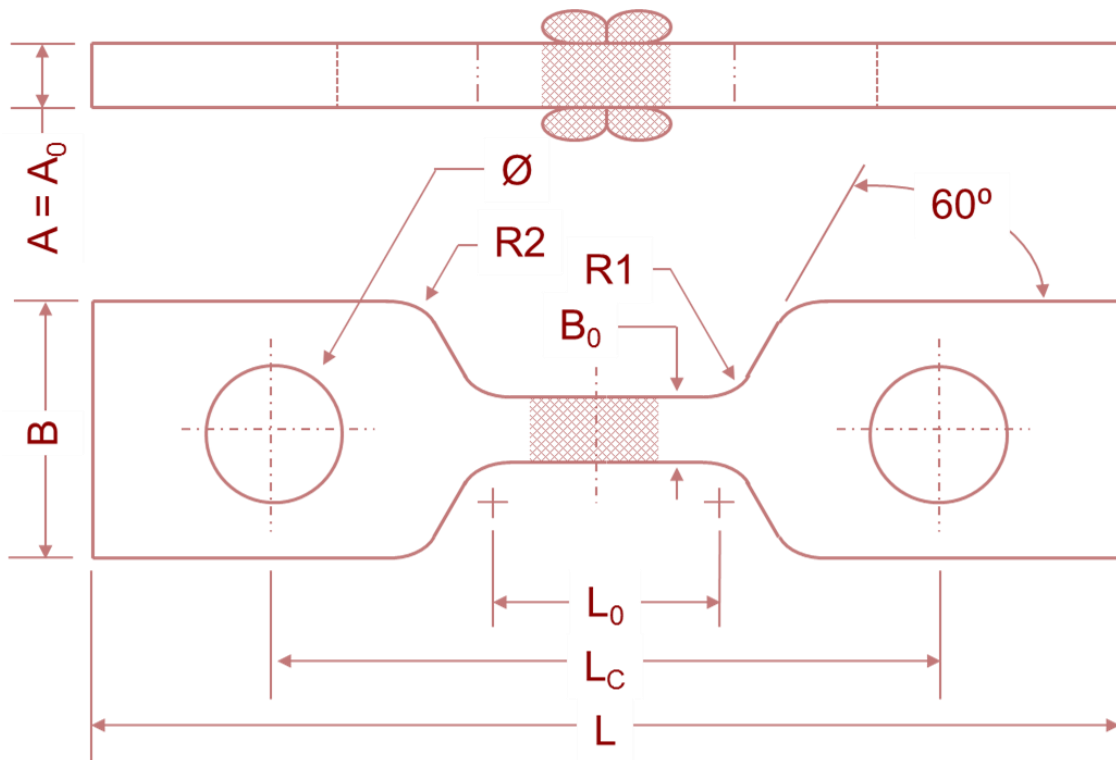
Figure 2-43 Tensile impact test coupon geometry from ASTM F2634-15 (2015)

2.5.4 Test standards

Table 2-8 shows the available destructive test methods with respective standards, specimen type, and time scale for qualifying butt fusion joints in PE pipes. This table is not exhaustive, listing only the some of the popular test standards and the table does not include the standards converted by other national bodies such as those that exist in countries such as Russia and China.

Table 2-8 Overview of the destructive tests and standards for butt fusion joints in PE pipes

Test	Standard	Specimen	Term
Hydrostatic pressure	ASTM F2164-13 (2013a) ASTM F2928-13 (2013b) ISO 1167-4 (2007d)	Pipe	Long
WPTCR	EN 12814-3 (BS, 2014) Annex B	Pipe	Long
Tensile	DVS 2203-2 (2010) EN 12814-2 (BS, 2000a)	Coupon	Short
Waisted tensile	EN 12814-7 (BS, 2002) ISO 13953 (2001)	Coupon	Short
Tensile impact	ASTM F2634-15 (2015) DVS 2203-3 (2011)	Coupon	Short
Three point bend	DVS 2203-5 (1999) EN 12814-1 (BS, 2000c)	Coupon	Short
Guided side bend	ASTM F3183-16 (2016d)	Coupon	Short
Tensile creep rupture	DVS 2203-4 (1997) EN 12814-3 (BS, 2014)	Coupon	Long

2.5.5 Comparison of the mechanical tests

TWI carried out a programme of work to compare the results from various short-term and long-term, coupon and whole pipe mechanical tests the findings of which were published at the Northern Area Western Conference (NACE) in 2010. Three distinct welding conditions were used to produce joints of different weld qualities based on the advice from the industry, Table 2-9. The first condition was according to the WIS 4-32-08 (2002). The second condition had the bead-up, fusion and cooling pressures raised from 19 to 95 bars. The third condition had the heater plate temperature lowered to 160 ^{0}C from 230 ^{0}C. Both second and third conditions were otherwise identical to the first condition. The welds were made in 355 mm SDR 17.6 black PE100 pipe. The ranking of the results of all the mechanical tests is listed in Table 2-10.

Table 2-9 Welding conditions (Troughton, 2010)

Test	Standard	Pressure (bar)	Temperature (^{0}C)
Condition 1	WIS 4-32-08	19	230
Condition 2	Raised pressure	95	230
Condition 3	Low temperature	19	160

Table 2-10 Comparison of the ranking of the results from the mechanical tests (Troughton, 2010)

Test	Property measured	Ranking		
		Condition 1	Condition 2	Condition 3
Bend	Maximum bend angle	No weld failures		
Tensile (dumb-bell specimen)	Tensile strength	No weld failures		
	Extension at break			
	Energy to break			
	Failure mode			
Waisted tensile	Tensile strength	H	H	L
	Extension at break	H	L	L
	Energy to break	H	M	L
	Failure mode	H	L	H
Coupon tensile creep rupture	Time to failure	L	L	H
WPTCR	Time to failure	M	H	L
Hydrostatic pressure	Time to failure	No weld failures		
(H = highest, M = mid, L = lowest)				

For the assessment of the butt fusion welds in PE pipes, the most representative test currently available is the WPTCR test because it can consistently generate long-term failure at the weld. The hydrostatic pressure tests were carried out for 1700 hours rather than failure as they did not show any fractures, therefore, they too did not differentiate between the weld conditions. The long-term tensile creep rupture test gave different results to the WPTCR test which is due to different stress field in the coupon and whole pipe specimens. The 3-point bend test and the tensile test using dumb-bell specimen geometry are the two short term tests that did not differentiate between the weld conditions; therefore, it is recommended that they are not used to assess the quality of the weld. It is recommended that energy to break value rather than tensile strength or the failure mode, is to be used for the waisted tensile tests which were able to discriminate the welding conditions. Normally, short-term tests are used to optimise the welding parameters; however, the short-term test that did discriminate between the welding conditions gave dissimilar results to the WPTCR test which implies that there exists a lack of optimisation in the welding parameters for the long-term performance of butt fusion welds (Troughton, 2010).

2.6 Summary

The integrity of butt fusion welding process has been developed empirically. Research has been conducted on individual parameters for PE material, pipe composition, welding, and testing in the form of devising theories, modelling, and testing. Therefore, there exists a need for understanding how the different welding procedures lead to minute changes in the microstructure and hence its effect on weld performance assessed in an appropriate manner.

3 Experimental Techniques

3.1 Introduction

This chapter is split into six subchapters. The first half of the chapter describes the general experimental details in this work including the HDPE pipe material used; the two butt fusion welding machines; the six welding procedures following relevant standards; and the sampling matrix (the cutting plans and sections for extracting different test specimens). The remaining half of the chapter consists of subchapters that give details in the testing methods and conditions, analysis procedures and modelling for specific area of investigations as discussed later in: Chapter 4: mechanical testing; Chapter 5: weld bead structure; and Chapter 6: weld microstructure, respectively.

3.2 Materials

A total of 50 metres of black 180 mm outer diameter SDR 11 HDPE pipe (Borealis Group, Australia) was used in this study. The pipe was extruded from BorSafe™ HE-3490-LS resin compounded using PE100 grade HDPE. The resin has a bimodal molecular weight distribution (MWD) giving good resistance to rapid crack propagation and slow crack growth, as claimed by the manufacturer Borealis. Some of the physical properties from the manufacturer's product data sheet are listed in Table 3-1. The complete list of physical properties can be found in Appendix B.

Table 3-1 Selected data from the HE-3490-LS Product Datasheet (Borealis Group, 2013)

Physical Properties		Typical Value	Unit	Test Method
Density	Base resin Compound	949 959	kg/m^3	ISO 1183/ISO 1872-2B
Tensile stress at yield	50 mm/min	25	MPa	ISO 527-2
Tensile strain at break		>600	%	ISO 527-2
Tensile modulus	1 mm/min	1100	MPa	ISO 527-2
Charpy impact, notched	0 ^{0}C	16	kJ/m^2	ISO 179/1eA
Hardness, shore d		60		ISO 868
Resistance to SCG	9.2 bar, 80 ^{0}C	>1000	h	ISO 13479
Thermal stability	210 ^{0}C	>20	min	EN 728

3.3 Welding Methodology

3.3.1 Welding standards

Three butt fusion welding standards used worldwide: WIS 4-32-08 (2002), DVS 2207-1 (2005) and ASTM F2620-12 (2012) were used to define welding procedures (or pressure and temperature pairing). The WIS 4-32-08 standard used to define WP1 was revised in 2016 (WIS) and the DVS 2207-1 standard used to define WP2 was revised in 2015 (DVS). For WP3 and WP4 denoted as "ideal" and "acceptable", the Plastic Pipe Institute (USA) 'Technical Report 33' (PPI, 2012) was used to define the welding parameters following the ASTM F2620-12 (2012) standard which was revised in 2013 (ASTM). The PPI report is a generic butt fusion joining procedure. The standard ISO 21307 (2011a) defines the single low pressure fusion jointing procedure in a similar manner to WIS and DVS standards; and defines the single high pressure fusion jointing procedure to ASTM standard. The remaining two procedures (WP5 and WP6, respectively) were not from the standards and were used to investigate the effect of extreme welding temperatures (low and high) at high fusion pressures. It was expected that the welds would differ in quality and structure due to the different setting of welding parameters.
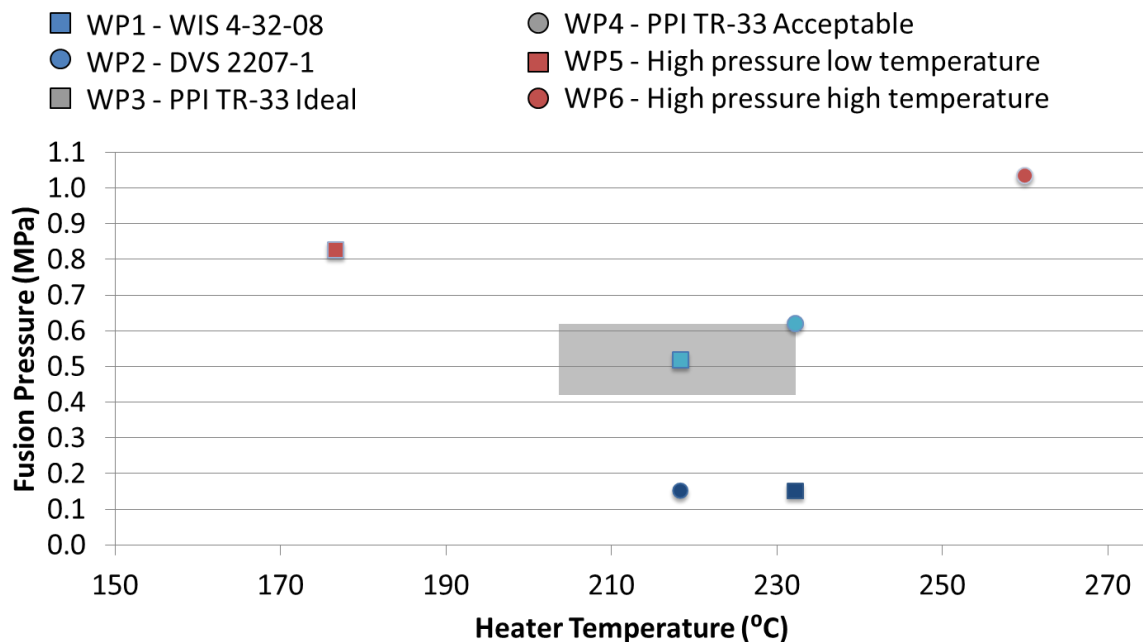
Figure 3-1 The heater temperature against fusion pressure plot of the welding procedures used in the study. Note that WP3 and WP4 represent the "ideal" and an "acceptable" conditions marked by the grey rectangle, representing the "acceptable" range of values defined in the ASTM F2620-12 standard.

3.3.2 The butt fusion welding machines

A Fusion Provida (UK) ABF315 butt fusion welding machine (Figure 3-2) was used to produce welds in accordance with the European standards (the WIS and DVS standards) and a McElroy (USA) DynaMC® 250-EP butt fusion welding machine (Figure 3-3) was used for the ASTM standards. The ABF315 is a semi-automatic butt fusion welding machine designed for the European standards which specify lower fusion pressure. The heating and cooling phases of the butt fusion welding cycle are automated. It prints a hardcopy of the weld report for record keeping. The 250-EP was used for ASTM-based welding pressure as it is designed for higher fusion pressure used in the USA. 250-EP is a manual butt fusion machine with a digital McElroy DATALOGGER® 4 for record keeping. Both machines are equipped with two pairs of gripping jaws with supporting inserts for the correct pipe size.
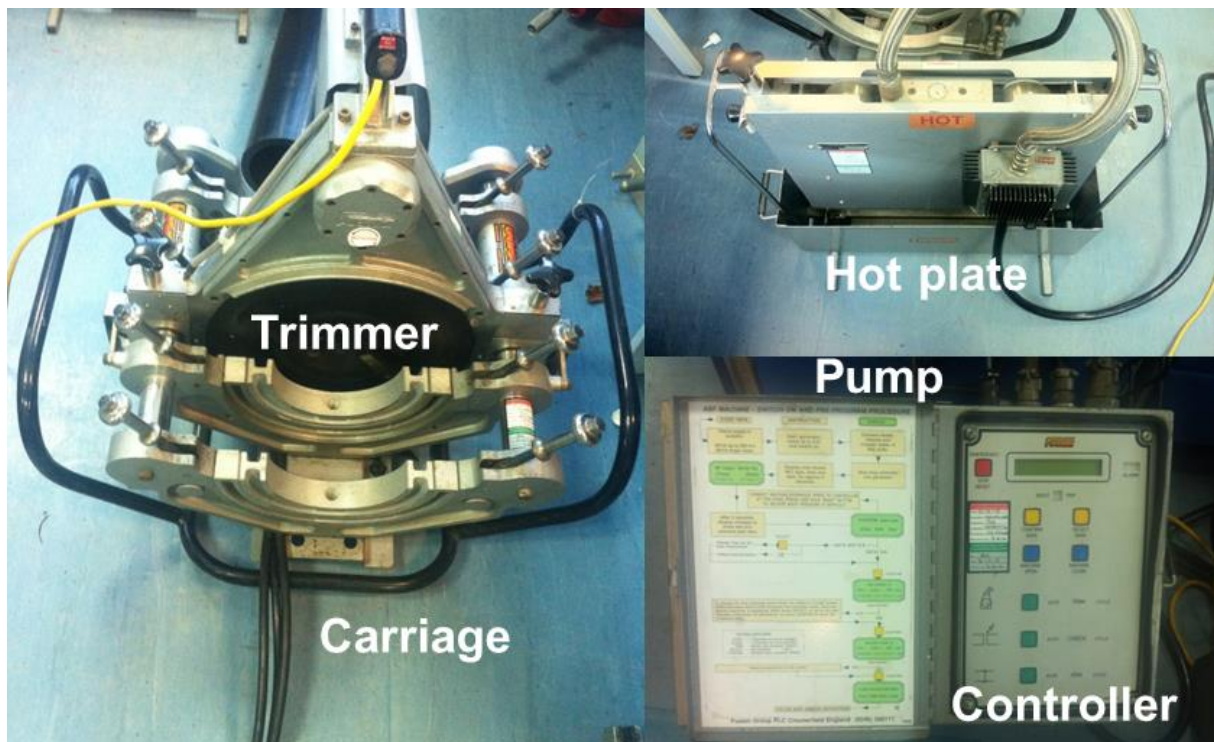
Figure 3-2 A Fusion Provida (UK) ABF315 butt fusion welding machine

A minor difference between the two machines is the movement of paired jaws; hydraulic power is used in both machines to move a single pair of jaws but ABF315 uses a mechanical linkage to move the second pair as well.
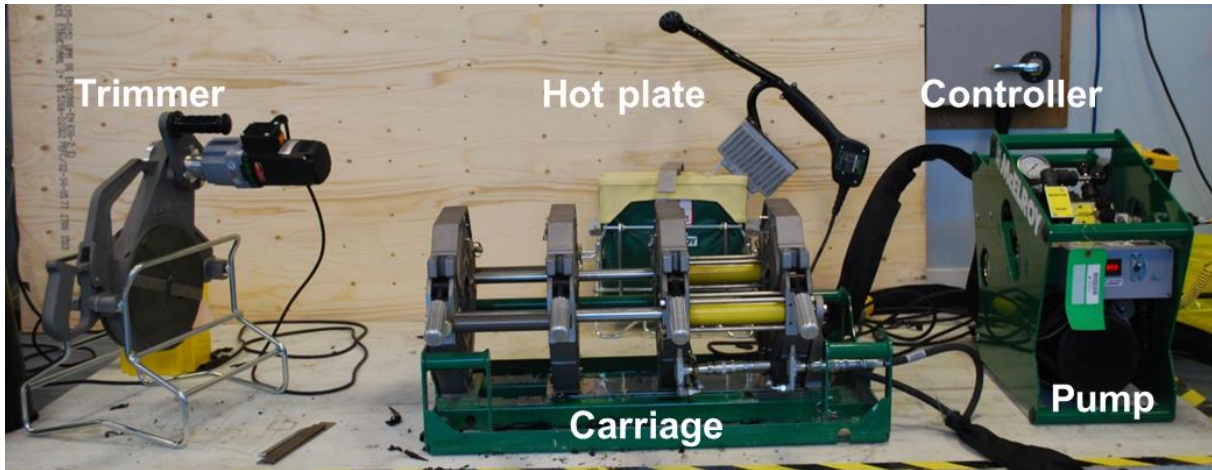
Figure 3-3 A McElroy DynaMC® 250-EP butt fusion welding machine

3.3.3 The butt fusion welding process

A schematic illustration of the welding process is given in Figure 3-4. The pipe sections are clamped in the pair of grips located on the two halves of a carriage, Figure 3-4a. A trimmer is installed between the carriage pairs and spun up to speed, Figure 3-4b. The carriage is used to bring the pipe sections forward and trimmed until a continuous strip of material is removed from both ends, Figure 3-4c. The pipe sections are separated, the trimmer is removed with the pipe trimmings, and the pipe ends are inspected to ensure that they were even and flat, Figure 3-4d. The pipe ends are brought together in the check cycle to be inspected for alignment and then separate to allow insertion of the heater plate, Figure 3-4e. The heater plate is inserted and the pipe ends are brought against it under initial bead-up pressure which is just sufficient to allow melting of any asperities in the pipe circumference and let the pipe end faces develop full contact with the heater plate, Figure 3-4f. A thin bead is formed on both pipe ends and the pipes remain in contact with the heater plate until the specified heat soak time, Figure 3-4g. The dwell stage follows immediately after the end of the heat soak time, the pipe sections separate from the heater plate which is removed while the sections are brought together under fusion pressure, Figure 3-4h. It is important that the dwell time is kept to the minimum to prevent the pipe ends from cooling excessively to the detriment of welding. The pipe sections are now joined under fusion pressure forming the full weld bead and they are held until the required time for cooling has elapsed forming a butt fusion joint, Figure 3-4i. The welded pipe is then numbered and the top of the pipe marked before removal.
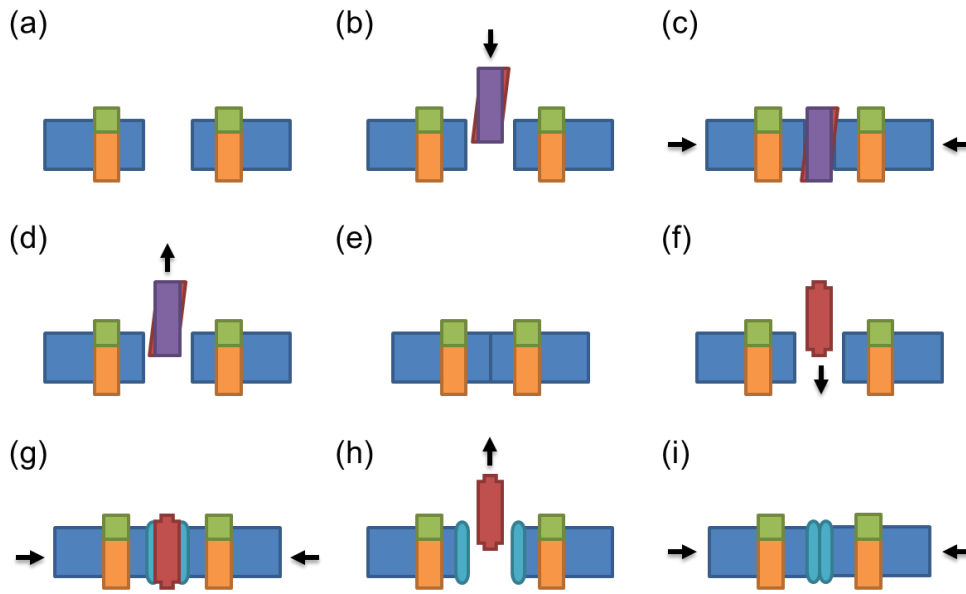
Figure 3-4 The butt fusion joining process for joining pipe

3.3.4 The welding procedures

The six different welding procedures, WP1-WP6, listed in Table 3-2, were used to weld 0.5 metre long sections of the pipe. A total of 48 welds were prepared, eight for each welding procedure. A dummy weld is used to ensure that the welding machine is functioning as required to ensure consistent quality and to remove any contamination on the trimmer and the heater plate transferred during the storage conditions. A dummy weld was produced beforehand for each procedure. The detailed weld reports for each procedure are provided in the Appendix C.

Table 3-2 Welding parameters of the six welding procedures (Shaheer, et al., 2016)

	Welding, Procedure	Interfacial Pressure, *MPa*	Heater Plate Temperature, *^0C*	Heating Time, *s*	Dwell Time, *s*	Fusion/Cooling Time, *s*
WP1	WIS 4-32-08	0.150	230	225	10<	600
WP2	DVS 2207-1	0.150	218	165	9<	1200
WP3	ASTM Ideal	0.517	218	435	15<	450
WP4	ASTM Acceptable	0.621	232	382	15<	450
WP5	High pressure low temperature	0.827	177	821	15<	450
WP6	High pressure high temperature	1.034	260	257	15<	450

3.4 Sampling of Test Specimens

One whole pipe long-term and three coupon short-term tests were planned for this study. Additionally, coupons were set aside for nanoindentation and for sectioning for use with other analytical techniques. The welds are allocated for different tests. For each welding procedure (WP1-6), all the welds except for those allocated for the whole pipe test are categorised under different cutting plans, as listed in Table 3-3 and the cutting plans are illustrated in Figure 3-5 (a-d). The arrangement of the coupon test specimen in the three cutting plans (a-c) is such that the five test specimens of each test share at least two common positions on the pipe circumference from three welds. The unused welded pipes and the welds used with cutting plan (d) were set aside in case additional coupon specimens were required for each welding procedure. The five samples for each type of test are colour coded with the keys provided in Table 3-4 and labelled depending on the type of short-term tests (2-6) and the position of cutting, A-E (Figure 3-5) with exception of A1-A4, the four additional specimens for waisted test per procedure cut from the spare in Figure 3-5 (d) for the welding procedures WP4-6 in order to improve statistical significance.

Table 3-3 Test matrix of welds (No. 1-48) used for WPTCR test and the test specimens using the cutting plans illustrated in Figure 3-5 (a-d).

Welding Procedures	Whole Pipe Tensile Creep Rupture Test	Cutting Plans				Dummy Welds	Unused Welds
		a	b	c	d		
WP1	1, 2, 3	4	5	6	-	7	8
WP2	9, 10, 11	12	13	14	-	15	16
WP3	17, 18, 19	20	21	22	24	23	-
WP4	25, 26, 27	28	29	30	32	31	-
WP5	33, 34, 35	36	37	38	40	39	-
WP6	41, 42, 43	44	45	46	48	47	-

Table 3-4 Colour coding of sample coupons for different tests used in the study

Tests	Sample Labels	Colour Code
Waisted tensile	2A, 2B, 2C, 2D, 2E, A1, A2, A3, A4	(red)
Tensile impact	3A, 3B, 3C, 3D, 3E	(orange)
Guided side bend	4A, 4B, 4C, 4D, 4E	(yellow)
Nanoindentation	5A, 5B, 5C, 5D, 5E	(green)
Analytical sectioning	6A, 6B, 6C, 6D, 6E	(blue)
Space Between cuts		
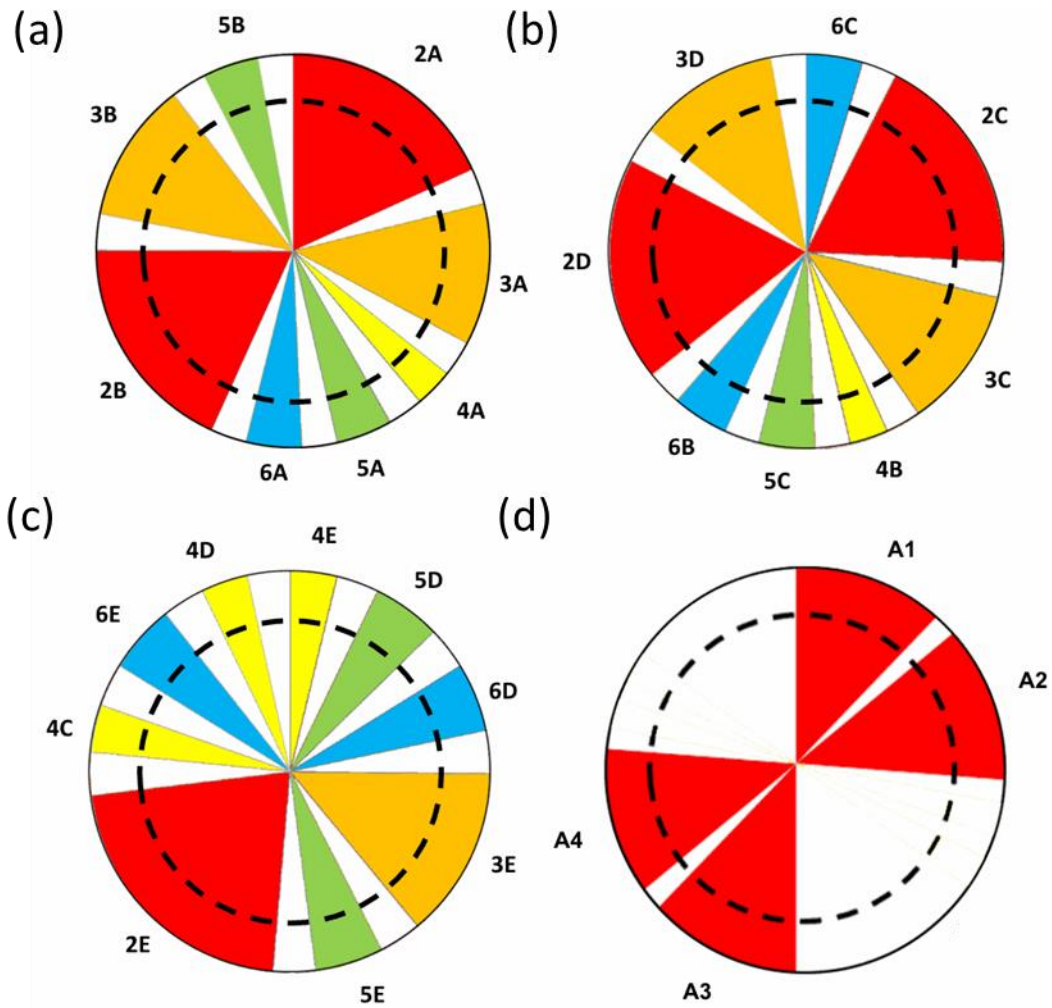
Figure 3-5 Cutting plans for the longitudinal sectioning of the welded pipes, for coupons testing and for the use of analytical techniques

The whole pipes will be cut to size for the WPTCR tests. The cutting and preparation of coupon test specimens will be completed in two stages; the near net shape of the coupon specimen will be cut form the pipes before being machined to the final high quality net shape.

4 Mechanical Testing

4.1 Introduction

This chapter describes the three short-term mechanical tests performed on coupons extracted from welded HDPE pipes, the methodology of the long-term whole pipe tensile creep rupture (WPTCR) test, and a FEA study to investigate the minimum length of pipe required for the WPTCR test. Each of the three mechanical (waisted tensile, tensile impact, and guided side bend) were tested with 5 test specimens (2A-E) each except for the waisted tensile test for which additional 4 test specimens (A1-4) were used. For waisted tensile test, the results of all test specimens were averaged for both pipe circumferential position and welding procedures (WP1-6). For tensile impact and guided side bend tests, all test specimens (3A-E and 4A-E, respectively) were averaged for each welding procedure (WP1-6) as the circumferential position has no bearing on specimen performance as confirmed by the results of the waisted tensile test. A statistical t-test discussed in Section 4.1.1 was used to determine if any statistically significant differences existed between welding procedures or circumferential positons of the test specimens using data from the three mechanical tests.

The waisted tensile test results are reported in three parts. The first section reports the total energy to break values for both circumferential position of the test specimens and the welding procedures. It is determined in this section that circumferential position has no impact on the results for the tensile impact and guided side bend test will only be reported according to the welding procedures. The second and third parts split the energy to break values of the specimens into 'before yield' and 'after yield' stages, respectively. The tensile impact test results are reported using only total energy to break values for each welding procedures. Since all the tensile impact test specimens yielded in the parent material, the splitting of the energy to break values into 'before yield' and 'after yield' stages would have been invalid. The results of waisted tensile and tensile impact tests are reported in joules (J) instead of Jmm^{-4} since all test specimens have identical nominal dimensions.

For guided side bend test results only the force value for each specimen has been provided due to all specimens passing the test. An attempt has been made to clarify these results using measurement from the specimen geometry which has been a challenge to machine a consistent specimen thickness.

The WPTCR test tests the welded pipes with loading conditions akin to those experienced in service. The specimen geometry and test setup in accordance with previous study conducted by Troughton and Brown (2003) is discussed. It was not possible to discuss the results as the test is currently ongoing; though the results will form part of future publications.

The last section of the chapter covers the FEA modelling of the long-term WPTCR test. The aim of the FEA modelling was to determine the minimum length of pipe required for testing 180 mm SDR 11 pipe in order to reduce the cost of testing and enable more tests specimen to be prepared from a limited length of available pipe.

4.1.1 Independent two-sample t-test

The results of the mechanical tests will be subjected to a statistical test. An independent two-sample t-test method was used to determine if one welding procedure or circumferential position of the specimen was statistically different from another welding procedure or circumferential position, respectively. The data (i.e. energy to break value) for each test was grouped according to either welding procedure or circumferential position. These groups were then compared in pairs i.e. WP1 against WP2-6 and WP2 against WP3-6, where each instance of comparison provided a probability regarding the confidence for a statically significant difference that existed for each instance. The probabilities provided for each unique instance were tabulated since comparing WP1 to WP2 is same as comparing WP2 to WP1. The probability values below 0.05 (5%) are to be interrupted as the difference between the welding procedures or the circumferential position of the test specimens to be statistically significant with a confidence of 95%.

4.2 Waisted Tensile Test

The purpose of the waisted tensile test is to assess the performance of butt fusion welded joint in PE pipes. The test enables the tensile force to be concentrated at the

weld through the specimen geometry. The test conducted in this study is derived from BS ES 12814-7:2002 and WIS 4-32-08 2002 (WIS, 2002).

4.2.1 Specimen geometry

The waisted tensile test specimen geometry is based on EN12814-7 2002; it is also similar to the specimen geometry recommended in WIS 4-32-8 2002 Appendix B. The thickness of the specimen is equal to the pipe wall, shown in Figure 4-1. It has been previously observed that the specified geometry allows the loading holes to yield. The test has been improved to prevent deformation of the loading holes by the addition of four holes surrounding each loading pin hole, Figure 4-2. These additional holes will be used to tightly secure the support plates using nuts and bolts, Figure 4-3. The beads are left intact.
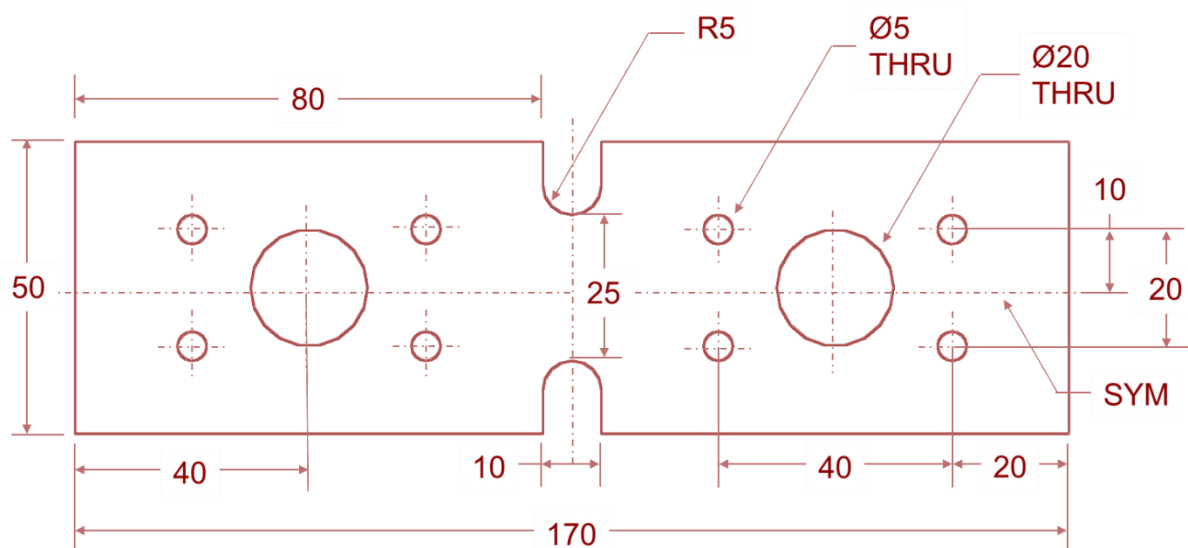
Figure 4-1 Improved waisted tensile test specimen geometry based on EN 12814-7 and WIS 4-32-08
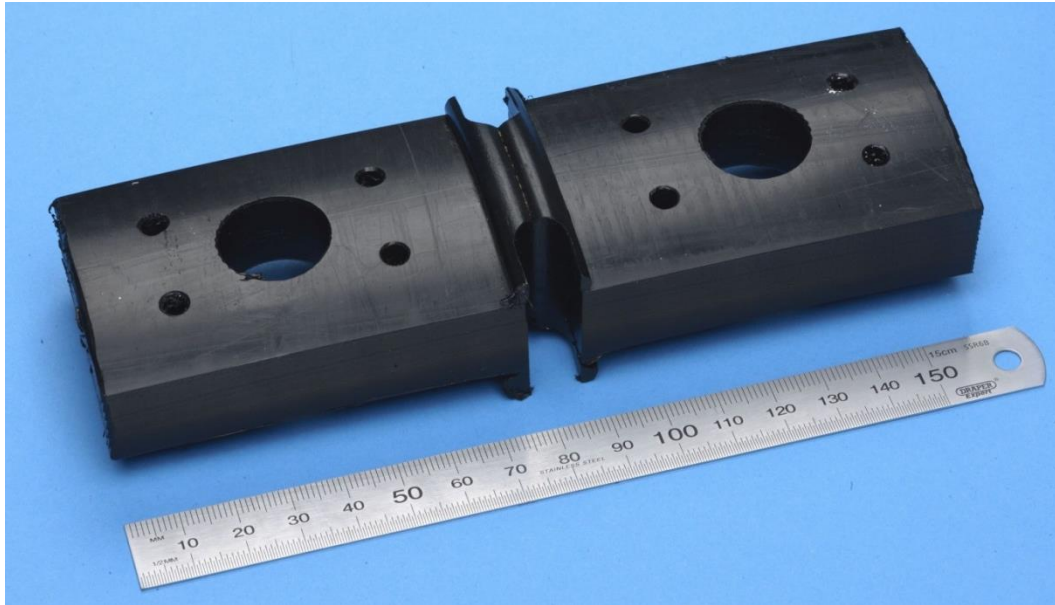
Figure 4-2 Improved waisted tensile test specimen geometry, based on EN 12814-7 and WIS 4-32-08 (TWI, 2016)
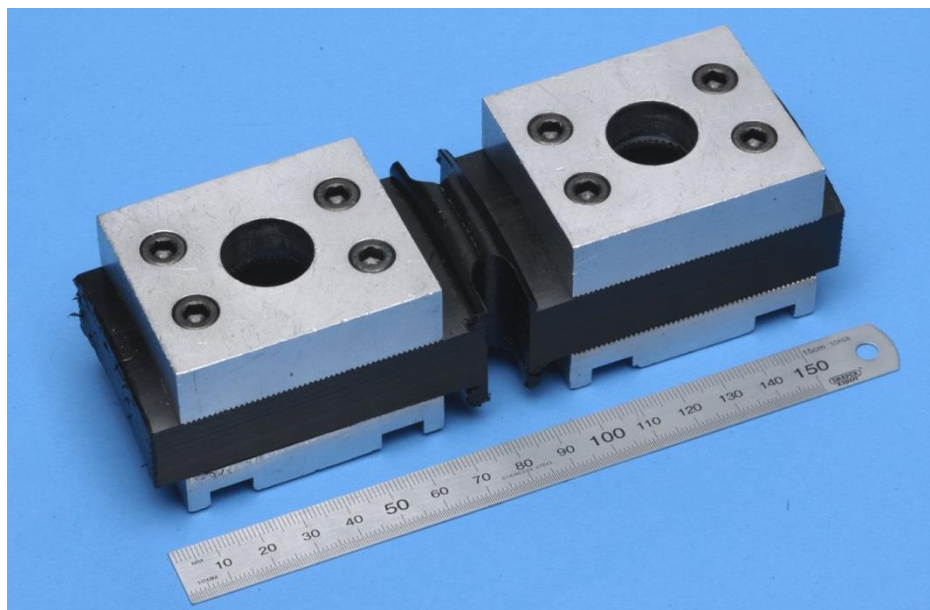
Figure 4-3 Waisted tensile test specimen with side support plates fitted (TWI, 2016)

4.2.2 Test setup

Figure 4-4 shows the arrangement of a typical waisted specimen in the 50 kN Hounsfield H50KC universal test machine using a test jig. The test machine had been calibrated by Sercal Materials Testing Machines Services Ltd, a UKAS accredited test machinery calibrator. All specimens were conditioned at room temperature (20 ºC ± 2) prior to testing.

Figure 4-4 Waisted tensile test specimen set-up inside the testing jig (TWI, 2016)

4.2.3 Methodology

Originally, five specimens were prepared per welding procedure. Later, spare welds were used to produce four additional waisted test specimens per procedure for the welding procedures 4-6 in order to improve statistical significance of the results. However, the preparation facility had been upgraded in the time spanning the production of first five specimens and the four additional specimens. The original specimens were prepared on a manually controlled machine but the latter additional specimens were produced using fully automated machines. The tests were conducted at a rate of 5 mm min^{-1} ± 10%. For each test specimen the following details were recorded: force/time graph, maximum force and elongation attained in the test and the manner of failure (whether brittle or ductile). The energy at yield and the energy to break or rupture were calculated from the force-time graph.

4.2.4 Results and discussion

All of the waisted tensile test specimens failed in a ductile manner and featured fracture surfaces similar to those shown in Figure 4-5. Figure 4-6 shows the stress-

strain curves for three high speed tensile impact specimens. For the waisted tensile the energy to break values test are listed in Table 4-1 and then the averaged values for each welding procedure are shown in Figure 4-7.

Figure 4-5 Image of the failure in a typical waisted tensile test specimen featuring ductile fracture surfaces at the weld

The unwelded specimen failed with energy to break value of 385 J which is 50% higher than the average energy to break value of 256 J for the welded specimens. There are no specimens who have energy to break value greater than that of the parent as listed in Table 4-1. The stress-strain curve of the specimen with the highest energy to break value is that of the unwelded parent material (334 J for the welded specimen), shown in Figure 4-6. The yield points of the three specimens are almost identical except for the strain values that they are reached at which is expected due to the following: the crystallinity of the weld region is higher, the material is orientated perpendicular to the tensile loading force, and the weld experiences reinforcement due to the weld beads shifting yield points of the welded specimens past the unwelded parent specimen. The weld regions are unable to deform like the parent material due to higher crystallinity and chain orientation. The parent material specimen in shows the lamellae undergoing strain-induced recrystallization at large deformations before failure.
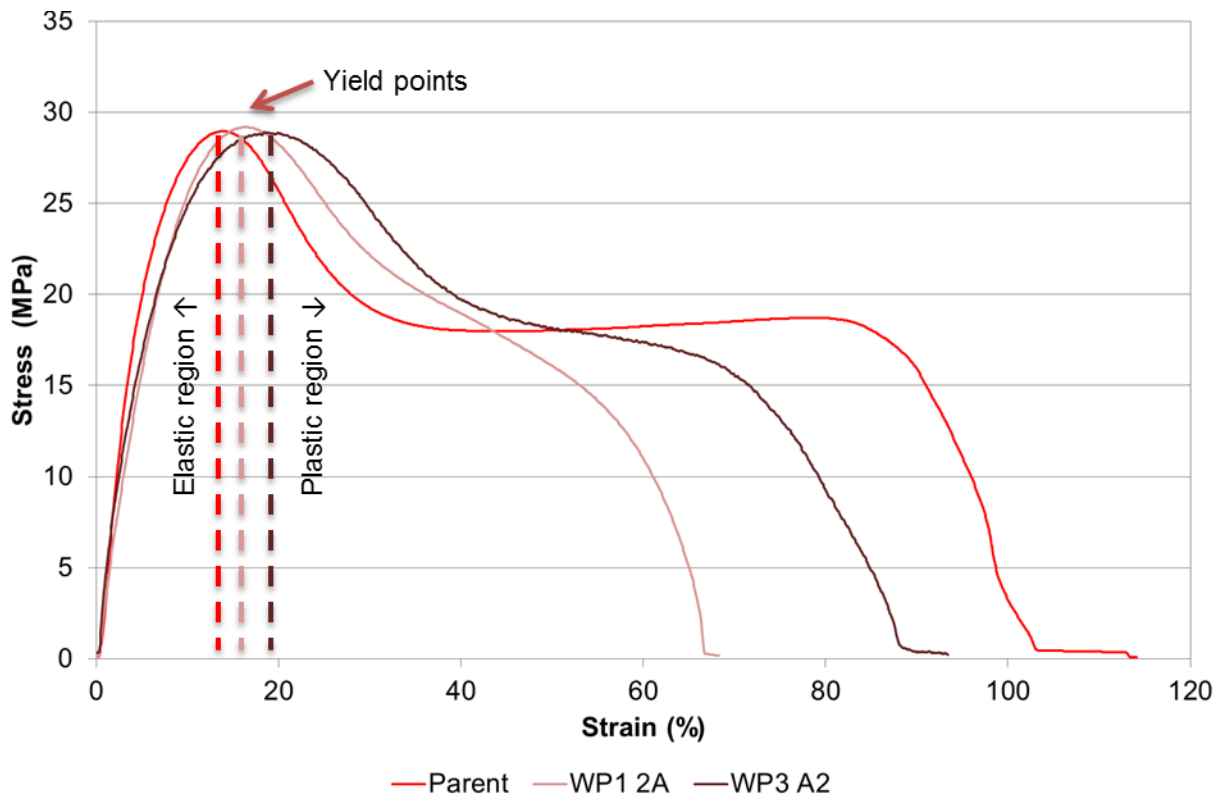
Figure 4-6 Engineering stress-strain curve for waisted tensile test results for the following specimens: unwelded parent material specimen (Parent), typical welded specimen (WP1-2A), and high deformation welded specimen (WP3-A2)

From Table 4-1, it is visible that the specimens A1-A4 from the spare welds show higher energy to break values than specimens labelled A-E.

Table 4-1 Energy to break values (J) arranged by welding procedure (WP1-6) and circumferential position (A-E and A1-A4)

	WP1	WP2	WP3	WP4	WP5	WP6
A	255	231	215	259	214	320
B	261	215	264	273	268	205
C	231	201	227	246	261	207
D	244	234	215	253	272	201
E	240	238	219	249	299	199
A1			305	310	311	206
A2			334	298	284	298
A3			314	304	292	219
A4			293	296	281	329
SD	10.76	13.79	44.75	24.30	26.38	52.36
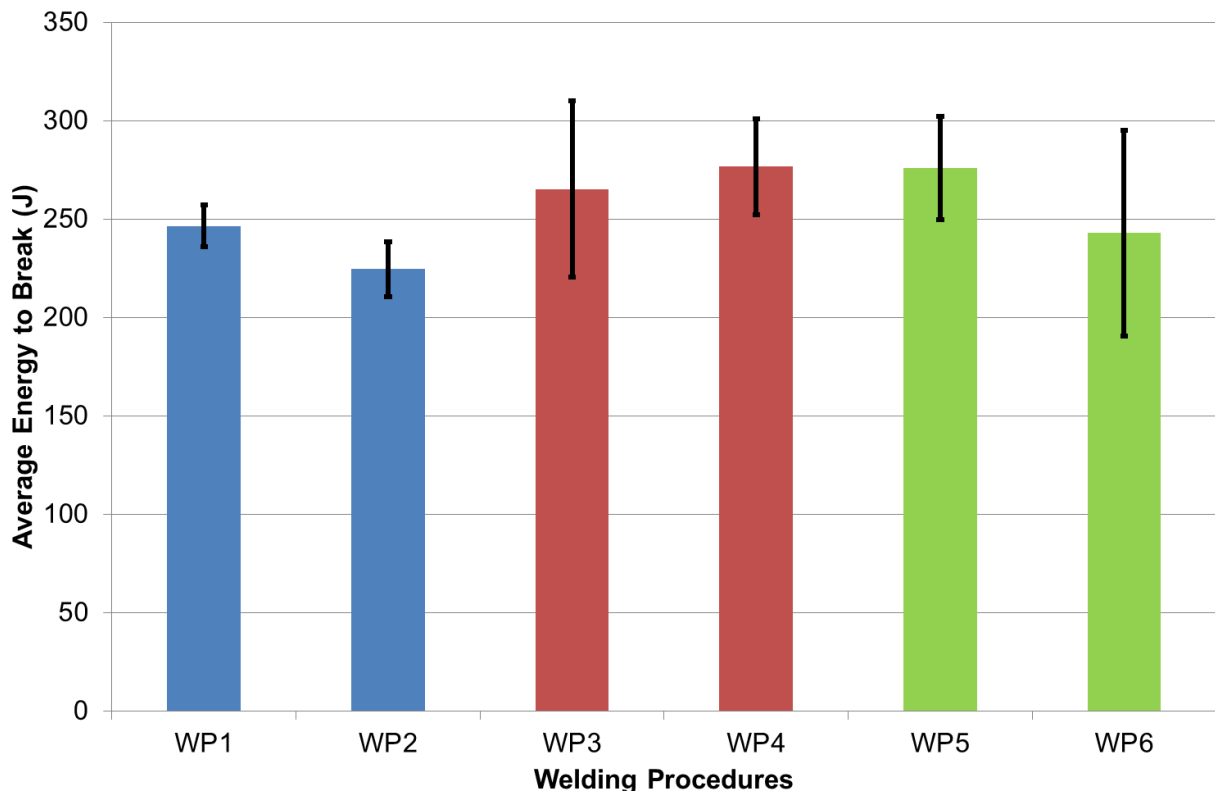
Figure 4-7 Averaged energy to break values for each welding procedure (WP1-6), error bars represent the standard deviation

The t-test values for welding procedures are shown in Table 4-2 and for circumferential positions are shown in Table 4-3. The t-test values show WP2 to be different than WP5 in Table 4-2, this is illustrated in Figure 4-7 where it can be seen that WP2 results do not overlap with those from WP5. More importantly, WP2 has the lowest overall energy to break values followed by WP1 and WP6. The standard deviation values of WP1 and WP2 are similar which is to be expected as both welding procedures were performed on the same welding machine.

Table 4-2 T-test table provides the probabilities for each instance of comparison of the welding procedures (WP1-6) based on the energy to break values to determine statistically significant difference between the welding procedures

	WP1	WP2	WP3	WP4	WP5	WP6
WP1		0.107	0.557	0.110	0.144	0.923
WP2			0.213	0.013	0.020	0.613
WP3				0.570	0.606	0.473
WP4					0.964	0.238
WP5						0.265
WP6						

The t-test values for circumferential position in Table 4-3 were above the threshold of 0.05 with the exception of C and D against A2 and A4. This is unexpected as circumferential positions of these specimens are similar: C with A2 and D with A4. Specimens A, C, A1, and A2 can be considered at the top of the pipe and the remaining specimens at the bottom of the pipe. The t-test value for differences in top (A, C, A1, and A2) and bottom (B, D, E, A3, and A4) specimens is 0.413, showing that circumferential position of the specimens are not of a concern across all welding procedures. The likely explanation for this anomaly is specimen preparation of the additional specimens (A1-4), as the stress-strain curves are similar in shape but the additional specimens were larger in area under the curve shown in Figure 4-7 previously.

Table 4-3 T-test table provides the probabilities for each instance of comparison of the circumferential positons (A-E and A1-4) based on the energy to break values to determine statistically significant difference between the circumferential positions

	A	B	C	D	E	A1	A2	A3	A4
A		0.964	0.459	0.663	0.791	0.425	0.119	0.399	0.139
B			0.398	0.640	0.796	0.352	0.053	0.313	0.065
C				0.692	0.616	0.137	**0.006**	0.102	**0.007**
D					0.872	0.212	**0.017**	0.172	**0.020**
E						0.293	0.050	0.259	0.060
A1							0.626	0.299	0.092
A2								0.561	0.875
A3									0.623
A4									

The t-test was then performed for the original and the additional specimens. The t-test provided the probability of 0.001, suggesting strongly that the additional specimens (A1-A4) have statistically significant difference in energy to break values, therefore the strength, when compared to the original specimens (A-E). The additional specimens (A1-A4) were prepared from welds that were made at the very end of the welding process. However, the pressure graphs of these welds were identical and so were the temperature readings of the hot plate. The statistically significant difference may stem from the machining of specimens, where the original and the additional specimens were machined by two different operators on two different machines. The manually operated machine relies on the skill of the operator

to consistently perform the cutting and milling operations across all specimens. The automated machine only relies on the operator to initially input the program that defines the cutting and milling operations. Additionally, the new machine was likely equipped with sensors that monitor the force required to hold the pipe section in place and adjust the said force accordingly during the machining process which may reduce the stress imparted during specimen preparation that may affect the joint strength. The dates of manufacture are also one year apart; it is possible that the stresses frozen from the welding process may have had time to relax for A1-A4 specimens.

The total energy to break value for each test specimen can be split at the point of specimen yielding. The contribution of the material towards the energy up until yield point comes from the viscoelastic properties. After the yield point the material is deforming plastically which leads to necking of the specimen and then failure by breaking. By splitting the energy to break at yield, it is possible to observe which region has greater contribution and if any relationship exists with the welding procedures. Analysis for circumferential positions will not be performed as it has no significant contribution on the results.

Table 4-4 lists the energy value at yield point for each welding procedure. Figure 4-8 shows the averaged values of energy at yield and Figure 4-9 the averaged values of energy after yield for each welding procedure. The t-test values for welding procedures for yield and after yield values are shown in Table 4-5 and Table 4-6.

Table 4-4 Energy at yield values (J) arranged by welding procedure (WP1-6) and circumferential position (A-E and A1-A4)

	WP1	WP2	WP3	WP4	WP5	WP6
A	66	65	73	73	67	79
B	65	66	72	69	69	72
C	66	66	68	67	68	71
D	64	66	68	71	70	72
E	69	65	72	73	69	77
A1			77	85	78	85
A2			79	83	76	89
A3			79	82	78	73
A4			77	77	76	90
SD	1.65	0.69	2.10	2.23	0.92	3.32

Figure 4-7 and Figure 4-9 are similar as the greater contribution towards energy to break values comes from the post yield region; on average the pre-yield region contributes 73 joules (28.5%) and post-yield region contributes 185 joules (71.5%).
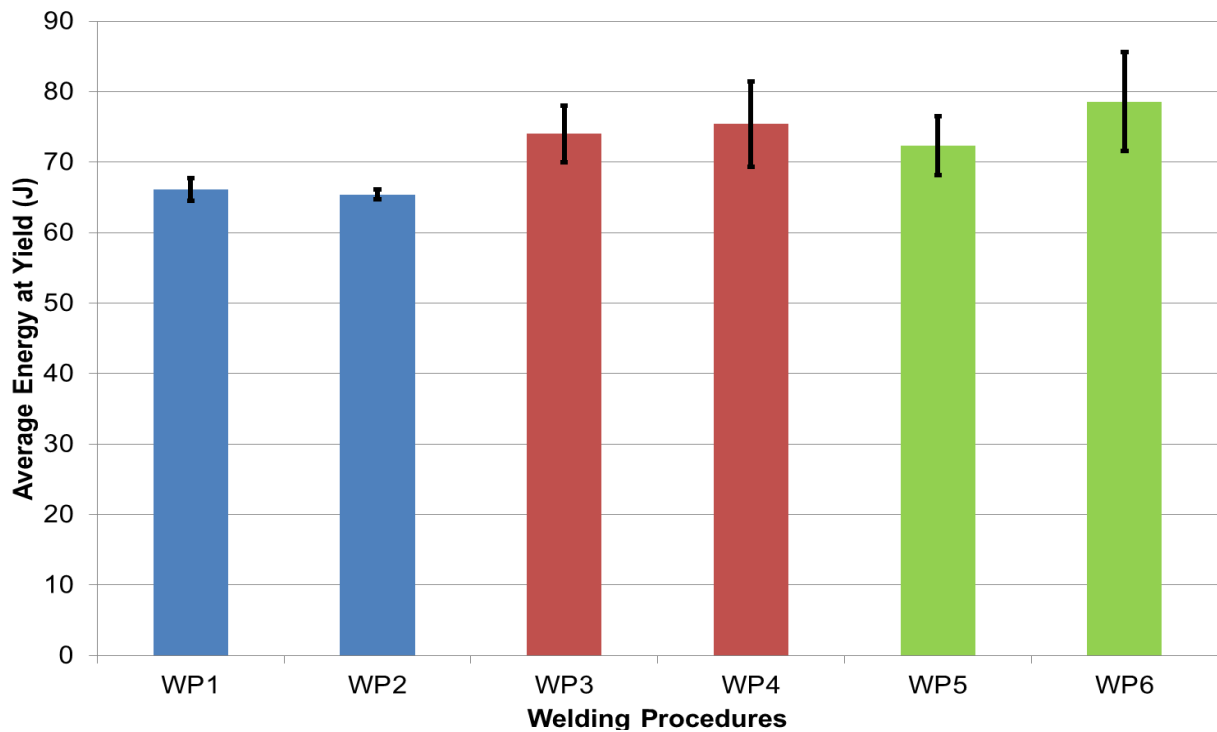
Figure 4-8 Averaged energy at yield for each welding procedure (WP1-6), error bars represent the standard deviation
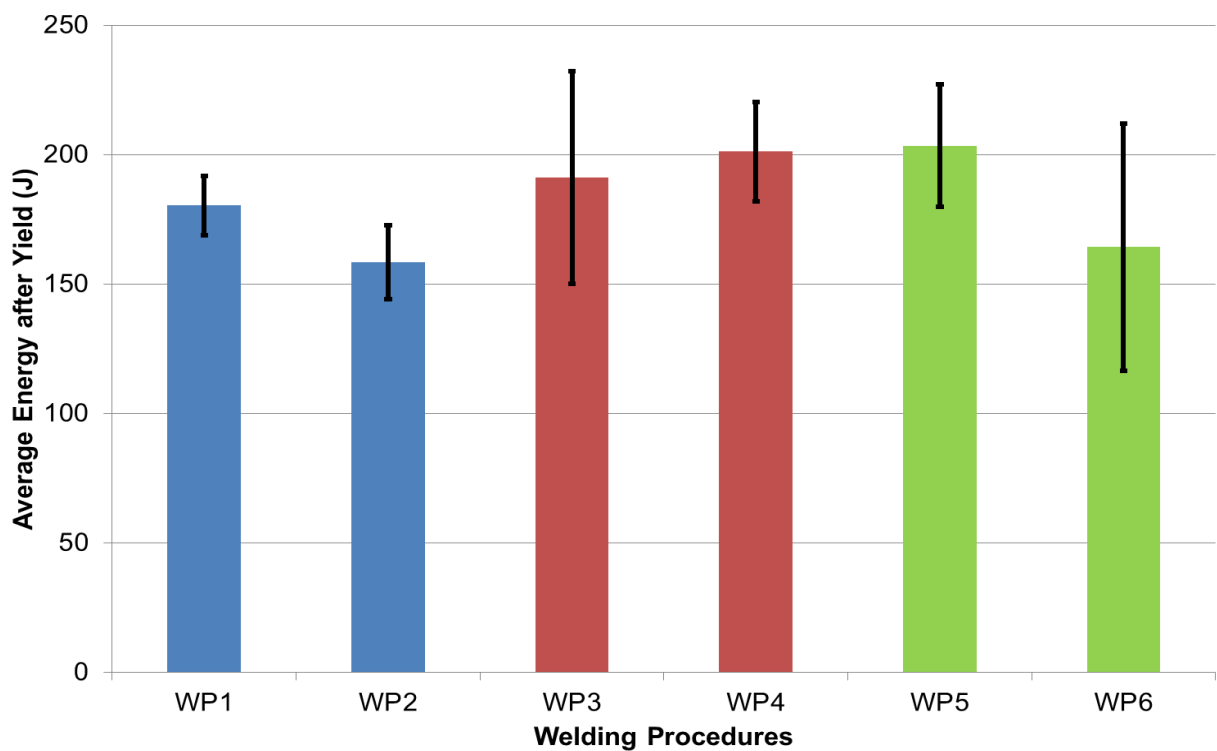
Figure 4-9 Averaged energy after yield for each welding procedure (WP1-6), error bars represent the standard deviation

The energy at yield values range from 64-90 joules corresponding to yield strength of 27.56-29.86 MPa, 10-19% higher than the manufacturer quoted 25 MPa. The t-test probabilities in Table 4-5 for WP1 and WP2 confirm that the energy to yield values were lower than those that are reported by other remaining welding procedures with the slight exception of WP1 to WP5, where the reported value is 0.057 which is greater than 0.05 threshold. This can be seen in Figure 4-8 that the energy to break values of WP1 and WP2 are consistently lower but with a smaller standard deviation than WP4-6, which may be due to the two different welding machines used. However, this trend for WP1 and WP2 is not repeated in Figure 4-9 which compares the energy to break values after yield; instead the t-test probabilities in Table 4-6 show only WP2 to be statistically different than WP4 and WP5. It can be seen in Figure 4-8 that the energy to break values mimics the increase in welding pressure across the welding procedures. In Figure 4-9, the effect of welding procedures is more pronounced in forms of the heat input and the resulting shape of the weld beads for the energy after yield. WP5 gives the highest values; this could be due to very long heating times allowing a steady annealing effect around the weld region which allows for higher loading by steadily enlarging the size of the weld region.

Table 4-5 T-test table provides the probabilities for each instance of comparison of the welding procedures (WP1-6) based on the energy at yield to determine statistically significant differences

	WP1	WP2	WP3	WP4	WP5	WP6
WP1		0.579	**0.018**	**0.047**	0.057	**0.025**
WP2			**0.009**	**0.032**	**0.032**	**0.018**
WP3				0.706	0.584	0.275
WP4					0.422	0.500
WP5						0.148
WP6						

Table 4-6 T-test table provides the probabilities for each instance of comparison of the welding procedures (WP1-6) based on the energy after yield to determine statistically significant differences

	WP1	WP2	WP3	WP4	WP5	WP6
WP1		0.132	0.711	0.170	0.203	0.637
WP2			0.283	**0.015**	**0.026**	0.867
WP3				0.665	0.611	0.405
WP4					0.882	0.170
WP5						0.160
WP6						

Each waisted tensile test specimen failed from the notch between the weld bead and the pipe wall where the notch is acting as a stress concentration. The ductile features consisted of long elongated tails and show some whitening of the areas being drawn into the necking region which is unstable. The waisted tensile test with statistical analysis was able to differentiate between the performances of the test specimens made with different welding procedures. The test was sensitive to specimen preparation and was also potentially affected by the performance of the welding machines as seen by the size of the standard deviation bars which are smaller for WP1-2 than WP4-6. The test confirms that the circumferential position of the specimens has no significant impact on the reported results. The energy to break values can be split at yield to potentially reveal new insights: on welding pressure during welding using energy at yield; and on heat input using energy after yield. The waisted tensile test confirms WP2 to be the lowest performing, and WP4-5 to be the highest performing welding procedures.

4.3 Tensile Impact Test

The high speed tensile impact test defined in ASTM F2634-10 is designed to determine the quality of butt fusion welded pipes made in the field or in qualification testing. The standard states that it can be used for determining the optimum welding parameters in butt fusion welding of PE materials. It does so by developing sufficient tensile impact energy to rupture the butt fused zone at specified strain rates.

4.3.1 Specimen geometry

The high speed tensile impact specimen geometry illustrated in Figure 4-10 is in accordance with that specified in the ASTM F2634-10 standard. The imperial dimensions were converted to metric units and care was taken to ensure the recommended tolerances were followed. The thickness of the specimen is equal to the pipe wall, shown in Figure 4-11.
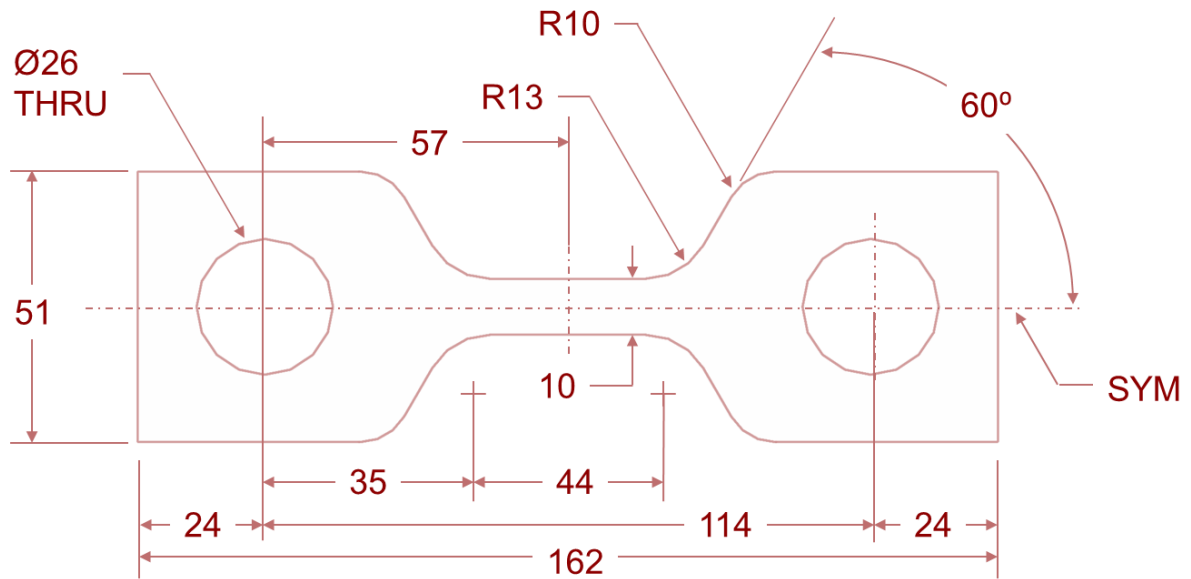
Figure 4-10 High speed tensile impact test specimen geometry with dimensions converted to metric system (rounded to the nearest mm) from ASTM F2634-10

Figure 4-11 High speed tensile impact test specimen (not actual specimen) (TWI, 2016)

4.3.2 Test setup

Figure 4-12 shows the arrangement of specimen in the 500 kN Instron 8500 universal test machine. All specimens were conditioned at room temperature (20 ºC ± 2) prior to testing.
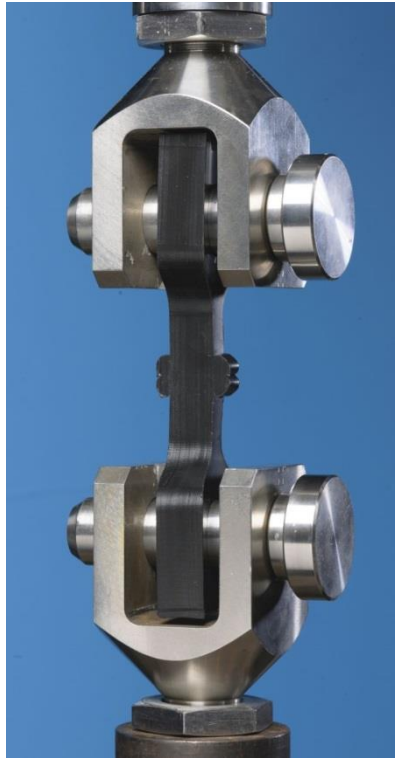
Figure 4-12 High speed tensile impact test specimen set-up inside the testing jig (TWI, 2016)

4.3.3 Methodology

Five specimens per welding procedure were prepared with the weld beads left intact. The tests were conducted at a rate 152 mm min^{-1} ± 10%. For each test specimen the following details were recorded: force-time graph, maximum force attained in the test, rupture energy, yield energy, yield stress, average high speed tensile impact test speed and documented type of rupture (brittle, ductile, or mixed) and its position.

4.3.4 Results and discussion

The fracture surfaces of the high speed tensile impact specimen are shown in Figure 4-13. Figure 4-14 shows the stress-strain curves for three high speed tensile impact specimens and Figure 4-15 provides the image of the three specimens to show the difference in their deformations. The energy to break values for the high speed tensile impact tests are listed in Table 4-7 and the averaged values for each welding procedure is shown in Figure 4-16. The t-test values for welding procedures are shown in Table 4-8; the t-test table for specimen position is not included due to lack of statistically significant values.
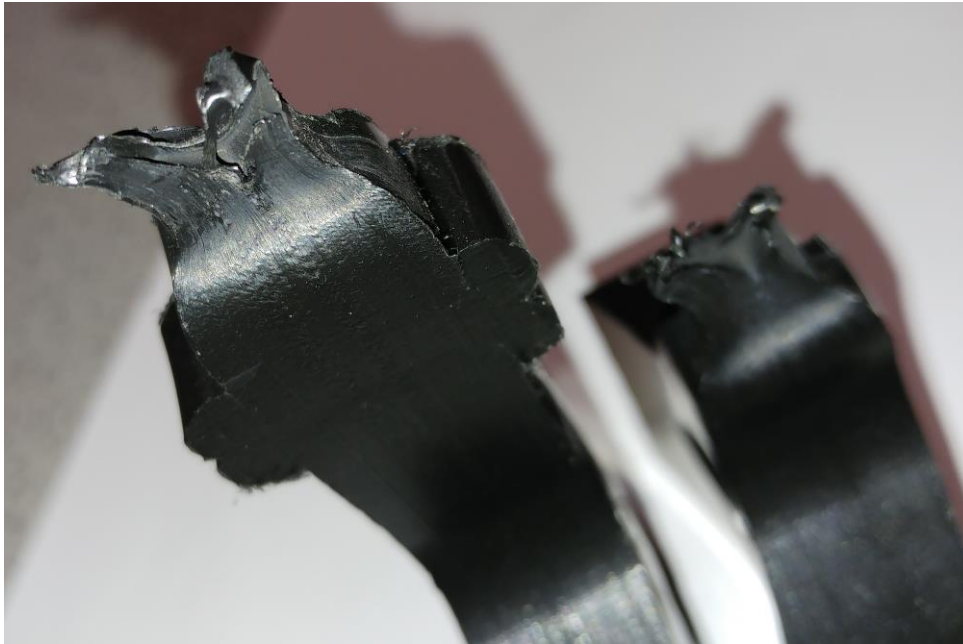
Figure 4-13 Image of typical failure in a typical high speed tensile impact test specimen featuring ductile fracture surfaces at the weld

The unwelded parent material specimen failed with energy to break value of 169 J which is higher than the average energy to break value of 136 J for the welded specimens. There are only four specimens who have energy to break value greater than that of the parent as listed in Table 4-7 from WP5 and WP6. The stress-strain curve of the specimen with the greatest energy to break value is shown in Figure 4-14, WP6-3A, experiences the largest strain before sudden failure. The behaviour of the three specimens is almost identical until the yield point after which it diverges. The before yield behaviour implies that the processing conditions for PE100 grade HDPE polymerisation, HE3490-LS resin compounding, and pipe extrusion appear broadly similar due to high strain rate. The divergence in post yield behaviour is expected due to the viscoelastic properties of the material at high strains amplifying the anisotropic properties stemming from pipe extrusion, machining defects, and minute differences in compounding heterogeneity. This divergence under appropriate conditions allows some specimens to draw material in the necking process due to the strain which causes mechanical instability. The drawing process ends due to insufficient strain-hardening caused by high strain rate or by low molecular weight region (Vincent, 1960). The welded specimen typically necked for approximately 10-15 mm against roughly, 25 mm of the unwelded parent and 50+ mm of the four high deformation welded specimens; all apparent in Figure 4-15 .
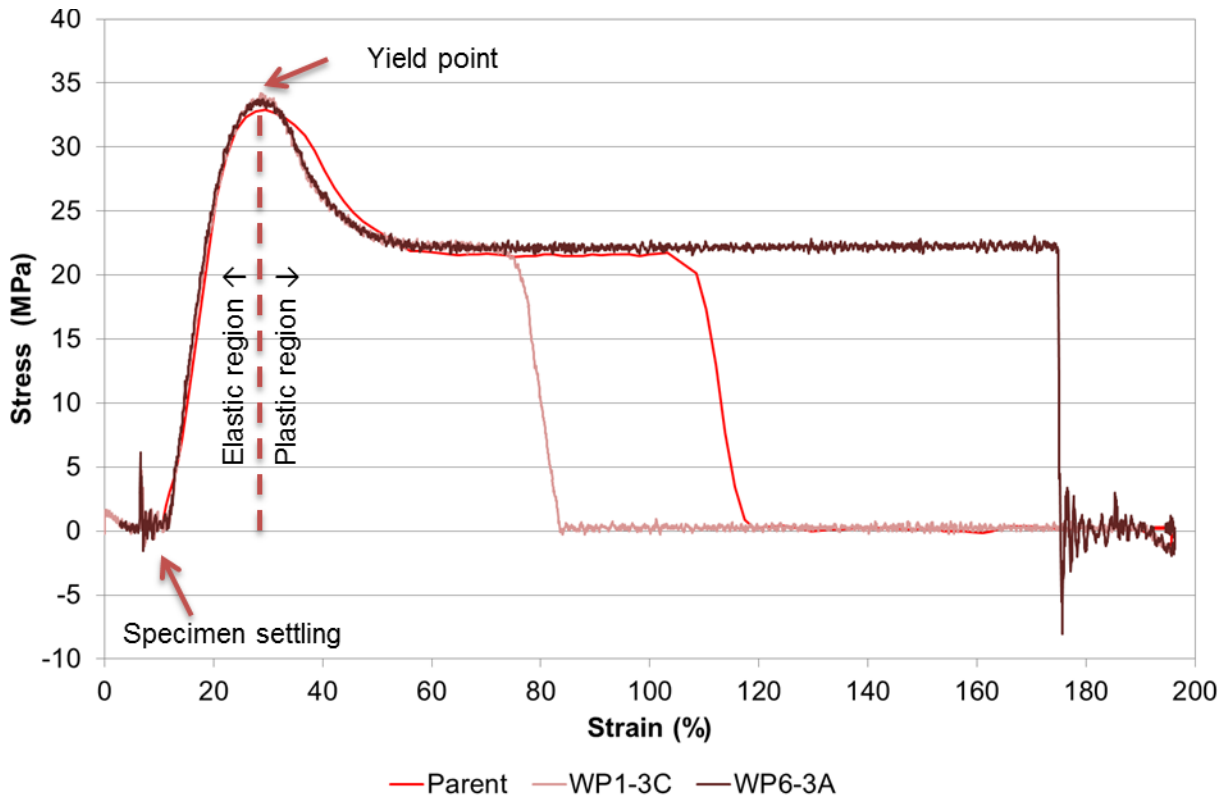
Figure 4-14 Engineering stress-strain curve for high speed tensile impact test results for the following specimens: unwelded parent material specimen (Parent), typical welded specimen (WP1-3C), and high deformation welded specimen (WP5-3A)

Figure 4-15 image of the high speed tensile impact specimens illustrating the difference in deformation left to right: unwelded parent material specimen (Parent), typical welded specimen (WP1-3C), and high deformation welded specimen (WP5-3A)

95

All of the high speed tensile impact specimens failed in a ductile manner as seen in Figure 4-13 and Figure 4-15. It has been previously shown that the high speed tensile impact test could not differentiate between the welding procedures by Hinchcliff and Troughton (1998) and therefore it is of little confidence in what can be concluded on weld strength from the results of failures occurring in the parent material. The energy to break values reported by the test cannot represent the energy required for the failure of the weld interfaces as all of the failures occurred in the parent material adjacent to the weld.

Table 4-7 Energy to break values (J) arranged by welding procedure and circumferential position (A-E)

	WP1	WP2	WP3	WP4	WP5	WP6
A	136	126	99	102	88	270
B	135	125	109	98	257	160
C	119	133	100	108	263	128
D	121	132	99	105	104	255
E	131	133	100	100	142	109
SD	**7.11**	**3.59**	**3.79**	**3.80**	**74.78**	**65.90**
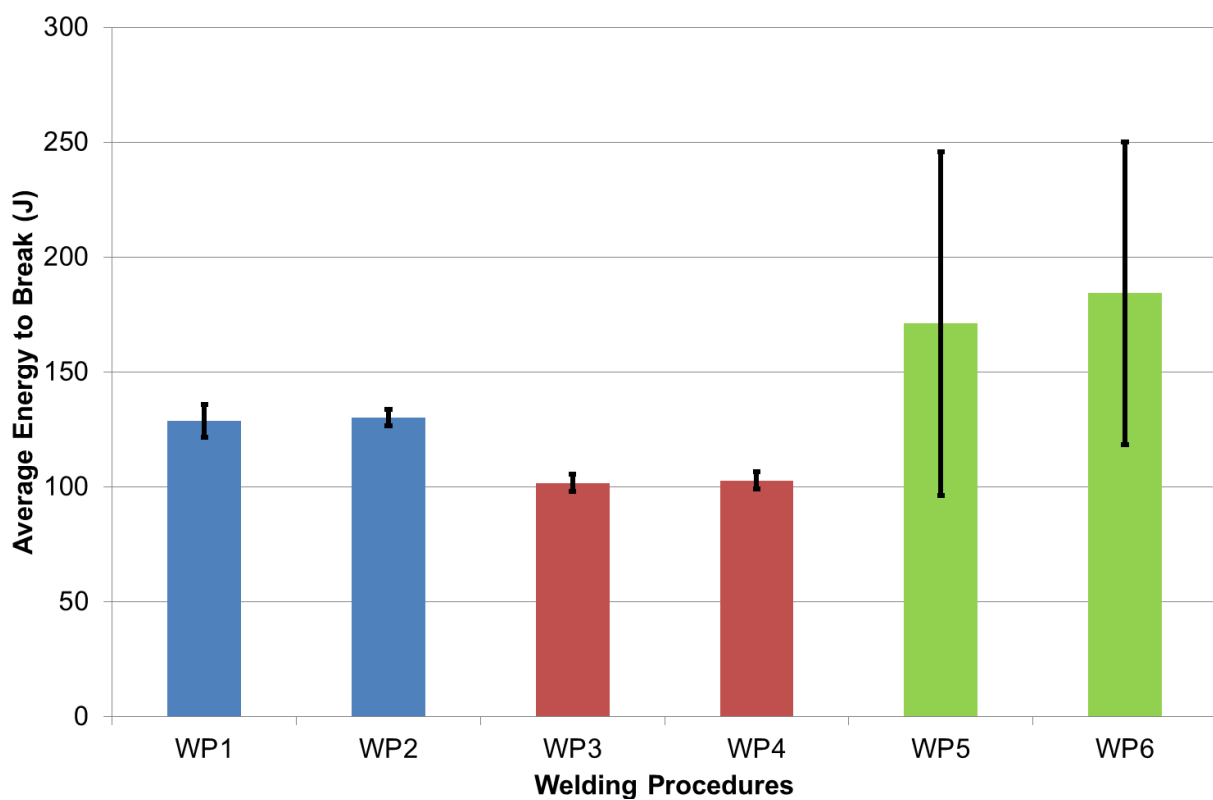
Figure 4-16 Averaged energy to break values for each welding procedure, error bars signify two standard deviations

A statistical t-test has been used to determine if the tensile impact test is able to differentiate between the welding procedures despite the specimen failures occurring in the parent material. As shown by Figure 4-6, the ASTM based WP3 and WP4 gave the lowest values followed by European WP1 and WP2. The non-standard WP5 and WP6 gave the highest values but with the largest standard deviation. The t-test probabilities in Table 4-8 show WP3 and WP4 to be statistically different (corresponding values below 0.05 threshold) than WP1 and WP2 due to little overlap in their energy to break values. The specimen preparation for all welding procedures was completed by the same operator using the same machine; therefore, the test results for WP5 and WP6 should not have such a large standard deviation.

Table 4-8 T-test table provides the probabilities for each instance of comparison of the welding procedures (WP1-6) based on the energy to break values to determine statistically significant difference between the welding procedures

	WP1	WP2	WP3	WP4	WP5	WP6
WP1		0.815	**0.001**	**0.002**	0.448	0.269
WP2			**0.000**	**0.000**	0.461	0.278
WP3				0.786	0.227	0.114
WP4					0.233	0.118
WP5						0.855
WP6						

The high speed tensile impact test fails the test specimens in the parent material rather than at the weld and thus not represent the weld strength when using different welding procedures. The geometry of the test specimens with the welds beads intact strengthens the weld area which causes the failure to start from the areas of stress concentration such as the notches between the weld beads and the pipe wall. The possible solutions to improve consistency in this test is to remove the weld beads and to conduct test in an environmental chamber with the temperature set below the glass transition temperature of the material being tested.

4.4 Guided Side Bend Test

The guided side bend test as defined in the ASTM F3183-16 (2016d) is designed to assess the ductility of a butt fusion joint. A lateral load applies a bending strain across the fusion zone. An advantage of this test is that it tests the whole fusion zone using full pipe wall thickness.

4.4.1 Specimen geometry

The guided side bend specimen geometry illustrated in Figure 4-17 in accordance with the standard which recommends a set preparation sequence where a 19 mm thick bend test coupon is rough cut from the pipe and machined into a guided side bend test coupon shown in Figure 4-18, the residual stress curves the specimen length towards the pipe centre. The length of the specimen is allowed a small range and the thickness is given a tolerance. The length of specimen at each side of fusion zone can be different; the test will not be affected. The standard test is recommended for pipes with the wall thickness greater than 25.4 mm.
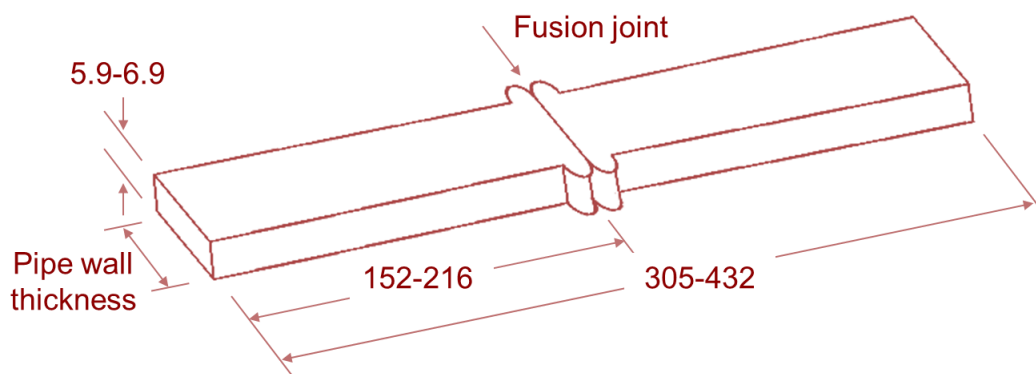
Figure 4-17 Guided side bend test specimen geometry adapted from ASTM F3183-16 (2016d)
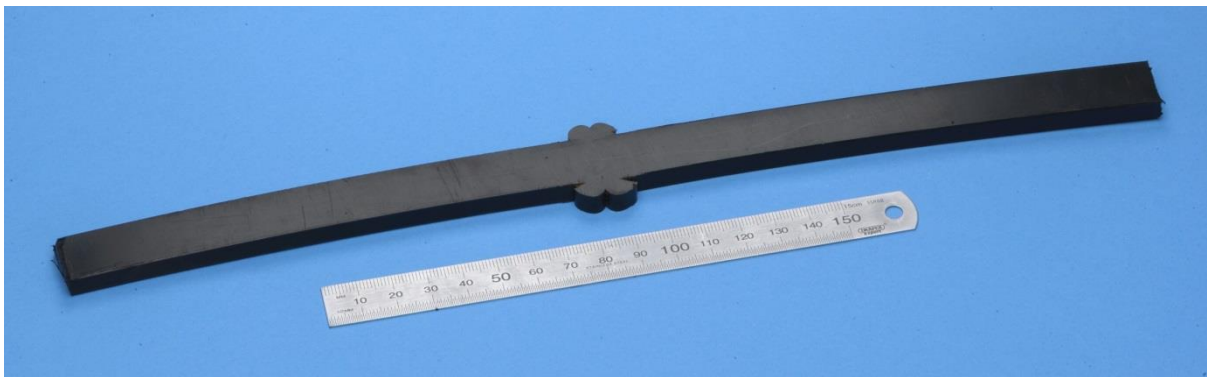
Figure 4-18 Guided side bend test specimen based on ASTM F3183-16 (2016d)

4.4.2 Test setup

Figure 4-19 shows the arrangement of the guided side bend test and instructs with regards to positioning of the specimen. All specimens were conditioned at room temperature (20ºC ± 2) prior to testing.
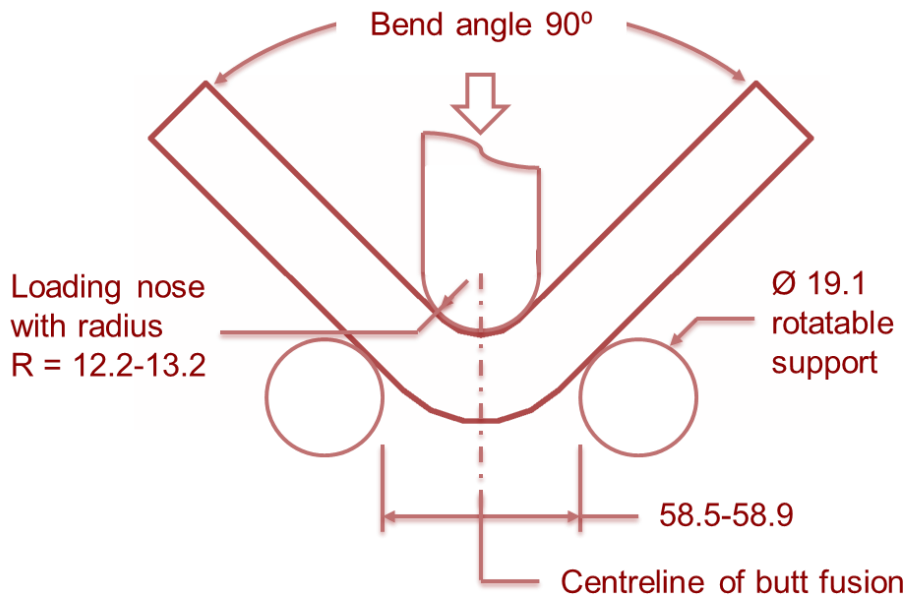
Figure 4-19 Schematic of guided side bend test apparatus adapted from ASTM F3183-16 (2016d)

4.4.3 Methodology

The test specimen is centred on the rollers and the loading nose was brought slowly in contact with the surface. The weld beads were used to visually align the centreline of the butt fusion joint with the loading nose. The tests were conducted at a rate of 76.2 mm min^{-1} ± 25.4 mm min^{-1}, at a constant, steady and uniform rate as specified in the standard. The test is to be stopped when the specimen reaches a bend angle of 90^0 or if the specimen fails before reaching 90^0, and the time recorded. Dummy specimens were used to ensure the performance of the test rig was as required in the standard. The dummy specimens showed no signs of cracking due to their ductility at 90^0 when the test was stopped. Therefore, the test was then extended to 45^0 bend angle which is the maximum possible bend angle allowed by the test rig, the dummy specimen still showed no signs of cracking. The peak force and time to end the test was recorded. A small mirror was installed beneath the rig to allow continuous observation of the specimen beneath the loading nose for any signs of cracking in accordance with the standard. The test sequence is shown in Figure 4-20.
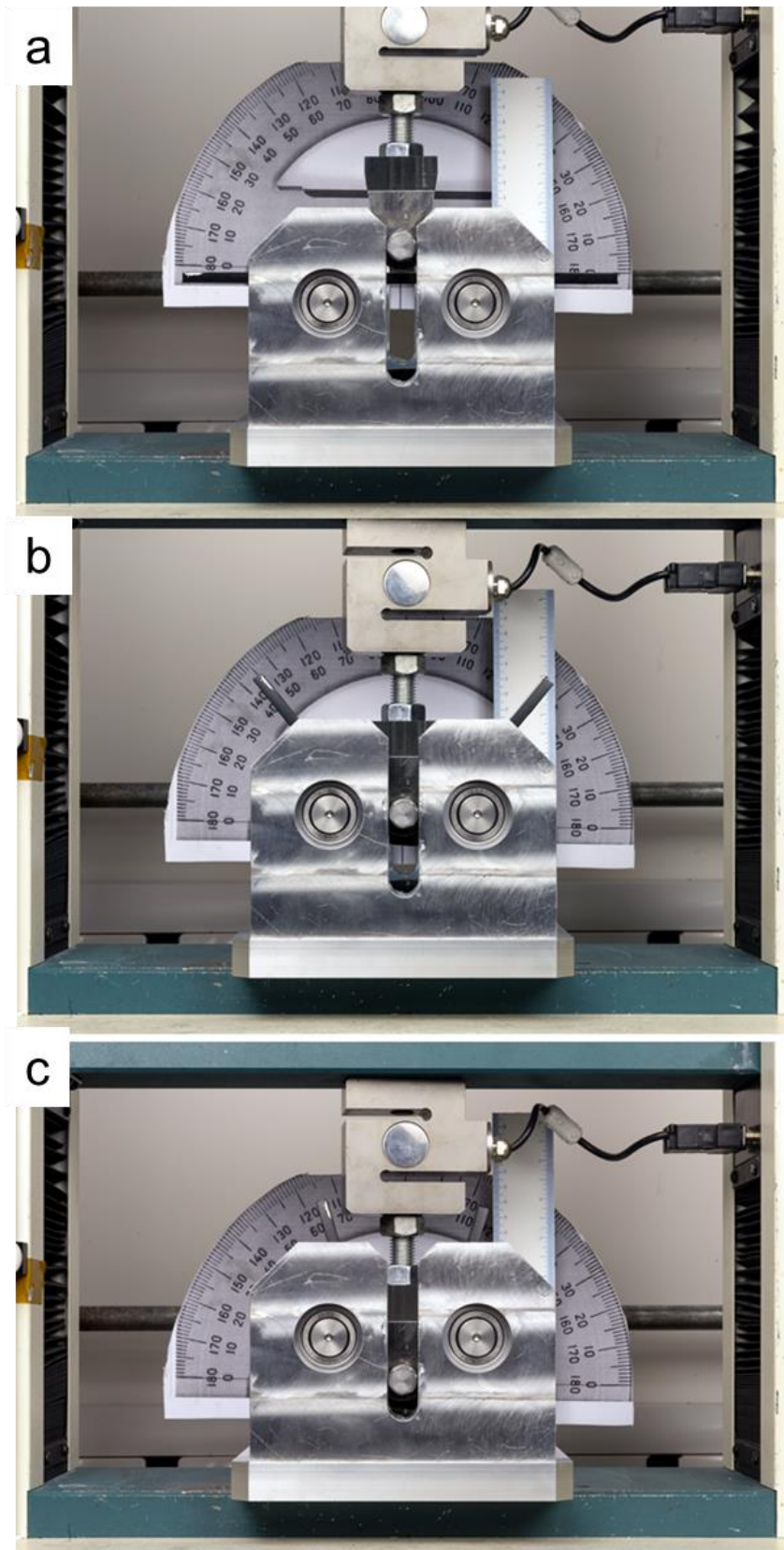
Figure 4-20 Image sequence of guided side bend test being performed where: the specimen is ready for testing (a), the specimen is at a bend angle of 90º (b), and the specimen is at a maximum allowable bend angle of 45º (c)

4.4.4 Results and discussion

The completed guided side bend test can be seen in Figure 4-21, where the ductility of the fusion zone without visible crack is shown in Figure 4-22. The maximum force reached by test specimens is tabulated in Table 4-9 and illustrated in Figure 4-23.
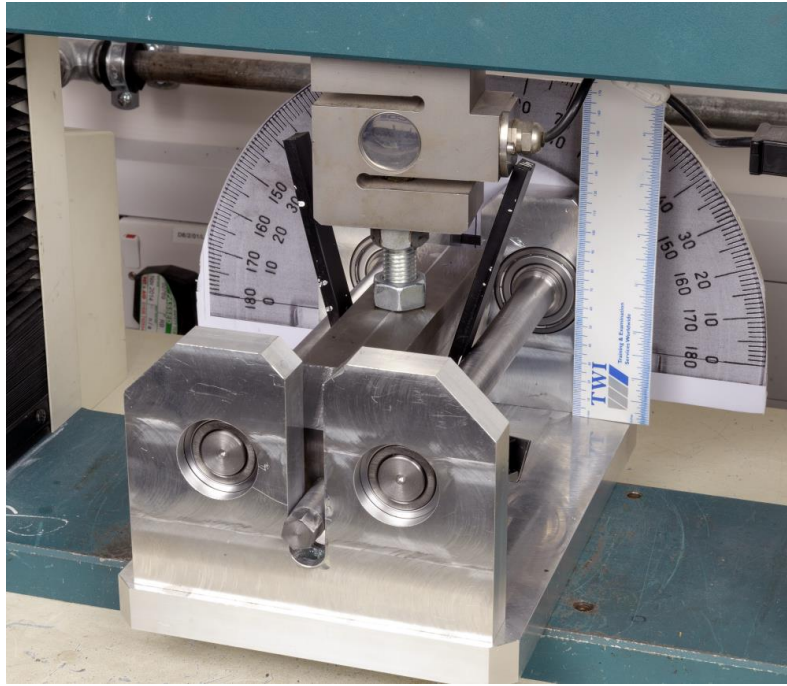
Figure 4-21 Completed guided side bend test at maximum bend angle of the test rig (TWI, 2016)
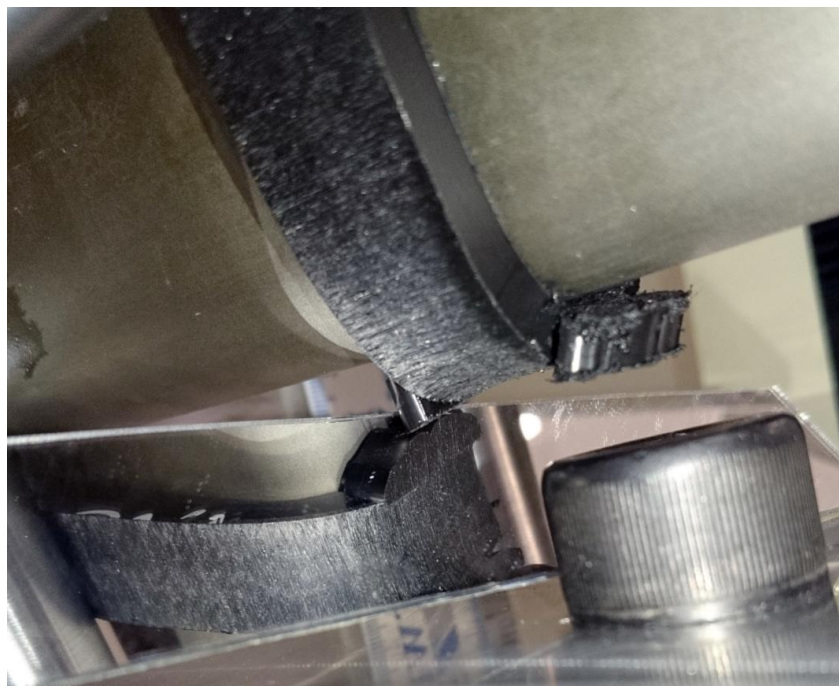
Figure 4-22 Photograph of guided side bend test specimen at maximum bend angle showing no visible cracks in the specimen

Table 4-9 Max force (N) for each welding procedure and circumferential position (A-E)

	WP1	WP2	WP3	WP4	WP5	WP6
A	307	300	299	335	290	285
B	289	289	327	270	300	330
C	334	290	275	337	302	327
D	307	302	265	269	302	350
E	317	274	309	315	335	327
SD	14.70	10.04	22.30	30.17	15.31	21.19
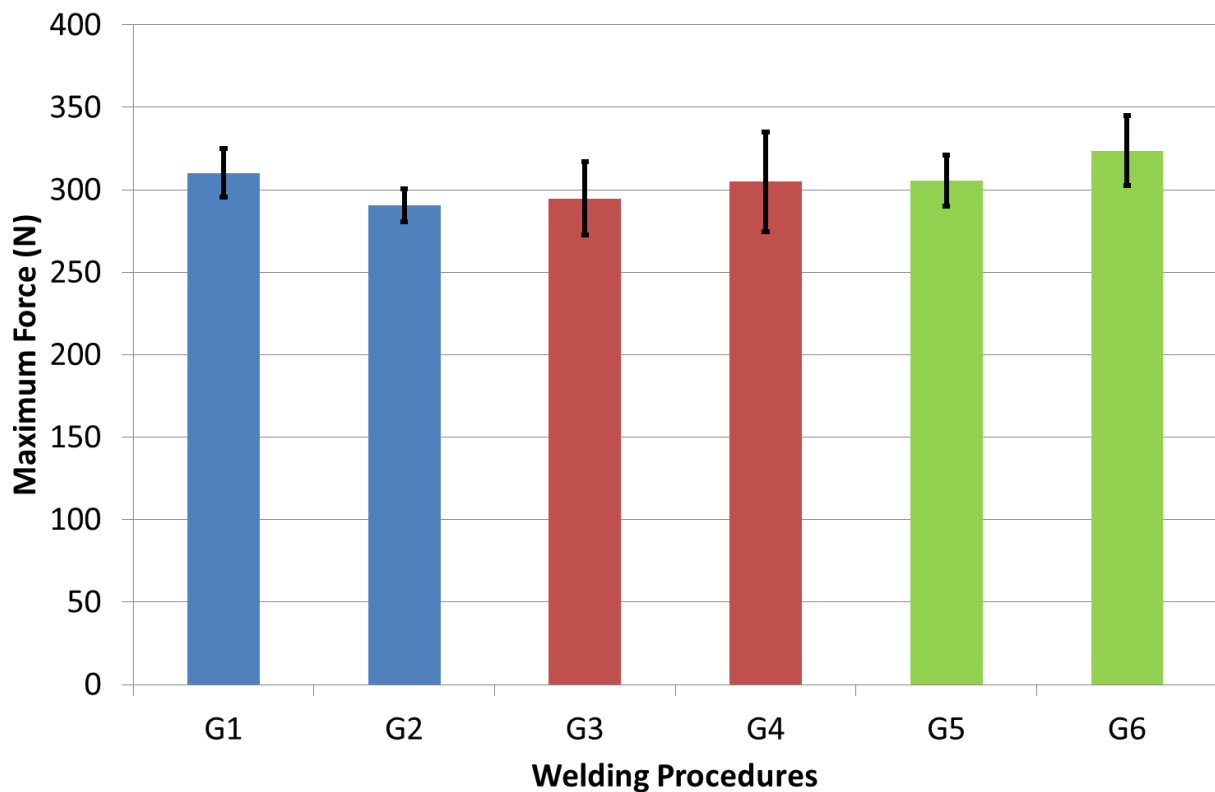
Figure 4-23 Averaged force for each welding procedure, error bars signify two standard deviations

All of the guided side bend test specimens passed the test criteria as specified in the standard with no sign of cracking when the bend angle at 90º and when it was increased to max of 45^0 as shown in Figure 4-21. This particular test is therefore unable to cause failure at the weld and unable to differentiate weld strength between the welding procedures.

The average maximum force for all procedures was 305 N. WP6, WP1 and WP5 had the higher maximum force values in that order while WP4, WP5 and WP2 had the largest standard deviation in that order. The difference in maximum force between specimens is likely to come from the variation in thickness given the large tolerance

6.4 ± 0.5 mm of allowed by the standard (ASTM, 2016d). It was noted by the operator preparing the guided side bend specimens, how difficult it was to firmly clamp the pipe section of such thickness and to machine the thickness as required consistently across the whole specimen geometry. It is also possible that the size and the shape of the weld bead left intact on the specimen had an effect.

It might be possible that the later revisions of the standard address the deficiencies of the guided side bend test by redefining the specimen geometry or the failure criteria. In a similar manner to tensile impact test, it may be possible to improve the consistency of the guided side bend test results by remove the weld beads.

4.5 Whole Pipe Tensile Creep Rupture Test

The whole pipe tensile creep rupture (WPTCR) test was developed at TWI (Troughton & Brown, 2003) to determine the long term performance of butt fusion welds in PE pipes. The WPTCR test subjects a whole pipe sample to a constant axial load at elevated temperature, inducing failure at the welded joint. Experimental regression curves of axial stress versus time to joint failure can then be produced that can be extrapolated back to real life pipe conditions.

4.5.1 Specimen geometry

The WPTCR is designed to take a variety of outer pipe diameters and pipe wall thicknesses. Currently, the length of pipe is limited to 650 mm sections due to the dimensions of the submersion tank.

4.5.2 Test setup

The WPTCR test schematic is shown in Figure 4-24, the pipe assembly is submerged in a water tank kept at 80 ^{0}C. Each pipe requires a pair of plate clamps that enclose the pipe ends and allow the push rod to induce 5.5 MPa of nominal constant axial tensile stress (Troughton & Brown, 2003), based on cross-sectional area of 180 mm outer diameter SDR11 PE100 pipe. The plate clamps are drilled to allow water to pass through. The time to failure and the failure mode is recorded. A total of 18 welded pipes representing the six welding procedures have been allocated for the WPTCR test.
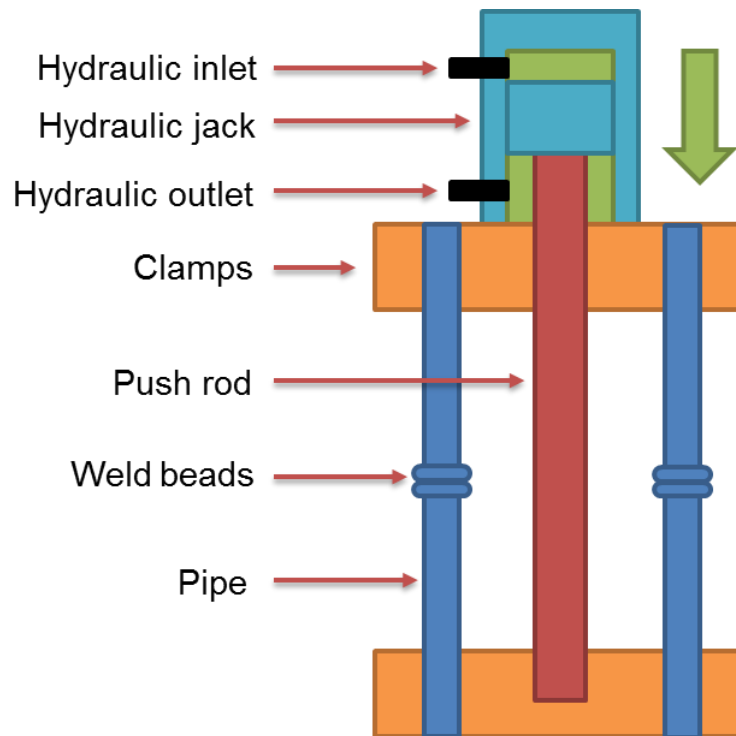
Figure 4-24 WPTCR loading arrangement schematic

4.5.3 Results and discussion

The welded pipes allocated for WPTCR test are currently being tested and the tests have been underway for over a year. There have been no failures so far in any of the pipe samples under test.

4.6 FEA: WPTCR

Currently, the WPTCR tests are conducted on 650 mm sections of pipe with the weld at the centre. It is prohibitive to use longer pipe lengths due to limited to the depth of the hot water tank. It would be beneficial to use smaller pipe lengths especially where long lengths of pipes are not available or where the weld is not centred requiring the pipe to be trimmed. The length of the pipe should be sufficient to prevent the effect of plate clamps from affecting the performance of the weld. It is known that there is a relationship between pipe parameters such as outer diameter, SDR and wall thickness etc. and the WPTCR pipe length. An FEA analysis was therefore carried out using a parametric study to determine what the minimum distance is between the end clamps and the butt fusion weld to avoid the effect of the pipe clamps on the stress in the weld. Table 4-10 lists the pipe outer diameters and SDR values that were used to generate a total of 128 pipe geometries using a Python script (located in Appendix E: 'E.1. WPTCR').

Table 4-10 List of outer diameters and SDRs used to produce parametric model cases for the WPTCR test, (Ceresana, 2012; Rapra Technology Limited, 1995; Plastics Europe, 2013)

Outer diameter (mm)	63, 90, 110, 125, 160, 180, 225, 250, 280, 315, 355, 400, 450, 500, 560, 630
SDR	7.4, 9, 11, 13.6, 17, 21, 26, 33

4.6.1   Material properties

The material properties for modelling the WPTCR at 80 ^{0}C were obtained from Es-Saheb's (1996) work. Young's modulus value of 480 MPa, tensile yield strength of 10 MPa, and Poisson's ratio of 0.5 was used. HDPE Poisson's ratio is 0.45 at 20 ^{0}C (Goodfellow Cambridge Limited, 2016), since it is a mechanical property it will be affected by raised temperature. Pandini and Pegoretti (Pandini & Pegoretti, 2011), who investigated time and temperature effects on Poisson's ratio of polybutylene terephthalate (PBT) which is a semi-crystalline polymer; concluded that Poisson's ratio increases with time and temperature while decreasing with strain rate. Poisson's ratio of PBT increased from 0.41 at 20 ^{0}C to 0.49 at 80 ^{0}C. For HDPE the Poisson's ratio of 0.5 at 80 ^{0}C was concluded by critically analysing the work of several authors (Es-Saheb, 1996; Tschoegl, et al., 2002; Merah, et al., 2006; Pandini & Pegoretti, 2011).

4.6.2   Modelling assumptions

An axisymmetric pipe bead-less model was used to represent the WPTCR test sample. The model was considered to have uniform material properties. The weld region was homogenised with the parent material. A symmetry boundary condition was used at the weld interface to reduce the computational cost of model, representing only half of a 1.5 metre length of pipe as presented in Figure 4-25. The axial tensile stress was applied as an elongation of 1.05% of the full pipe length at the grips, ~16 mm in total, to induce a tensile stress of 5.5 MPa. It was expected that the model will remain below the elastic limit of HDPE at 80 ^{0}C as the load induced is below the 10 MPa yield point at 80 ^{0}C. The model used a structured mesh consisting of 6000-258000 CAX4R elements depending on the parametric geometry of each case, each element being 0.25 mm^2. All results were reported as non-averaged Von Mises stress.
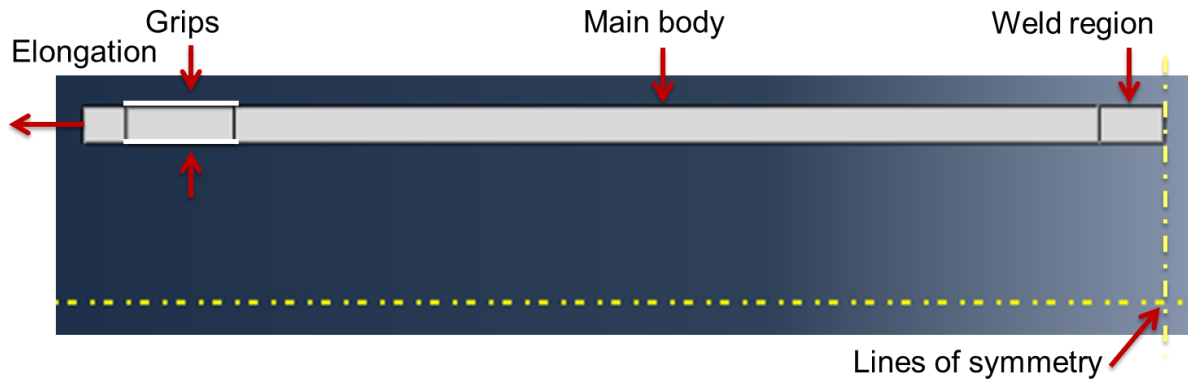
Figure 4-25 Schematic of a FEA model of WPTCR test (not to scale)

4.6.3 Mesh sensitivity

To confirm the accuracy of the models results, a mesh sensitivity analysis was conducted for 180 mm SDR 11 pipe size. The element size was varied from very coarse 100 mm^2 to very fine and computationally expensive 0.01 mm^2. The mesh convergence is shown in Figure 4-26 where the total number of the elements is plotted against the minimum pipe length calculated from the model. The mesh converges by element size of 6.25 mm^2. This element size is suitable for models using comparable loading conditions that induce pipe wall stress of 5.5 MPa. However, it is recommended to use the element size of 0.25 mm^2 to appropriately mesh smaller geometry features with sufficient number of elements without greatly increasing computation costs.
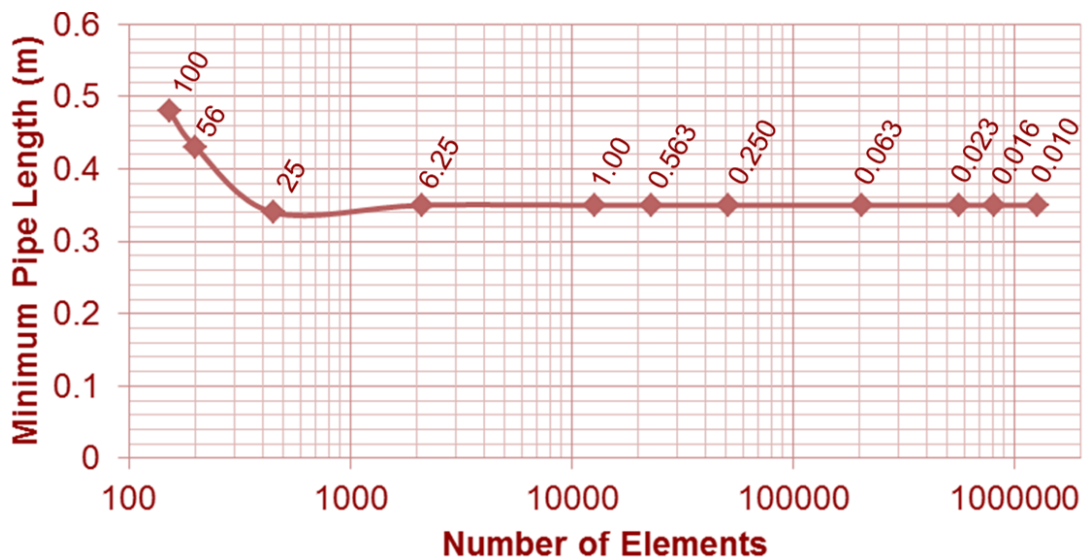
Figure 4-26 Number of elements against the minimum pipe length with element size data labels in mm^2

106

4.6.4 Results and discussion

The Von Mises stress distribution is reported in Figure 4-27 for the modelling of the WPTCR test, showing the paths across the mesh where the data is extracted. The area of interest highlighted in Figure 4-27 is expanded in Figure 4-28. The extracted data is plotted against the undeformed axial distance in Figure 4-29.
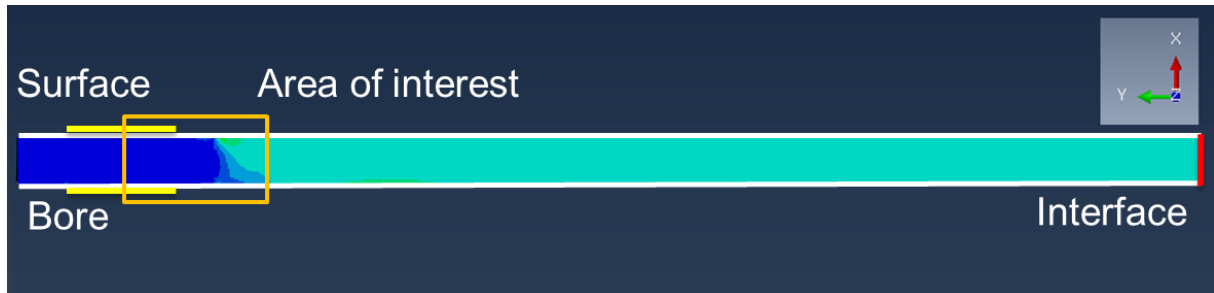
Figure 4-27 Von Mises stress distribution overlaid with data extraction paths using white lines for the pipe bore and surface and red vertical line for the weld interface; the location of the clamps is shown with bold yellow lines; and area of interest region highlight in orange rectangle which is illustrated in Figure 4-28 (not to scale)

A very small region at the surface of the model where the clamp region ends has yielded, as seen in Figure 4-28. The maximum stress value reported in Figure 4-28 is almost twice that of the yield value at 80 °C (Es-Saheb, 1996). This is due to large local deformation which is being prevented by clamps in the FEA model. The small size of this region totalling a few elements at most is not expected to invalidate the results from the remaining model. In the WPTCR tests, the yield always occurs at the weld due to weld geometry and changes in the local material properties.
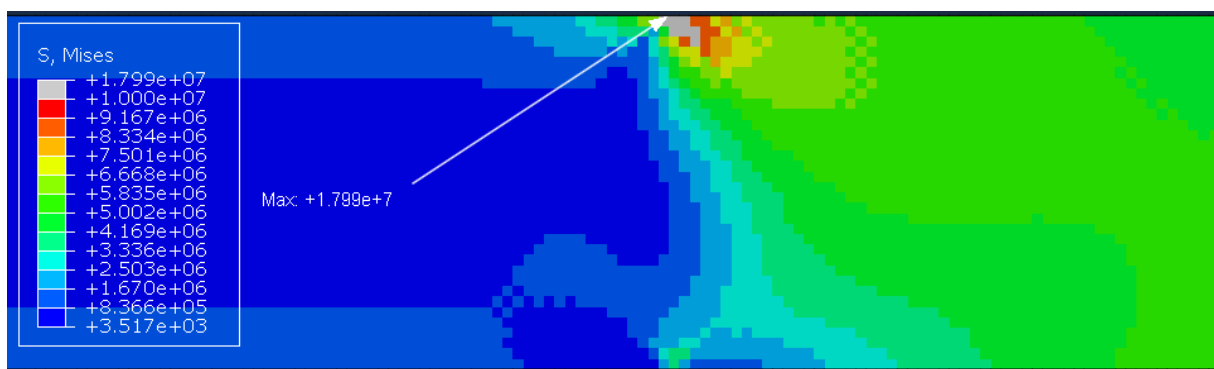
Figure 4-28 Expanded area of interest showing Von Mises distribution and the location of maximum stress (not to scale) for 180 mm SDR 11 PE100 pipe (Case 43, Table 4-9)

For 180 mm SDR 11 pipe the point where the stresses in the pipe wall stabilise by meeting the set criteria can be seen in the Figure 4-29; this occurs at 0.575 metres from the weld interface. The pipe length from 0.575 metres to the weld interface

therefore has uniform stress distribution and can be removed. It is expected that the weld region will occupy less than 0.02 metre of pipe length based on the measurements of the weld beads. Since only half the pipe is modelled, the minimum total length of the pipe obtained from the FEA model must be doubled; giving 0.35 metres for 180 mm SDR 11 PE100 pipe.

The effect of the weld region on the stress distribution in the adjacent pipe wall regions and how long does stress in the pipe wall takes to stabilise, both have not been modelled in this study. The stresses in the weld regions are likely to be arising from changes in the local material properties due to welding and the weld beads. It is expected that the geometry of the weld beads will contribute negatively in form of stress concentrations and positively by reinforcing the pipe's weld region in a manner similar to barrel hoops. The latter effect of weld beads could be significant as the clamps prevent the pipes from expanding due to elongation and the Poisson's effect will contract the pipe's diameter at the weld interface. Therefore, it is likely that the minimum length required for WPTCR will increase.
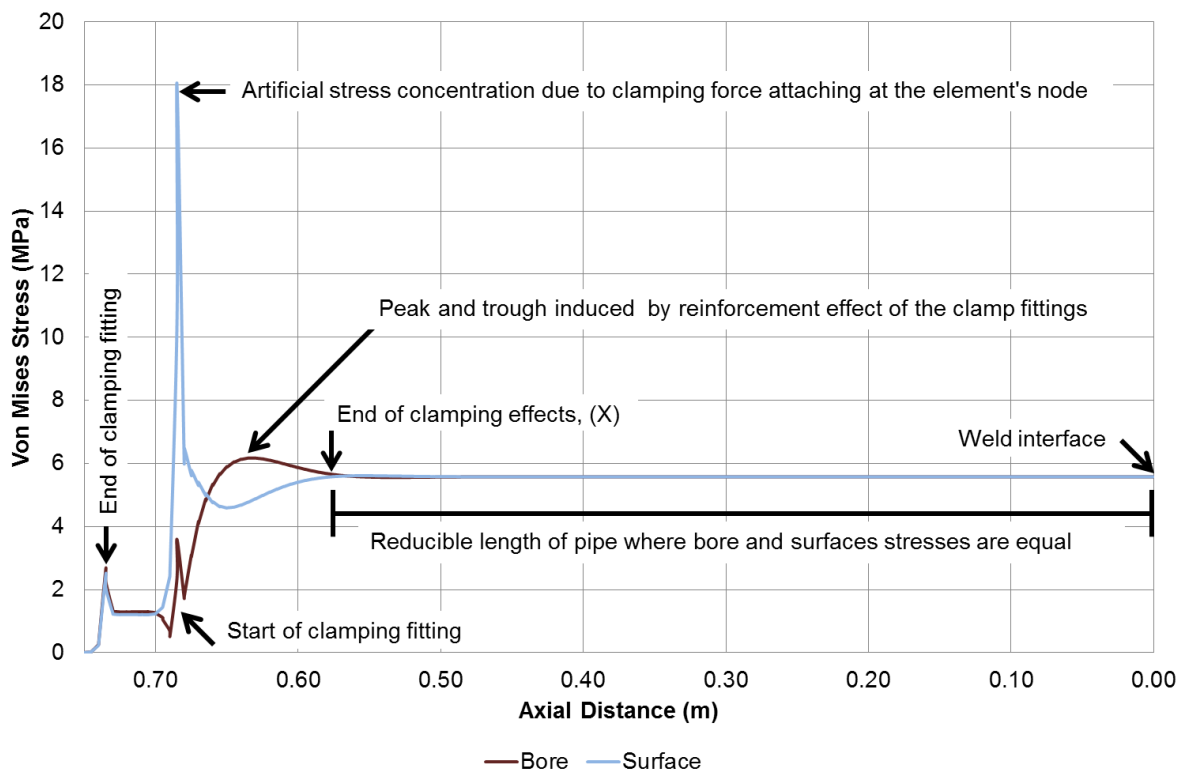
Figure 4-29 Von Mises stress against axial distance for 180 mm SDR 11 PE100 pipe (Case 43, Table 4-9), where the end of clamping effects are defined as the difference between stress values obtained from the pipe bore (the internal surface) and pipe surface (the outer surface) to be less than 1% of the stress at the weld interface

The average Von Mises stress in the pipe wall for majority of the pipe wall is obtained from the weld interface is 5.59 ± 0.09 MPa for all 128 cases. The models were designed to induce Von Mises stress close to 5.5 MPa as experienced by pipes undergoing WPTCR tests.

The criteria for obtaining the minimum length of pipe is set at a difference of less than 1% of the stress at the weld interface, between the Von Mises stress values obtained from the pipe bore (the pipe inner surface) and the pipe surface (the pipe outer surface). This value (typically 0.56 MPa) is chosen to ensure that the stress distribution has sufficient distance from the fitting clamps to stabilise in the pipe wall.

Table 4-11 contains the results of the parametric study, the minimum pipe length required for all 128 cases. The cases where the values are higher than the 0.65 metres limit of the current test rig are in bold. The values from Table 4-11 are illustrated in Figure 4-30 plots the pipe wall thickness against the minimum length.

Table 4-11 Minimum pipe length required for the WPTCR test, calculated from the parametric FEA model

Cases	OD	SDR							
		7.4	9	11	13.6	17	21	26	33
1-8	63	0.22	0.21	0.2	0.2	0.19	0.18	0.18	0.19
9-16	90	0.26	0.24	0.24	0.23	0.22	0.21	0.2	0.19
17-24	110	0.28	0.28	0.26	0.25	0.24	0.23	0.22	0.24
25-32	125	0.31	0.29	0.28	0.27	0.25	0.24	0.26	0.25
33-40	160	0.36	0.34	0.32	0.3	0.29	0.32	0.31	0.28
41-48	180	0.39	0.36	0.35	0.33	0.31	0.35	0.32	0.31
49-56	225	0.45	0.42	0.4	0.38	0.35	0.4	0.38	0.35
57-64	250	0.49	0.46	0.43	0.41	0.45	0.43	0.41	0.38
65-72	280	0.53	0.5	0.47	0.44	0.49	0.47	0.44	0.41
73-80	315	0.58	0.54	0.51	0.48	0.54	0.51	0.49	0.45
81-88	355	0.64	0.6	0.56	0.52	0.59	0.56	0.52	0.48
89-96	400	**0.71**	**0.66**	0.61	0.57	**0.66**	0.62	0.58	0.54
97-104	450	**0.78**	**0.72**	**0.67**	0.63	**0.72**	**0.68**	0.64	0.58
105-112	500	**0.85**	**0.79**	**0.74**	**0.68**	**0.79**	**0.74**	**0.69**	0.64
113-120	560	**0.94**	**0.87**	**0.81**	**0.75**	**0.87**	**0.81**	**0.76**	**0.69**
121-128	630	**1.04**	**0.96**	**0.9**	**0.82**	**0.97**	**0.9**	**0.84**	**0.77**
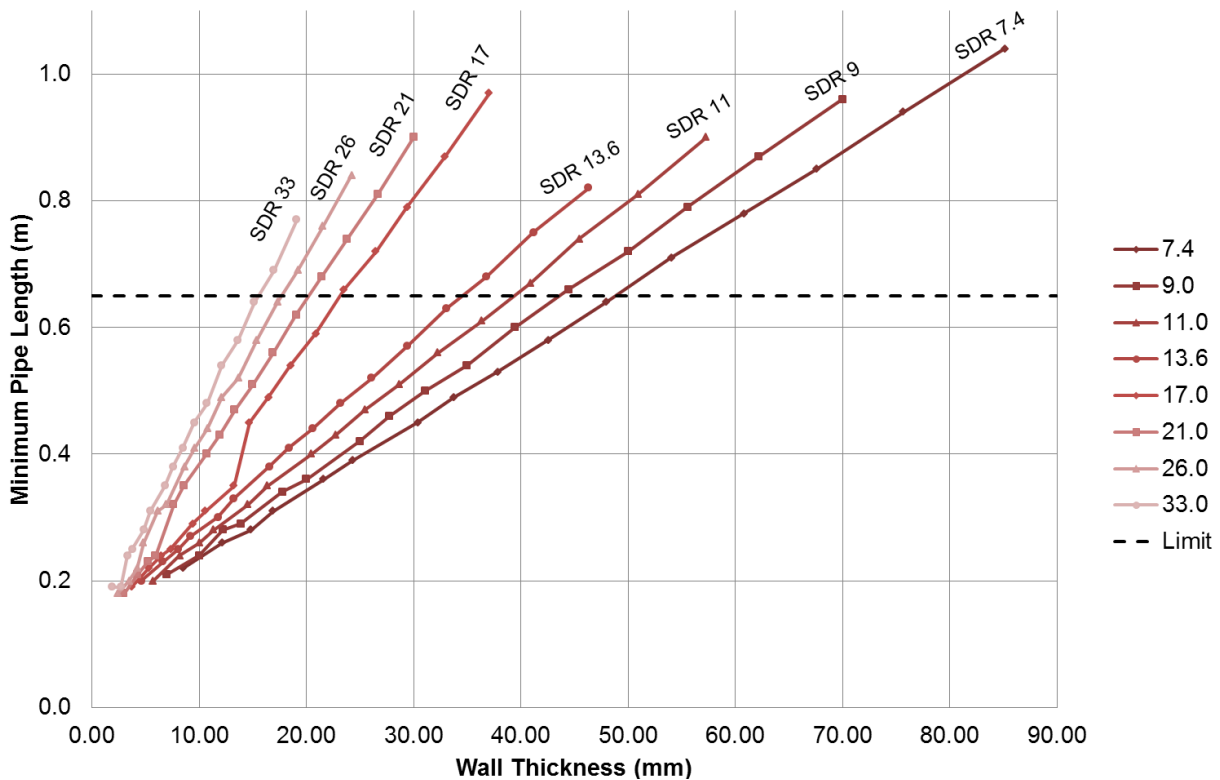
Figure 4-30 Plot of pipe wall thickness against the minimum pipe length arranged by SDR, the dotted black line marks the largest pipe size currently testable by the WPTCR test rig

Using the data provided in the Table 4-11 and taking into account the validity of the FEA model based on the assumptions made, pipes with the outer diameter larger than 355 mm should be tested with caution and where possible the largest length of pipe should be used. From Figure 4-30 it can be inferred that the minimum pipe length correlates closely with the pipe outer diameter, more so than the SDR as it has greater influence on the pipe wall thickness. The findings of WPTCR FEA study show the importance of the pipe length based on the pipe outer diameter and SDR. The study shows that the wall thickness alone cannot be used to determine the minimum pipe length required to avoid the effect of pipe clamps on the pipe wall stresses. The FEA models can be improved by modelling the material property changes in the weld region and by including the geometry of the weld beads. Lastly, the study shows the importance of FEA models as it would have been prohibitively expensive to physically carry out this study.

4.7 Summary

A comparison was made between the three short term coupon test methods. The waisted tensile test proves to be more consistent than the high speed tensile impact and the guided side bend tests, in differentiating between the welding procedures.

An independent two-sample t-test was used to ensure that any findings were statistically significant. For waisted tensile test the t-test was used for comparison of welding procedures and circumferential positons of specimen, the latter comparison was determined to be insignificant impact on the test performance. The t-test was then used to compare the waisted tensile energy for welding procedures split between before-yield and after-yield regions of the stress-strain curve. For high speed tensile impact the t-test was only used for comparing the welding procedures despite all of the test specimens failing in the parent material. The ductility of the HDPE which allows for necking is dependent on the strain rate (El-Bagory, et al., 2014; Ye, et al., 2015). The high strain rate of 152 mm min^{-1} ± 10% for the high speed tensile impact test conducted at room temperature combined with the specimen geometry where the weld beads have a reinforcing effect caused the failures to occur in the parent material. The t-test was not reported for the guided side bend test as the HDPE material proved too flexible in the specimen geometry to fail as required by the test.

Both waisted tensile and high speed tensile impact tests showed necking in some of the higher performing test specimens corresponding to higher energy to break values. The tests were conducted at room temperature which is between the T_g and T_m temperature range, this range is also designated as the cold drawing zone where stable neck propagation is quite likely; the necking observed was quite unstable and failed due to the stress concentration effects of the notch between the weld beads and the pipe wall.

Unfortunately, it was not possible to complete the experiment part of the long-term WPTCR test in the allotted time due to unforeseen logistical and technical difficulties.

However, the WPTCR test was modelling using FEA to determine the minimum pipe length without actually testing a large variety of pipe size which would have been extremely difficult to source from the same resin material and company. The model is capable to predict the effect on stress distribution from the grip of the end clamps and calculate the minimum length necessary for WPTCR tests. Through the use of Python scripting the FEA modelling proved to be incredibly valuable by reducing the need for extensive experiments.

5 Weld Bead Structure

5.1 Introduction

Stress concentration at the weld bead in butt fusion welding may cause premature failure in the specimens of mechanical tests (Chapter 4) and thus the influence of weld bead is studied in detail in this chapter.

The weld bead structure chapter is split into three sections. The first section defines the weld bead parameters that will be used in upcoming section, using optical techniques. The second section conducts a parametric study for each weld bead parameter to identify those that have a larger influence on the distribution of stresses in the pipe wall using FEA modelling. The main parts of this work have been presented at the NAFEMS UK conference (Shaheer, et al., 2016). The last section conducts modelling on digitised weld bead geometries from first section and compares the results to those obtained in the parametric study; this comparison helps rank and validate the most influential weld bead parameters affecting stresses in the pipe wall.

5.2 Weld bead parameters

5.2.1 Introduction
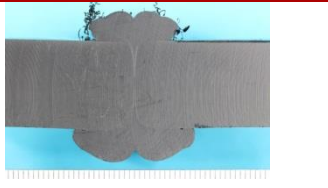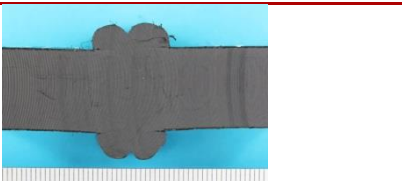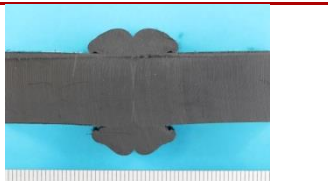
The weld bead structure has been analysed on macro-scales and micro-scales. In this section, several optical techniques were used to identify the appropriate weld bead parameters before macrographs of the weld bead specimens were digitised. The digitised geometry supplemented with optical microscopy to derive a list of appropriate values for each parameter.

5.2.2 Macrographs

Macrographs were used to analyse the weld bead structure on the macro-scale. The weld bead specimens were taken from three circumferential positions ("top", "bottom" and "side") on the pipe for each of the six welding procedures. Table 5-1 lists the three different circumferential positions from which the bead specimens were taken for two of the six welding procedures to illustrate the size difference between the weld beads produced by the European and the US welding procedures. The two

European welding procedures produce smaller weld beads than the four US welding procedures due to lower fusion pressure. Some of the specimens were cut for conducting trails with other analytical techniques before the macrographs were obtained. Table 5-1 has been expanded in the Appendix D as Table D-1 which shows the macrographs of the three positions for all of the six welding procedures.

Table 5-1 Macrographs of samples listed by position for welding procedures WP1 and WP3 (the complete list is located in Table D-1 in the Appendix D), the pipe outer surface is always at the top for comparison

Pipe Position	WP1	WP3
Bottom		
Top		
Side		

The images were captured using a mounted Canon EOS 550D DLSR. It was not possible to capture clearly the internal weld structure using the macrography technique, as the material appears uniform unless the surface is heat treated and the images are captured at an angle. Parameters that can be used to capture the features of the weld bead are illustrated in Figure 5-1; their location is identical for both inner and outer weld beads. The bead height and bead width are easily measureable but the bead angle can be difficult to measure due to the curvature of the weld bead. The macrography images would allow the weld bead geometry to be digitised for use in FEA modelling.
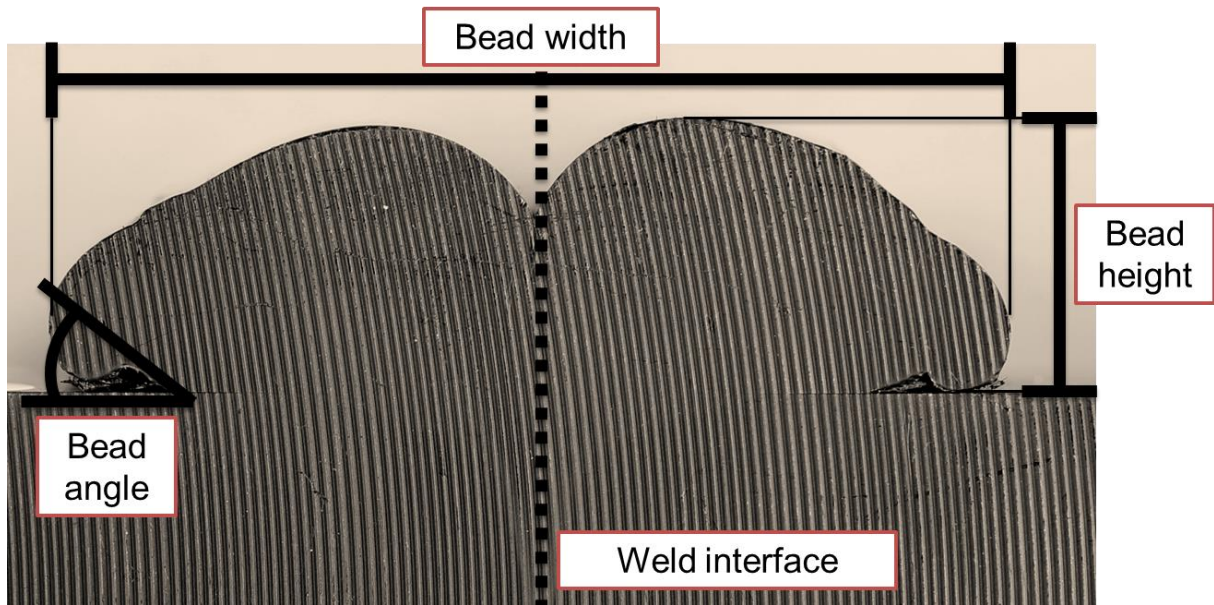
Figure 5-1 Common weld bead features with the weld interface shown by the dotted line

The circumferential position of the weld bead changes the bead geometry. For the bottom position; the outer weld beads drop away from the pipe wall and the inner weld beads rest on the pipe wall, due to gravity. For the top position the opposite behaviour is observed; the outer weld beads rest on the pipe wall and the inner weld beads drop away from the pipe wall, again due to gravity. Both outer and inner weld beads at the top and bottom circumferential positions are symmetrical across the weld interface. For the two side circumferential positions, the behaviour of the weld bead is mirrored across the pipe axis therefore only a single macrograph specimen is needed to represent the side circumferential position. The top of half of the outer weld bead sways away from the pipe wall and the bottom half sags due to gravity towards the pipe wall as it is hinged at the weld interface. The top half of the inner weld bead again sways into the pipe wall due to the wall curvature. The bottom half of the inner weld bead due to weight of the top half sags until it supported on the pipe wall. The inner weld bead increases the contact area on pipe wall due to the pipe wall's curvature as the bead is hinged at the weld interface. The sagging of weld beads due to gravity continues until the pipe has sufficiently cooled to solidify the shape.

5.2.3 Optical microscopy

An attempt was made to study the micro-scale features using an optical microscope equipped with 5X and 20X zoom lenses. It was difficult to differentiate the inner weld structure from the surrounding parent material, however, the zoomed high resolution images captured via the Scentis microscope software showed that the weld bead joins the inner weld structure closer to the weld interface then shown by the macrographs, the joining location will be referred to as the side notch. Figure 5-2 shows an optical microscope image at 5X resolution that can be used to calculate the bead angle of 23.56º using a circle 43.61 µm in diameter with its centre 100 µm from the side notch. However, the image illustrates the difficulty of confirming exactly where the weld bead fuses with the pipe. Figure 5-3 is an optical microscope image at 20X resolution that shows a fissure that begins from the side notch and gradually filled solid by fibrils of polymer material, closing the gap with increasing density moving further away from the side notch. Therefore, it is also difficult to ascertain an exact value for the side notch radius that is formed between the weld bead and the pipe wall as example of which is shown in Figure 5-2.
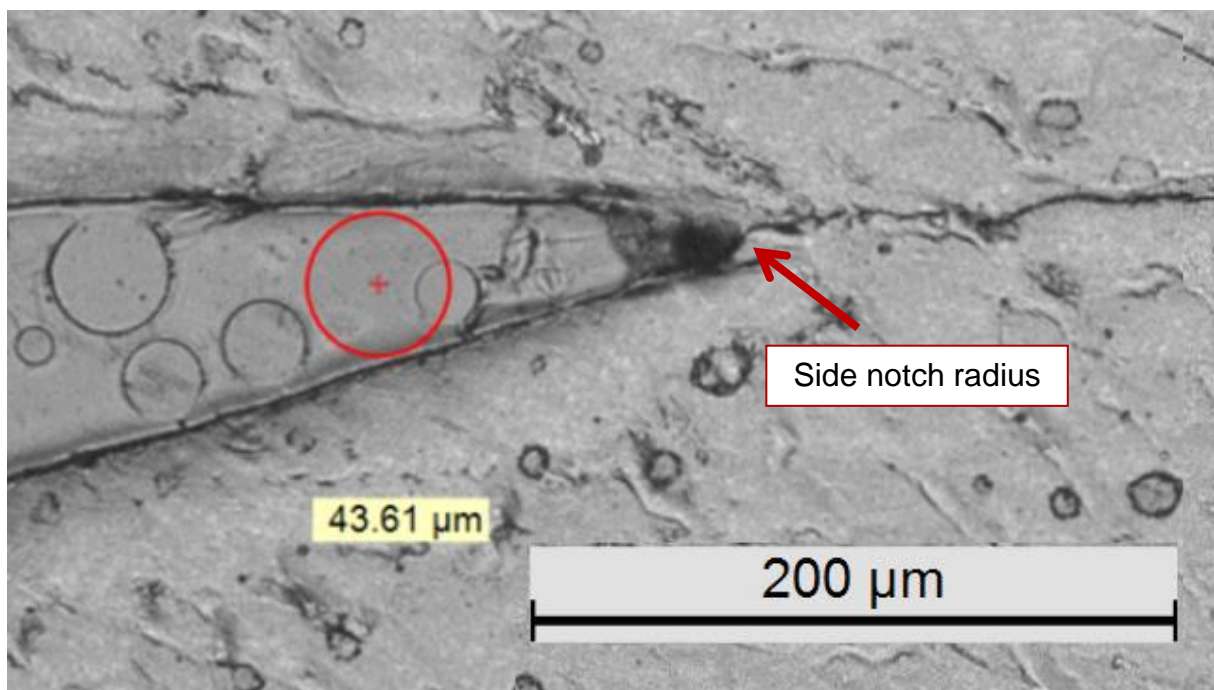
Figure 5-2 Microscope image of bead angle of 23.56º formed between the pipe wall and the inner left weld bead, (Image: DMR2500M-22514 - W30-5D - RBL - 0004 – Copy), Olympus BX41 LED at 5X resolution equipped with SC30 digital camera

115
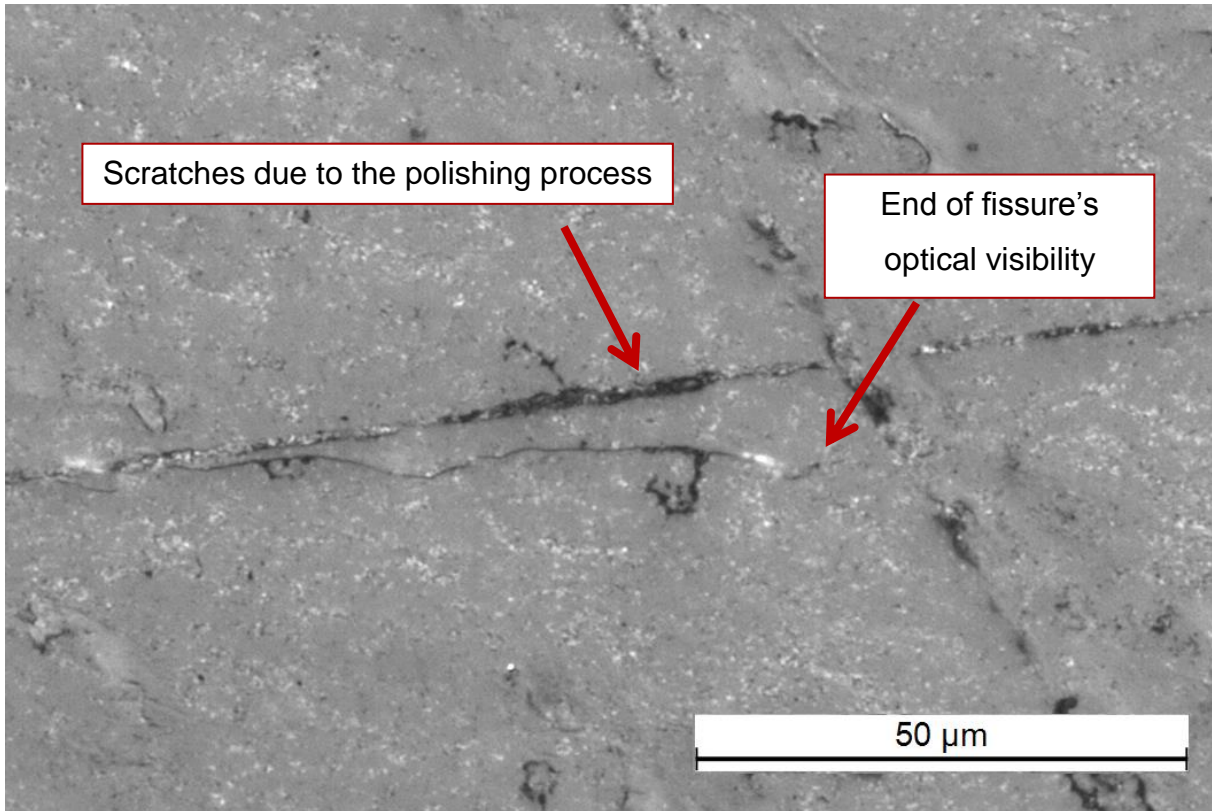
Figure 5-3 Microscope image of the fissure (indicated by the arrow) leading from the bead angle between the weld bead and pipe wall, (Image: DMR2500M-22514 - W30-5D - RBL – 0003), Olympus BX41 LED at 20X resolution equipped with SC30 digital camera

The weld bead specimens were heat treated to allow the internal structure of the weld and the shape it forms when joining the weld beads, to be optically visible. The process allowed for two additional weld bead parameters to be defined: the central notch height and the root length. The central notch height is defined from the pipe wall to the central notch between the left and right halves of the weld bead. The root length is defined by the distance between the edges where the weld bead is attached to the pipe wall after the specimen had undergone heat treatment (as illustrated in Figure 3-21 and 3-22). A travelling microscope set-up ('Starret Kinemetric' travelling microscope, 'Ag Neovo' display screen and 'Quadra-Chek 200' counter) was then used to measure the central notch height and the root length.

5.2.4 Transmission light microscopy

In order to determine where exactly the weld beads join the parent material and to validate the measurement of root length performed using the traveling microscope, it was required to perform microtomy of the macrograph specimens. Each microtomed slice was captured using transmission light microscope (TLM). The boundary of the weld beads can be seen distinctly against the pipe wall as the weld beads join in and

form part of the melt zone in Figure 5-4. Due to the difficulties in microtomy, it was not possible to preserve the whole weld bead, but only the area where they attach to the pipe wall. The TLM images validated the measurement of root length performed by the travelling microscope, which saved considerable time and effort that would have been required by the TLM procedure.
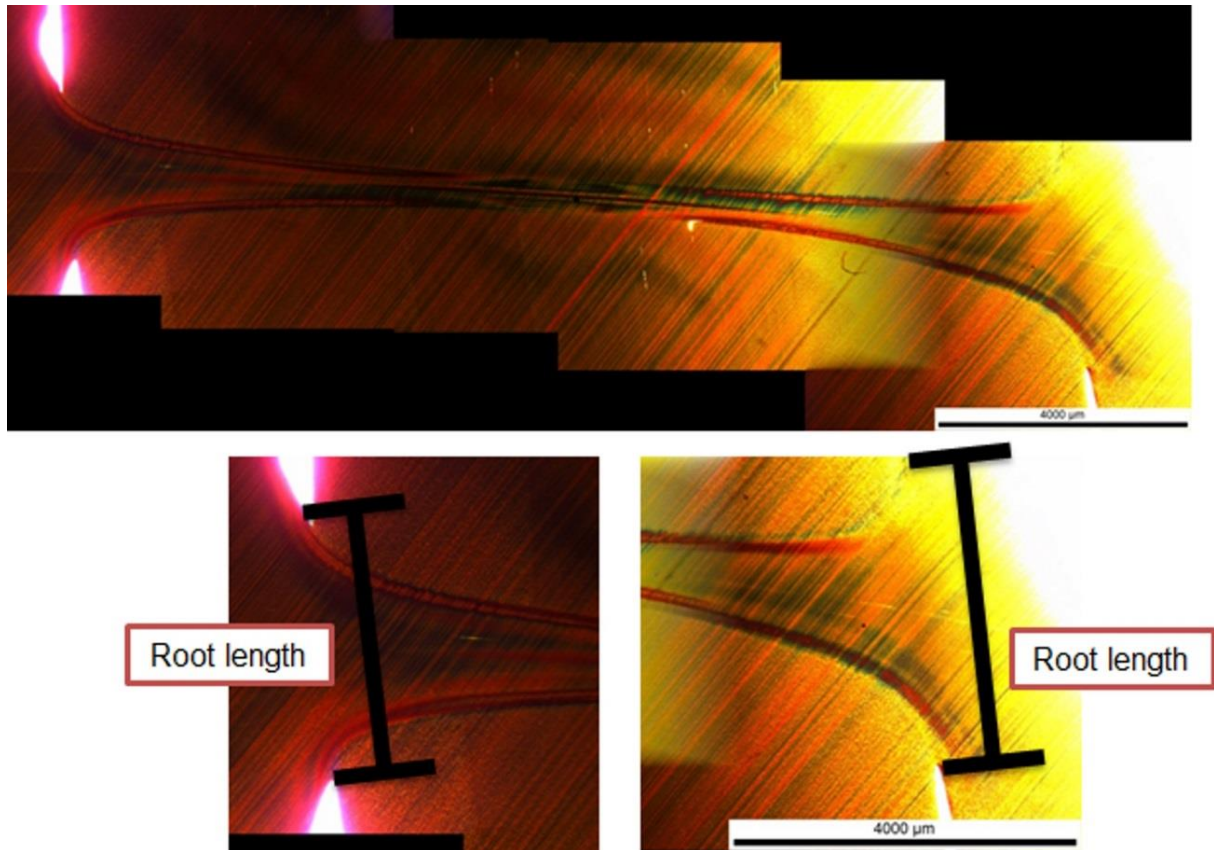
Figure 5-4 A composite transmission light image of a microtomed full slice (top) and enlarged regions of inner and outer weld beads locations (bottom) showing the root length (Olympus BH-2 transmission microscope with QImaging Retiga 2000R camera)

5.2.5 Summary

Macrography with heat treatment can be used to identify and measure the common weld bead parameters. Optical microscopy can be used to identify side notch radius between the weld bead and the pipe wall. Lastly the transmission light microscopy is able to provide a detailed image a welds internal feature embedded in the pipe wall; quality dependent on the microtomy procedure. The central notch height and root length are expected to be more likely to affect pipe wall stresses than bead width and bead height. Figure 5-5 shows the location of these new parameters with the parameters identified from the macrographs on a specimen heat treated to show the internal weld structure.

117
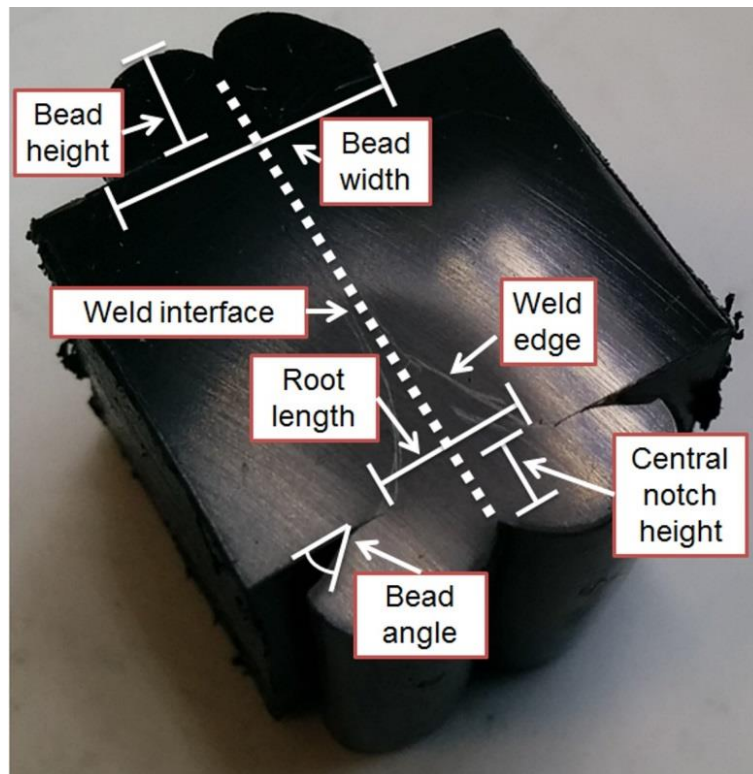
Figure 5-5 The five defined weld bead parameters: bead angle, bead height, bead width, central notch height and root length; some of the parameters are difficult to visualise optically unless the macrograph specimen is heat treated or require the use of an optical microscope

The data of the weld bead parameters extracted from the macrographs can be found in Appendix D: Table D-2 for top position; Table D-3 for bottom position; and Table D-4 for side position. Table D-5 in the Appendix D provides the minimum, maximum, range, and average values for the inside beads, the outside beads for each weld bead parameter.

5.3 FEA: Parametric Study of the Weld Beads

5.3.1 Introduction

This section of the chapter describes the parametric modelling of the weld bead parameters identified in the previous section to reveal the influence of weld beads on stress concentration. The bead angle was the first parameter to be investigated as it needs to be modelled separately from other parameters in order to reduce the complexity of geometry automation. It is expected that an increase in side notch radius located at the joint of the weld bead and the pipe wall, will reduce the maximum stress. The root length and central notch height parameters are expected to have a greater influence on the stress distribution than the bead height and bead width due to the way they interact with the pipe wall. Therefore, the bead height and

bead width parameters are not investigated. Additionally one of the two parameters, central notch height and root length, will have proportionally greater influence on the maximum stress due to its orientation relative to stresses that reside in the pipe wall.

A Python script (located in Appendix E: 'E.2. Weld Bead Models') was developed for automated modelling of side notch radius, central notch height, and root length. A flow diagram of how the Python script operates is shown in Figure 5-6.

The flow diagram behaves in the following manner:

1. A list of design cases is generated based on the user input of the parameters
2. The variable for each design case are read by the script portion that generates the input file
3. The design case variables are used to generate the case geometry, mesh, and apply load in the model which is written as a input file
4. A log entry for the model case is written after generation of each input file
5. The solver runs the input file, computes the model, and writes the completed analysis in an output file
6. The viewer captures the images of the model output and extracts the results
7. The results are logged against the design case in the results file
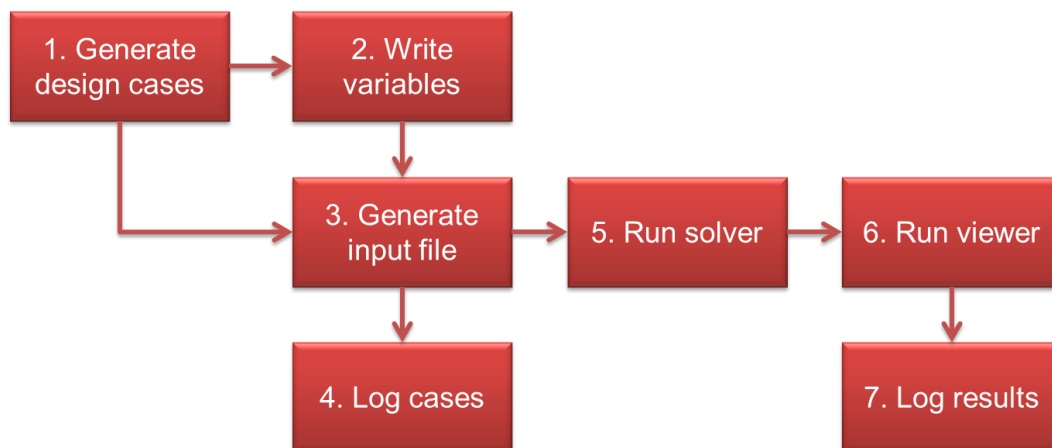
Figure 5-6 Flow diagram of the parametric modelling Python script

5.3.2 Modelling assumptions

The axisymmetric model representing the WPTCR test specimen from Chapter 4 was adapted for investigating the influence of weld bead parameters on stress concentration. In that bead-less model the pipe wall region surrounding the weld bead had a uniform distribution of stress of 5.5 MPa. This observation was used to

reduce the size of the parametric weld bead models from 1.5 m to 100 mm. The load applied as a pressure of 5.5 MPa at the pipe ends and a symmetry boundary condition was used at the weld interface to reduce the computational cost of the model. The model assumed uniform material properties for both the weld region and the parent material. The bead angle models used a free mesh consisting of approximately 14000 CAX4R elements with each element being 0.0625 mm^2 on average. CAX4R elements are quadrilateral with only 4 nodes; they are all linear reduced-integration elements which allow the model to resolve quickly. These models only looked at how each weld bead parameter acts on stress concentration sites, which are the areas where the weld bead forms sharp side notches against the pipe wall. With the exception of the weld bead angle models, the models for all other weld parameters are generated using the Python script. The Python script generated models used approximately 6000 ± 1000 CAX4R in a free mesh, elements ranging in size from 18.975 μm^2 to 0.25 mm^2 depending on their respective location. For the side notch radius models, 20 elements were used to mesh the curvature. All results are reported as non-averaged Von Mises stress. It was expected that the model remained below the elastic limit of HDPE at 80 ^{0}C as the 5.5 MPa stress is well below the yield value of 10 MPa as discussed in Section 3.5.5.4.

5.3.3 Model details

The weld bead parameter models are shown in the following figures: weld bead angle in Figure 5-7; the base model in Figure 5-8; the side notch radius models in Figure 5-9; the central bead notch height models in Figure 5-10; and the bead root length models in Figure 5-11.The side notch radius models are shown zoomed to illustrate the relative difference between the largest and the smallest bead radii. The side notch radius, central notch height and root length models make use of the base model where Table 5-2 lists the material properties, common model parameters, and weld bead parameter values.
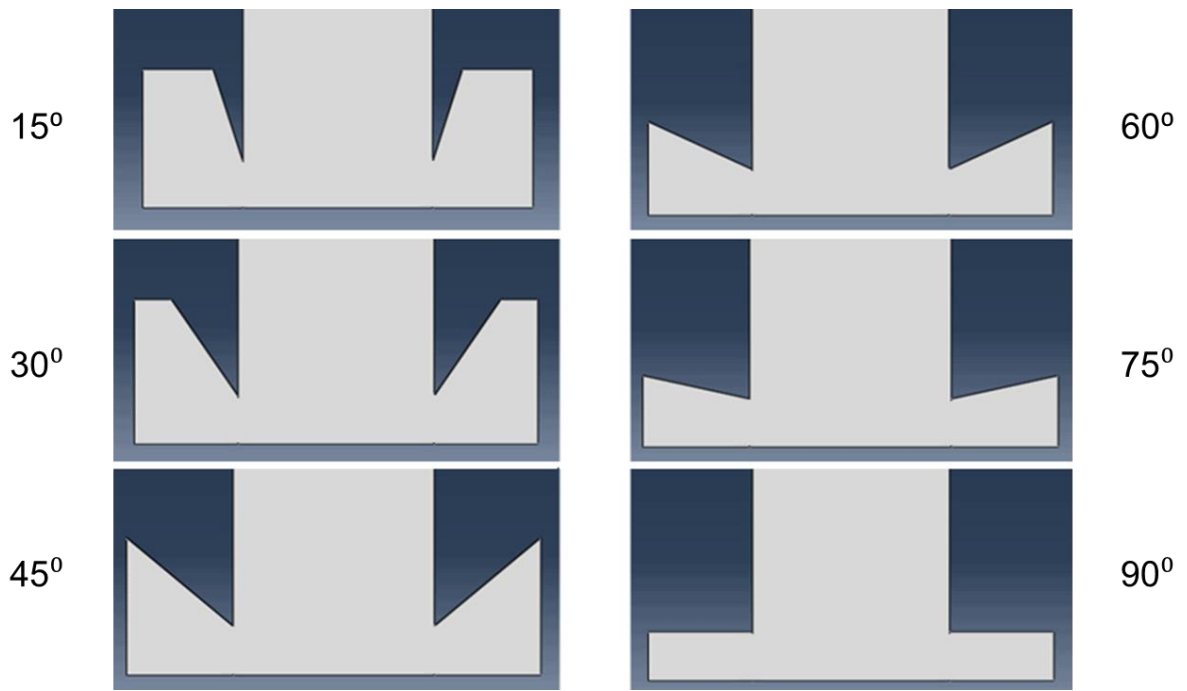
Figure 5-7 Weld bead angle models ranging from 15^0 to 90^0 in 15^0 increments
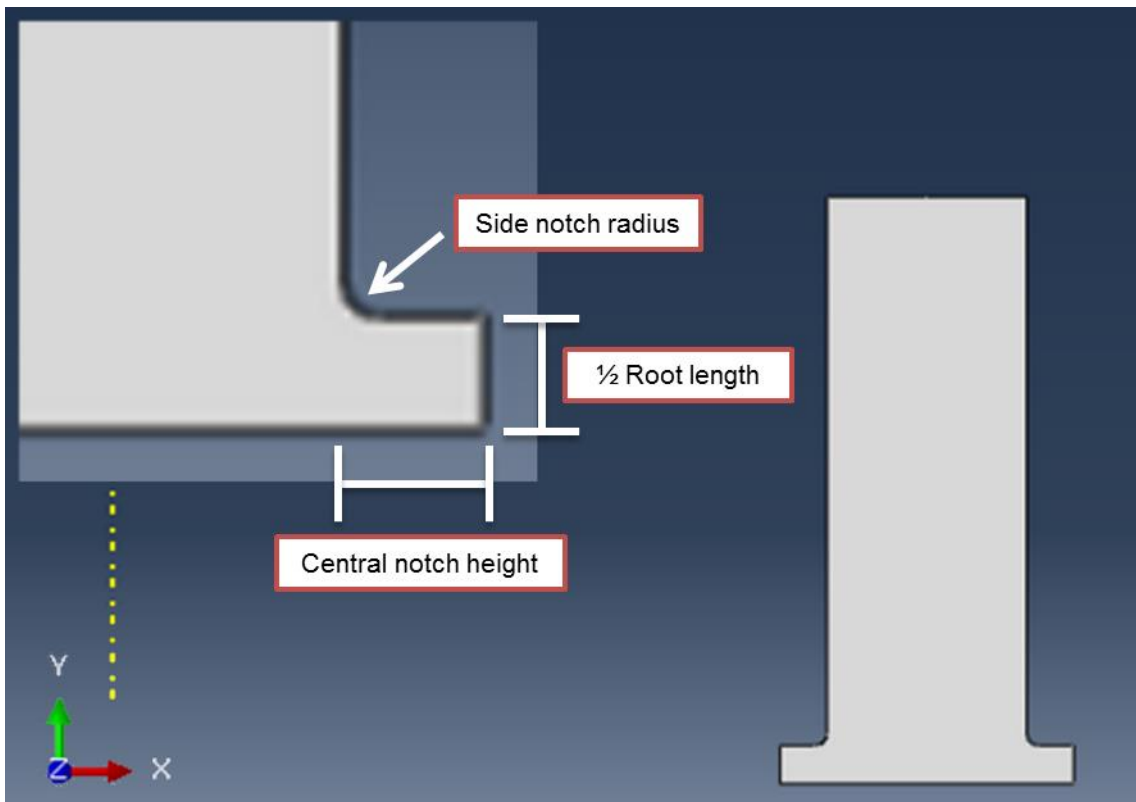
Figure 5-8 The base model generated from the Python script, the dotted yellow line represents is the axisymmetric axis
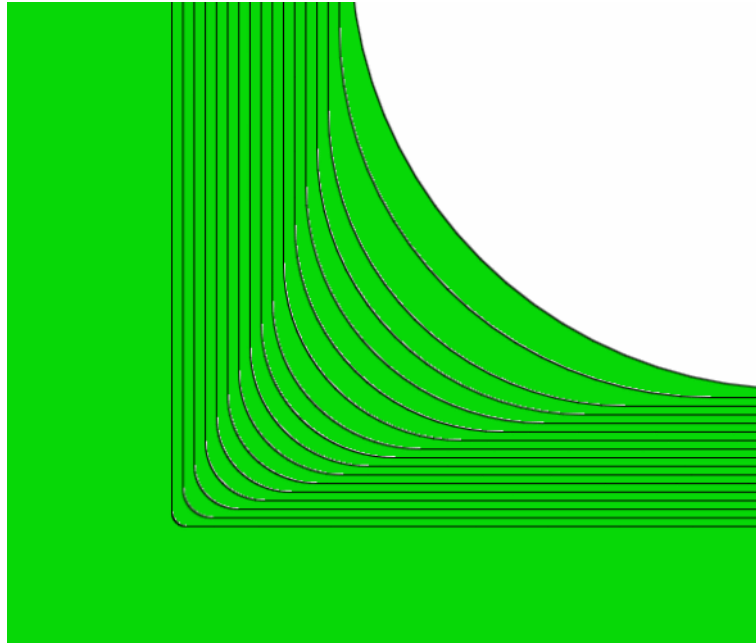
Figure 5-9 Side notch radius models that are overlapped, showing the smallest (foreground) to the largest (background) models, 0.1 mm to 3 mm
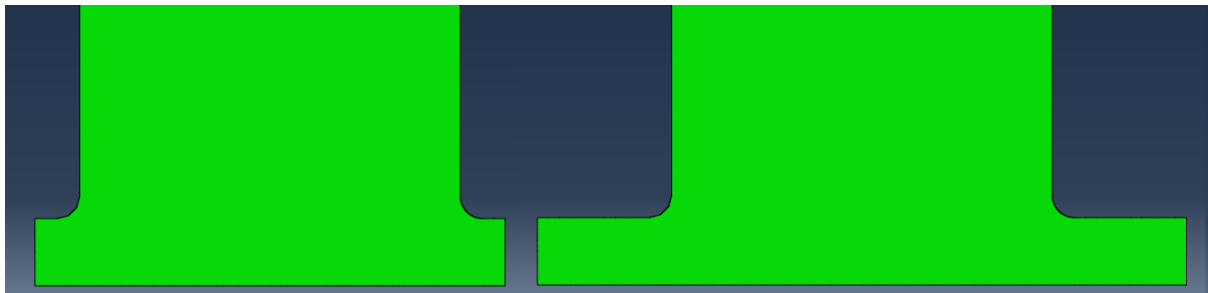
Figure 5-10 Weld bead central notch height models showing the smallest (left) and the largest (right) models, 2 mm to 6 mm

Figure 5-11 Weld bead root length models showing the smallest (left) and the largest (right) models, 2 mm to 10 mm

122

Table 5-2 Material properties, common parameters and the list of weld bead parameter values

Field	Unit	Weld Bead Models		
		Side notch radius	Notch height	Root length
Material properties	Young's (MPa)	480		
	Yield (MPa)	10		
	Poisson's ratio	0.5		
Pipe dimensions	OD	180		
	SDR	11		
Weld bead dimensions	Side notch radius	Varied	4	6
	Central Notch height	1	Varied	6
	Root length	1	4	Varied
Parameter values	Side notch radius	0.1, 0.2, 0.3, 0.4, 0.5, 0.6, 0.7, 0.8, 0.9, 1, 1.2, 1.4, 1.6, 1.8, 2, 2.5, 3		
	Central notch height	2, 2.5, 3, 3.5, 4, 4.5, 5, 5.5, 6		
	Root length	2, 2.5, 3, 3.5, 4, 4.5, 5, 5.5, 6, 6.5, 7, 7.5, 8, 8.5, 9, 9.5, 10		

5.3.4 Results and Discussion

The results of the simulated models, as detailed in Section 3.6.2: investigating each of the following weld bead parameters:

- Bead angle (Section 5.3.4.1)
- Side notch radius (Section 5.3.4.2)
- Notch height (Section 5.3.4.3)
- Root length (Section 5.3.4.4)

Stress concentration spots are identified and the maximum Von Mises stresses are plotted against the range of parameters of interests to evaluate the influence of them. The 5.5 MPa wall stress was used to normalise the maximum stress to report as a percentage in brackets.

5.3.4.1 Bead angle

For investigating the bead angle parameter, the weld bead geometry has a root length fixed at 6 mm and the notch height fixed at 7 mm. However, an additional parameter of bead width is used to ensure that bead angle can properly form against the pipe wall and it is fixed at 20 mm. The deformed FEA results are shown in Figure 5-12 for the six different bead angle values. The results of the bead angle models in Figure 5-13 show that the stress reduces as the angle formed at the weld root between the bead and the pipe wall increases, reducing from 8.43 MPa (153.27 %) at 15^0 to 7.30 MPa (132.72 %) at 90^0.
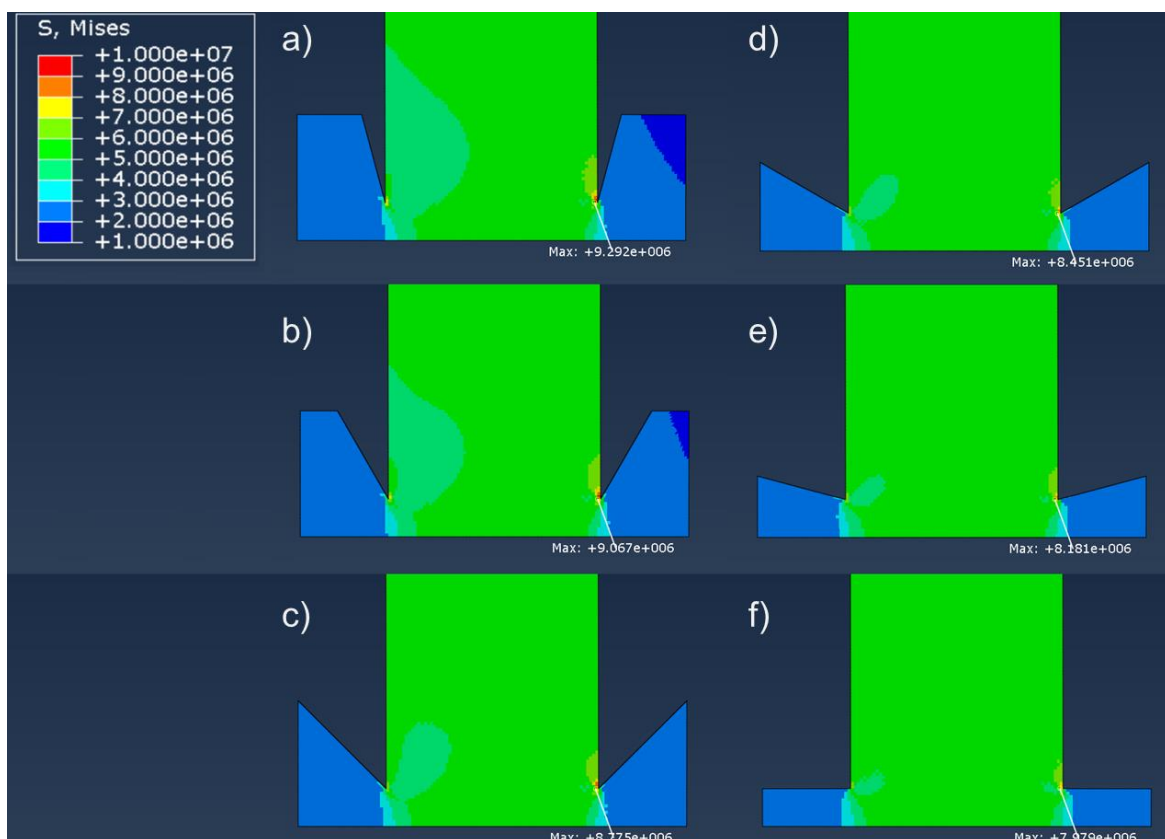
Figure 5-12 Deformed FEA results for bead angle parameters shown for the values of 15^0 (a), 30^0 (b), 45^0 (c), 60^0(d), 75^0 (e), and 90^0 (f)
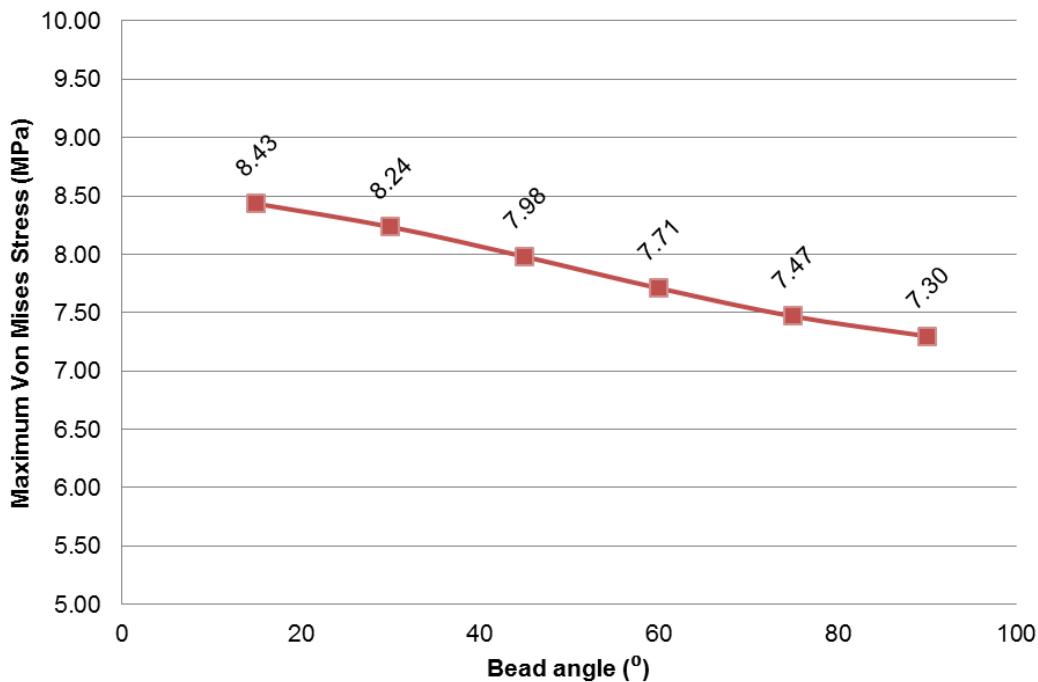
Figure 5-13 Plot of the maximum Von Mises stress against the bead angle

The bead angle models reduce the maximum stress by 20% when going from 15^0 to 90^0. The relationship is between the bead angle and the Von Mises stress is almost linear and inversely proportional, with the range of angles studied. However, it is possible that the stress increase is steeper or exponential as the bead angle approached 0^0. Due to the difficulty in accurately measuring bead angles below 15^0 using high magnification optical microscopes, it was decided that a low resolution travelling microscope will be used to measure the bead angles at the outer edges of the weld beads rather than at the weld interface. The bead angles measured this way were all larger than 15^0, therefore, the six data points above 15^0 are sufficient in this study.

5.3.4.2 Side notch radius

To investigate the weld bead parameter of side notch radius, the notch height was set at 4 mm and the root length set at 6.5 mm. The deformed FEA results are shown in Figure 5-14 for 0.1 mm, 1 mm, and 3 mm values. For the reported results of side notch radius models in Figure 5-15, as expected, the maximum stress increase rapidly for sharp side notch (e.g. it reaches to 17.94 MPa (326.18%) for 0.1 mm side notch radius) but will reduce with the increase in the side notch radius and approaches a constant value of approximately 7 MPa (127.27%), the average stress away from the bead when the radius is greater than 1 mm.

125
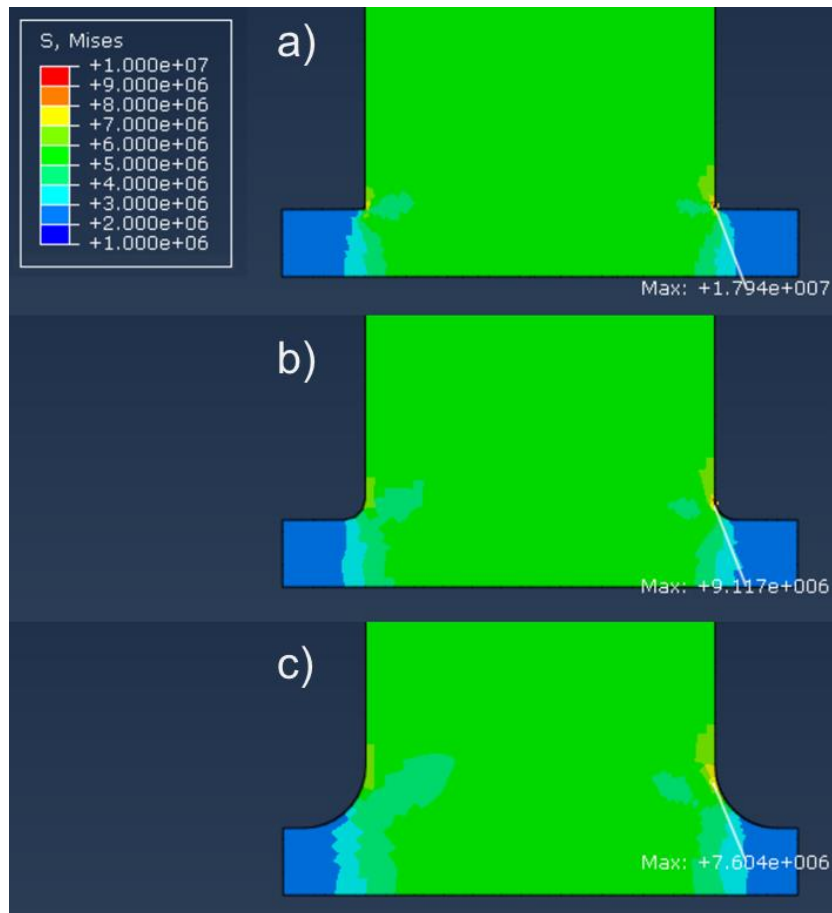
Figure 5-14 Deformed FEA results for side notch radius parameters shown in order (top to bottom| for values of 0.1 mm (a), 1 mm (b) and 3 mm (c)
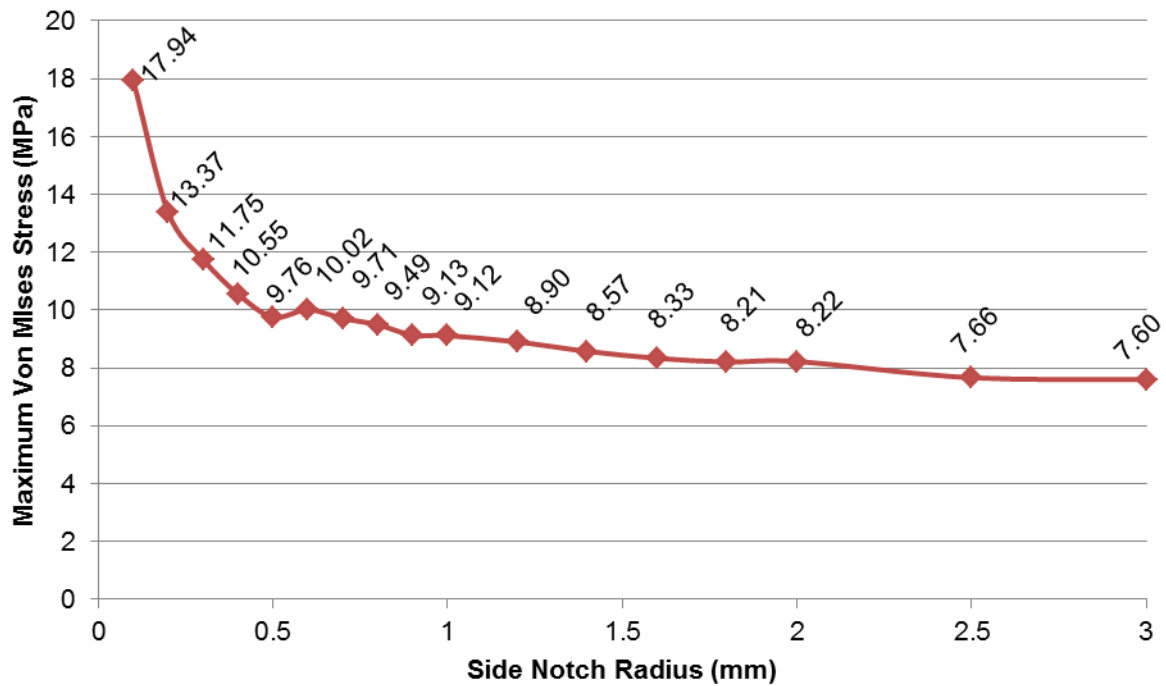
Figure 5-15 Plot of the maximum Von Mises stress against the side notch radius

126

For the side notch radius models, 1 mm can be seen as the transition point between sharply decreasing and gently decreasing stress. In comparison with the max stress for side notch radius of 1 mm, 0.1 mm radius increases the stress by 160.36% while 3 mm radius decreases the stress by 27.63%. It is worth noting that the smallest side notch radius modelled was 0.1 mm, which is still 5 times larger than the radius (22 µm) measured from the 20X optical microscopy image (see Section 3.6.1.3). The observed radius was derived by drawing a circle with a centre 100 µm away from the actual side notch radius which was not easily measureable as the notch continued in the material as a hairline fissure. It was expected that there would be an even sharper rise in stress concentration for side notch radius values below 0.1 mm, the modelling of such small radii would require a very refined mesh or increasingly finer element size which would get computationally very expensive.

The side notch radius of 1 mm will be used to investigate the two remaining weld bead parameters, notch height and root length. The 1 mm value for the side notch radius is suitable as it limits the size of the smallest elements in the mesh and in turn the number of elements required to complete the mesh. Having the side notch radius smaller than 1 mm reduces the size of the elements on the curvature and consequently increases the variation in size of the elements across the mesh. Conversely, having a side notch radius size larger than 1 mm may interfere with the smallest values of the notch height and root length parameters

5.3.4.3 Notch height

A root length value of 6.5 mm was used to investigate the notch height parameter. The deformed FEA results are shown in Figure 5-16 for the notch height parameters. The effect of notch height on the maximum Von Mises stress can be seen in Figure 5-17. The maximum stress for notch height decreases from 9.28 MPa (168.73%) for 6 mm to 8.80 MPa (160.00%) for 2 mm, the highest value stands at 9.44 MPa (171.64%) for 5.5 mm.
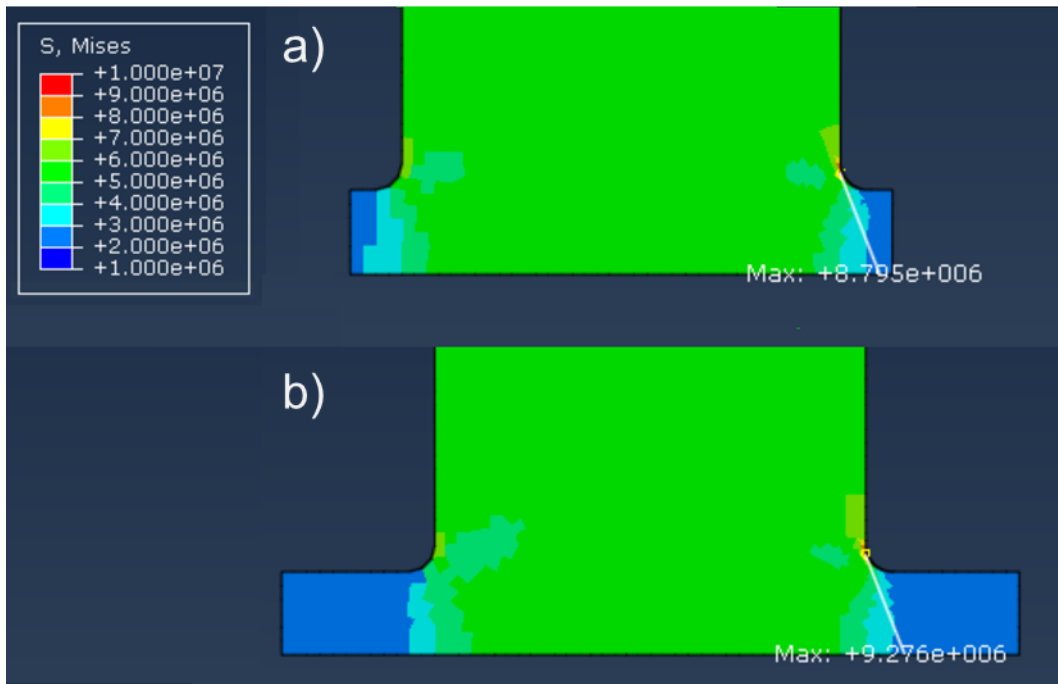
Figure 5-16 Deformed FEA results for notch height parameters shown in order (top and bottom| for values of 2 mm (a) and 6 mm (b)
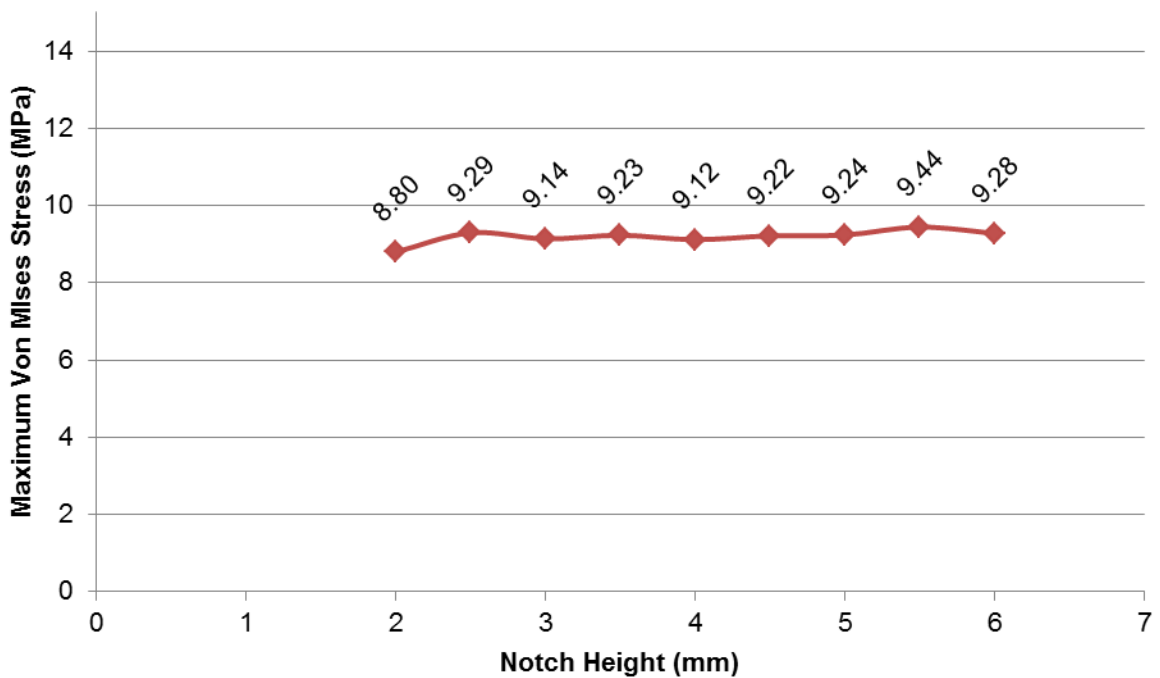
Figure 5-17 Plot of the maximum Von Mises stress against notch height

The difference between the stress values for the largest and smallest value for the notch height is 0.64 MPa (11.64%) and the average value is 9.19 MPa (167.09%). It is possible that for notch height values below 2 mm the stress decrease further but in practise the minimum bead notch height is larger than 2 mm.

5.3.4.4 Root length

A notch height value of 4 mm was used to investigate the root length parameter. The deformed FEA results are shown in Figure 5-18 for the root length parameters. The effect of root length on the maximum Von Mises stress can be seen in Figure 5-19. The maximum stress for root length decreases from 10.48 MPa (190.55%) for 10 mm to 7.48 MPa (136.00%) for 2 mm.
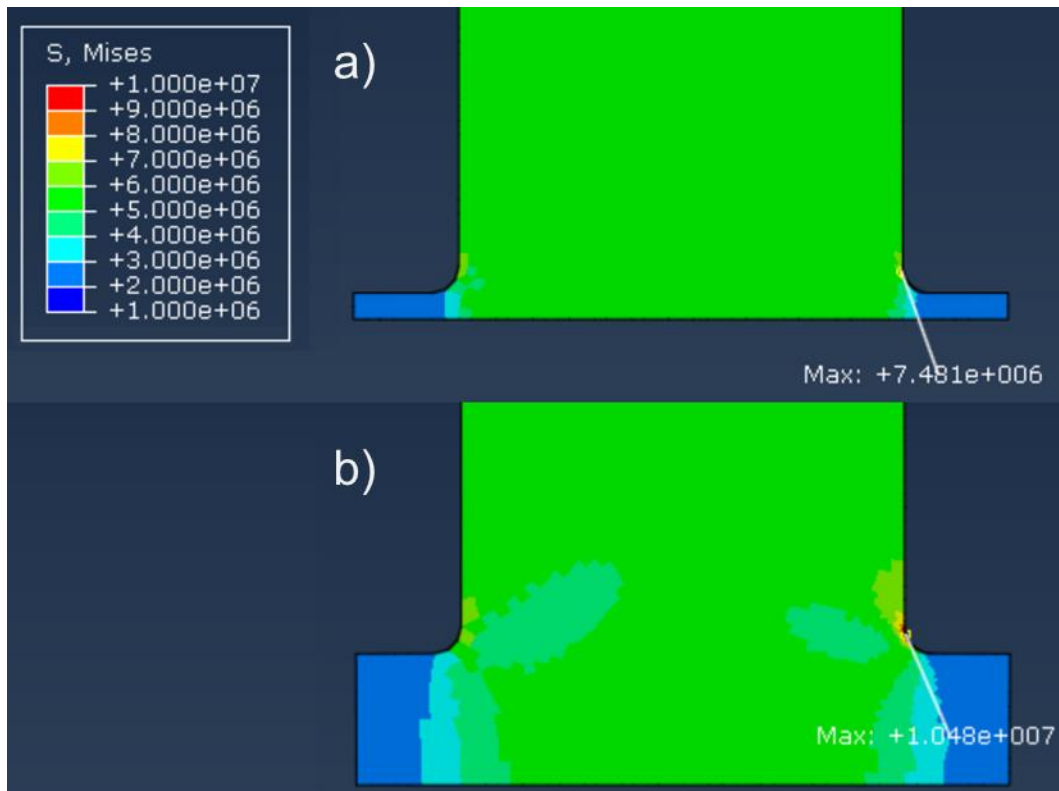
Figure 5-18 Deformed FEA results for root length parameters shown in order (top and bottom| for values of 2 mm (a) and 10 mm (b)
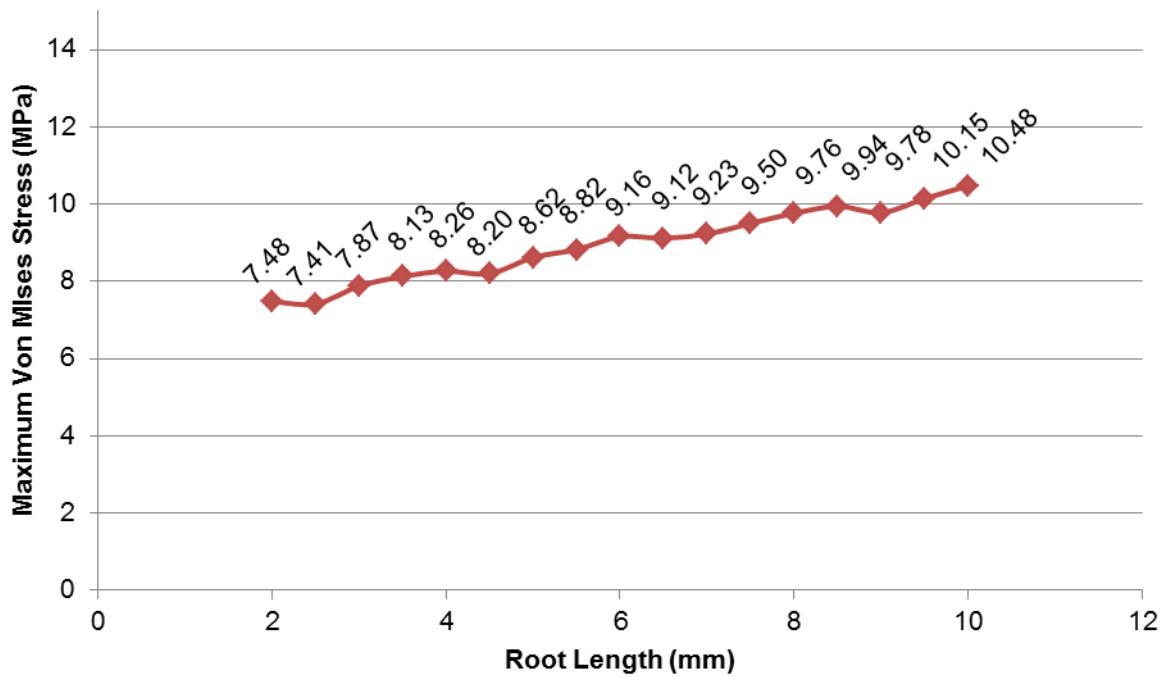
Figure 5-19 Plot of the maximum Von Mises stress against root length

The difference between the stress values for the largest and smallest value for the root length is 3 MPa (54.55%). The relationship between the maximum Von Mises stress and root length is linear and where the stress increase is proportional to the size of the root length.

5.3.5 Summary

The bead angle is linear and inversely proportional to the stress but it is also difficult to define; in practise has quite a narrow range of angles. The influence of side notch radius is inversely proportional to its size and becomes non-linear as the radius is reduced. The root length parameter has relatively greater influence on the stress concentration than notch height parameter; their influences are much milder than that of the side notch radius parameter.

The main limitation of the parameteric models is the fact that each parameter is varied independently with the rest of the parameters fixed at a constant value and thus not possible to see the joint influence based on multiple parameters acting simultaneously. Therefore it is necessary to model realistic cases based on the geometry derived from the macrographs, in the next section.

130

5.4 FEA: Realistic Bead Geometry

5.4.1 Introduction

This section builds upon the models used for parametric bead modelling and adapts them to be valid when using realistic weld bead geometries digitised from the macrographs. The aim of this modelling work is to identify if the key weld bead parameters that affect the stresses in the pipe wall in realistic bead shape are similar to those identified in the parametric study and where the stress concentration occurs.

5.4.2 Modelling assumptions

A base model (Figure 5-20) was prepared to include the central notch height and root length. Almost all of the realistic weld bead geometries have features such as minute gaps, seams and folds. The base model was used to investigate the effect of seams that are formed due to the bead width extending past the root length, yet resting on the pipe wall. The seam feature in FEA functions by doubling the number of nodes on edges where seams are assigned. These doubled nodes can then separate as required to represent the areas of the weld bead in intimate contact with the pipe yet not fused. The seam feature was necessary as the realistic bead shapes often rest on the pipe wall without joining it. In order for the seam to function, general contact condition was enabled to prevent self-intersection of the geometry. The seam feature effectively allowed 0^0 bead angle despite the extended contact of the weld beads against the pipe wall since the weld beads only join the pipe wall along the weld bead root length.

The weld bead geometries were prepared as axisymmetric models with 5.5 MPa of uniform stress applied to the pipe wall. The material was treated as uniform and homogenous using material properties derived and discussed in Section 3.5.5.4. Only the base model investigating the use of seams used a symmetry boundary condition at the weld interface, all other models were without the symmetry boundary condition. The results are reported as non-averaged Von Mises stress. The full length of realistic weld bead geometry was 100 mm. The base model used 4000 CAX4R elements and the realistic weld bead models used 8000 ± 500 CAX4R elements and 20-200 CAX3 elements, the elements ranging in size from 0.0066 mm^2 to 0.37 mm^2 depending on their respective location. Both models used free mesh with internal partitions to ensure structured mesh formation where possible.

5.4.3 Model details

The base model is shown in Figure 5-20 which is used as a template for generating 18 models, one each for each of the three circumferential positions and the six welding procedures. Figure 5-21 show the models based on realistic weld bead geometries digitised from the macrographs for three different circumferential positions for WP3. Figure 5-22 shows the typical location and the number of seams in a realistic weld bead geometry model. The seams would allow the weld bead regions that are in contact with the pipe wall but not joined with the pipe wall, to separate from the pipe wall. The separation of the weld bead will change the bead angle or increase the stress in the pipe wall if the weld bead moves against it. With the exceptions of how the pipe wall stress is applied as pressure and the length of the pipe modelled, the realistic weld bead models are otherwise identical to the FEA models used for WPTCR study in Section 3.5.5.
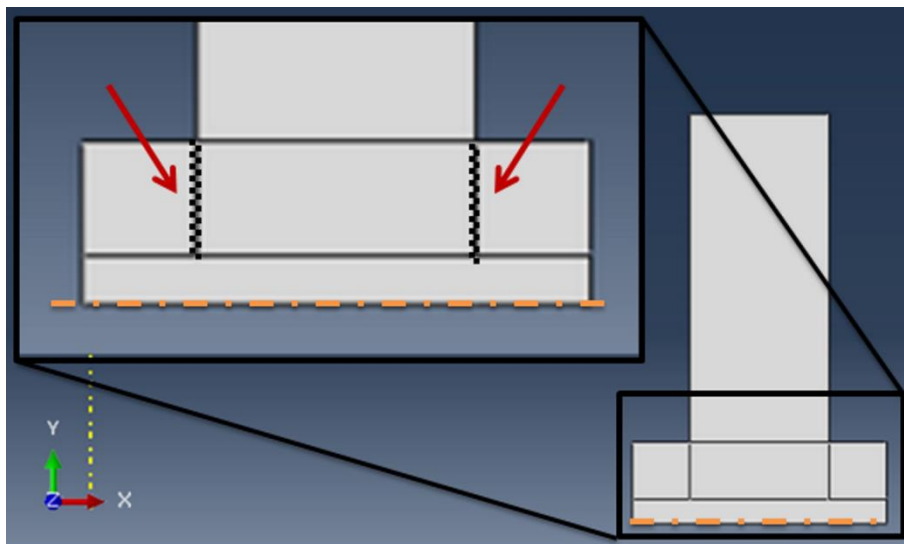
Figure 5-20 The base model used for investigating the seams feature, the locations of the seams are marked by 2 vertical zig-zag lines highlighted by the arrows, the two horizontal dash-dot show the weld interface, the single vertical dash-dot line shows the pipe axis, and the internal horizontal black lines show the partitions made to allow a structured mesh to be generated
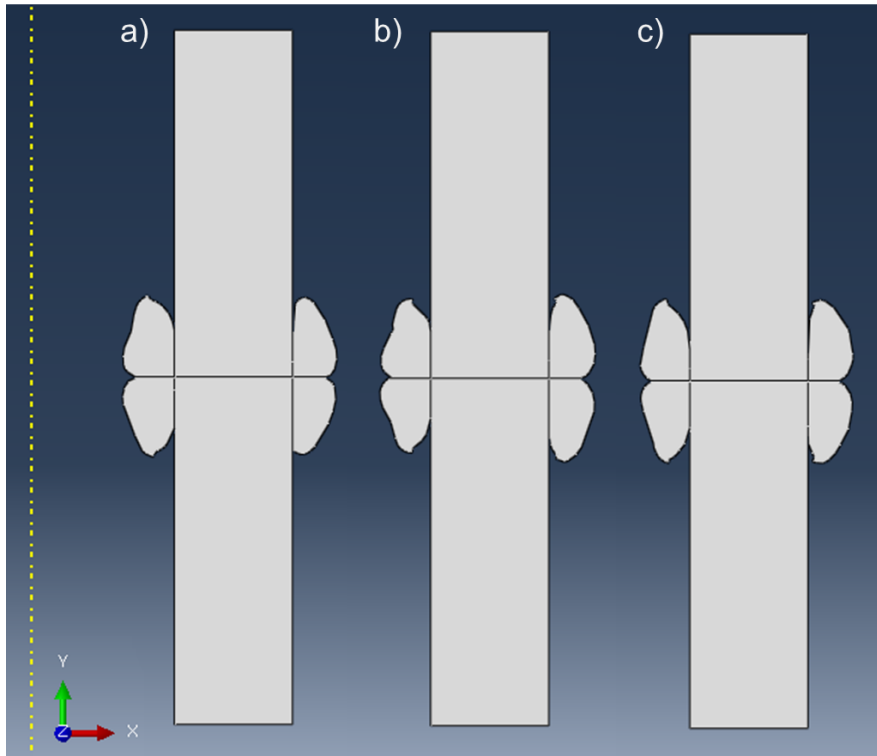
Figure 5-21 The realistic weld bead geometry models for three circumferential positions of WP3: bottom (a), top (b), and side (c), the internal black lines show partitions made to allow for a structured mesh to be generated and the dotted vertical line shows the pipe axis marking the inside
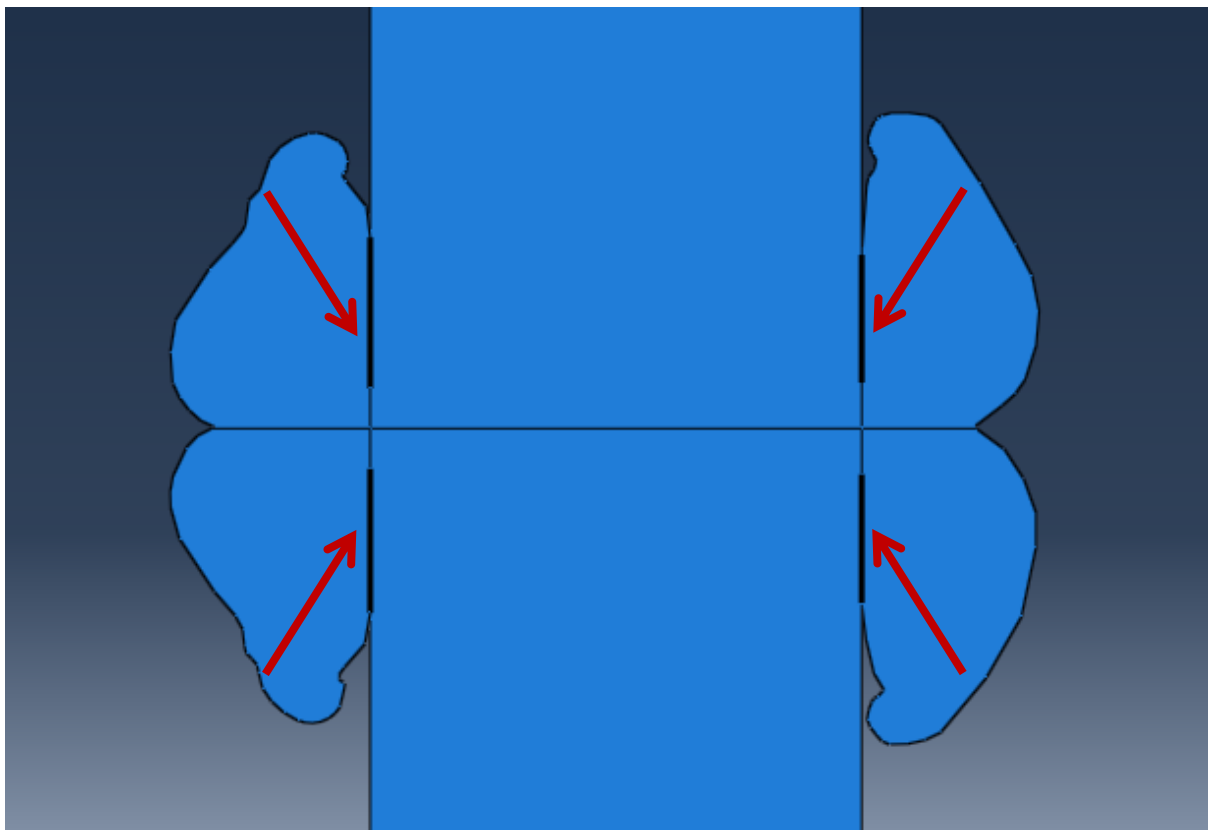
Figure 5-22 WP6 side model with the location of seams indicated by the arrows

5.4.4 Results and Discussion

Carrying out the FEA modelling with the digitised weld bead geometries had been challenging and highlighted numerous issues that had to be resolved to obtain FE models that are realistic representation of the beads. Firstly, the cutting of macrograph specimens from the pipe led to lowering of the weld area relative to the cut ends due to stress relaxation. This deviation from straight wall pipe geometry required adjustment in the positioning of the inner and outer weld beads relative to the pipe wall. Secondly, the bead geometry had to be optimised by combining extremely short edges without changing the overall geometry to accommodate suitable model meshes. The short edges cause unnecessary concentration of elements in the local area, distorting the model mesh. This process simplified the model geometry, but also deviates the model geometries from the realistic weld bead shapes. Lastly, the boundary between the beads and the pipe wall had to be maintained due to separation from lack of fusion outside the root length. This led to small voids to be located between the beads and the pipe wall for some models; some voids are visible in the macrographs shown in the Appendix D in Table D-1. The HDPE material itself is highly plastic but the current FEA models remained below the elastic limit using homogenised material properties across the model. The local areas where the stress is above the yield value of 10 MPa will be likely due to small geometry features such as the voids that are contributing towards the concentration of the stress. The impact of such features can be reduced by removing the elements affected by poor geometry of the weld beads during the post-processing process. This step was necessary only in few models to ensure that the location of the maximum Von Mises stress is correctly identified.

The results of modelling for the six welding procedures and three circumferential positions are reported in Table 5-3 with normalised percentage value in brackets. The Von Mises plot of realistic weld beads for the three WP3 circumferential positions is shown in Figure 5-23. Von Mises plots for the remaining welding procedures and circumferential positions can be found in Appendix F.
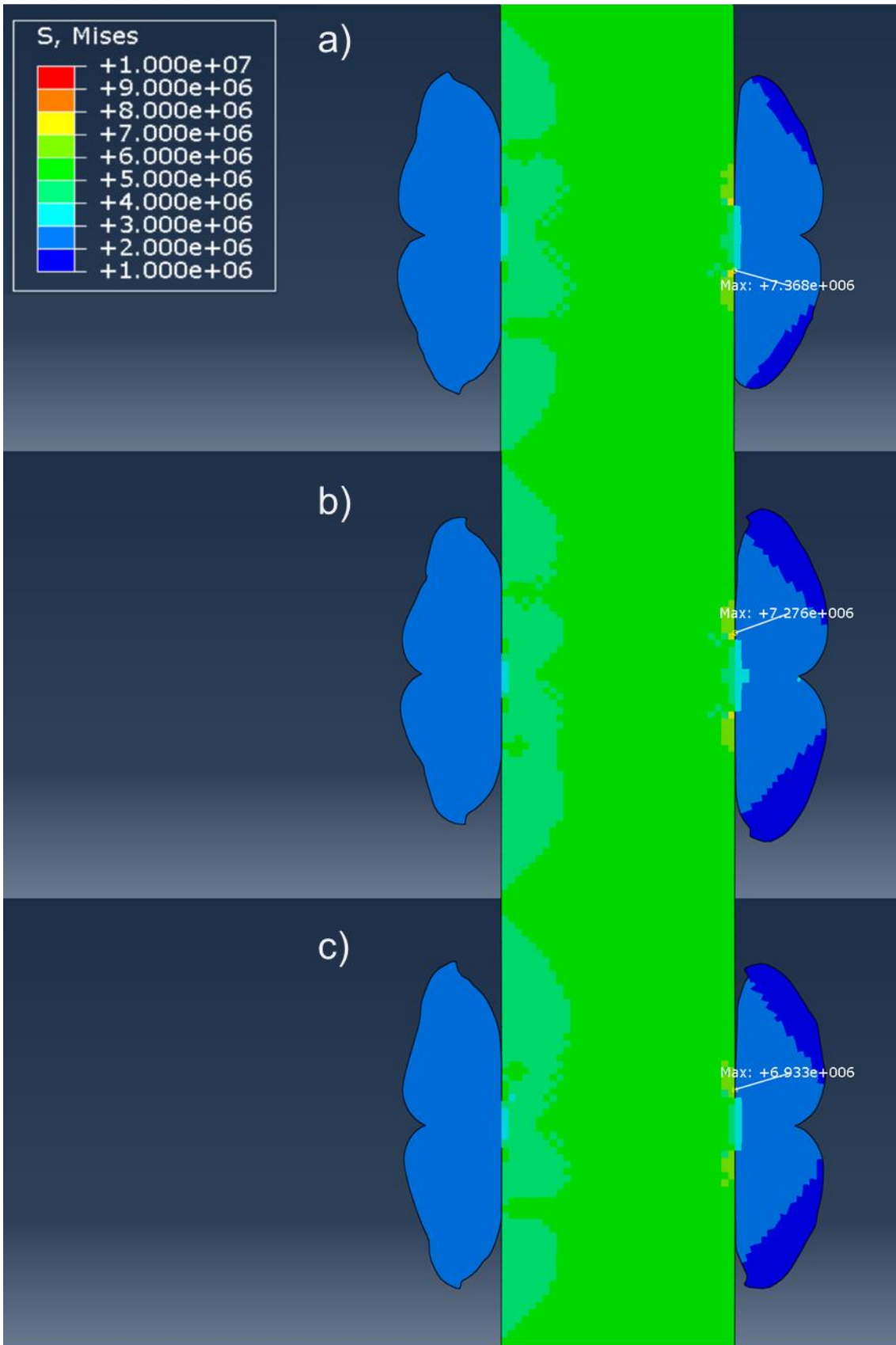
Figure 5-23 FEA results of realistic weld bead shape models of WP3 for three circumferential positions: bottom (a), top (b), and side (c)

135

Table 5-3 Maximum Von Mises stress (MPa) for realistic weld bead geometries

Von Mises	Bottom	Top	Side	WP Average
WP1	7.08 (128.71%)	7.38 (134.20%)	8.13 (147.84%)	**7.53 (136.92%)**
WP2	7.55 (137.31%)	6.97 (126.76%)	7.40 (134.45%)	**7.31 (132.84%)**
WP3	7.37 (133.96%)	7.28 (132.29%)	6.93 (126.05%)	**7.19 (130.77%)**
WP4	6.99 (127.05%)	7.25 (131.89%)	7.17 (130.38%)	**7.14 (129.78%)**
WP5	7.24 (131.58%)	6.85 (124.56%)	6.80 (123.62%)	**6.96 (126.59%)**
WP6	7.00 (127.29%)	7.62 (138.49%)	6.64 (120.73%)	**7.09 (128.84%)**
Circumferential Position Average	**7.20 (130.98%)**	**7.23 (131.37%)**	**7.18 (130.51%)**	**7.20 (130.95%)**

Figure 5-24 shows the Von Mises stress at each of the three circumferential positions for the six welding procedures. The averaged stress concentration for each circumferential position is: 130.98% for bottom; 131.37% for top; and 130.51% for side.
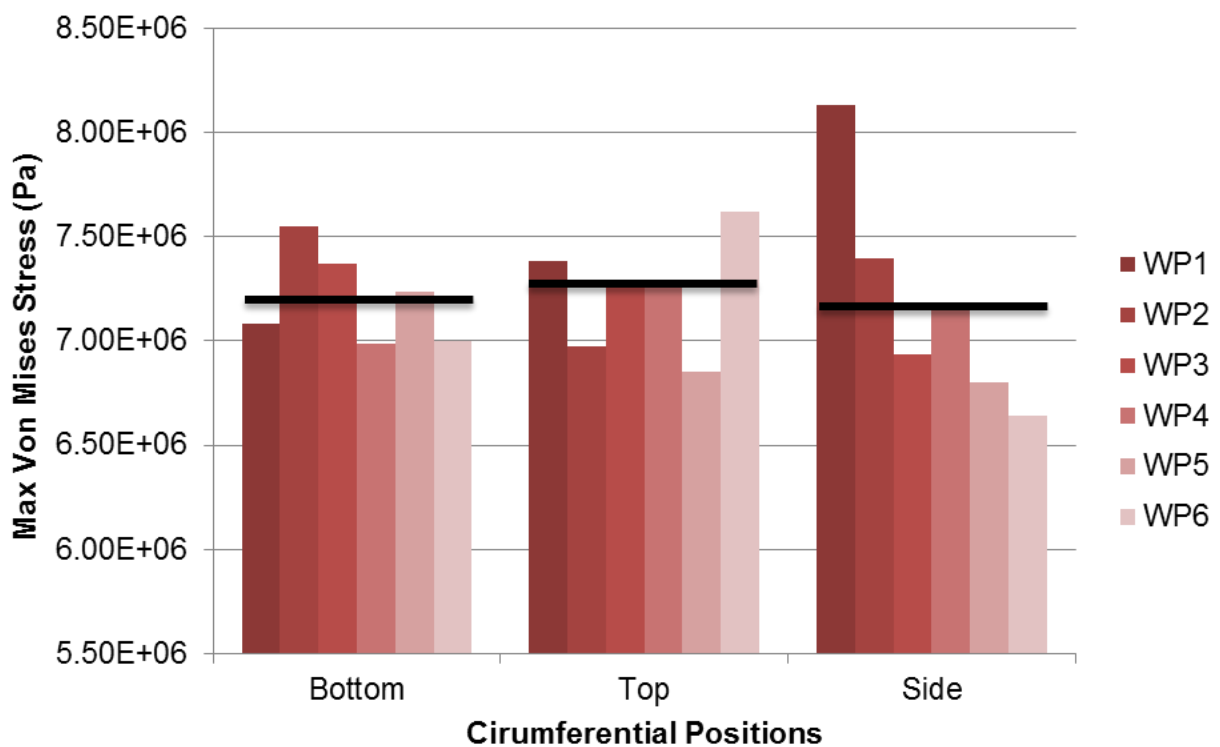
Figure 5-24 Outer weld bead position against the max Von Mises stress, the black lines represent the averaged stress for each circumferential position

136

Figure 5-25 shows the Von Mises stress at each of the six welding procedures for the three circumferential positions. The averaged stress concentration for each welding procedures is: 136.92% for WP1; 132.84% for WP2; 130.77% for WP3; 129.78% for WP4; 126.59% for WP5; and 128.84% for WP6.
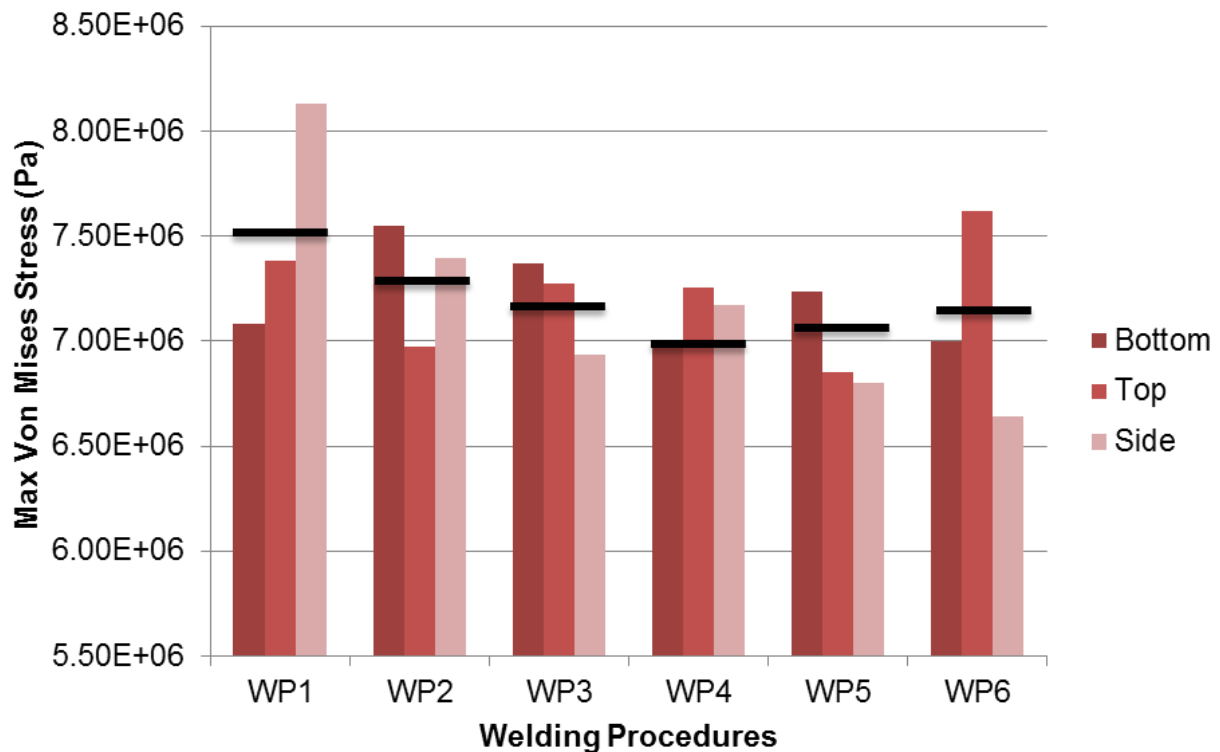
Figure 5-25 Welding procedures against the max Von Mises stress, the black lines represent the averaged stress for each welding procedure

The difference in stress concentration due to the circumferential positon of the weld bead is minimal as seen in Figure 5-24. However, the side position has greater variance (27.11%) in the stress concentration when compared to the bottom (10.25%) or top (13.93%) positions. Similarly for welding procedures as seen in Figure 5-25, the variance in the stress concentration was: WP1 (19.13%); WP2 (10.55%); WP3 (7.91%); WP4 (4.84%); WP5 (7.96%); and WP6 (17.76%). WP1 and WP6 had the highest variance and WP5 had the lowest variance in stress concentration. For stress concentration across all three positions, WP4 had the lowest values and WP1 had the highest values. There is a very gradual decrease in stress concentration which weakly correlates against the increasing fusion pressure across the welding procedures.

5.4.5 Summary

The effect of circumferential position on the stress concentration is insignificant. The effect of welding procedures has a very weak correlation on the stress concentration, inversely proportional to the fusion pressure. Due to complex interaction between the weld bead parameters in realistic weld bead, it is difficult to ascertain if a particular weld bead parameter has a greater contribution towards stress concentration than others as seen in the previous section.

The largest stresses are always located at the notches between the outer beads and the pipe wall as seen in Figure 5-23; on average the increase in stress is 30% of the pipe wall stresses. The stress in the pipe wall is tensile in nature; therefore, as the pipe is extended the diameter of the pipe contracts due to Poisson's ratio. This effect is most pronounced at the weld section due to its proximity being at the greatest distance from the pipe ends where the stress is applied. The weld beads act as small reinforcement akin to hoops on a barrel. The outer bead moves away from the pipe wall and inner bead moves with the pipe wall due to the angle of the weld beads and the contraction of the pipe wall. It was observed that the location of initial cracks in the failure of waisted tensile specimens (Section 4.2) coincides with the location of stress concentration seen in the realistic bead models.

The impact of the findings of these FEA studies is towards the conformity of the stress concentration towards the notches on the outer bead, for both circumferential position of the weld bead and the different welding procedures. This holds true provided the welding has been performed without misalignment or pipe slippage, the increase in stress will be approximately 30% at the outer weld notches. A small amount of misalignment or pipe slippage may not be apparent during visual inspection. The digitised macrograph geometries of the pipe being investigated can locate the cause of stress concentration to a greater accuracy then visual inspection alone. However, further work is required to confirm which of the weld bead parameters has the most significant contribution towards stress concentration in realistic weld bead geometries.

6 Weld Microstructure

6.1 Introduction

The weld microstructure was explored using a combination of techniques including nanoindentation (NI), transmission light microscopy (TLM), differential scanning calorimetry (DSC), and thermal FEA modelling. These techniques were used to investigate the formation, identification, and measurement of the weld features: the melt zone (MZ); the heat affected zone (HAZ); and the weld beads. The aim is to identify how the weld features affect the thermal (crystallisation) and mechanical properties (hardness and elastic modulus); and correlate the findings to the results of the mechanical tests and weld bead studies.

The nanoindentation was used to identify variation of the hardness and the elastic modulus across centre of the welds. The FEA thermal modelling was used to predict the volume of the molten material and, together with TLM, to correlate to the size and the geometry of the weld beads for each welding procedure. The DSC study builds upon the NI results to verify and support the previous findings regarding the variation of local crystallinity or degree of crystallisation within weld microstructure. The key contribution of the chapter concludes by proposing a new geometry for butt fusion joints in HDPE pipes. The NI, TLM, and DSC techniques when combined enabled better understanding in formation of the welds beads and the microstructure of welds.

Several parts of this chapter have been presented at the IIW 2016 Annual Assembly, Australia and form part of a publication in the 'Welding in the World' journal (Shaheer, et al., 2016) which includes: the NI results; data from TLM; the results of initial trial of the DSC; and the thermal FEA modelling.

This subchapter details the methodology for: conducting the nanoindentation tests; performing the DSC experiments to validate the findings of the nanoindentation investigation; and lastly, the method used for performing a thermal FEA study that ties the findings from the nanoindentation and DSC results. The subchapter briefly details the short trials carried out to assess other analytical techniques that showed potential to complement the nanoindentation results when looking at weld features.

6.2 Nanoindentation

6.2.1 Introduction

Nanoindentation (NI) is a translation of macro-scale hardness testing through indentation to nano-scale (Fischer-Cripps & Anthony, 2010; Qian, et al., 2005). Several of the earliest hardness mechanical techniques, precursor to NI, are now over 100 years old. However, technological developments in the early 1970s have enabled extraction of material properties such as the elastic modulus in the sub-micron range. The NI technique involves using a very hard (usually synthetic diamond based) indenter of a known geometry to perform indentations while very accurately measuring force and depth (Sattler, et al., 2010). The load-displacement curve is used, in conjunction with the material properties and geometry of the indenter, to derive the material properties of the material under test (Poon, et al., 2008). The typical apparatus compromising the nanoindentation system is depicted in Figure 6-1.

A micro-structural level understanding is lacking regarding the weld geometry and properties and how the weld interacts with the parent material. Nanoindentation is one of the few techniques that enable the investigation of the micro-mechanical properties of HDPE pipes welds. Henceforth, any improvements in the fundamental understanding of how polymer welding processes affect the weld micro-structure would be highly beneficial in advancing the reliability and performance of HDPE piping systems. The very high spatial resolution of the NI technique has been used to measure the variability of the material properties across the HDPE welds.
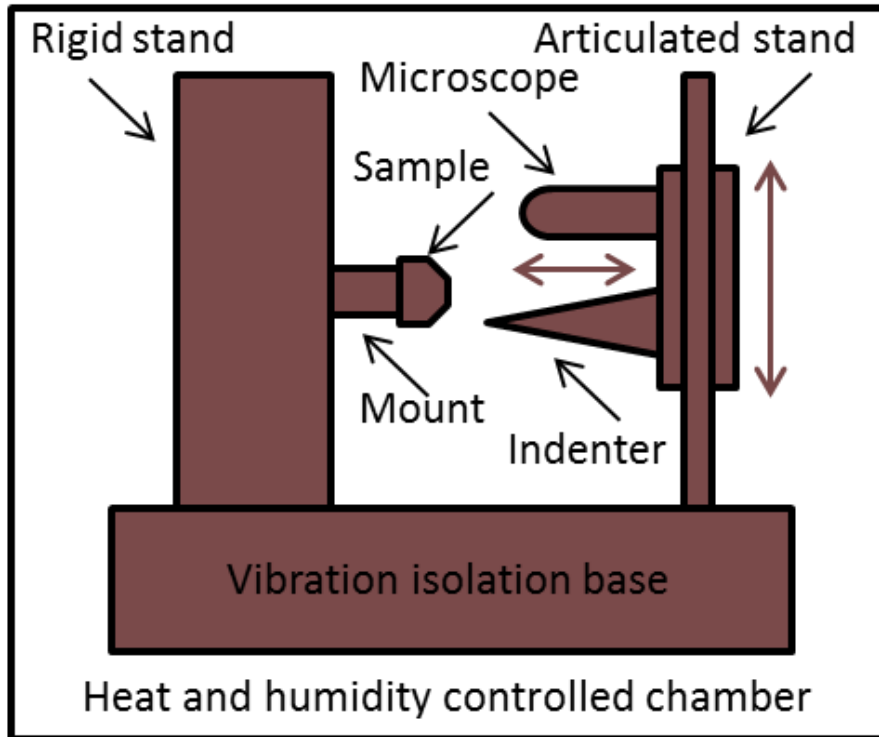
Figure 6-1 Schematic arrangement of a nanoindentation machine

6.2.2 Specimen preparation

The NI specimens were cut from the butt fusion joint with the weld bead intact, with the weld in the centre, as sketched in Figure 6-2. The cuts were made at low speeds to ensure to mitigate induced heating of the samples before polishing the cut surfaces. These specimens, measuring 25 mm by 25 mm were machined to ensure that the indentation surface was parallel to the back of the specimen. The test surfaces of each specimen were then grinded and polished with successively finer grades of abrasive silicon carbide paper to achieve an average surface roughness of 2.5 μm (Cheng & Cheng, 2004).The polished specimen were glued with a thin layer of suitable adhesive (superglue for HDPE specimens) to the mounting bolt in the orientation presented in Figure 6-3. The adhesive was given time to dry before testing of the specimen.
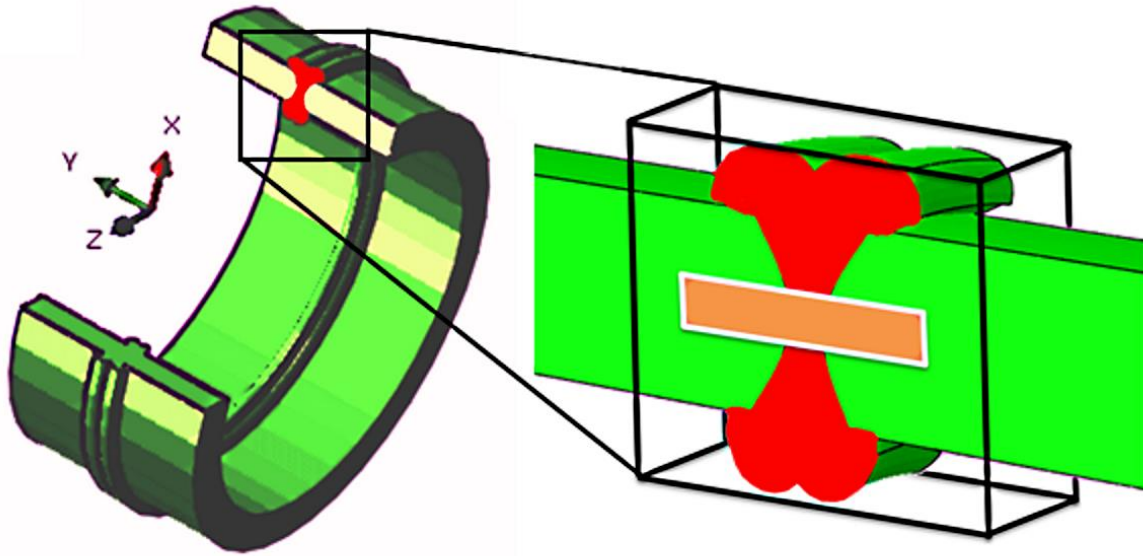
Figure 6-2 Sketch of welded HDPE pipe showing the location of the weld and the melt zone in red and the specimen for NI (enclosed in the box) where the location of the indentation grid across the weld is highlighted by the orange rectangle (Shaheer, et al., 2016)
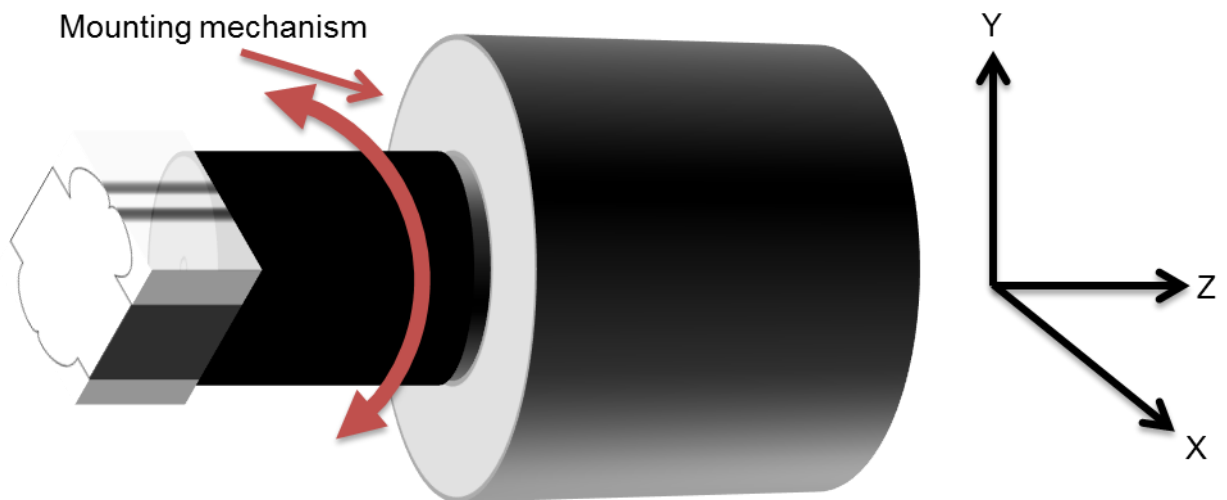
Figure 6-3 Illustration of the mounting mechanism, the bold arrow shows the Z-axis rotation of the specimen

6.2.3 Indentation test parameters

Several nanoindentation trials were conducted in order to establish suitable test parameters in order to investigate the variation in material properties across the weld interface, these parameters are listed in Table 6-1. These trials investigated the effects of loading value, loading rate, indentation area, heat treatment, indentation grid arraignment, and indentation grid density. The Berkovich indenter was selected due to its conformity arising from its simple 3-sided shape and supporting literature (Fischer-Cripps & Anthony, 2010; Zhang, et al., 2005).

Table 6-1 Nanoindentation experiment parameters (Shaheer, et al., 2016)

Parameter	Value
Indenter, type	Berkovich
Load, mN	150
Speed, µm/ minute	10
Hold time, -s	12.5
Displacement (estimated), µm	15

6.2.4 Methodology

A grid of 60 columns by 3 rows of indents, spaced 100 µm apart, justified over the weld interface at the centre of the pipe wall thickness was used for each specimen and is shown in Figure 6-4. It was suggested by the TLM images that 60 columns per row would be sufficient in capturing the effects of welding (Gwynne, et al., 2010). All welding procedures were tested using this arrangement except for last specimen, which used a grid of 120 columns by 3 rows indents. The larger grid was used to ensure that effects of welding well past the weld interface into the parent material are also accounted for, if any. The nanoindenter required the operator to calibrate the distance between the indenter and the specimen surface after every millimetre of indents to ensure accuracy of the indentations. Therefore, it was not possible due to the prohibitive cost to use the larger grid layout for every specimen from the onset. All of the nanoindentation tests were completed by a trained operator for the nanoindenter.
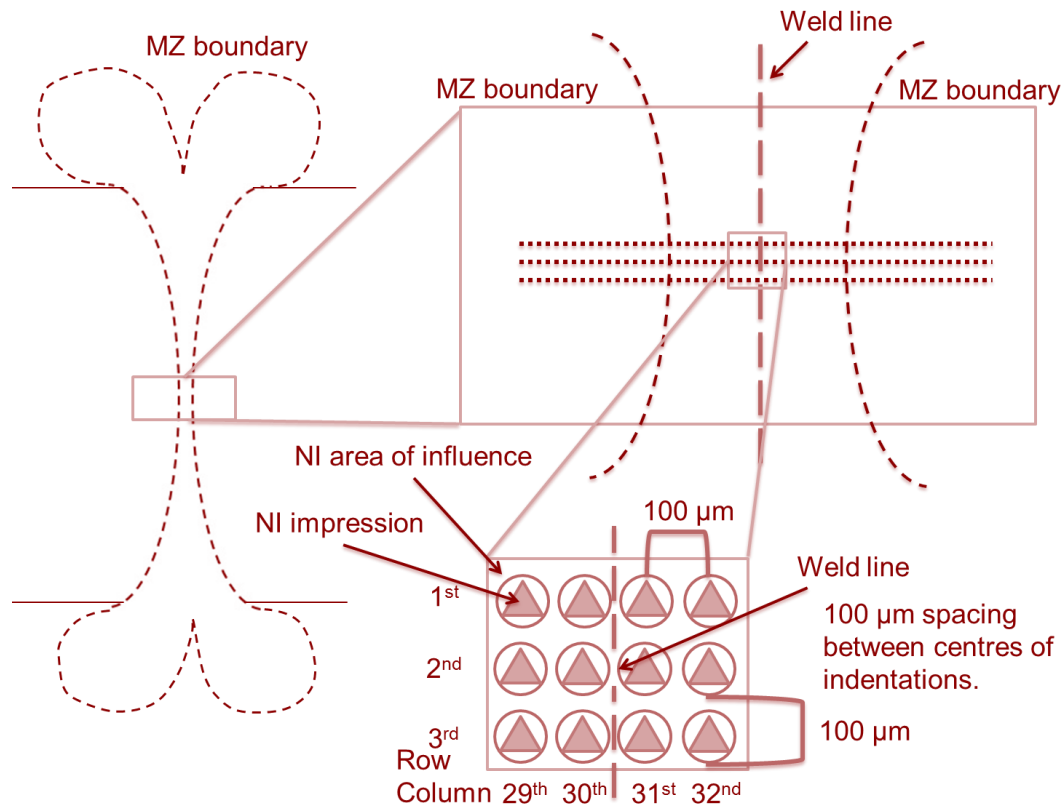
6.2.5   Results and Discussion

The nanoindentation (NI) technique is very sensitive to surface perturbations (Zhang, et al., 2005; Rocha, et al., 2013 ; Rodriguez, et al., 2012); the results reported were averaged from the three indentations rows in each column. The scatter could have been reduced by using larger loads. However, this would be at the expense of resolution since the indents would be larger and therefore the distance between them would need to be increased. The distance of 100 μm between the indentations was verified in the trial to be sufficient prevent interference in indentations from their neighbours. This would in turn require that the number of indentation rows be increased so there are more indents located in regions of interests and to provide an appropriate average, increasing the overall cost.

The parent material hardness was 0.0538 GPa with a standard deviation of 0.0021 GPa and elastic modulus was 1.358 GPa with a standard deviation of 0.0296 GPa, both properties were obtained using the first five and last five indents (for each welding procedure and averaged) which are expected to be in the parent material

which is sufficiently far away from the weld interface. Table 6-2 lists the parent material properties of hardness and elastic modulus for each welding procedure.

Table 6-2 NI-derived parent material properties for each welding procedure (Shaheer, et al., 2016)

Welding Procedure	Hardness (GPa)	Elastic Modulus (GPa)
WP1	0.0522	1.340
WP2	0.0571	1.415
WP3	0.0516	1.343
WP4	0.0530	1.335
WP5	0.0555	1.360
WP6	0.0536	1.356
Average	**0.0538**	**1.358**

Figures 6-1 to 6-6 show the hardness (top) and elastic modulus (bottom) values across the butt fusion weld for each of the six welding procedures, overlaid with the TLM images at the same scale. For reference, the microscopy images of the specimens for each welding procedure captured after nanoindentation are provided in Appendix G.
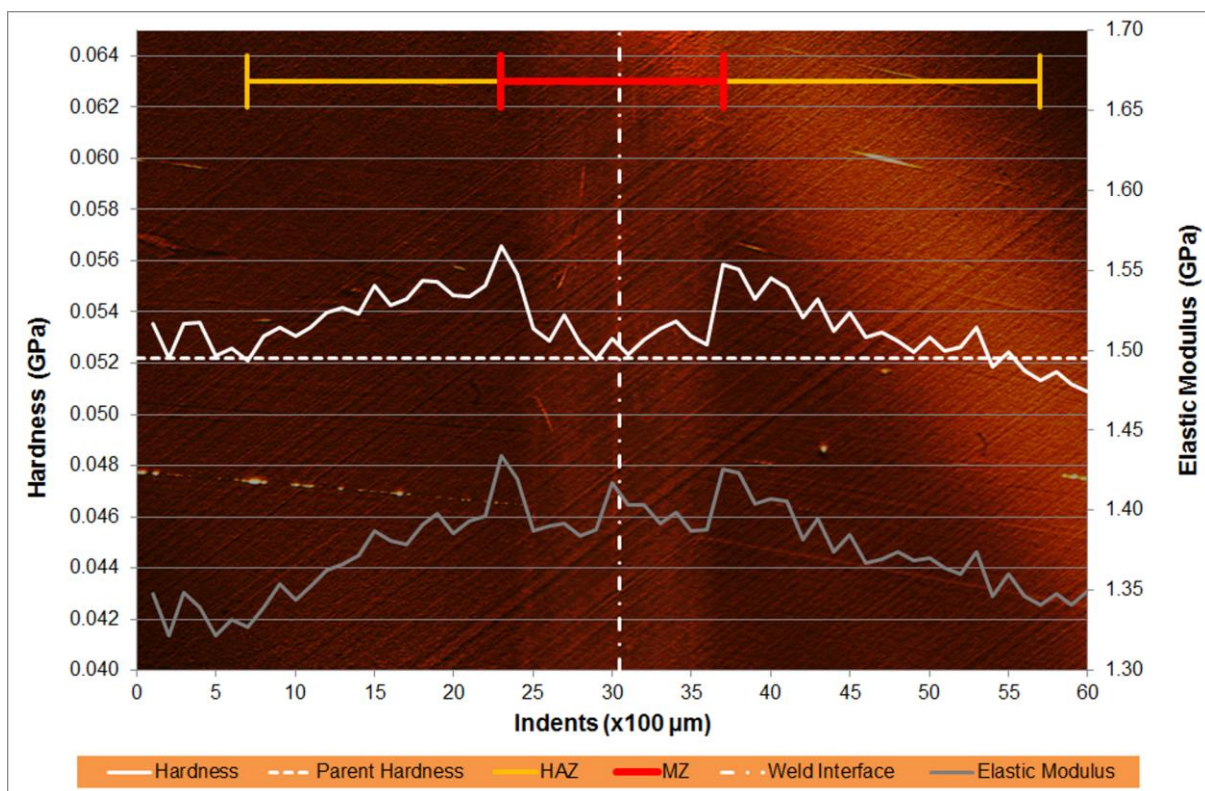
Figure 6-5 Nanoindentation graphs overlaid with TLM image for WP1 (Shaheer, et al., 2016)

145
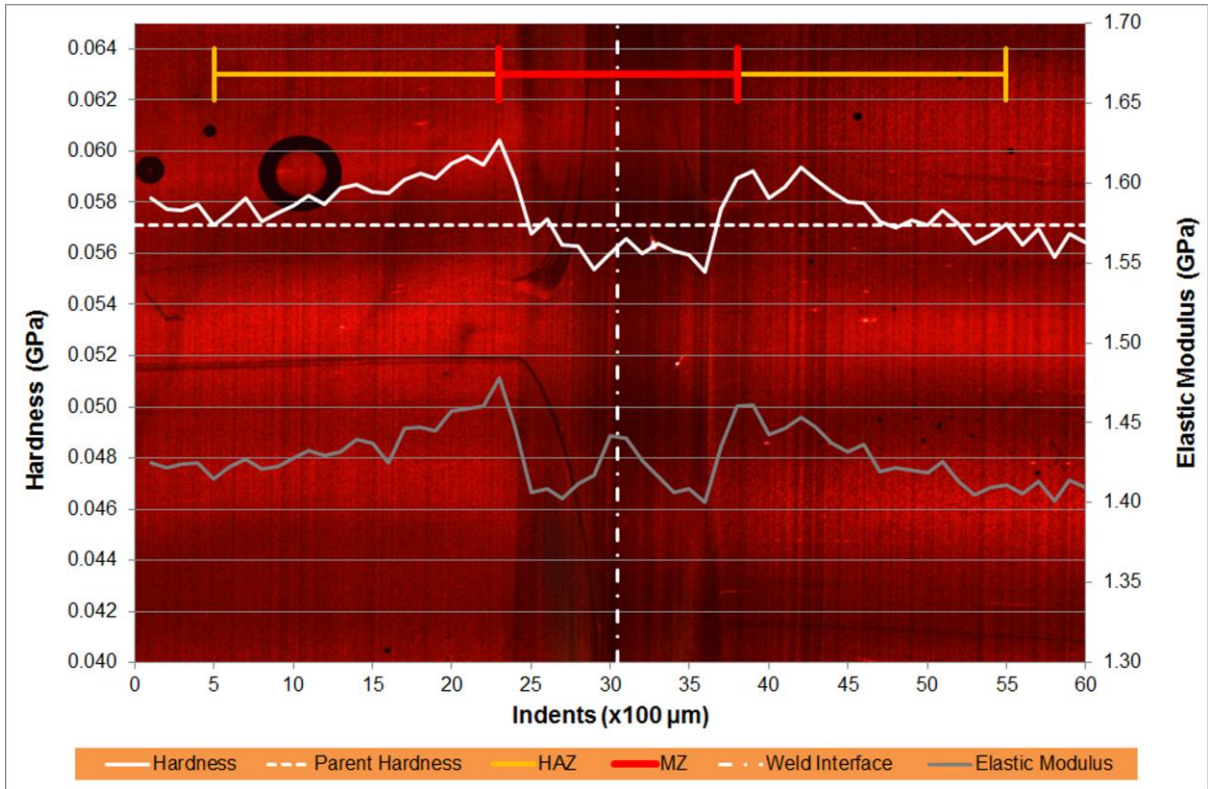
Figure 6-6 Nanoindentation graphs overlaid with TLM image for WP2 (Shaheer, et al., 2016)
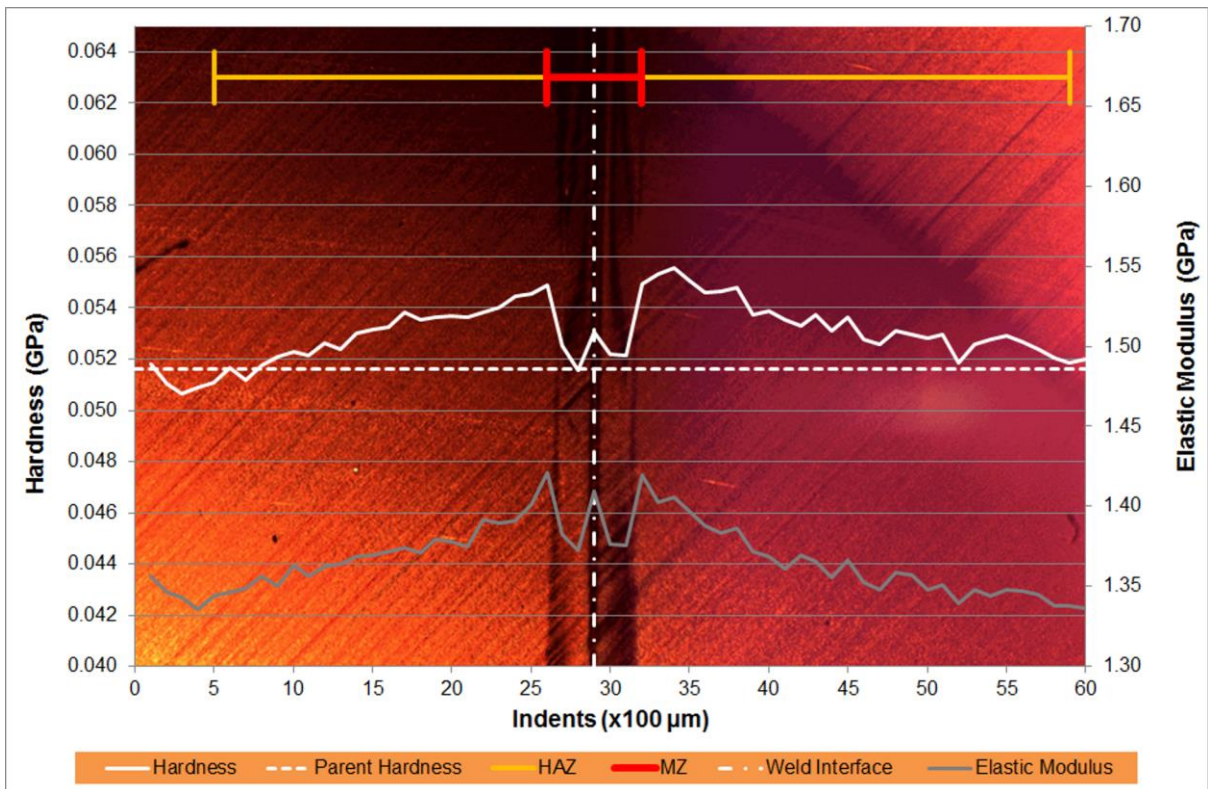
Figure 6-7 Nanoindentation graphs overlaid with TLM image for WP3 (Shaheer, et al., 2016)

146
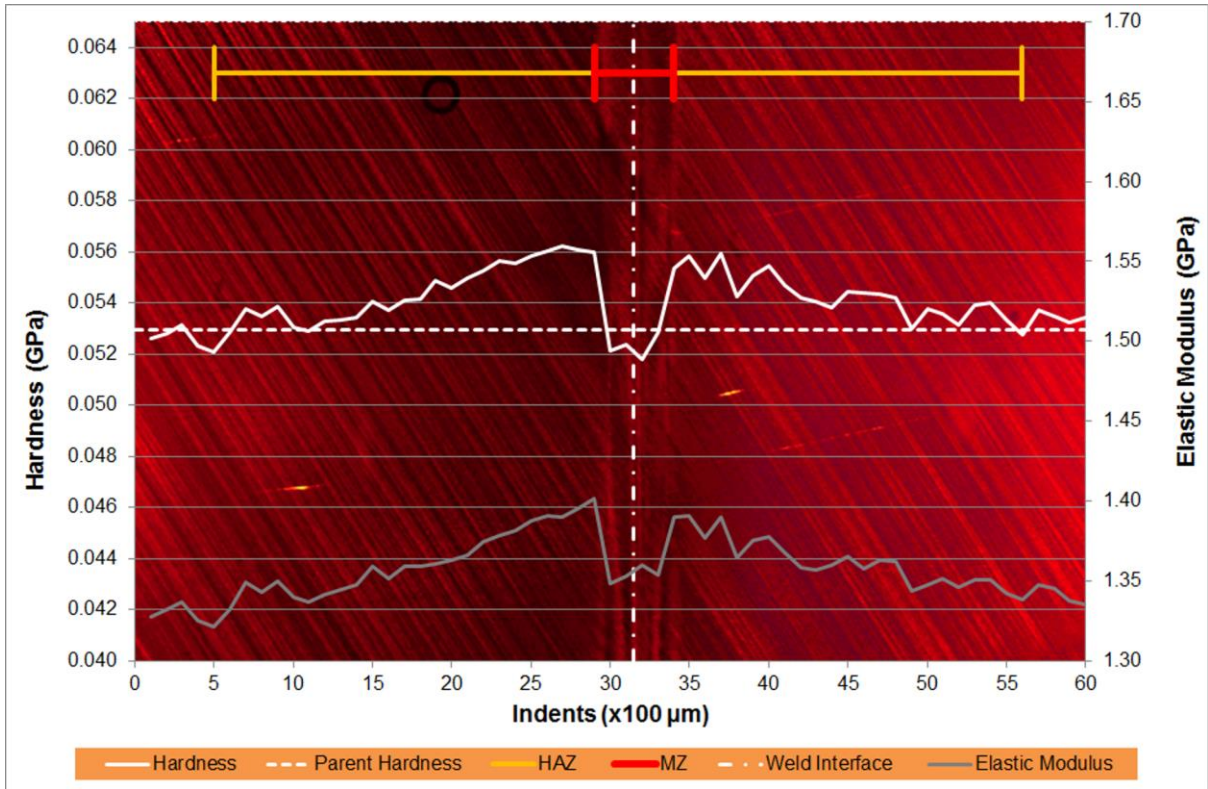
Figure 6-8 Nanoindentation graphs overlaid with TLM image for WP4 (Shaheer, et al., 2016)
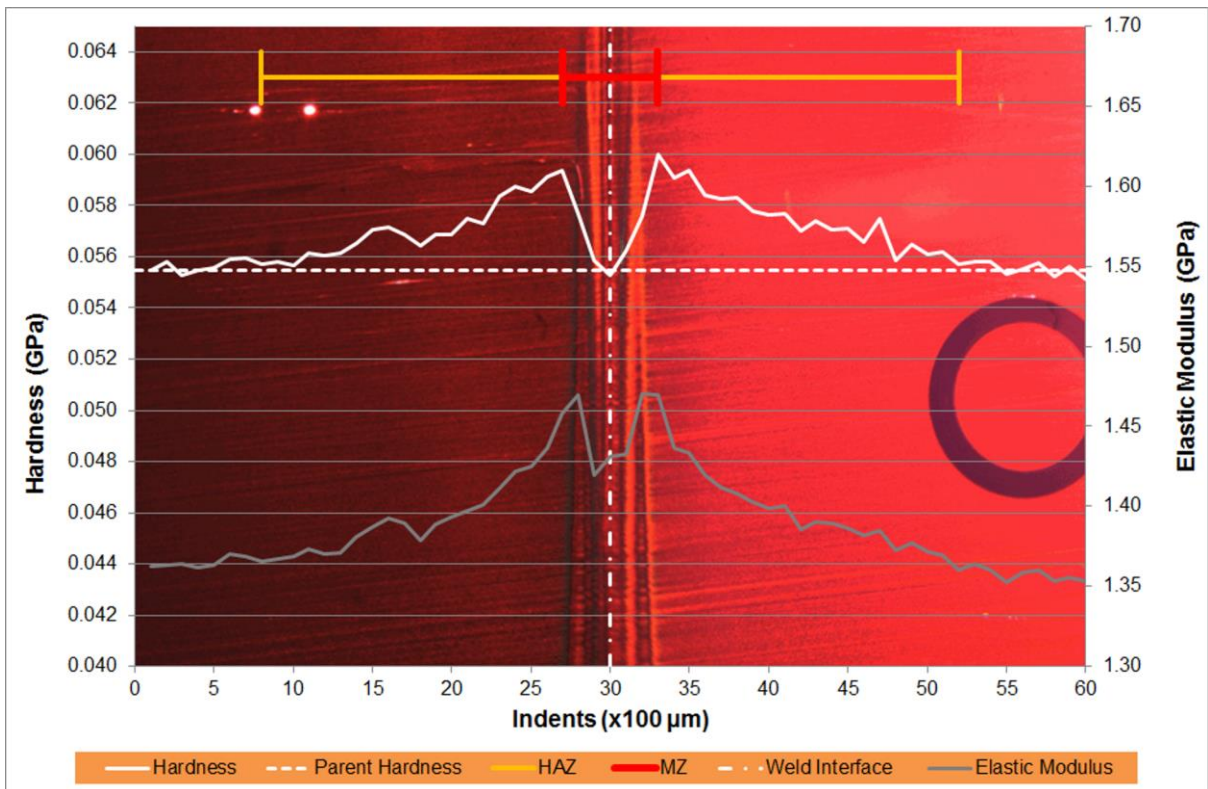
Figure 6-9 Nanoindentation graphs overlaid with TLM image for WP5 (Shaheer, et al., 2016)

147
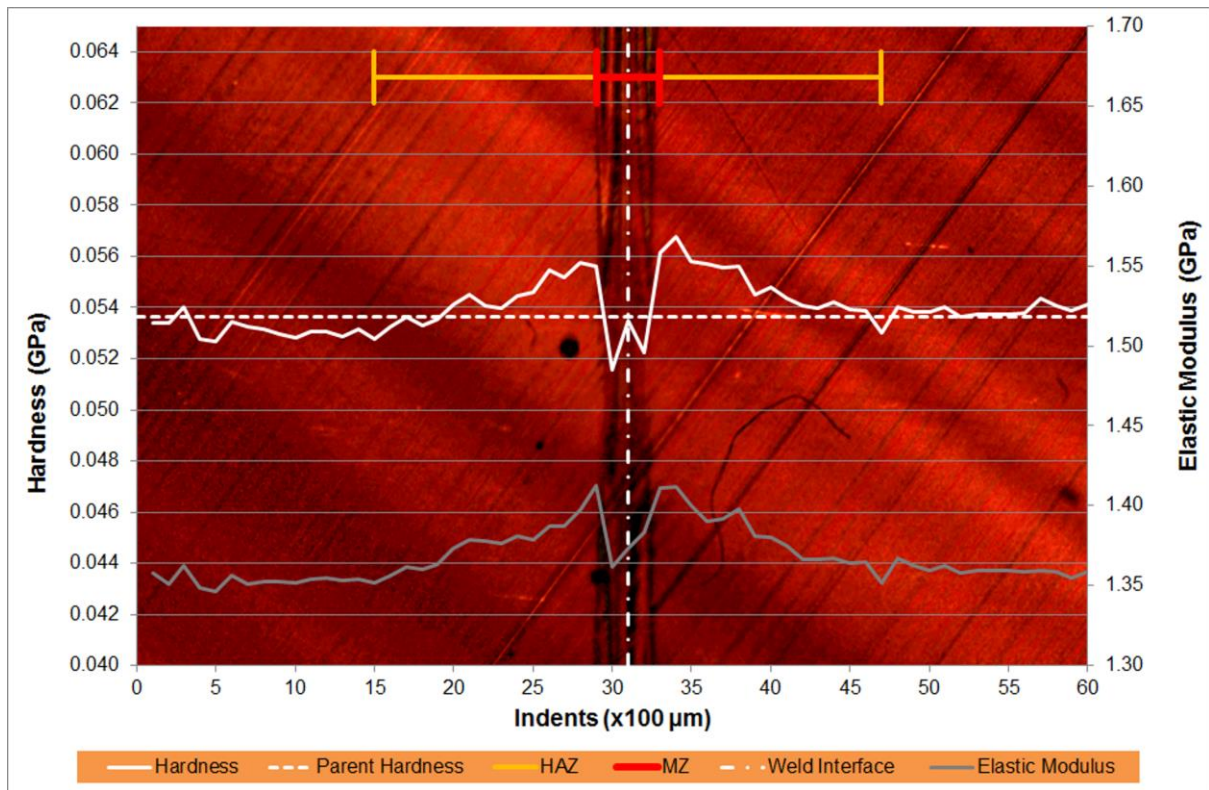
Figure 6-10 Nanoindentation graphs overlaid with TLM image for WP6 (Shaheer, et al., 2016)

Figure 6-11 is the full version for WP2 (Figure 6-6) using extended indentation zone (from 60 to 120 indents) to confirm if weld microstructure features being investigated are within the region bounded by the 60 indent grid. Figure 6-11 was truncated to allow a suitable comparison of WP2 against the other procedures using overlaid TLM image as discussed in Section 6.2.4.

The Figures of the nanoindentation results show very good correlation between the position of the peaks in both hardness and elastic modulus, and the boundary of the melt zone (MZ). Inside the MZ there is a sharp reduction in hardness and elastic modulus; whereas outside the MZ, there is a more gradual decrease in material properties until they match the reported parent material values of hardness and elastic modulus listed in Table 6-2 for each welding procedure. Therefore, nanoindentation suggests the influence of heat dissipation from the melt zone extends much further than the MZ itself into the parent material; the heat affected zone (HAZ), forming a second boundary with the parent material. It should be noted that the HAZ boundary cannot be seen in the TLM image, as the heat flux is insufficient to alter the material optically. This variation in mechanical properties will be discussed later together with the DSC characterisation (Section 6.3) in relation to the variation of crystallisation during welding. The extended indentation test in Figure 6-11 ensured exposure of the HAZ boundary where the hardness and elastic modulus values become constant close to that of the parent is within the region covered by the original indentation grid of 60 indents. As indents 1-30 and 91-120 are in the parent material for WP2 in Figure 6-11, only the truncated version of WP2

149

shown in Figure 6-6 will be discussed alongside other welding procedures in the upcoming sections.

In the previous Figures, a distinct twin-peak pattern is visible that shows an increase in both hardness and elastic modulus across the weld region. The twin-peaks bind a valley the roughly the size of the MZ at the weld interface which has both material properties at approximately the same values as the parent material; the MZ therefore should effectively behave in the same manner as the parent material. The material properties at the peaks are 5-6% higher for each welding procedure than the parent material as shown for both peaks in Table 6-3.

Table 6-3 Hardness and elastic modulus values for the two peak positions with a percentage increase against the parent material values in the brackets, for each welding procedure (Shaheer, et al., 2016)

Welding Procedure	Hardness				Elastic Modulus			
	Peak 1	%	Peak 2	%	Peak 1	%	Peak 2	%
WP1	0.0566	8.42	0.0558	7.00	1.435	7.03	1.426	6.37
WP2	0.0604	5.81	0.0589	3.25	1.478	4.42	1.461	3.19
WP3	0.0549	6.33	0.0549	6.39	1.421	5.80	1.419	5.68
WP4	0.0560	5.67	0.0553	4.50	1.402	4.99	1.390	4.12
WP5	0.0594	7.05	0.0600	8.12	1.458	7.22	1.470	8.11
WP6	0.0557	3.90	0.0567	5.79	1.413	4.20	1.411	4.07
Average	**0.0572**	**6.19**	**0.0570**	**5.82**	**1.434**	**5.60**	**1.429**	**5.24**

Figure 6-12 and Figure 6-13 depict the average values of hardness and elastic modulus within the indented zones for each welding procedure. They showed overall a slight increase in both hardness and modulus in comparison with the parent material for most welding procedures. This observation is also reflected by the higher averaged (for each welding procedure) total depth of indentation in Figure 6-14 and the depth of plastic indentation which is not recovered in Figure 6-15. The elastic indentation depth can be calculated by subtracting the plastic indentation depth from the total indentation depth, as shown in Figure 6-12.
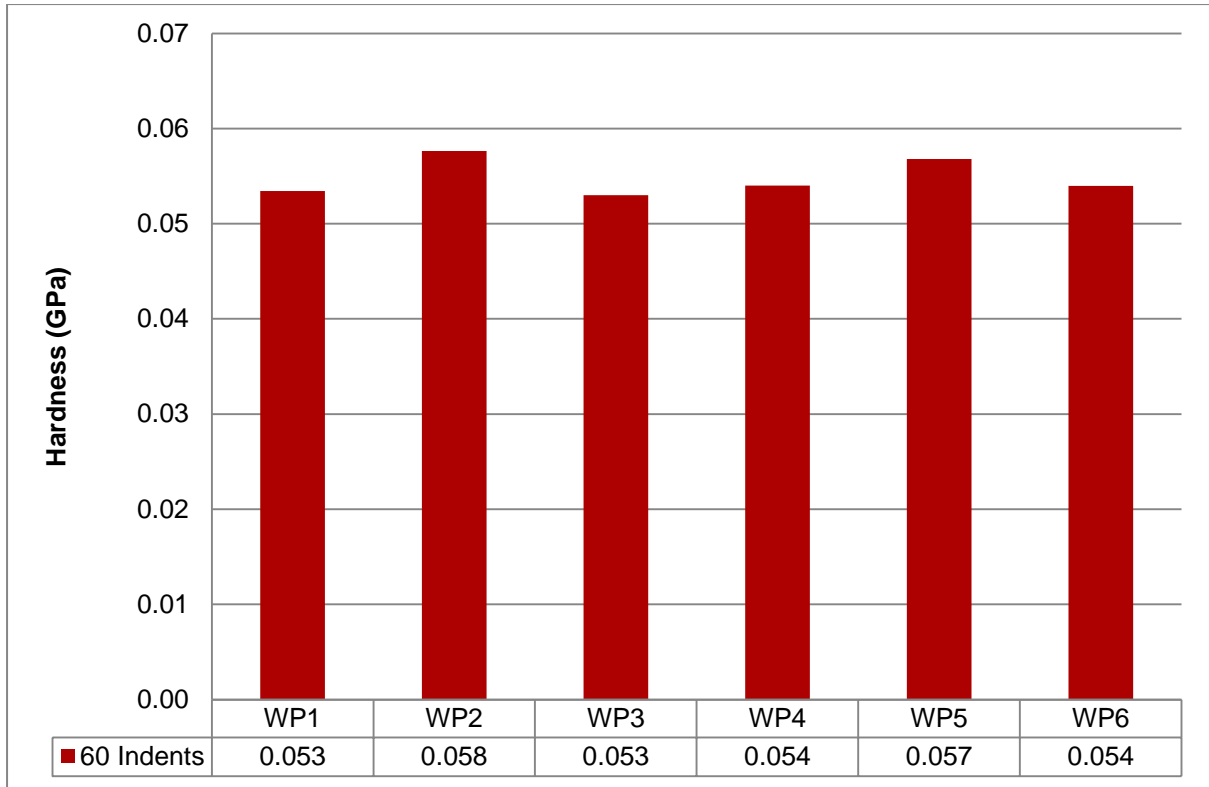
Figure 6-12 Plot of averaged hardness in the indented zones for each welding procedure for comparison

	WP1	WP2	WP3	WP4	WP5	WP6
■ 60 Indents	0.053	0.058	0.053	0.054	0.057	0.054
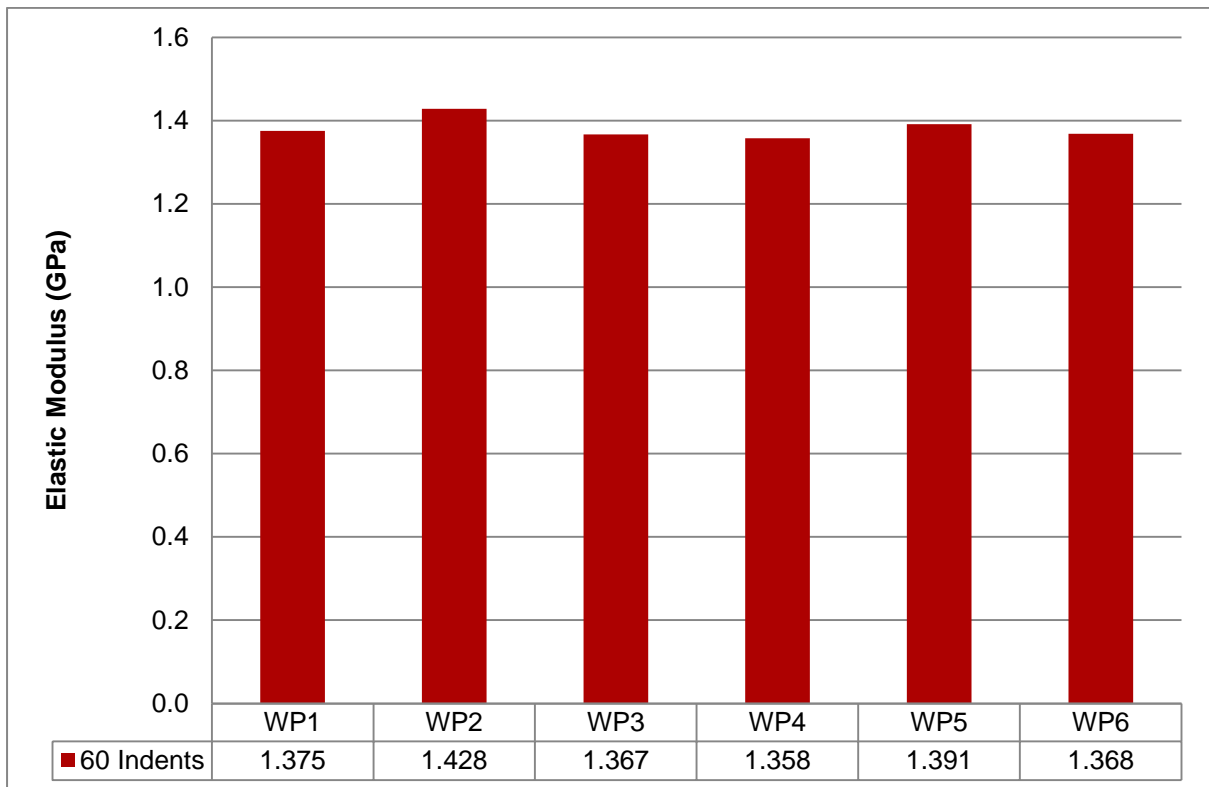
Figure 6-13 Plot of averaged elastic modulus in the indented zones for each welding procedure for comparison

	WP1	WP2	WP3	WP4	WP5	WP6
■ 60 Indents	1.375	1.428	1.367	1.358	1.391	1.368

151

	WP1	WP2	WP3	WP4	WP5	WP6
■ 60 Indents	11763	11367	11809	11726	11463	11721
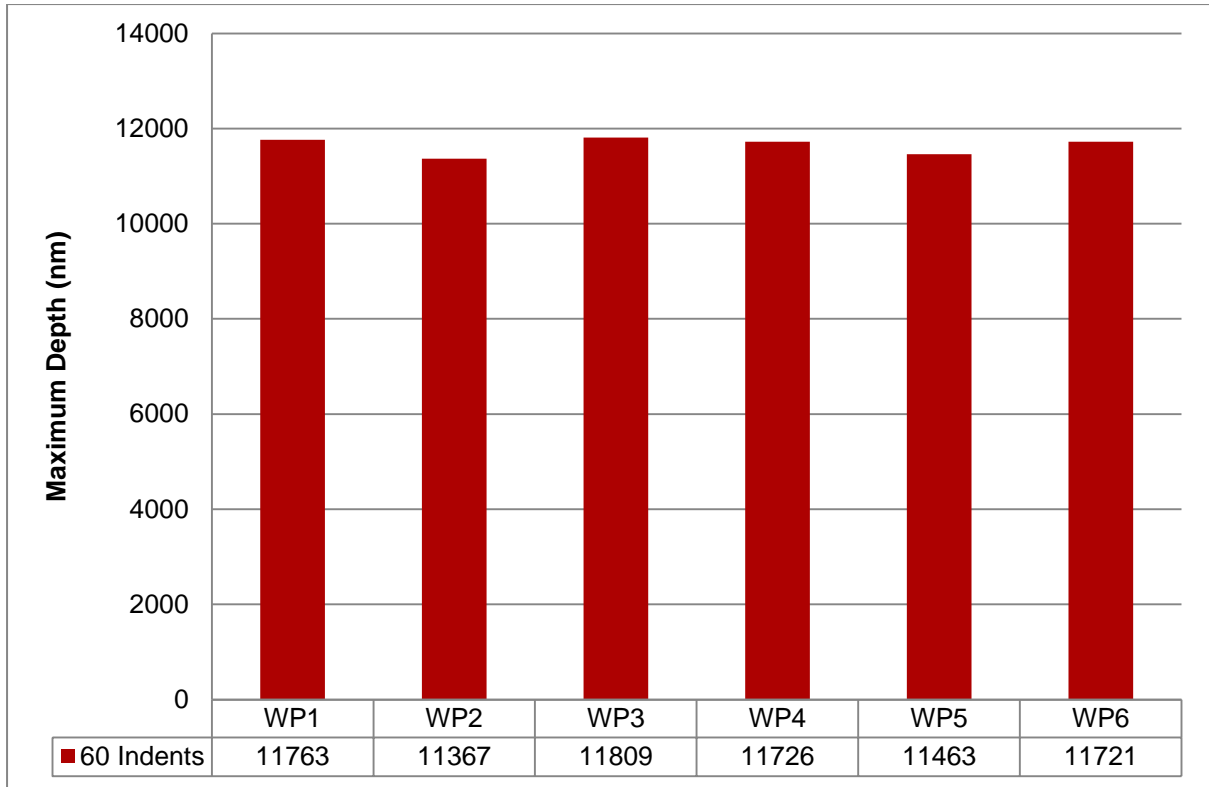
Figure 6-14 Plot of averaged total depth of indentation for each welding procedure for comparison

	WP1	WP2	WP3	WP4	WP5	WP6
■ 60 Indents	10706	10309	10750	10649	10385	10653
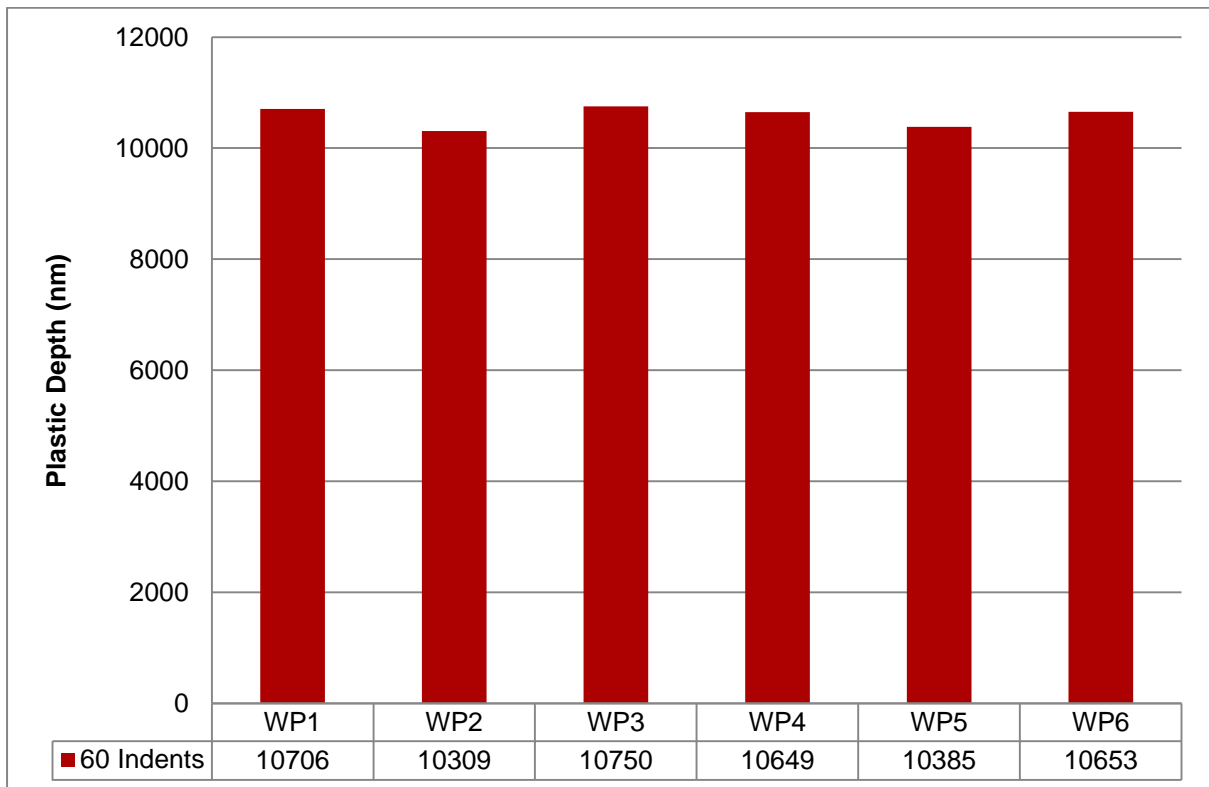
Figure 6-15 Plot of averaged plastic indentation depth for each welding procedure for comparison

152

60 Indents	1057	1057	1059	1077	1078	1068
	WP1	WP2	WP3	WP4	WP5	WP6
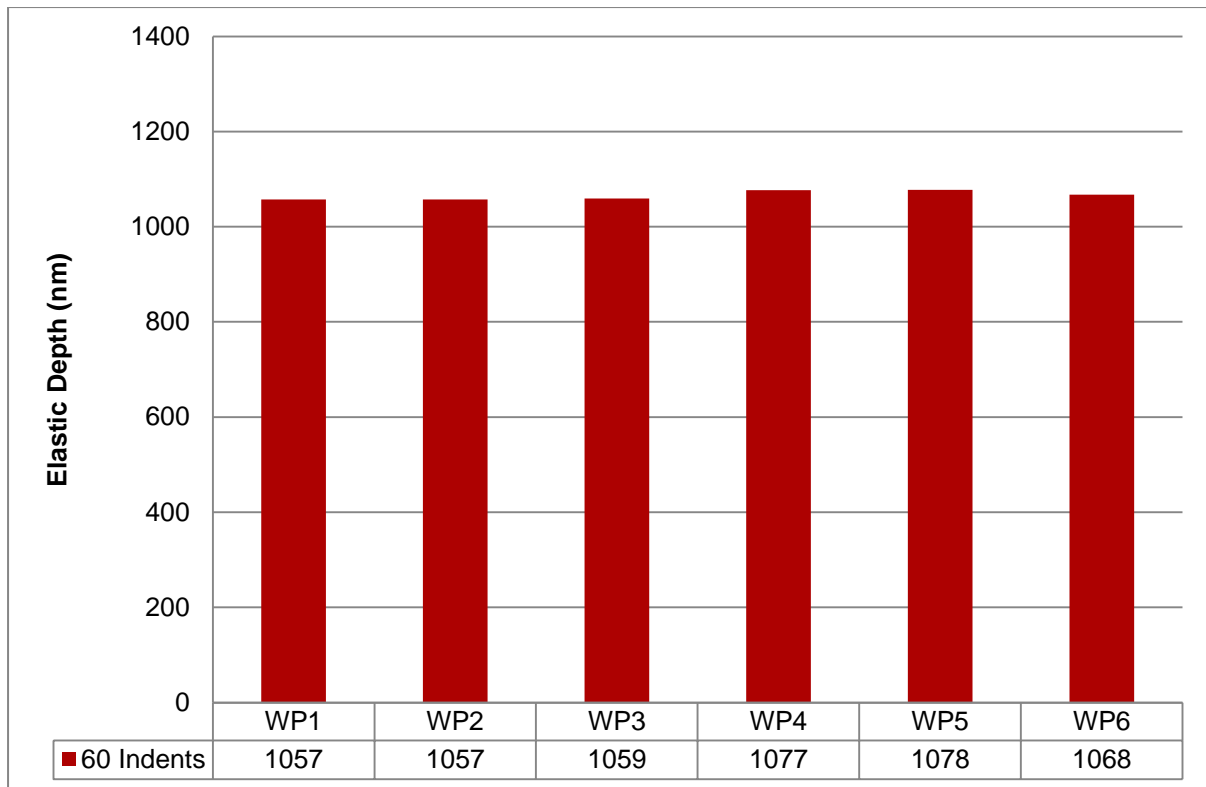
Figure 6-16 Plot of averaged elastic indentation depth for each welding procedure for comparison

WP2 and WP5 provided slightly higher values of hardness and elastic modulus than the other welding procedures. Both hardness and elastic modulus are inversely proportional to the maximum depth of indentation. All results show similar hardness to the parent material while practically matching the elastic modulus of the parent material as shown in Table 6-4. The welding process affects the maximum depth by 5.15% across all welding procedure. The welding process lowers the elastic depth by 9.26% and increase the plastic depth by 6.86%, hinting at lowered ductility of the weld region. The welding process has almost negligible impact on the elastic modulus but the hardness is reduced by 17.54% due to the valley forming between the two peaks as seen in Figures 6-1 to 6-7.

Table 6-4 Data listed according to nanoindentation location for comparison against parent material, averaged across all welding procedures

Data	Hardness	Elastic Modulus	Maximum Depth	Plastic Depth	Elastic Depth
Unit	GPa	GPa	nm	nm	nm
Parent	0.058	1.380	11071	9896	1175
60 Indents	0.055	1.381	11641	10575	1066
% difference against parent material					
60 Indents	-17.54	0.09	5.15	6.86	-9.26

The elastic modulus reported by NI is 24% higher than the values reported by the pipe manufacturer; this is likely due to size effect of NI (Huang, et al., 2006) and due to different strain rates (Oyen & Cook, 2002) used by the pipe manufacturer. Further work is required to confirm the exact reason for the 24% increase in the elastic modulus reported by NI.

6.2.6 Summary

The nanoindentation technique has been shown to be able to particularly sensitive to the change in material properties across the weld region and improves upon the work of Lach, et al. (2013). Such sensitivity to material property changes can then be used to define the weld zones; that in turn can be used to differentiate between the welding procedures if not the quality of the weld. NI also shows that the MZ region surrounding the weld interface should behave in a similar manner to the parent material due to similar material properties if the welding is performed in accordance with the welding procedure and best practice.

6.3 DSC

6.3.1 Introduction

Differential scanning calorimetry (DSC) measures the amount of heat required to raise the temperature of a sample and a reference, as a function of temperature. It only requires small samples weighing in milligrams and therefore when DSC is used in combination with microtomy; it is possible to obtain local thermal history and crystallinity at resolution of 50 µm. The results of DSC were compared with the NI results for WP2 and WP6; from the results insights on the size of different weld features are drawn.

6.3.2 DSC parameters

The parameters used for the DSC cycle are listed in Table 6-5. The TA Instruments Q2000 DSC machine was calibrated according to manufacturer's guidelines using indium for temperature and heat flow (20-180 ^{0}C) before usage. The reported energy value of 293 J/g enthalpy for HDPE at 100% crystallinity (Joshi, et al., 2006) was used to calculate the crystallinity of each sample for comparison with other material properties. The nitrogen gas flow rate was set at 50 ml/min.

Table 6-5 The order of DSC cycle and their parameters

Cycle	Range	Rate/hold time
Heating	20-180 ^{0}C	10 ^{0}C/min
Isotherm	5 ^{0}C	min
Cooling	180-20 ^{0}C	20 ^{0}C/min

6.3.3 Initial trial

Initial DSC trials were conducted on material extracted from both the parent and the weld region to serve two purposes. The first purpose was to ensure that the DSC was sufficiently sensitive to determine the difference in crystallinity between the parent and the weld material. The second purpose of the trial was to develop appropriate DSC parameters and testing methodology. The heating and cooling rates were effectively doubled to the values given in Table 6-5, saving several minutes per specimen. The parent and the weld specimen weighed 2.46 mg and 2.22 mg, respectively. The trial was performed using Tzero® standard aluminium pans and lids. The pan and lid were weighed before the parent material was placed in and then weighed after sealing to accurately record the weight of the sealed specimen. The trial followed the cycle and parameters listed in Table 6-5.

The DSC heating plots for the parent pipe and the weld regions are shown in Figure 6-17. The onset of melting begins at 80 ºC as the shorter polymer chains and other low molecular weight molecules loosen. The melting is fully taking place from at 105 ºC and onwards until peaking at 127 ºC for parent and 129 ºC for weld samples.

Equation 6-1 was used crystallinity calculated for the parent material was 63.8% and for the weld material was 67.8%.

Equation 6-1

$$Crystallinity = \frac{Energy\ of\ the\ specimen}{Enthalpy\ of\ HDPE\ at\ 100\%\ Crystallinty}$$
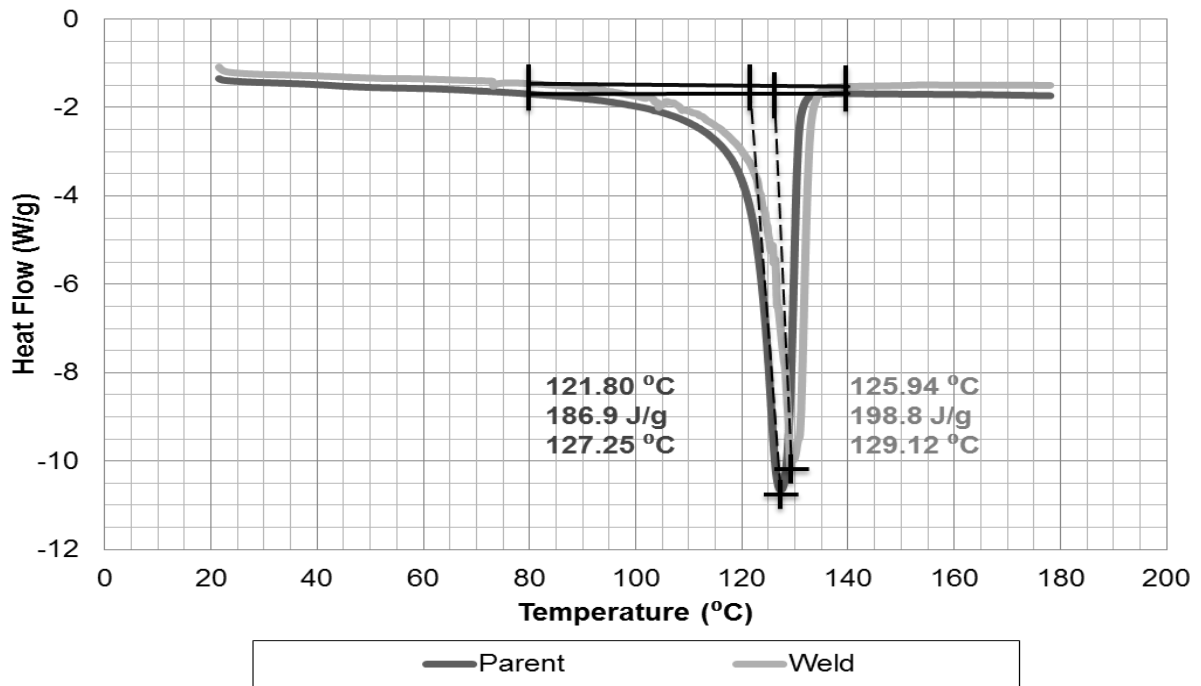
Figure 6-17 Temperature against heat flow plot of DSC for the parent and the weld regions during the heating scan (Shaheer, et al., 2016)

6.3.4 Methodology

The Figure 6-18 shows the steps of preparing the DSC sample prior to microtomy which is described in Figure 6-19. Although it was prohibitively expensive to test every 50 µm slice in this work, this method does allow for labelling and storage of every slice for testing in the future. A total of thirty slices per procedure were used for DSC testing for WP2 (European) and WP6 (US). The slices were distributed approximately in the following manner: six in the HAZ, twelve in the MZ, and twelve in the parent. The DSC specimens were cut from the microtomed slices and placed in Tzero® standard aluminium pans. The pans were sealed using Tzero® standard aluminium lid using a sample press.
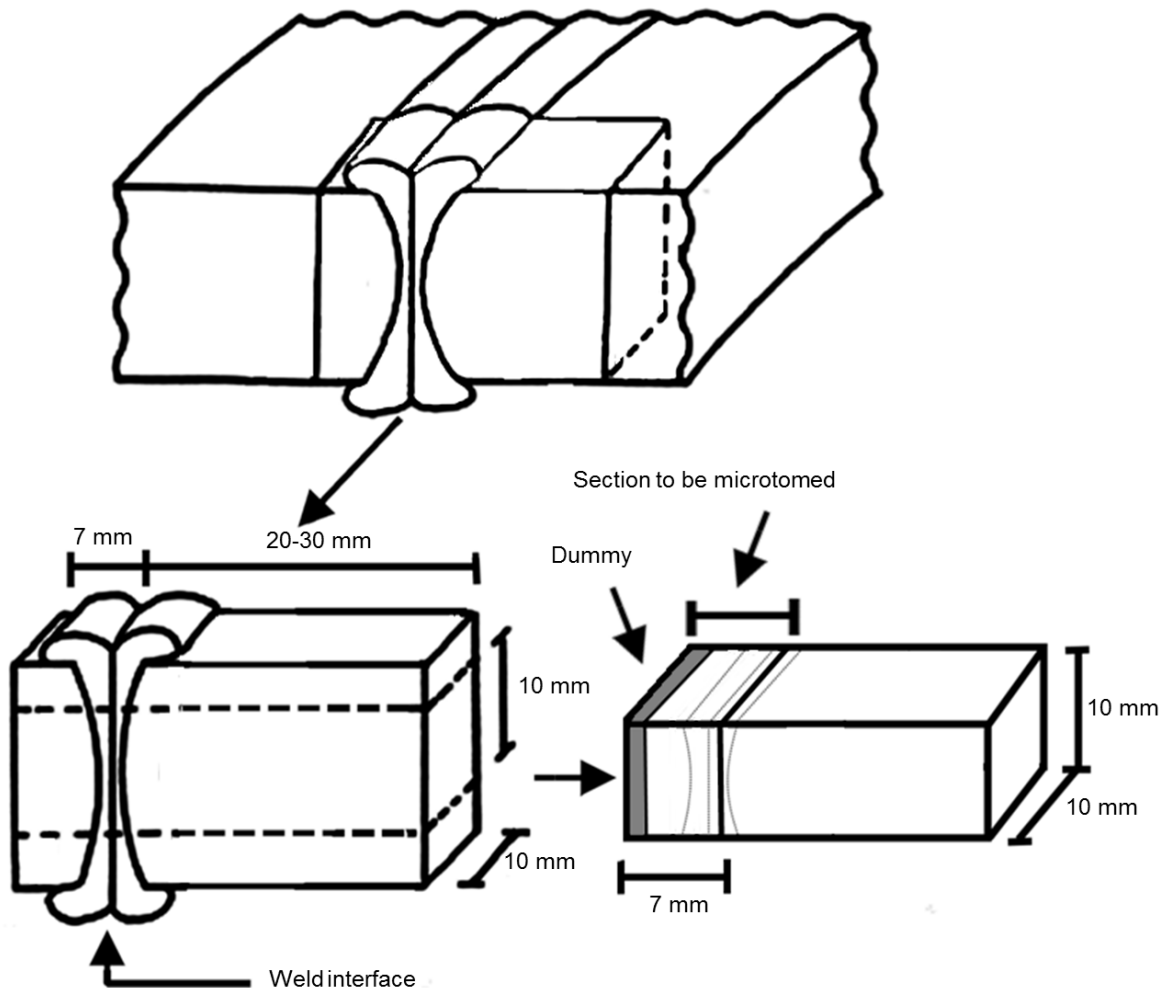
Figure 6-18 Sequence of positioning and extraction of DSC sample prior to microtomy from left half of the weld
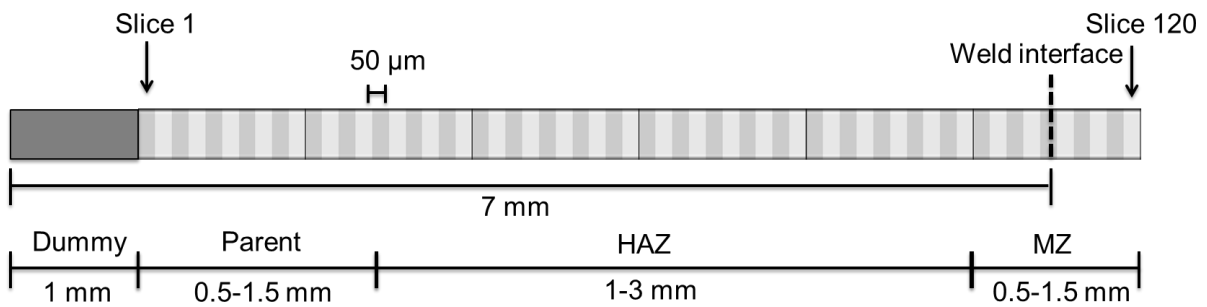
Figure 6-19 DSC specimen positioning and labelling diagram for use during microtomy, the different regions are considered as guidelines

After the completion of the DSC trials, six additional slices for WP2 and nine additional slices for WP6 were tested in the regions of interests. The additional slices were tested to rule out unexpected results due to accidental contamination or improper sealing of the lid to the pan during the preparation process. Contaminated specimen may report peaks shifted from the norm and leaky containers may

157

contaminate the DSC cell which may affect the results of upcoming specimens. The average specimen weight was 1.62 mg with a standard deviation of 0.39 mg.

6.3.5 Results and Discussion

The purpose of the DSC technique is to obtain the enthalpy of crystallisation or the energy required to transition the solid to liquid, for each microtomed slice. The value is calculated by integrating the heat flow from 80 ºC to 140 ºC. By dividing the result by the enthalpy of crystallisation for HDPE at 100% crystallinity (this quantity is also known as the specific heat of fusion) the degree of crystallinity is obtained for the microtomed slice, as described in Section 3.7.2.

Crystalline regions require more energy than amorphous regions to melt when a material is transitioning from solid to liquid. This also hold true in reverse for HDPE where the liquid phase is cooling into solid phase, the cooling rate dictates the size of crystalline regions and the degree of crystallisation.

The enthalpy of crystallisation for the microtomed slices from the DSC results are presented with the hardness obtained from the NI experiments to allow comparison of the position of the weld regions for WP2 in Figure 6-20 and for WP6 in Figure 6-21. Due to the cost of the DSC, it was only possible to test two out of the six welding procedures and only 30-40 microtomed slices out of the total numbers of slices microtomed. Therefore WP2 and WP6 were selected to represent the European and US, respectively based on fusion pressure. The weld features of WP1 and WP2 are almost identical and likewise for WP4-6. The DSC results have been translated on the horizontal axis to match the weld interface position with the NI results and excess points from the DSC results have been truncated.
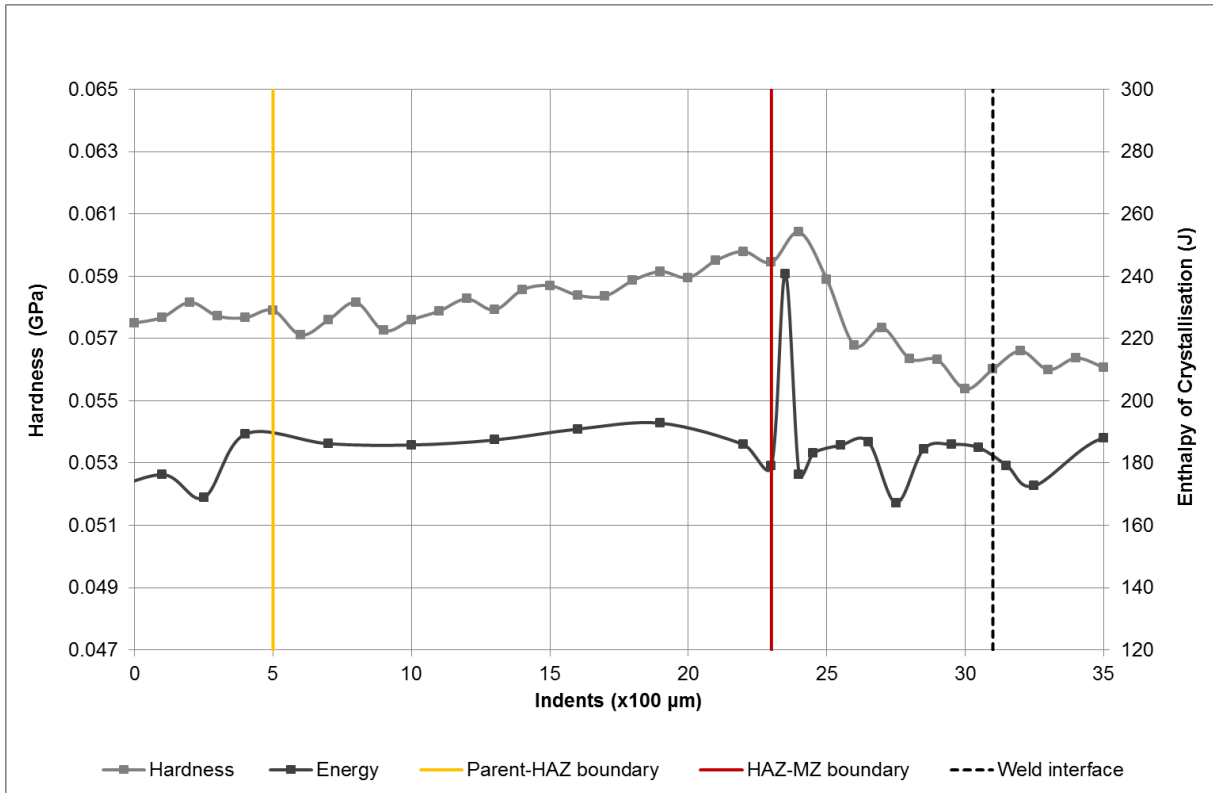
Figure 6-20 Comparison of enthalpy of crystallisation (Energy) from DSC and NI hardness across the weld for WP2
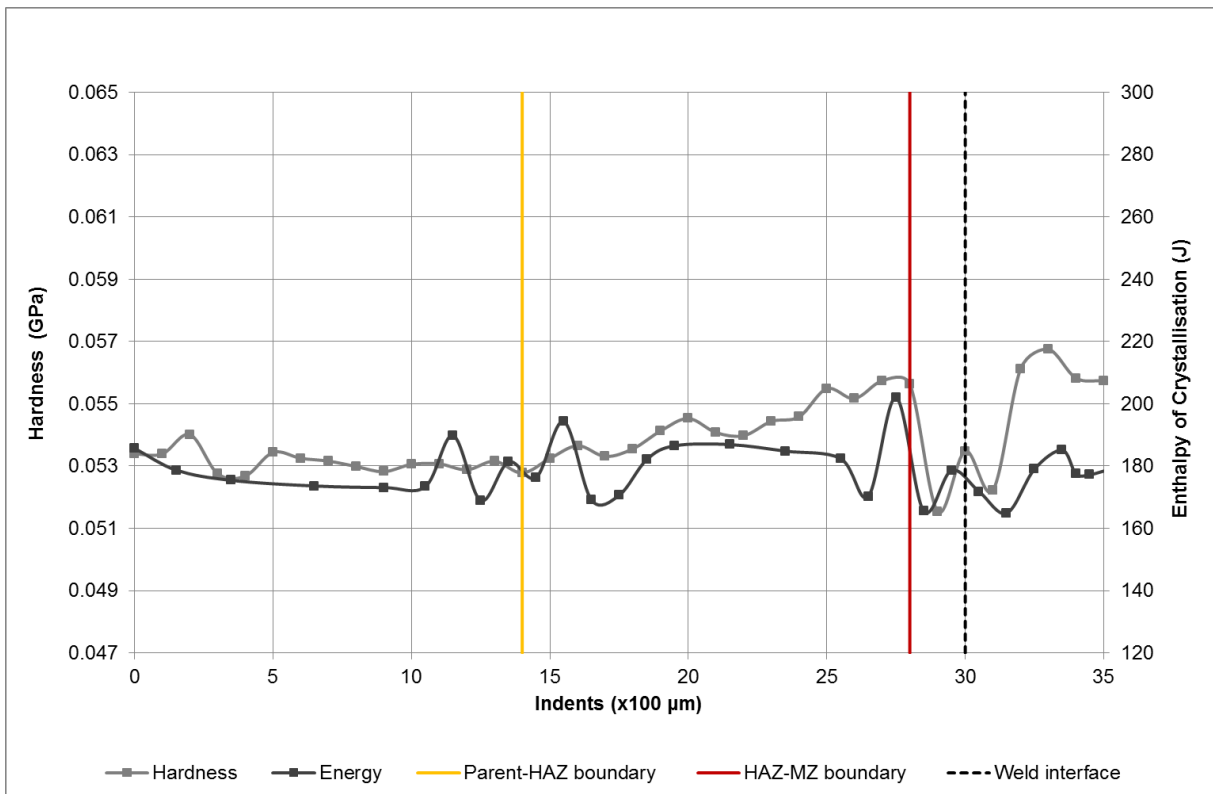
Figure 6-21 Comparison of enthalpy of crystallisation (Energy) from DSC and NI hardness across the weld for WP6

159

Apart from some exceptional points of fluctuation (e.g. between the 1st and 5th indents for WP2 in Figure 6-20 and between 11th and 17th indents for WP6 in Figure 6-21, the DSC results follow closely the pattern shown by the NI hardness from the parent material up to the weld interface for WP2 (Figure 6-20) and WP6 (Figure 6-21) and thus revealing the correlation of degree of crystallisation to the hardness in both welds. The crystalline regions are harder than amorphous regions. The hardness of the melt zone matches the hardness of the parent material. However in the HAZ region, the degree of crystallinity increases due to additional heat imparted from the MZ which has an annealing effect on the crystalline regions.

It is possible using DSC and NI plots to determine boundaries of zones (MZ and the HAZ) and estimate their width. For WP2, in Figure 6-20, the weld interface is located at 31st indent and the boundary of the HAZ-MZ boundary is indicated by the peak at 23rd indent. Therefore, from the DSC results the width of the MZ for WP2 can be estimated to be no larger than 1600 µm. Lastly, the parent-HAZ boundary is expected no earlier than 5th indent based on the NI results. For WP6 in Figure 6-21, the weld interface is located at 30th indent and the MZ-HAZ boundary can be identified at 28th indent and the parent-HAZ boundary at 14th indent. The MZ is contained between 28th and 33rd indents from the DSC, reaching an estimated 400 µm in width. The MZ width is estimated for DSC as the height of the microtomed slice is at least 10 mm at the centre of the pipe wall; unlike NI results where the height of the indentation grid is only 300 µm at the centre of the pipe wall. Since the MZ widens as it approaches the pipe wall surfaces, it is expected that the microtomed slices which cover 10 mm out of approximately 17 mm wall thickness, are likely to report slightly wider MZ then the NI grid which is very thin and at the centre of the pipe wall. The HAZ is likely to be bounded based on NI results between the 5th and the 23rd indent for WP2, and the 14th and the 28th indent for WP6. These estimates of size features are summarised in Table 6-2.

In comparison with WP6, the MZ size for WP2 is almost doubled to tripled. This is likely due to the higher fusion pressure and heater plate temperature of WP6, forcing greater amount of material outwards in to the weld beads from the centre of the pipe wall which can be seen in the size of the weld beads for both welding procedures (see Table D-1 in Appendix D).

Table 6-6 Estimated boundaries and width of zones based on DSC and NI results for WP2 (120 indents) and WP6 (60 indents)

Procedure	Source	Feature	Indents	Size (µm)
WP2	NI	Weld interface	31	
	DSC	MZ	23-31	<1600*
	NI	HAZ (single side)	5-23	1800$^\xi$
WP6	NI	Weld interface	30	
	DSC	MZ	28-33	<500
	NI	HAZ (single side)	14-28	1400$^\xi$

* Only half of the MZ is confirmed by the indents

ξ DSC is performed on only half the weld so actual value will be double

The anomalous fluctuation in the DSC results may be reduced by using more microtomed slices. Since each microtome slice is 50 µm thick, it is possible to achieve DSC data 50 µm apart as compared with 100 µm apart for the NI data. It would also be possible to produce multiple cuttings per microtomed slice, given the average weight of the cuttings to be only 1.62 mg (standard deviation of 0.39 mg) and weight of the microtomed slice is around 4.75 mg. Although these measures could potentially reduce fluctuation and give much higher spatial resolution of crystallinity, the DSC analysis would be highly time-consuming is as each test runs for approximately thirty to forty minutes. Due to this reason, it was uneconomical to perform higher resolution DSC for WP2 and WP6, or for every welding procedure.

Initially a total of 30 slices for WP2 and 29 slices for WP6 were tested. In order to ensure the cause of fluctuations was not due to slices being contaminated, additional 6 slices for WP2 and 10 slices for WP6 were then tested at the regions of fluctuation. The extra slices in the region reaffirmed the fluctuations reported for both welding procedures to not be due to contamination or deficiency in performance of the DSC experiment. The fluctuation could be possibly due to thermal history imparted in the pipe during the extrusion process. However, it will be extremely costly to verify through the use of DSC due to the number of slices required and so alternative methods that can calculate crystallinity without requiring testing of numerous 50 µm microtomed slices would be more appropriate.

6.3.6 Summary

The DSC technique is able to provide a detailed insight into the thermal history of each microtomed slice. The resolution of the technique is dependent on the thickness of the microtomed slices. The DSC was able to show the variation in the degree of crystallinity across the weld regions matches that of hardness values obtained from the NI results. The largest contribution towards the hardness property like several others properties comes from the crystalline regions or the degree of crystallinity. The DSC verifies the finding of the NI, specifically regarding the weld regions (MZ and HAZ) and their sizes.

6.4 FEA: Thermal Modelling

6.4.1 Introduction

Thermal modelling was conducted to predict how far heat travels into the pipe from the pipe end in contact with the heater plate. The pipe material is assumed to be homogenous and conduct heat uniformly. The FEA models for each welding procedure differed in heat soak time and heater plate temperature. The DSC results were used to validate the FEA models through comparison of the modelled MZ size against the optically measured MZ size. The models were then used to predict the size of the HAZ and compare against the HAZ size from the NI results. The HAZ is not optically visible and NI overestimates HAZ size due to the limitations of NI spatial resolution. Thermal FEA modelling has provided a new way to visualise the welding cycle for easy comparison between the different welding procedures.

6.4.2 Assumptions

The modelling only accounted for conductive heat transfer, which should have the largest contribution. The pressure was not modelled in order to reduce the complexity of the thermal model. Therefore, no bead was formed and the melt/heated material did not experience any deformation.

6.4.3 Model details

Thermal modelling of the heating cycle of the welding process was carried out using axisymmetric pipe geometry in Abaqus 6.13-1, shown in Figure 6-22. The temperature distribution at the end of the heating cycle along the centre of the pipe wall was calculated. The mesh density was 1 mm^2. Only half the pipe was modelled

as it was considered symmetrical about the weld interface. The mesh consisted of 8000 DCAX4 elements, each element being 1 mm^2 in size.
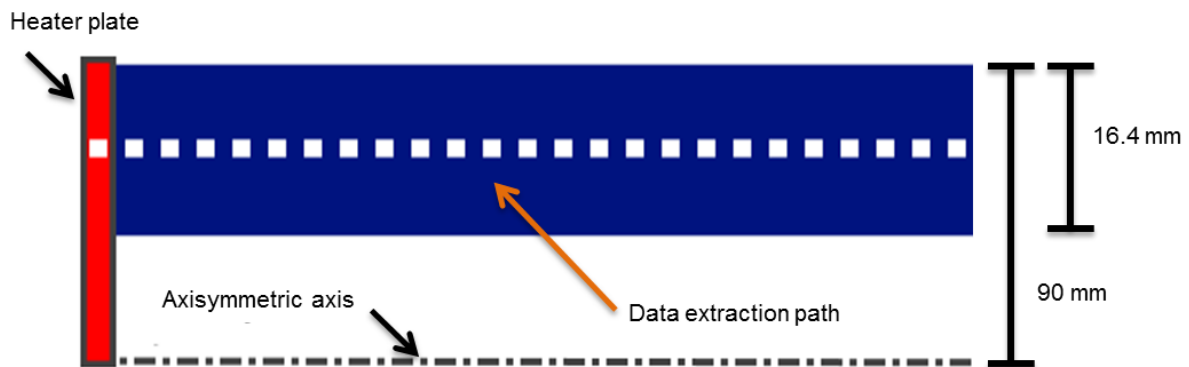
Figure 6-22 Schematic of the thermal model

6.4.4 FEA Validation

The thermal FEA models were validated using a combination of data from the DSC, the TLM, and the macrographs. The area of the deformed MZ was calculated using the polarised TLM image, which required the microtomed slices to be 20±5 µm with an area of 10 by 17 mm to include the full pipe wall. It was not possible to preserve the weld beads in the TLM image during microtomy. Macrographs were used to calculate the area of the weld beads formed by deformation of the MZ due to pressure. Both the TLM MZ area and the area of the weld beads from the macrographs were added to obtain an undeformed MZ area for each welding procedure. The melt temperature obtained from the DSC was used to mark the MZ boundary in the FEA models. The distance of the MZ boundary from the weld interface was multiplied by the pipe wall thickness to obtain undeformed MZ area from the FEA and compared with the previously measured undeformed MZ area.

6.4.5 Results and Discussion

In this section, heat transfer and temperature profile in the pipe near the hot plate is modelled using FEA in order to predict the amount of molten materials in the undeformed MZ. The amount of material in the MZ measured from the TLM images was added to the molten material is squeezed out into the weld beads measured from the macrographs, to calculate the total amount of molten material for each welding procedure. The measured molten material is correlated to the undeformed MZ from FEA model for each welding procedure. The correlation confirms the

163

accuracy of the thermal models which will be then used to predict the size of the HAZ to support the results of NI and DSC.

A typical thermal profile from the FEA analysis is shown in Figure 6-23 with a representation of the heater plate superimposed for illustrative purposes. The effect of the different welding procedures can be observed by extracting the values of temperature versus distance from the heater plate from the FEA models at the end of the heating stage as shown in Figure 6-24. The horizontal line marks the melting point, as obtained from the DSC curves from the parent pipe. A complete picture of the welding cycle is mapped in Figure 6-25 with colour-coded temperature ranges, which allows for an easier comparison of how far heat has travelled and how long it took to travel, for the different welding procedures.
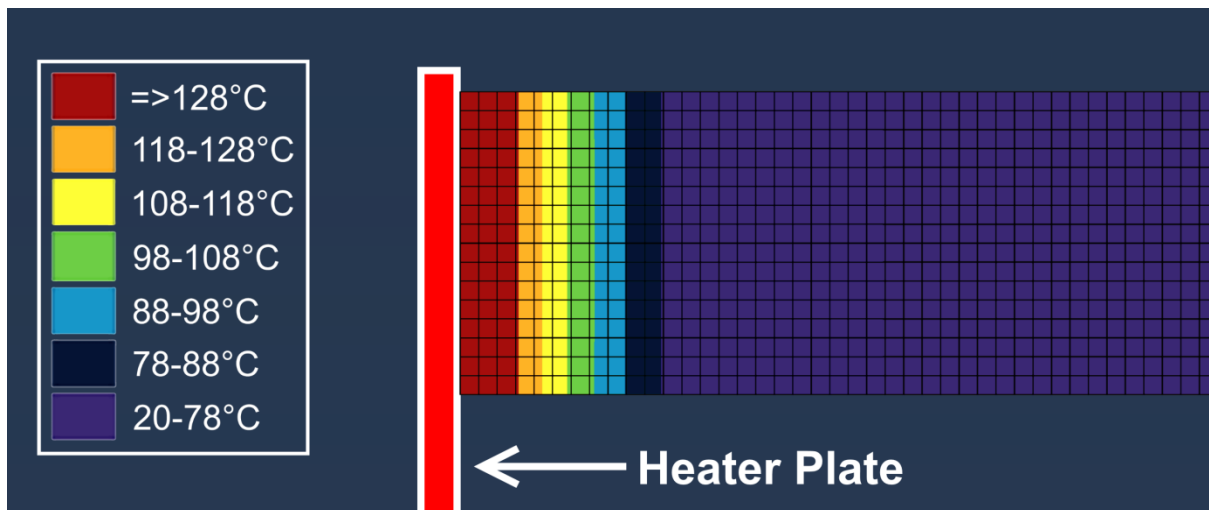
Figure 6-23 Thermal profile from the FEA model at the end of heating stage for WP1, each square is 1 mm^2 (Shaheer, et al., 2016)
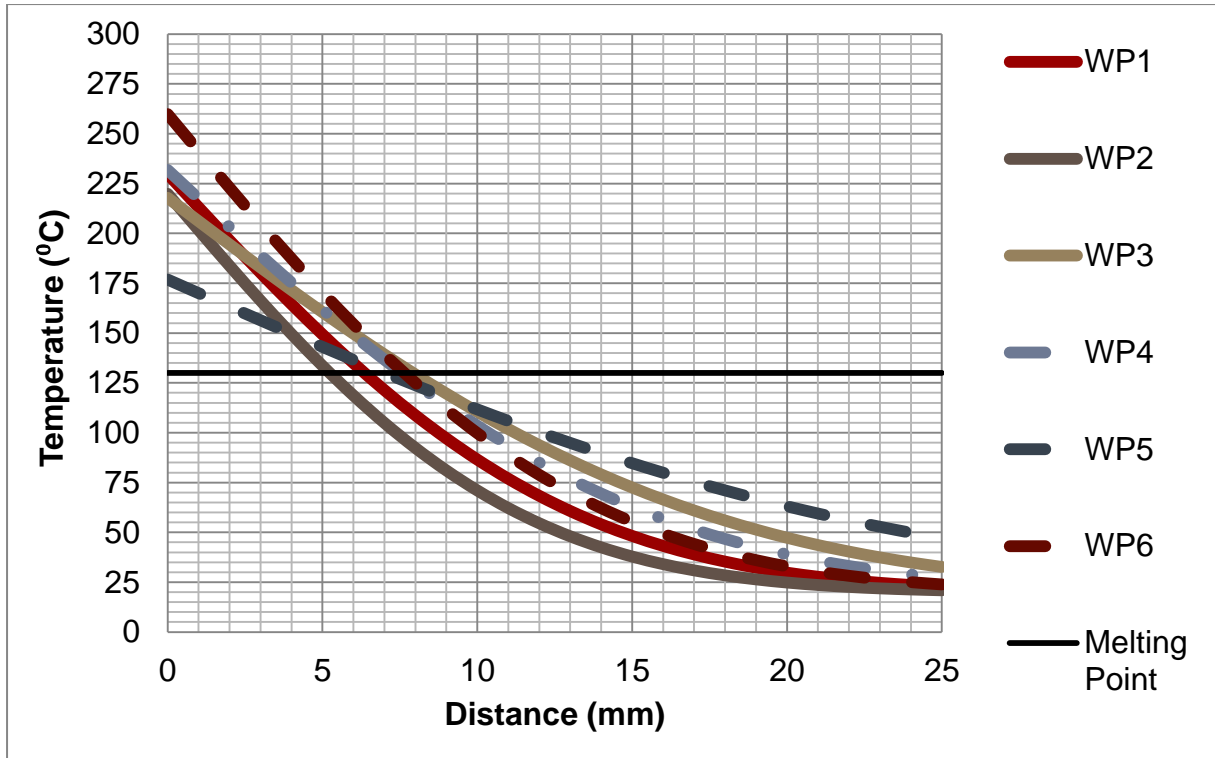
Figure 6-24 Temperature profile for each welding procedure at the end of the heating stage in comparison with the melting point of parent HDPE (Shaheer, et al., 2016)
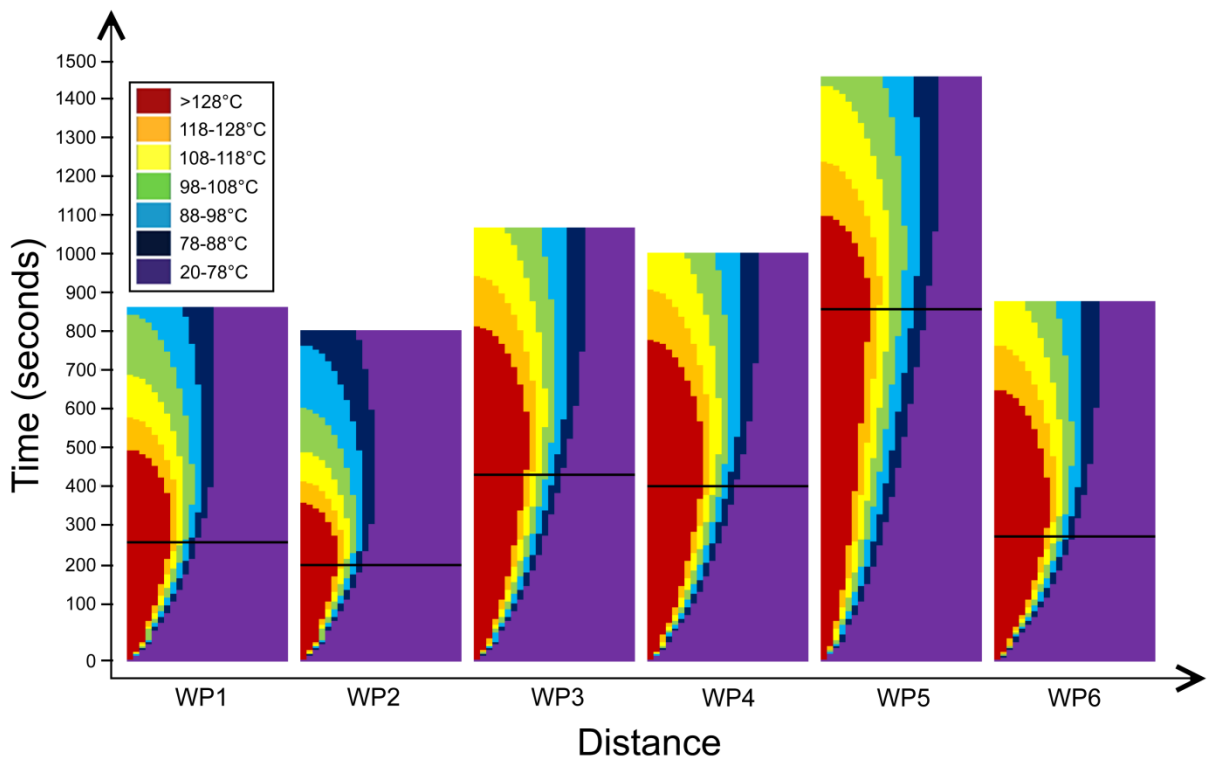
Figure 6-25 Temperature profiles for each procedure plotted in time-distance space. where each distance bar is 25 mm horizontally and the end of heating stage is marked by a black line for each procedure: WIS 4-32-08 (WP1), DVS 2207-1 (WP2), PPI TR-33 Ideal (WP3), PPI TR-33 Acceptable (WP4), High pressure low temperature (WP5), and High pressure high temperature (WP6) (Shaheer, et al., 2016)

165

Figure 6-25 also provides a new approach for visually comparing the welding cycle of different welding procedures. The maximum distances into the HDPE material that reached the melting point for each welding procedure were determined from Figure 6-25 and were doubled in order to determine the width of the total undeformed MZ (for both ends to be welded). These values are given in Table 6-7.

Table 6-7 Calculated width of undeformed MZ, W$_F$, from thermal FEA models for the different welding procedures (Shaheer, et al., 2016)

Welding Procedure	FEA Width at MZ (W$_F$), mm
WP1	12.1
WP2	10.0
WP3	15.8
WP4	15.9
WP5	14.7
WP6	14.3

6.5 Melt Zone

Although the FEA models did not account for deformation of the melt, the undeformed melt zone width (W$_F$ in Table 6-7) can be used to calculate the amount of molten material. Figure 6-26 shows a schematic of the MZ in the undeformed state and the cross sectional area of the MZ (Figure 6-18a) and the actual deformed state in the welded samples (Figure 6-18b).

$$MZ\ Area\ from\ FEA\ (A) = W_F \times t$$

$$Actual\ MZ\ Area = Area(1) + Area\,(2) + Area\,(3)$$
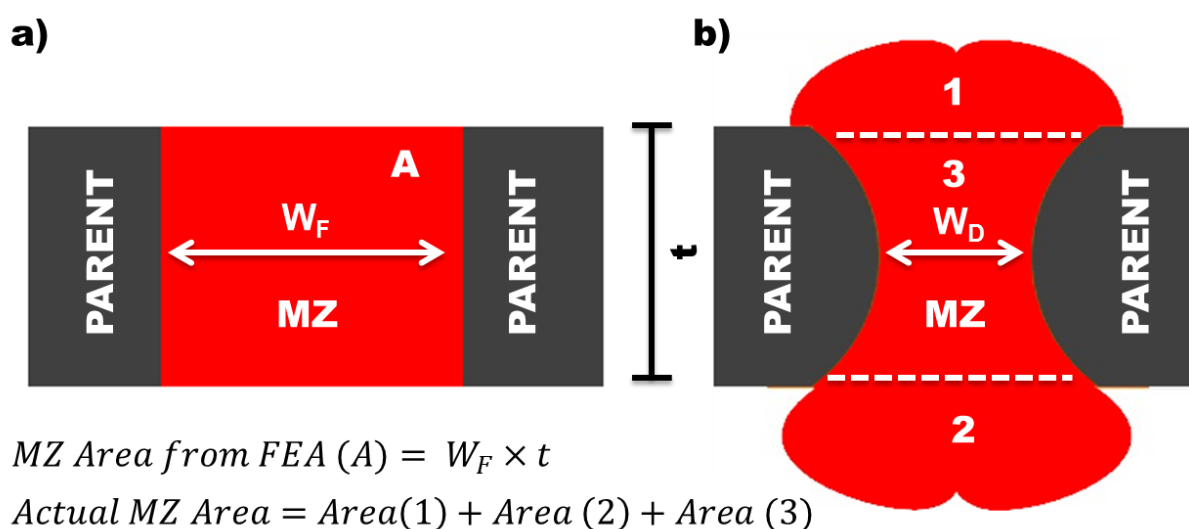
Figure 6-26 Cross section showing transition of the molten materials from MZ in: the undeformed state (a) to the deformed state (b) (Shaheer, et al., 2016)

The area of the FEA melt zone was calculated using W_F in Table 6-7 and the wall thickness t. The area of the melt zone from the welded samples was calculated by measuring the area of the weld beads from the macrographs and the area of the visible melt zone from the TLM images. The comparison of the two is shown in Table 6-8, which reveals a good correlation between the two MZ cross section areas. The small differences between the two areas stem from the limitations of the FEA models which does not model losses to the environment or deformation since the models are thermal only. The effect of deformation would be minimal as the pipe material is preserved into the weld beads and to be unaffected by compression due to force exerted by the welding machine applying fusing pressure in the cooling stage.

Table 6-8 comparison between the two MZ cross section areas in Figure 6-18 (Shaheer, et al., 2016)

Welding Procedure	Macrography (1)+(2), mm^2	TLM (3), mm^2	Total Measured Area (1)+(2)+(3), mm^2	FEA Area (A), mm^2
WP1	140	33	173	198
WP2	109	51	160	164
WP3	253	27	280	259
WP4	256	28	284	260
WP5	220	13	233	240
WP6	197	19	216	234

A comparison of the deformed melt zone widths (W_D) determined from TLM and NI is given in Table 6-9 which shows a reasonable correlation between the two different methods. Although this could be improved by increasing the spatial resolution of NI results as currently it overestimate the MZ width. The MZ expands outwards towards the pipe surfaces, similar to manner shown in Figure 6-26 in the deformed state.

Table 6-9 Comparison of MZ widths as determined from TLM and NI for the different welding procedures (Shaheer, et al., 2016)

Welding Procedure	Melt Zone Width (W_D), mm	
	TLM	NI
WP1	1.15	1.40
WP2	1.04	1.50
WP3	0.45	0.60
WP4	0.43	0.50
WP5	0.40	0.60
WP6	0.43	0.40

6.6 Heat Affected Zone

Despite not being observed optically, the existence of the HAZ, where the mechanical properties of the material have been changed due to the annealing below the melting point, was indicated by the nanoindentation results. Figure 6-27 illustrates the location of the HAZ surrounding the MZ and defines the method for calculating the undeformed HAZ width in a similar manner to the undeformed MZ width in Section 6.5.
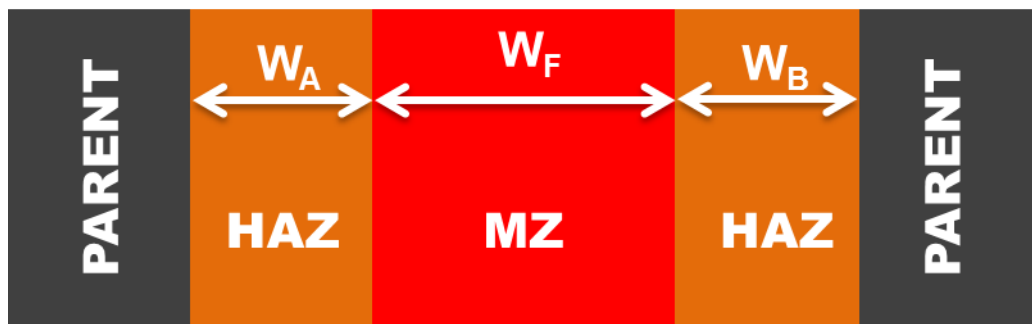
$$HAZ\ Width = W_A + W_B$$

Figure 6-27 Illustration of the HAZ width in an undeformed state (Shaheer, et al., 2016)

The process of annealing functions by allowing the polymer chains to form part of the existing crystalline regions and promote their growth. Since annealing is a function of both temperature and time, therefore, it requires the material temperature above 80 ºC but below 128 ºC for a sufficient length of time in order to have an effect on the material properties. The annealing of the material in the HAZ continues until the MZ has dissipated sufficient thermal energy into the surrounding regions below the melting temperature (around 128 ºC), as the surrounding region above the melting temperature would form part of the MZ. By the end of the heating phase at which point the MZ acts as a reservoir of heat at a temperature of at least 128 ºC and continues to supply thermal energy into the HAZ. Hence the twin-peaks of hardness and elastic modulus are located directly at the HAZ-MZ boundary as seen in Section 6.2. The parent-HAZ boundary temperature would therefore be sufficiently above 80 ºC to allow sufficient time for annealing to take place before the material cools. The material in the HAZ region cools by transferring heat into the parent material and the environment; the material properties forming a slope from the peak at the HAZ-MZ boundary to the level of parent material at the parent-HAZ boundary.

It was seen in Section 6.3.3 that the melting process is not immediate or linear; instead the reduction in heat flow at the weld accelerates at 105 ºC for the weld region in the DSC trial. It was also found that the temperature of 105 ºC at the parent-HAZ boundary provided the best correlation between the HAZ widths reported by nanoindentation results and the thermal FEA models, consistent across all welding procedures. Lower temperature values (below 105 ºC) underestimated and higher temperature values (above 105 ºC) overestimated the size of the HAZ and provided increasing poor correlation the further temperature was from 105 ºC. Table 6-10 shows a comparison of HAZ width as determined from the NI results and from the thermal FEA models.

Table 6-10 HAZ widths listed by technique and welding procedure (Shaheer, et al., 2016)

Welding Procedure	Heat Affected Zone Width, mm	
	NI	From FEA*
WP1	3.60	2.96
WP2	3.50	1.98
WP3	4.80	4.82
WP4	4.60	4.38
WP5	3.80	7.49
WP6	2.80	3.46
* The temperature of the parent-HAZ boundary set at 105^{0}C during welding		

The differences between thermal FEA models and NI results for the HAZ width are probably due to lack of heat loss in the modelling and coarse spatial resolution in the NI results. WP2 has the smallest value of HAZ width from the thermal FEA model. This is probably due to WP2 having a 60 second shorter heat soak time and 10 ºC lower heater plate temperature than WP1; these differences produce a smaller MZ width size and less overall heat flux leading to a smaller HAZ width. WP5 has the largest value of HAZ width from the thermal FEA model; this is due to WP5 having the longest contact time of the pipe against the heater plate.

6.7 Other techniques assessed

Dynamic mechanical analysis (DMA), Fourier transform infrared spectroscopy (FTIR), and X-ray diffraction (XRD) were also used to study the weld features but

they were deemed unsuitable without significant investment in their application after each of their initial trials.

6.7.1 DMA

DMA analyses the viscoelastic properties of materials which consist of the combined properties of elastic solids and Newtonian fluids. Stress is proportional to strain for small deformations in elastic solid, therefore stress is considered independent of the strain rate. For Newtonian fluids, the viscous stresses due to flow are linearly dependent on the local strain rate. DMA applies a sinusoidal force and measures the resultant displacement in the material. For both cases the stress is proportional to strain. Polymers like HDPE which exhibit semi-crystalline structure have properties which show some phase lag between stress and strain during a DMA test. The DMA was used to obtain the complex modulus of one parent material and one weld specimen. A single cantilever test was used, shown in Figure 6-28. The primary issue with DMA was the weld region under tested made constituted approximately 5% of the specimen length. Therefore, it would be difficult to ascertain differences in the results are due to the welding procedures.
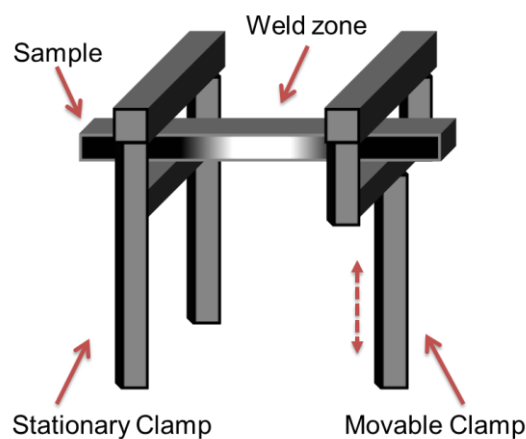
Figure 6-28 DMA specimen geometry

6.7.2 FTIR

A brief trial of FTIR was conducted at Brunel. FTIR functions due to absorption of some frequencies (wavenumbers) and transmission of others, depending on the different bonds under infrared radiation. Crystalline and amorphous regions absorb different infrared frequencies. These characteristics frequencies can be used to determine the crystallinity and with aide of a polariser the orientation of crystalline regions. The FTIR results were extremely noisy across the spectrum as seen in

Figure 6-29 and there was insignificant difference between the spectra for the MZ and the parent material. The infrared microscope and the polariser attachments were not available, otherwise it would have possible to reduce the size of scan area to 50 µm^2 and improve the signal-to-noise ratio via the polariser by blocking frequencies given off by additives, dye pigments, and stabilisers (Stevens, 1990).
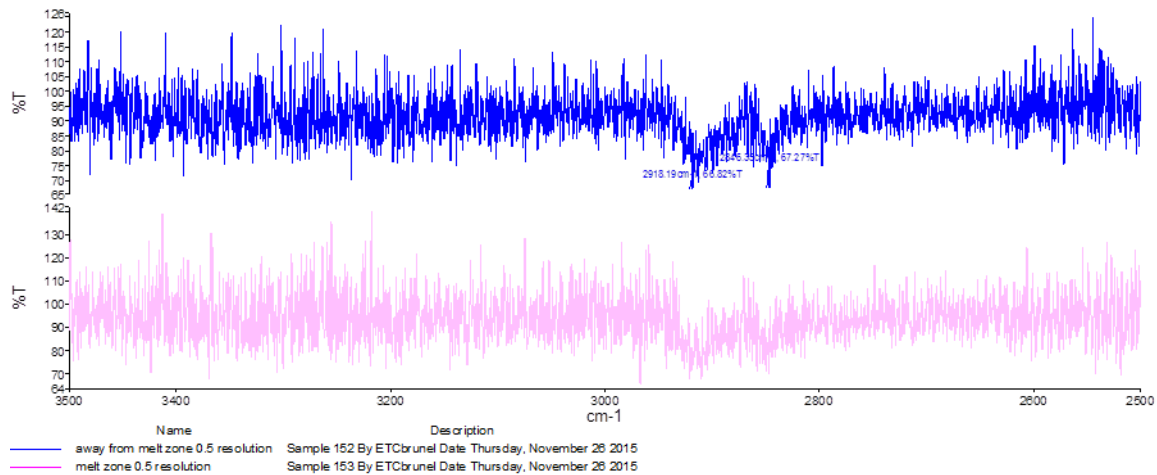
Figure 6-29 FTIR results chart for the parent material and the melt zone

6.7.3 XRD

XRD was used to measure the crystallinity in different parts of the weld; unfortunately the technique was limited by the focusing equipment which could not reduce the width of the scan area below 1 mm. The crystallinity of the specimen is calculated by diffracting the X-rays off the specimen. A ratio of scattering of crystalline to total scattering of crystalline and amorphous regions gives the percentage crystallinity of the specimen. Figure 6-30 shows the positions and Figure 6-31 shows the XRD scattering for the parent, the weld, and the weld bead. A baseline scattering due to background sources has to be removed before the calculation for crystallinity using appropriate curve fitting techniques. The Bruker D8 Advance XRD machine at TWI reported the following crystallinity values after manual curve fitting using EVA software between 10^0 to 50^0 reflection angles: 75.2% for the parent; 78.3% for the weld; and 76.9% for the weld bead. The manual curve fitting introduces subjectivity in the calculation of crystallinity and the poor spatial resolution makes XRD unsuitable for analysing the weld at microscales without the appropriate focusing equipment.
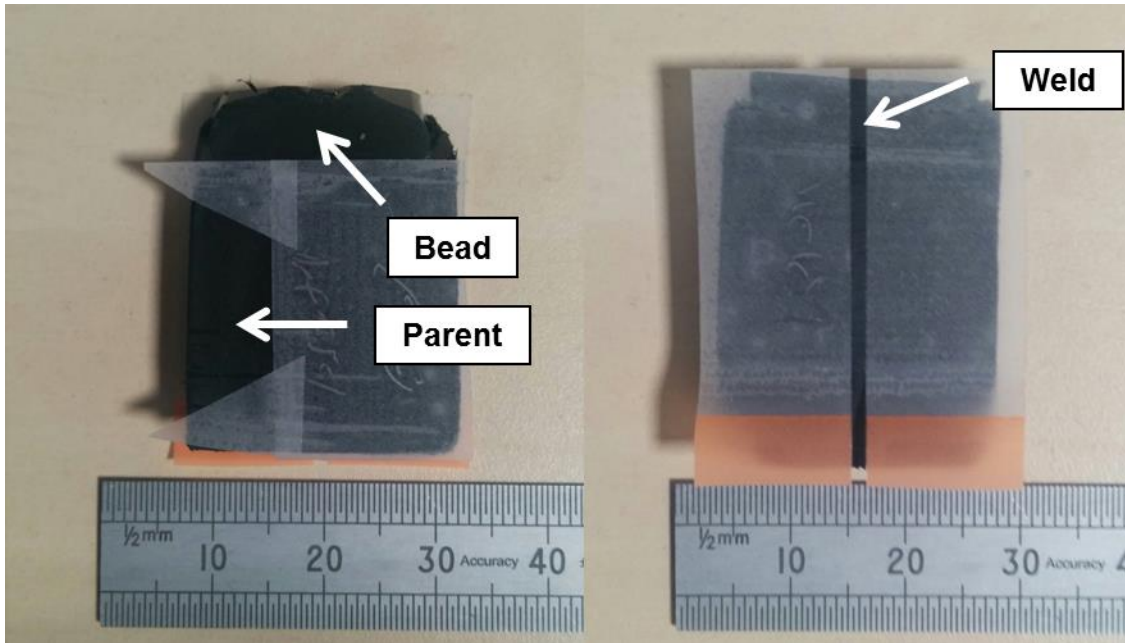
Figure 6-30 The parent, the weld and the weld bead positions of XRD crystallinity trials, the plastic material on top of the specimens shows the area covered during the XRD trial
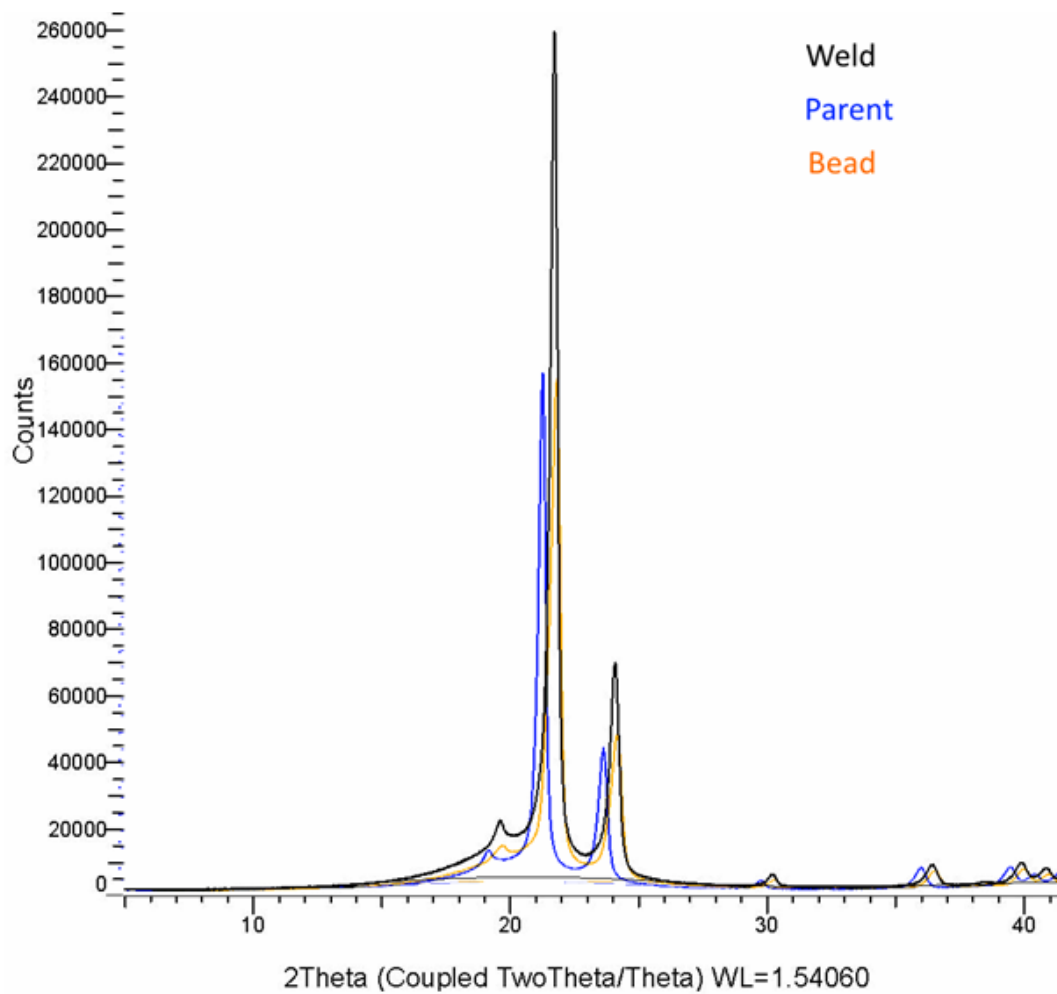
Figure 6-31 XRD scattering counts against scattering angle for the parent, the weld, and the weld bead

172

6.8 Summary

The nanoindentation technique has proven to be a valuable tool in characterising and mapping the variation in the material properties across butt fusion welds in HDPE pipe. The nanoindentation results show that butt fusion welds have a melt zone, where the material was melted during the welding operation and also have a heat affected zone, where the material was annealed, resulting in an increase in mechanical properties at the boundary of HAZ-MZ.

The DSC technique was used to verify the nanoindentation results by correlating degree of crystallinity against the reported changes in the material properties across the weld. DSC was able to confirm the size of the MZ but did not show a noticeable change in crystallinity in the HAZ. DSC also facilitated in determining the effect of annealing by providing a rich thermal history for each specimen.

A thermal FEA model has been used to suggest that the parent-HAZ boundary is located where the material temperature has reached a temperature around 105 ºC during the welding operation. The FEA models were verified using MZ and weld bead areas calculated from macrographs and TLM images. These models were then used to calculate the width of parent-HAZ boundary and the boundary temperature. The temperature profiles derived from thermal models provide a fresh method for visually comparing the different welding procedures and to estimate the size of the weld regions. The accuracy of thermal models would have been greatly improved had they account for the deformation of the pipe wall against the heater plate in a manner similar in the works of Yoo, et al. (2017).

The size of the MZ is smallest at the centre of the pipe wall, and widens as it gets closer to the pipe surfaces as seen in Section 5.2.4. It is also possible that the HAZ expands in a similar manner but not necessarily the same extent as the MZ, as the parent-HAZ boundary is likely limited to a set distance from the MZ by the thermal conductivity of the material. Therefore, a new weld geometry can be proposed for the butt fusion joints in HDPE pipes, as illustrated in Figure 6-32. The geometry of the HAZ is based on the assumption that the heat transfer is only occurring in the horizontal direction along the pipe wall and the HAZ width remains constant from the MZ-HAZ boundary.
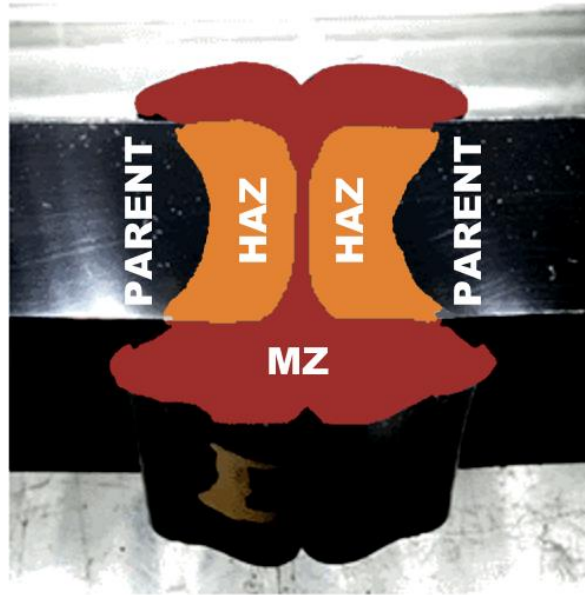
Figure 6-32 Proposed MZ and HAZ in a butt fusion welded HDPE pipe (Shaheer, et al., 2016)

7 Discussion

7.1 Introduction

Chapter 4-6 each concluded either with a chapter summary or individual section summaries. This Chapter highlights and discusses the key contributions from each Chapter and concludes by evaluating the objectives set out in Chapter 1.

7.2 Mechanical Testing

Three mechanical tests were conducted on the coupons cut from the welded pipes: the waisted tensile test, high speed tensile impact test; and the guided side bend test. The results of the tests were subjected to a statistical t-test to ensure that the test findings were sufficiently rigorous to be statistically significant rather than by chance alone. Table 7-1 provides for each welding procedures: the welding parameters; the energy input due to temperature and heat soak time; and the results for each mechanical test. It should be noted that only the waisted tensile test results are valid as all of the failure for high speed tensile impact tests occurred in the parent material and no failures occurred in the guided side bend test. The circumferential positions of the different test specimens around the pipe circumference did not have any statically significant effect on their test performance.

Table 7-1 Comparison of the welding parameter and the results from the mechanical tests

Welding Procedure	Units	WP1	WP2	WP3	WP4	WP5	WP6
Pressure	MPa	0.150	0.150	0.517	0.621	0.827	1.034
Temperature	^{0}C	230	220	218	232	177	260
Heat soak time	s	257	199	465	402	859	274
Energy input	kJ	24.0	20.5	30.4	30.3	30.9	27.8
Waisted	J	246	224	265	277	276	243
Tensile Impact	J	129	130	102	103	171	184
Guided Side Bend	N	310	291	295	305	306	324

7.2.1 Waisted tensile tests

All waisted tensile specimens failed at the weld in a ductile manner with the failure starting from the notches between the weld bead and the pipe wall; energy-to-break values were used to indicate the weld quality. WP4 and WP5 reported the highest

energy to break values implying the greatest weld strength of the six welding procedures. WP6 demonstrated the highest energy until the yield point due to longest elongation, showing to be the most elastic welding procedure. Previous work completed by Hinchcliff and Troughton (1998) using waisted tensile specimen reported energy to break values for increased pressure welding pressure similar to WP3 to be lower. The lowest values for reduced temperature welding procedure with similar temperature to WP5 than the standard condition, performed identical to WP1. Work completed by PE100+ Association reported for large diameter PE100 pipe (Beech, et al., 2008; Beech, et al., 2010; Beech, et al., 2012), the lowest values for 'single low pressure' condition identical to WP2 followed by 'single high pressure' condition identical to WP3. The highest values were reported by the 'dual low pressure' condition defined in WIS-32-08 and ISO 21307. The study published over three conference papers reported energy to break values corrected for aspect ratio to also comparison between different SDR ratios for the same pipe diameter (Wilson, 1995; Hill, et al., 2001).

Pre-yield energy almost mimics the increase in fusion pressure with the exception of WP5. This suggests that fusion pressure compresses the molten material and positively correlates with energy to break values. The heater plate temperature negatively correlates with energy to break, possibly due to higher temperature requiring less heat soak time. The heat soak time has a strong positive correlation with energy to break values as it affects, the heat input, the recrystallization, and annealing at the weld region. Thermal FEA modelling was carried for each welding procedure based on the heat soak time and the heater plate temperature. The result of the modelling allowed for the calculation of the energy input from the heater plate and power consumption for each welding procedure. The thermal modelling results were used to calculate the energy input into pipe material from the heater plate. Figure 7-1 shows a reasonable positive correlation between the energy input by the heater and the waisted tensile energy to break. There is likely an upper bound for the heater after which the HDPE material starts to degrade, reflecting poor energy to break performance as a result.
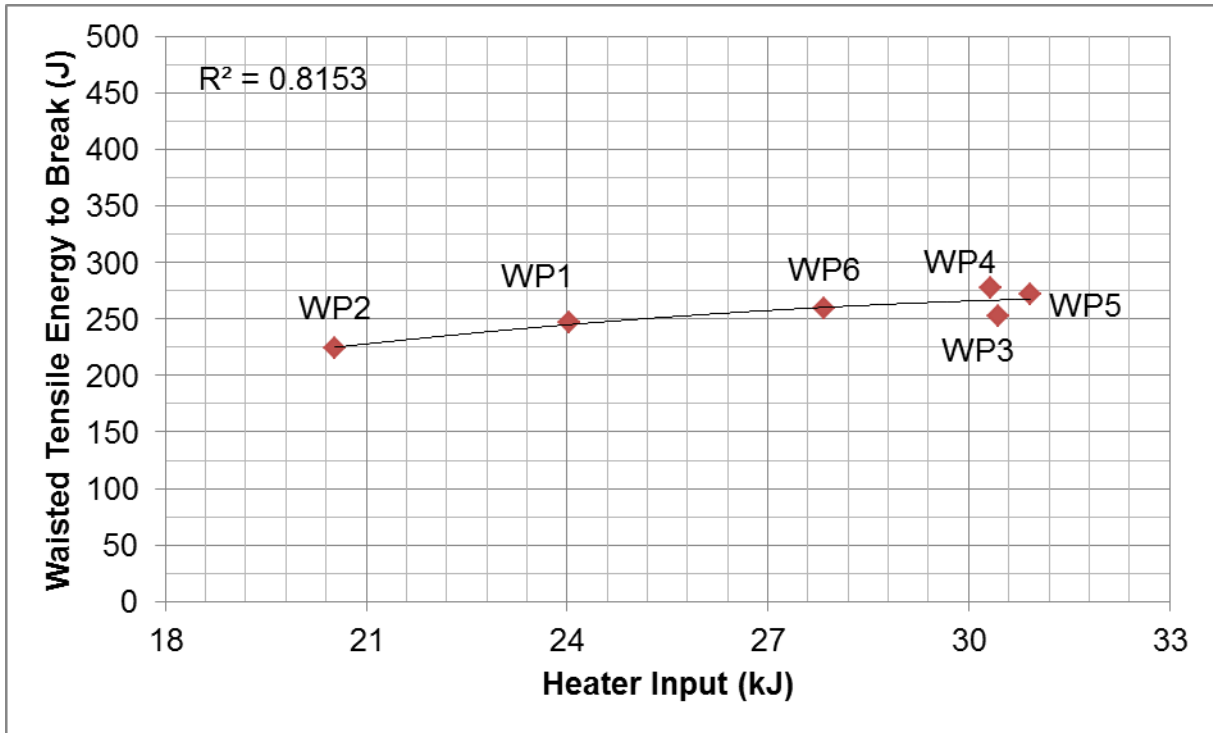
Figure 7-1 Comparison of energy from heater input against waisted tensile energy to break

The statistical t-test comparing the original and the additional specimens provided the probability of 0.001. The change of machining from manual for the original specimen to CNC controlled for the additional specimens was attributed to higher energy to break values seen in the latter specimens. Another reason is likely due to secondary crystallisation due to low T_g of HDPE, occurring at room temperature over the period of one year in storage, for the additional specimens before preparation (Halary, et al., 2011).

7.2.2 High speed tensile impact test

The high speed tensile impact test failed to generate failures at the weld with beads as all specimens failed in the parent material, several millimetres away from the weld region and thus they were unable to indicate the weld strength. It is possible the test may cause the specimen to fail at the weld if the weld beads are removed as they have a reinforcing effect in the weld region. In practise the removal of the weld bead is application dependent and not always possible in the case of the butt fusion welding of coiled pipes. Therefore, it is recommended that the geometry of test is altered to accommodate the weld beads and allow the failure to be guided towards the weld in the same manner as the waisted tensile test.

7.2.3 Guided side bending tests

The guided side bend specimens all passed the test criteria with no signs of cracking despite the bend angle being increased to 45° and no statistical difference has been shown between the welding procedures. The test standard (ASTM, 2016d) recommends the test for pipes with wall thickness greater than 25.4 mm yet allows for adaption for thinner pipes. It appears that HDPE pipes with wall thickness below 25.4 mm in this study are too ductile for this test to distinguish between the welding procedures and possibly also the HDPE material when machined down 6.4 mm test specimen thickness, likely even if it obtained from pipes thicker than 25.4 mm. The rest might yield result if the specimens are aged leading to brittle behaviour.

7.2.4 Whole pipe tensile creep rupture test

Unfortunately, it was not possible to complete the experiment part of the long-term WPTCR test in the allotted time due to unforeseen logistical and technical difficulties.

A FEA model representative of the WPTCR test was used to predict the effect on stress distribution from the grip of the end clamps and calculate the minimum pipe length required for the test. To avoid time consuming testing of excessively long welded pipes the FEA model was scripted using Python and the modelling proved to be incredibly valuable by reducing the need for extensive experiments.

7.3 Weld Bead Structure

Macrographs were used to identify the weld bead parameters. They were digitised for use in FEA modelling, and were subject to heat treatment to reveal the MZ. The microtomy technique was developed to produce large microtomed slices ranging from 20 ± 5 μm in thickness for TLM. Both high magnification optical microscopy and TLM were used to refine the key weld bead parameters of root length and notch height while concluding the difficulty in defining the fillet radius formed between the weld beads and the pipe wall. TLM was determined to be the most appropriate technique for measuring the MZ due to its resolution.

The basic weld bead parameters were derived from the macrographs and optical microscopy. Parametric modelling of the weld bead parameters was conducted in FEA and scripted to allow simulations of stress concentration on simplified bead geometry of over 50 models. Among the geometric parameters, the root length has

the highest effect on the stresses in the pipe wall. Therefore, welding procedures that reduce the size of root length determined from the welding pressure and the heat input, will benefit from the reduction in the pipe wall stress.

The realistic bead geometry was obtained from the digitised macrographs. The geometry was analysed for stress concentration and their location using FEA. The weld bead geometry contributes on average a 30% increase in the pipe wall stress due to stress concentration effect of the notches formed between the weld bead and the pipe wall. The shapes of weld beads from WP1 have the highest and WP4 have the lowest, stress values for stress concentration. The top outer bead position had the highest stress value followed by the bottom and the side weld bead position on the circumference but the difference was minimal at less than 1% proving that circumferential position does not have an impact on the stress concentration unless the welded pipe has been misaligned or the welding machine applied the fusion pressure unevenly.

The weld beads have a reinforcing effect at the weld in a manner similar to hoops on a barrel but the notches that form between the weld beads and the pipe wall due to the welding process create at least six sites of stress concentrations where cracks can initiate. In practise, cracks are more likely to initiate from the one of the three stress concentration location on the outer weld beads which are subject to greater amount of stress than the inner weld beads; depending on the loading conditions and shape of the weld beads.

7.4 Microstructure

The weld microstructure was explored using nanoindentation (NI) technique with a resolution of 100 µm. The NI technique currently provides a signature 'two peaks and a valley' pattern in the material properties across the weld interface for each welding procedure. For comparison with the NI results, microtomy was conducted to produce 50 µm thick slices for DSC for two welding procedures. The DSC technique confirms the variation of crystallinity in the weld and correlates well to the variation of hardness and elastic modulus values measured across the weld by the NI technique.

The thermal FEA models were validated using the MZ size and the weld bead geometry derived from the macrography and the TLM images. The models were

used to predict the size of the HAZ, which compares well with the size of HAZ obtained from NI for most welding procedures. The FEA models with the DSC and the NI results were used to conclude the parent-HAZ boundary temperature to be 105 ^{0}C. The heat map of pipe wall extracted from the FEA results provides a novel way of visualising the welding procedures for comparison and evaluation. The heat map summarises the amount of heat input in a welding cycle and how far the heat has travelled into the pipe material which can be used to approximate the size of the weld features.

The combined analytical techniques above lead to a proposal for new weld zone geometry consisting of a melt zone (MZ) next to the weld interface surrounded by the heat affect zone (HAZ) for butt fusion joints in HDPE pipes. The size of each zone can be quantified using NI, DSC, and TLM. The MZ widens to the size of root length as it meets the outer and inner pipe wall surfaces. Therefore, the purposed geometry also shows the HAZ to closely follow the shape of the MZ which acts as a heat reservoir for annealing the material in the HAZ. The data from NI and DSC techniques will be useful in modelling the behaviour of butt fusion welds in detail.

7.5 Evaluation of the objectives

This PhD work was aimed to address the current stratification of welding parameters specified in the standards currently being used worldwide. Existing best practice was be identified by running a range of short term coupon tests on the parameters specified in each of the popular standard welding procedures. By optimising the welding parameters, most favourable combination for structural integrity of a butt fusion weld can be specified. The objectives are evaluated below:

- Compare the short-term and long-term mechanical properties, and weld microstructure, of butt fusion joints in PE pipes made according to different national and international welding procedures.

Six welding procedures derived from different welding procedures were used to make the butt fusion joints. Only the short term properties were compared via mechanical testing as it was not possible to complete the WPTCR test.

- Determine the effect of the size, geometry and structure of the weld and weld beads on the mechanical properties of the joint.

The circumferential position had no impact on the weld performance. Higher fusion pressure led to smaller MZ width but larger weld beads. The heat soak time and temperature correspond to the MZ area. NI technique provided twin-peaks and valley distribution of hardness and elastic modulus in the MZ and showed annealing of the material in the HAZ towards the MZ. DSC supported the NI results and determined the increase in crystallinity to be the cause of higher values of the material properties in the weld region.

- Determine the optimal structure of a butt fusion weld in PE pipe to obtain maximum joint integrity.

Reduction in the size of the root length was seen to diminish the stresses in the pipe wall, achieved by low pressure welding procedures. The weld beads provided reinforcement to the pipe wall in similar manner to that of hoops on a barrel. However, the notches formed against the pipe wall act as stress concentrators. Removal of the outer weld bead may be beneficial as the stress in the pipe wall due to them is greater than that from the inner weld bead.

- Determine the most appropriate method for qualifying butt fusion welding procedures.

The most appropriate short term method for qualifying butt fusion welding procedures is the waisted tensile test with the improved geometry which mitigates the deformation in the loading pin holes. Alternatively heat map can be used to determine the amount of heat input which correlates well with the weld performance.

- Determine which of the current standard butt fusion welding procedures produces welds with the highest mechanical integrity.

WP4 and WP5 were the highest performing welding procedures in the waisted tensile test. WP4 which is derived from the ASTM F2620 (2013c) is recommended among the current standards based on the short term coupon tests.

8 Summary and Conclusion Remarks

8.1 Overview

Butt fusion welding is a popular joining process and a dominant one in the joining of pipelines. Different welding procedures and conditions are recommended in standards adopted worldwide in different industries by established standards organisations: ASTM F2620-12 (2012b) revised in 2013 (ASTM), DVS 2207-1 (2005) revised in 2015 (DVS), ISO 21307 (ISO, 2011a), TR-33 (PPI, 2012), and WIS 4-32-08 (2002) revised in 2016 (WIS). These standards were used to derive the following six welding procedures:

- WP1 WIS 4-32-08
- WP2 DVS 2207-1
- WP3 PPI TR-33 Ideal (based on ASTM F2620-12)
- WP4 PPI TR-33 Acceptable (based on ASTM F2620-12)
- WP5 High pressure low temperature
- WP6 High pressure high temperature

The welding procedures were studied in attempt to provide information for future harmonisation of these standards. A total of 48 pipes were welded following each welding procedure (eight per procedure) to provide test specimens for comparative studies in mechanical testing, weld bead structure, and weld microstructure to investigate the features of butt fusion welds. While it was not possible to show which welding procedure results in best weld properties, several deficiencies were highlighted in the recommended mechanical tests. A more systematic study in experiment design will help to optimise welding parameters for optimum weld quality. The process of joining and testing methods also require understanding of the fundamental butt fusion weld features such as: the geometry of the weld region; the weld microstructure; and optimisation of the test specimens and the mechanical test parameters. The main conclusions in each of the areas highlighted the key contributions of the investigations; except for optimisation of test specimens and the mechanical test parameters which are outside the scope of the study.

8.2 Key Contributions

- Provided that the butt fusion welding has been performed in accordance with the welding procedures as defined in the standards and best practise, the butt fusion welds will provide satisfactory performance despite the large differences in welding parameters seen in the published standards.

- Two out of the three mechanical tests failed to differentiate effectively between the different welding procedures. The waisted tensile test was the only effective test by causing the failure to occur in the weld region for every test specimen. The HDPE material is too ductile for the guided side bend test and the tensile impact test would only be effective if the weld beads are removed, due to the test specimen geometry.

- The FEA method was used to calculate the minimum length of pipe required for the WPTCR test, providing a table optimum length for extensive range of pipe geometric specification.

- The FEA modelling of the weld bead parameters identified the weld bead root length to be a key parameter and provided insight into the relationship of the weld bead geometries, the pipe wall stresses, and the location of the stress concentrations.

- Modelling of heat conduction led to new method of mapping the temperature profile that can be used to not only compare the welding procedures but also predict the size of undeformed melt zone and heat affected zone.

- A new weld zone geometry is proposed, that consist of the melt zone bounded by the heat affect zone identifiable at high resolution using the NI and the DSC techniques which provides useful information for modelling the behaviour of butt fusion welding.

- The results of the work conducted have formed part of six conferences and one journal paper. For each technique utilised, a procedure has been written to allow proper use of the said technique.

9 Recommendations

9.1 Introduction

The popularity of the butt fusion welding process is likely to increase in the future. There are several world nations that have migrated to use of polymer pipes and are coming to understanding the importance in fundamental research for long-term safe and reliable operation of welded pipelines. The recommendations for further work are to be continued in the following areas:

(i)   Optimisation of welding parameters for each material

(ii)   Development and comparison of mechanical tests

(iii)   Advances in FEA modelling from macro to micro scales

(iv)   Exploration of new applications of current and future analytical techniques

(v)   Dissemination of acquired knowledges, best practises, and democratisation of advance tools

9.2 Welding

There are several parameters that compromise a welding procedure. A design of experiment study using flat HDPE sheets would allow investigating a large range of such parameters with numerous test specimens inexpensively. The optimised values for the welding parameters can then be used to produce butt fusion welding pipes for closer to the real world applications using different pipe dimensions. Potentially also reducing the energy cost associated with the butt fusion welding in the process.

9.3 Mechanical Testing

A larger number of coupon tests should be investigated with a range of geometries. The results of high speed tensile impact tests may have been useful if the geometry forces the failure at the weld in a manner similar to the waisted tensile test. Although in this study it was investigated which test out of three mechanical tests proved the most useful, it would have been more beneficial to ask how each test itself can be improved.

9.3.1 WPTCR Test

It was not possible to conduct the WPTCR tests in the time frame of the PhD. The literature has shown the WPTCR test to be able to determine the long-term performance of butt fusion welds, more credibly than the hydrostatic pressure test. The long-term test results could then be correlated with the short-term coupon tests and microstructural studies to develop new areas such as shaping the weld bead shapes to reduce stress concentrations or using annealing techniques to improve mechanical properties around the weld, in the field of butt fusion joining technology.

9.4 Realistic Weld Bead Modelling

The weld bead models were limited to the elastic region. The next step would be to model using plastic material properties and the viscoelastic behaviour of the polymer. It is recommended to use a commercial software package such as 'PolyUMod' that has advanced developed material models for FE analysis. The TLM images can be used to accurately size the geometry of the MZ and techniques such as NI or DSC to size the HAZ in the geometry. In addition, a coupled thermal mechanical simulation using accurate material properties would be able to model the effects of both heat and pressure by deforming the pipe wall as the joining takes place. Similarly, the stress analysis of cracks and seams at the notches formed between the weld beads and the pipe wall should be conducted using crack modelling techniques such as the extended finite element method (XFEM) or the virtual crack closing technique (VCCT).

9.5 Weld Bead Microstructure

9.5.1 Nanoindentation

This work has only investigated the weld at the centre of the pipe wall. It would be useful to explore the change in the structure and material properties closer to the pipe wall surfaces. A longer indent matrix would allow hardness and elastic modulus across the weld interface, ensuring the larger HAZ and MZ regions are confidently included in the grid. A taller indentation matrix would ensure that any variation of properties in the pipe wall from the outer to the inner surface is observed.

The methodology of nanoindentation itself can be improved via reduction in surface roughness. The current grinding and polishing methodology allowed a surface

roughness of 2.5 µm. It would be possible to achieve finer surface roughness by utilising diamond pastes for polishing or developing chemical polishing methods. Polishing with diamond paste could produce a ¼ µm roughness, yet the technique would need to be improved to ensure the diamond particles do not embedded in the relatively soft polymer material. In the case of chemical polishing, care needs to be taken to ensure the crystallinity of the specimen remains unchanged. Some of the etchants are known to increase the crystallinity of the polymer by dissolving the amorphous regions at the surface.

9.5.2 DSC

The DSC proved useful in providing crystallinity values across the weld interface with a spatial resolution of 50 µm. Due to the cost it was only possible to perform DSC on one half of the weld and on a limited number of slices. DSC performed on a full range of microtomed slices across the weld interface would provide crystallinity results like the nanoindentation. The accuracy of the data can be improved by testing multiple cuttings per slice and a greater number of slices. There is potential to reduce the cost of the DSC through: streamlining of the microtomy process; specimen preparation; and automation of the DSC tests using an automatic feeder.

9.5.3 FTIR

The literature has shown that FTIR, if used with a microscope and polariser attachments, can supplement the DSC by providing similar spatial resolution for crystallinity values in addition to providing crystal orientation.

9.5.4 Neutron diffraction

Neutron diffraction is a potential technique for verifying the results of DSC and potentially NI. The technique uses a powerful neutron source such as a synchrotron and operates in a similar manner to XRD but using neutrons. The biggest advantage of neutron diffraction is the penetration depth of several centimetres, therefore it is possible to obtain a three dimensional map of crystallinity, orientations, and stresses in the weld region. The difficult aspect of this technique is access as there are very few places in the world with the appropriate facilities and there is often a long waiting list for researchers.

9.6 Miscellaneous

Several experimental and analytical techniques were gradually developed as part of the PhD. The development of these techniques was documented in form of operating procedures to ensure that practical knowledge is passed and common mistakes are not repeated by new users of the technique. It would be useful to disseminate these operating procedures as often for specialised techniques it is difficult to find documentation necessary to replicate the findings without prior experience of the said technique.

9.6.1 Democratisation of FEA modelling

A fresh trend in the finite element industry is that of democratisation of finite element modelling. FEA modelling has been developed for past few decades and with advances in computing technology it is possible to use it more frequently. In an engineering environment, FEA modelling is almost as popular as CAD tools but requires an FEA analyst to properly utilise it. With the advent of cloud technology, it is possible to code the model generation, simulation, and reporting to be automated with minimal intervention from the analyst. The thermal welding, weld bead shape, and the parametric WPTCR test models can all be coded in the cloud and presented with an intuitive GUI interface. A user without FEA background can then choose to generate reports from the model geometry or the initial conditions specific to their case.

10 References

Al-Shamrani, A. A., 2010. *Characterisation, optimisation, and modelling of PE blends for pipe applications.* Loughborough: Loughborough University.

Amghizar, I., Vandewalle, L. A., Van Geem, K. M. & Marin, G. B., 2017. New trends in olefin production. *Engineering,* 3(2), pp. 171-178.

Anand, J. N. & Karam, H. J., 1969. Interfacial contact and bonding in autohesion I-contact theory. *The Journal of Adhesion,* 1(1), pp. 16-23.

Arbeiter, F. J., Pinter, G. & Frank, A., 2013. *Impact of single and dual pressure butt-weldeing procedures on the reliability of PE 100 pipe welds.* Lyon, Society of Plastic Engineers.

ASM International Handbook Committee, 1988. *Engineering Plastics.* Ohio: ASM International.

ASTM, 1999. *ASTM D2444 - Standard Test Method for Determination of the Impact Resistance of Thermoplastic Pipe and Fittings by Means of a Tup (Falling Weight),* s.l.: ASTM International.

ASTM, 2002. *ASTM F2231 - Standard Test Method for Charpy Impact Test on Thin Specimens of Polyethylene Used in Pressurized Pipes,* s.l.: ASTM International.

ASTM, 2010. *ASTM D256-10e1 - Standard Test Methods for Determining the Izod Pendulum Impact Resistance of Plastics,* s.l.: ASTM International.

ASTM, 2012a. *ASTM D2737 REV A - Standard Specification for Polyethylene (PE) Plastic Tubing,* s.l.: ASTM International.

ASTM, 2012b. *ASTM F2620 - Standard Practice for Heat Fusion Joining of Polyethylene Pipe and Fittings,* s.l.: ASTM International.

ASTM, 2013a. *ASTM F2164 - Standard Practice for Field Leak Testing of Polyethylene (PE) and Crosslinked Polyethylene (PEX) Pressure Piping Systems Using Hydrostatic Pressure,* s.l.: ASTM International.

ASTM, 2013b. *ASTM F2928 - Standard Practice for Specimens and Testing Conditions for Testing Polyethylene (PE) Pipe Butt Fusions Using Tensile and Hydrostatic Test Methods,* s.l.: ASTM International.

ASTM, 2013c. *ASTM F2620 - Standard Practice for Heat Fusion Joining of Polyethylene Pipe and Fittings,* s.l.: ASTM International.

ASTM, 2015. *ASTM F2634 - Standard Test Method for Laboratory Testing of Polyethylene (PE) Butt Fusion Joints using Tensile-Impact Method,* s.l.: ASTM International.

ASTM, 2016a. *ASTM D1248 - Standard Specification for Polyethylene Plastics Extrusion Materials for Wire and Cable,* s.l.: ASTM International.

ASTM, 2016b. *ASTM D2122 - Standard Test Method for Determining Dimensions of Thermoplastic Pipe and Fittings,* s.l.: ASTM International.

ASTM, 2016c. *ASTM D2513 REV A - Standard Specification for Polyethylene (PE) Gas Pressure Pipe, Tubing, and Fittings,* s.l.: ASTM International.

ASTM, 2016d. *ASTM F3183 - Standard Practice for Guided Side Bend Evaluation of Polyethylene Pipe Butt Fusion Joint,* s.l.: ASTM International.

Atkinson, J. R. & deCourcy, D. R., 1981. Assessment of fusion joint quality and some evidence for the presence of molecular orientationin butt-fusion welds in polyethylene pipes. *Plastics and Rubber Processing and Applications,* Volume 1, pp. 287-292.

Awaja, F., 2016. Autohesion of polymers. *Polymer,* 97(5), pp. 387-407.

Awaja, F. et al., 2009. Adhesion of polymers. *Progress in Polymer Science,* 34(9), pp. 948-968.

Barber, P. & Atkinson, J. R., 1972. Some microstructural features of the welds in butt-welded polyethylene and polybutene-1 pipes. *Journal of Materials Science,* Volume 7, pp. 1131-1136.

Bartolai, J., Simpson, T. W. & Xie, R., 2016. *Predicting strength of thermoplastic polymer parts produced using additive manufacturing.* Texas, The Minerals, Metals & Materials Society, pp. 951-963.

Beech, S. H., Grieser, J., Lowe, D. & Vanspeybroeck, P., 2010. *Harmonisation of polyethylene pipe butt fusion procedures and test methods.* Vancouver, Plastic Pipe Conference Association.

Beech, S. H., Hutten, A. & Ritz, M., 2008. *Harmonisation of polyethylene pipe butt fusion procedures and test methods.* Budapest, Plastic Pipe Conference Association.

Beech, S. H., Salles, C. & Schulte, U., 2012. *Harmonisation of polyethylene pipe butt fusion procedures and test methods - Final Conclusions.* Barcelona, Plastic Pipe Conference Association.

Bellis, M., 2013. *The History of Plastics.* [Online]
Available at: http://inventors.about.com/od/pstartinventions/a/plastics.htm
[Accessed Oct 2013].

Bolton, W., 2013. *Production Technology: Processes, Materials and Planning.* Revised ed. s.l.:Elsevier .

Bonten, C. & Schmachtenberg, E., 2001. A new hypothesis to describe the mechanisms acting in a welded joint of semicrystalline thermoplastics. *Polymer Engineering and Science,* 41(3), pp. 475-483.

Borealis Group, 2013. *HE3490LS Product Datasheet,* s.l.: s.n.

Boukhili, R. & Gauvin, R., 1990. Aspects of the ductile-brittle transition in fatigue. *Journal of Materials Science Letters ,* 9(4), pp. 449-450.

Bowman, J., 1997. A review of electrofusion joining process for polyethylene pipe systems. *Polymer Engineering and Science ,* 37(4), pp. 674-691.

Bowman, J. & Parmar, R., 1989. The importance of axial misalignment on the long term strength of polyethylene pipe butt fusion joints. *Polymer Engineering and Science ,* 29(19), pp. 1406-1411.

Brinken, F., 1982. *A theoratical approach to the practical problem involved in jointing different PE grades.* New York, Plastic Pipe Conference Association.

Brown, C. & Troughton, M. J., 2003. *Qualifying long-term performance of butt fusion welds in PE pipes from short-term tests,* Cambridge: TWI.

Brown, H. R., 1982. A model for brittle-ductile transitions in polymers. *Journal of Materials Science,* 17(2), pp. 469-476.

Brown, H. R., 1991. The adhesion between polymers. *Annual Review of Material Science,* Volume 21, pp. 463-489.

Brydson, J. A., 1999. *Plastics Materials.* 7th ed. Oxford: Elservier.

BS, 2000a. *BSI BS EN 12814-2 - Testing of Welded Joints of Thermoplastics Semi-Finished Products - Part 2: Tensile Test,* s.l.: BSI.

BS, 2000b. *BSI BS EN 12814-6 - Testing of Welded Joints of Thermoplastics Semi-Finished Products - Part 6: Low Temperature Tensile Test,* s.l.: BSI.

BS, 2000c. *BSI BS EN 12814-1 - Testing of welding joints of thermoplastics semi-finished products Part 1: Bend tests - CORR 14807: November 28, 2003,* s.l.: BSI.

BS, 2001a. *BSI BS EN 12814-8 - Testing of Welded Joints of Thermoplastics Semi-Finished Products - Part 8: Requirements - CORR 14808: November 28, 2003,* s.l.: BSI.

BS, 2002. *BSI BS EN 12814-7 - Testing of welded joints of thermoplastics semi-finished products - Part 7: Tensile test with waisted test specimens,* s.l.: BSI.

BS, 2010. *BSI BS EN 1555-2 - Plastics piping systems for the supply of gaseous fuels - Polyethylene (PE) Part 2: Pipes,* s.l.: BSI.

BS, 2011. *BSI BS EN 12201-2 + A1 - Plastics piping systems for water supply, and for drainage and sewerage under pressure - Polyethylene (PE) Part 2: Pipes - CORR: January 31, 2012; AMD: November 30, 2013,* s.l.: BSI.

BS, 2014. *BSI BS EN 12814-3 - Testing of welded joints in thermoplastics semi-finished products Part 3: Tensile creep test,* s.l.: BSI.

Bucknall, C. B., Drinkwater, I. C. & Smith, G. R., 1980. Hot plate welding of plastics: factors affecting weld strength. *Polymer Engineering & Science ,* Volume 20, pp. 432-440.

Callister, W. D., 2003. *Material Science and Engineering: An Introduction.* International Eiditon ed. Utah: John Wiley and Sons.

Ceresana, 2012. *Market Study: Plastic Pipes - World.* 1st ed. Konstanz: Ceresana.

Chang, P.-H. & Teng, T.-L., 2004. Numerical and experimental investigation on the residual stresses of the butt-welded joints. *Computational Materials Science,* Volume 29, pp. 511-522.

Chekal, B. P., 2002. *Understanding the roles of chemically-controlled and diffusion-limited processes in determining the severity of autoacceleration behavior in free radical polymerization.* s.l.:Northwestern University.

Cheng, Y.-T. & Cheng, C.-M., 2004. Scaling, dimensional analysis and indentation measurements. *Material Science and Engineering,* Volume 44, pp. 91-149.

Crawford, R. J., 1998. *Plastics Engineering.* s.l.:Butterworth Heinemann.

Crawford, S. L. et al., 2008. *Preliminary assessment of NDE methods on inspection of HDPE butt fusion piping joints for lack of fusion,* Washington: Pacific Northwest National Laboratory.

Deblieck, R. A., van Beek, D. J., Remerie, K. & Ward, I. M., 2011. Failure mechanisms in polyolefines: the role of crazing, shear yielding and the entanglement network. *Polymer,* Volume 52, pp. 2979-2990.

deCourcy, D. R. & Atkinson, J. R., 1997. The use of tensile tests to determine the optimum conditons for butt welding polyethylene pipes of different melt flow index. *Journal of Materials Science,* 12(8), pp. 1535-1551.

DIN, 1965. *DIN 8075 - Pipes of High-density PE (High-density Polyethylene); Type 1; General Quality Requirements, Testing,* s.l.: DIN.

DIN, 2011. *DIN 8075 - Polyethylene (PE) pipes - PE 80, PE 100 - General quality requirements, testing; Text in German and English,* s.l.: DIN.

Dodin, M. J., 1981. Welding mechanisms of plastics: a review. *The Journal of Adhesion,* 12(2), pp. 99-111.

DVS, 1997. *DVS 2203-4 - Testing of welded joints of thermoplastics plates and tubes - Tensible creep test,* s.l.: DIN.

DVS, 1999. *DVS 2203-5 - Testing of welded joints ofthermoplastics plates and tubes - Technological bend test,* s.l.: DIN.

DVS, 2005. *DVS 2207-1 - Welding of thermoplastics - Heated tool welding of pipes, pipeline components and sheets made of PE-HD,* s.l.: DIN.

DVS, 2010. *DVS 2203-2 - Testing of welded joints between panels and pipes made of thermoplastics - Tensile test,* s.l.: DIN.

DVS, 2011. *DVS 2203-3 - Testing of welded joints between panels and pipes made of thermoplastics - Tensile impact test,* s.l.: DIN.

DVS, 2015. *DVS 2207-1 - Welding of thermoplastics - Heated element welding of pipes, piping parts and panels made out of polyethylene,* s.l.: DIN.

El-Bagory, T. M., Sallam, H. E. & Younan, M. Y., 2014. Effect of strain rate, thickness, welding on the J-R curve for polythylene pipe materials. *Theoretical and Applied Fracture Mechanics,* Volume 74, pp. 164-180.

Es-Saheb, M. H., 1996. The temperature effects on high density polyethylene (HDPE) pipes. *Journal of King Abdulaziz University Engineering Sciences,* Volume 8, pp. 47-60.

Ezekoye, O. A., Lowman, C. D., Fahey, M. T. & Hulme-Lowe, A. G., 1998. Polymer weld strength predictions using a thermal and polymer chain diffusion analysis. *Polymer Engineering and Science,* June.38(6).

Faraz, A., Nisar, S. & Khan, M. A., 2014. Effect of welding parameters on the structural performance of fusion welded extruded and injection molded HDPE joints. *Journal of Space Technology,* 4(1), pp. 114-119.

Fischer-Cripps, T. & Anthony, C., 2010. *Nanoindentation.* 2nd ed. New York: Springer.

Földes, E. & Szigeti-Erdei, A., 1997. Migration of additives in polymers. *Journal of Vinyl & Additive Technology,* 3(3), pp. 220-224.

Frank, C., 2001. *Polymerisation techniques - dispersed systems.* California: Standford University.

Galchun, A. et al., 2015. Nanostructurisation and thermal properties of polyethylenes' welds. *Nanoscale Research Letters,* 10(138), pp. 1-6.

Goodfellow Cambridge Limited, 2016. *Goodfellow material property catalogue.* [Online]
Available at: www.goodfellow.com
[Accessed 2016].

Grandclement, G., 1989. *Proceedings of the 11th Plastic Fuel Gas Symposium.* San Francisco, American Gas Association, pp. 159-168.

Grewell, D. & Benatar, A., 2007. Welding of plastics: fundamentals and new developments. *International Polymer Processing,* 22(1), pp. 43-60.

Grimm, R. A., 1990. Fusion welding techniques for plastics. *Welding Journal,* pp. 23-28.

Gwynne, J. H., Oyen, M. L. & Cameron, R. E., 2010. Preparation of polymeric samples containing a graduated modulus region and development of nanoindentation linescan techniques. *Polymer Testing,* Volume 29, pp. 494-502.

Halary, J. L., Lauprêtre, F. & Monnerie, L., 2011. *Polyer materials: macroscopic properties and molecular interpretations.* New Jersey: Wiley.

Hill, D. J., Wilson, K. A. & Headford, A. L., 2001. *Butt fusion of large diameter thick wall pipes.* Munich, Plastic Pipe Conference Association.

Hill, D. J., Wilson, K. A. & Headford, A. L., 2001. *Butt fusion welding of large diameterthick wall pipes.* Munich, Plastic Pipe Conference Association.

Hinchcliff, F. A. & Troughton, M. J., 1998. *Structural integrity of butt fusion welds in polyethylene pipes - comparison of short-term coupon tests,* Cambridge : TWI Ltd.

Huang, Y. et al., 2006. A model of size effects in nano-indentation. *Journal of the Mechanics and Physics of Solids,* Volume 54, pp. 1668-1686.

Hui, C., Ruina, A., Creton , C. & Kramer, E., 1992. Micromechanics of crack growth into a craze in a polymer glass. *Macromolecules,* 25(15), pp. 3948-3955.

Huo, H. et al., 2013. In situ studies on the temperature-related deformation behaviour of isotactic polypropylene spherulites with unixial stretching: the effect of crystallisation conditons. *Polymer Engineering and Science,* 53(1), pp. 125-133.

Ilie, S., 2009. *Polymeric Materials Review on Oxidation, Stabilization and Evaluation using CL and DSC Methods,* s.l.: CERN.

Inc, B. W., 2009. Stress Relaxation and Creep. *Technical Tidbits*, Issue 12.

ISO, 1996. *ISO 161-1 - Thermoplastics Pipes for the Conveyance of Fluids - Nominal Pressures - Part 1: Metric Series - Third Edition,* s.l.: ISO.

ISO, 1997a. *ISO 13480 - Polyethylene Pipes - Resistance to Slow Crack Growth - Cone Test Method - First Edition,* s.l.: ISO.

ISO, 1997b. *ISO 179-2 - Plastics - Determination of Charpy Impact Properties - Part 2: Instrumented Impact Test - First Edition; Technical Corrigendum 1: 11-15-1998,* s.l.: ISO.

ISO, 2000a. *ISO 180 - Plastics - Determination of Izod Impact Strength - Third Edition,* s.l.: ISO.

ISO, 2000b. *ISO 6603-1 - Plastics - Determination of Puncture Impact Behaviour of Rigid Plastics - Part 1: Non-Instrumented Impact Testing - Second Edition,* s.l.: ISO.

ISO, 2000c. *ISO 6603-2 - Plastics - Determination of Puncture Impact Behaviour of Rigid Plastics - Part 2: Instrumented Impact Testing - Second Edition,* s.l.: ISO.

ISO, 2001. *ISO 13953 - Polyethylene (PE) Pipes and Fittings - Determination of the Tensile Strength and Failure Mode of Test Pieces from a Butt-Fused Joint - First Edition,* s.l.: ISO.

ISO, 2005. *ISO 2505 - Thermoplastics pipes - Longitudinal reversion - Test method and parameters - Second edition,* s.l.: ISO.

ISO, 2006a. *ISO 1167-1 - Thermoplastics pipes, fittings and assemblies for the conveyance of fluids Determination of the resistance to internal pressure Part 1: General method - First Edition,* s.l.: ISO.

ISO, 2007a. *ISO 4427-1 - Plastics piping systems - Polyethylene (PE) pipes and fittings for water supply - Part 1: General - First Edition,* s.l.: ISO.

ISO, 2007b. *ISO 4427-2 - Plastics piping systems — Polyethylene (PE) pipes and fittings for water supply — Part 2: Pipes - First Edition,* s.l.: ISO.

ISO, 2007d. *ISO 1167-4 - Thermoplastics pipes, fittings and assemblies for the conveyance of fluids — Determination of the resistance to internal pressure — Part 4: Preparation of assemblies - First Edition,* s.l.: ISO.

ISO, 2008a. *ISO 13477 - Thermoplastics pipes for the conveyance of fluids — Determination of resistance to rapid crack propagation (RCP) — Small-scale steady-state test (S4 test) - Second Edition,* s.l.: ISO.

ISO, 2008b. *ISO 11357-6 - Plastics — Differential scanning calorimetry (DSC) — Part 6: Determination of oxidation induction time (isothermal OIT) and oxidation induction temperature (dynamic OIT) - Second Edition,* s.l.: ISO.

ISO, 2009. *ISO 13479 - Polyolefin pipes for the conveyance of fluids — Determination of resistance to crack propagation — Test method for slow crack growth on notched pipes - Second Edition,* s.l.: ISO.

ISO, 2010. *ISO 179-1 - Plastics — Determination of Charpy impact properties — Part 1: Non-instrumented impact test - Second Edition,* s.l.: ISO.

ISO, 2011a. *ISO 21307 - Plastics pipes and fittings - Butt fusion jointing procedures for polyethylene (PE) pipes and fittings used in the construction of gas and water distribution systems - Second Edition,* s.l.: ISO.

ISO, 2011b. *ISO 1133-1 - Plastics - Determination of the melt mass-flow rate (MFR) and melt volume flow rate (MVR) of thermoplastics - Part 1: Standard method - First Edition,* s.l.: ISO.

ISO, 2012. *ISO 527-1 - Plastics - Determination of tensile properties - Part 1: General principles - Second Edition,* s.l.: ISO.

ISO, 2014a. *ISO 4437-1 - Plastics piping systems for the supply of gaseous fuels - Polyethylene (PE) - Part 1: General - First Edition,* s.l.: ISO.

ISO, 2014b. *ISO 4437-2 - Plastics piping systems for the supply of gaseous fuels - Polyethylene (PE) - Part 2 Pipes - First Edition,* s.l.: ISO.

ISO, 2015a. *ISO 6259-1 - Thermoplastics pipes - Determination of tensile properties - Part 1: General test method - Second Edition,* s.l.: ISO.

Janson, L.-E., 1989. *Plastic pies for water supply and sewage disposal.* Stockholm: NESTE Chemicals.

Joshi, M., Butola, B. S., Simon, G. & Kukaleva, N., 2006. Rhelogical and viscoelastic behavior of HDPE/Octamethyl-POSS nanocomposites. *Macromolecules,* 39(5), pp. 1839-1849.

Kakani, S. L., 2004. *Material Science.* s.l.:New Age Publishers.

Kinloch, A. J., 1987. *Adhesion and adhesives.* 2 ed. s.l.:Springer Netherlands.

Kostic, M. M. & Reifschneider, L. G., 2006. Design of extrusion dies. *Encyclopedia of chemical processing,* pp. 633-649.

Lach, R. et al., 2013. Assessment with indentation techniques of the local mechanical behavior of joints in polymer parts. *Polimery,* 58(11-12), pp. 900-905.

Lai, H. S., Tun, N. N., Yoon, K. B. & Kil, S. H., 2016. Effects of defects on the failure of butt fusion welded polythylene pipe. *International Journal of Pressure Vessels and Piping,* Volume 139-140, pp. 117-12.

Leskovics, K., Kollar, M. & Barczy, P., 2006. A study of structure and mechanical properties of welded joints in polyethylene pipes. *Materials Science and Engineering A,* Issue 419, pp. 134-143.

Lester, G. H., 2003. *Corrugated Polyethylene Pipe Design Manual and Installation Guide.* Irving: PPI.

Maine, L. & Stafford, T. G., 1985. *PE jointing techniques.* York, Plastic Pipe Conference Association.

Malguarnera, S. C. & Earles, L. L., 1982. *The quality assurance of head fused thermoplastic pipeline joints.* San Franciso, Brookfield Center, CT: Society of Plastics Engineers, Inc. (SPE), pp. 279-282.

Merah, N., Saghir, F., Khan, Z. & Bazoune, A., 2006. Effect of temperature on tensile properties of HDPE pipe material. *Plastics, Rubber and Composites,* 35(4).

Mohitpour, M., 2008. *Energy supply and pipeline transportation, challenges and oppurtunities.* 1st ed. New York: ASME.

Neubert, W. & Mack, W. A., 1973. Getting a bead on welding of plastic pipe and fittings. *Plastics Engineering*, Volume 29, pp. 40-43.

Nicholson, J., 1991. *The Chemistry of Polymers.* Cambridge: Royal Society of Chemistry.

Nonhof, C. J., 1996. Optimisation of hot plate welding for series and mass production. *Polymer Engineering and Science,* 36(9), pp. 1184-1195.

NPR, 2009. *The History Of Plastic: From Billiards To Bibs.* [Online]
Available at: http://www.npr.org/templates/story/story.php?storyId=114331762
[Accessed Oct 2013].

O'Connell, P. A., Duckett, R. A. & Ward, I. M., 2002. Brittle-ductile transitions in polythylene. *Polymer Engineering and Science ,* 42(7), pp. 1493-1508.

Ogawa, T., 1992. Effects of molecular weight on mechanical properties of polypropylene. *Journal of Applied Polymer Science,* 44(10), pp. 1869-1871.

Osbourne, J., 2013. Thermoplastic pipes - lighter, more flexible solutions for oil and gas extraction. *Reinforced Plastics*, January/February, pp. 33-38.

Osswald, T., 2011. *Understanding Polymer Processing.* Munich: Hanser.

Otaigbe, J. U., 1996. *Polymerisation processes MSE 383, Unit 2-1.* Iowa: Materials Science and Engineering Department, Iowa State University.

Oyen, M. L. & Cook, R. F., 2002. Load-displacement behaviour during sharp indentation of viscous-elastic-plastic materials. *Journal of Materials Research,* 18(1), pp. 139-151.

Pandini, S. & Pegoretti, A., 2011. Time and temperature effects on Poisson's ratio of poly(butylene terephthalate). *eXPRESS Polymer Letters,* 5(8), pp. 685-697.

Parmar, R., 1986. *The long-term behaviour of butt fusion welds in polyethylene pipeline systems.* London: Brunel University.

Parmar, R. & Bowman, J., 1989. Crack initiation and propagation paths for brittle failures in aligned and misaligned pipe butt fusion joints. *Polymer Engineering & Science,* 29(19), pp. 1396-1405.

Peterlin, A., 1971. Molecular model of drawing polyethylene and polypropylene. *Journal of Materials Science ,* Volume 6, pp. 490-508.

PipeLife International GmbH, 2000. *LLLD : Specialities : Products :: Pipelife International :: Producer of Plastic Pipe Systems and Fittings, Manufacturer and Sales.* [Online]
Available at: http://www.pipelife.com/com/products/specialities/long_length.php
[Accessed 05 08 2016].

Piringer, O. G. & Baner, A. L., 2008. *Plastic packaging: Interactions with food and pharmeceuticals.* 2 ed. s.l.:John Wiley and Sons.

Plastics Europe, 2013. *Plastics - the Facts 2013,* s.l.: The Plastic Portal.

Plastics Technology, 2005. No.5 - Twin-Screw Extrusion. *Plastics Technology*, October.

Pokharel, P., Kim, Y. & Choi, S., 2016. Microstructure and mechanical properties of the butt joint in high density polyethylene pipe. *International Journal of Polymer Science,* p. 13.

Poon, B., Rittel, D. & Ravichandran, G., 2008. An analysis of nanoindentation in linearly elastic solids. *International Journal of Solids and Structures,* Issue 45, pp. 6018-6033.

Potente, H., 1977. On the theory of heated-tool butt welding. *Kunststoffe,* Issue 67, pp. 98-102.

Potente, H. & de Zeeuw, K., 1979. *Non-destructive testing of heated tool butt welded pipes using optical methods.* Brighton, Plastic Pipe Conference Association.

PPI, 2012. *PPI TR-33 - Generic Butt Fusion Joining Procedure for Field Joining of Polyethylene Pipe,* s.l.: PPI.

PPI, 2014. *Handbook of PE.* 2nd Edition ed. s.l.:Plastic Pipe Institute Inc.

Qian, L. et al., 2005. Comparison of nanoindentation hardness to microhardness. *Surface and coatings technology,* Volume 195, pp. 264-271.

Ram, A., 1997. *Fundamentals of polymer engineering.* New York: Plenum Press.

Rapra Technology Limited, 1995. *Development in the European extrusion industry: machinery, manufacturersm and markets,* 1-85957-035-6: Rapra Technology Limited.

Rashid, H., 1997. *Butt fusion welding of polyethylene pipes.* London: Brunel University.

Rauwendaal, C., 2014. *Polymer Extrusion.* 5th ed. Munich: Hanser.

Riahi, M., Kooshanyan, K. & Ghanati, M. F., 2011. Analysis of effect of pressure and heat on mechanical characteristics of butt fusion welding of polyethylene pipes. *Polymer-Plastics Technology and Engineering,* Volume 50, pp. 907-915.

Rocha, J. R. et al., 2013. Polymer indentation with mesoscopic molecular dynamics. *Materials Research Society,* 28(21), pp. 3043-3052.

Rodriguez, S. A., Alcala, J. & Souza, R. M., 2012. The reduced modulus in the analysis of sharp instrumented indentation tests. *Journal of Material Research,* 27(16), pp. 2148-2161.

Rosen, S. L., 1993. *Fundamental principles of polymeric materials.* 2nd ed. New York: John Wiley and Sons.

Sattler, K. et al., 2010. Theory of nanoindentation. In: *Handbook of Nanophysics.* s.l.:Taylor and Francis.

Schneider, K., 2010. Investigation of structural changes in semi-crystalline polymers during deformation by synchrotorn X-ray scattering. *Journal of Polymer Science: Part B: Polymer Physics,* Volume 48, pp. 1574-1586.

Shaheer, M., Troughton, M., Khamsehnezhad, A. & Song, J., 2016. *Parametric study of simplified weld bead geometries of butt fusion welded polymer pipes to determine the stress concentration factor.* Telford, NAFEMS.

Shaheer, M., Troughton, M., Song, J. & Khamsehnezhad, A., 2016. *A study of the micro-mechanical properties of butt fusion welded joints in HDPE pipes using the nanoindentation technique.* Melbourne, TWI.

Shillitoe, S., Day, A. J. & Benkreira, H., 1990. A finite element approach to butt fusion welding analysis. *Proceedings of Institute of Mechanical Engineers,* 204(2), pp. 95-101.

Skinner, S., 2014. *Hydralic Fluid Power - A Historical Timeline.* s.l.:Lulu.com.

Stevens, M. F., 1995. *An appraisal of the UK market for plastic pipes.* York, Plastic Pipe Conference Association.

Stevens, S. M., 1990. *Examination of crystallinity in polyethylene and polypropylene welds using Fourier transform infrared-microspectroscopy,* Cambridge: TWI Ltd.

Stevens, S. M., 1993. *Structure evaluation of polyethylene and polypropylene hot plate welds,* Cambridge: TWI Ltd.

Stokes, V. K. & Hobbs, S. Y., 1989. Strength and bonding mechanism in vibration-welded polycarbonate to polyetherimide joints. *Polymer Engineering and Science,* 29(23), pp. 1667-1676.

Troughton, M., 2010. *A comparison of mechanical test methods for butt fusion joints in polyethylene pipes.* Calgary, Alberta, TWI.

Troughton, M. J. & Booth, G. S., 1996. *Structural integrity of butt fusion welded polyethylene pipe - a review,* Cambridge: Abington Publishing.

Tschoegl, N. W., Knauss, W. G. & Emri, I., 2002. Poisson's ratio in linear viscoelasticity - a critical review. *Mechanics of Time-Dependent Materials,* Volume 6, pp. 3-51.

Tubi Group, 2014. *Mobile Modular Extrusion.* [Online]
Available at: http://tubigroup.com/mobile-modular-extrusion/

TWI, 2006. *Plastics joining - butt fusion and electrofusion welding.* 3.0 ed. s.l.:TWI Ltd.

TWI, 2011. *Welding techniques for thermoplastics.* [Online]
Available at: http://www.twi-global.com/technical-knowledge/job-knowledge/welding-techniques-for-thermoplastics-055/
[Accessed 09 2014].

TWI, 2016. *Image database.* s.l.:TWI Limited.

Udomphol, T., 2007. *Creep and Stress Rupture Presentation,* Nakhon Ratchasima: Suranaree University of Technology.

Ulrich , H., 1993. *Introduction to industrial polymers.* Munich: Hanser.

Van Krevelen, D. W., 1997. *Properties of Polymers.* Third, completely revised edition ed. Amsterdam: Elsevier.

Vincent, P. I., 1960. The necking and cold-drawing of rigid plastics. *Polymer,* Volume 1, pp. 7-19.

Vlachopoulos, J. & Strutt, D., 2002. Basic heat transfer and some applications in polymer processing. In: A. R. Calhoun & J. Golmanavich, eds. *Plastics Technician's Toolbox.* s.l.:Society of Plastics Engineers, pp. 21-33.

Voyutskii, S. S., 1963. Autohesion and adhesion of high polymers. *New York: Wiley-Interscience.*

Watson, M. N., 1988. *The butt fusion jointing process - fundamental aspects.* Bath, Plastic Pipe Conference Association.

Wilson, K. A., 1995. *Verification of butt fusion weld quality in large diameter PE100 pipes.* Edinburgh, Plastic Pipe Conference Association.

Wilson, K. A., 1995. *Verification of butt fusion weld quality in large diameter PE100 pipes.* Edinburgh, Plastic Pipe Conference Association.

WIS, 2002. *WIS 4-32-08 Issue 3 - Specification for the fusion jointing of polyethylene pressure pipeline systems using PE80 and PE100 materials,* s.l.: WIS.

WIS, 2016. *WIS 4-32-08 Issue 4 - Specification for the fusion jointing of polyehtylene pressure pipeline system using PE80 and PE100 materials,* s.l.: WIS.

Wohler, F., 1862. Bildung des Acetylens durch Kohlenstoffcalcium. *Annalen der Chemie und Pharmacie,* Volume 124, p. 220.

Wool, R. P., 2006. Adhesion at polymer-polymer interfaces: a rigidity percolation approach. *Comptes Rendus Chimie,* 9(1), pp. 25-44.

Wool, R. P., Yuan, B. L. & McGeral, O. J., 1989. Welding of polymer interfaces. *Polymer Engineering and Science,* 29(19), pp. 1340-1367.

Wu, J. et al., 2001. Controlling molecular mobility and ductile-brittle transitions of polycarbonate copolymers. *Journal of Polymer Science: Part B: Polymer Physics,* Volume 39, pp. 1730-1740.

Ye, J., André, S. & Farge, L., 2015. Kinematic study of necking in a semi-crystalline polymer through 3D digital image correlation. *International Journal of Soilds and Structures,* Volume 59, pp. 58-72.

Yoo, J. H. et al., 2017. Numerical analysis of the heat transfer and fluid flow in the butt-fusion welding process. *Korea-Australia Rheology Journal,* 29(1), pp. 37-49.

Yousefpour, A., Hojjati, M. & Immarigeon, J.-P., 2004. Fusion bonding/welding of thermoplastic composites. *Journal of Thermoplastic Composite Materials,* Volume 17, pp. 303-341.

Yuan, B. L. & Wool, R. P., 1990. Strength development at incompatible semicrystalline polymer interfaces. *Polymer Engineering and Science,* 30(22), pp. 1454-1464.

Yu, K., Morozov, E. V., Ashraf, M. A. & Shankar, K., 2017. A review of the design and analysis of reinforced thermoplastic pipes for offshore applications. *Journal of Reinforced Plastics & Composites,* 36(20), pp. 1514-1530.

Zaitsev, K. I., 1972. Cause of fracture of joints in plastic pipelines, and calculation of optimum process parameters for welding them. *Welding Production ,* Issue 19, pp. 20-22.

Zaitsev, K. I., 1973. Relationship between paths of fracture and structure of butt welds in polythylene tubes. *Welding Production ,* Issue 20, pp. 18-20.

Zhang, Y. W., Zhang, C. Y., Zeng, K. Y. & Shen, L., 2005. Nanoindentation of polymers with a sharp indenter. *Journal of materials research,* 20(6), pp. 1597-1606.

Appendix A: PhD Gantt Chart

Table A-1 The Gantt chart showing timeline for conducting the key tasks

Task	2013 O(1)	N(2)	D(3)	2014 J(4)	F(5)	M(6)	A(7)	M(8)	J(9)	J(10)	A(11)	S(12)	O(13)	N(14)	D(15) Holiday	2015 J(16)	F(17)	M(18)	A(19)	M(20)	J(21)	J(22)	A(23)	S(24)	O(25)	N(26)	D(27)	2016 J(28)	F(29)	M(30)	A(31)	M(32)	J(33)	J(34)	A(35)	S(36)	O(37)	N(38)	D(39)
Literature review	X	X	X	X	X	X	X	X	X	X	X	X	X	X	H	X	X	X	X	X	X	X	X	X	X	X	X	X	X	X	X	X	X	X	X	X	X	X	X
Project plan	X	X	X	X	X								X	X	H										X														
Definition of welding and testing matrix		X	X	X			X						X	X	H										X														
Material acquisation, preparation and training			X	X	X	X							X	X	H					X					X			X											
Welding trials according to different standard procedures						X	X								H																								
Butt fusion according to different standard procedures							X	X	X						H																								
Mechanical tests									X	X	X	X			H	X	X	X	X	X	X	X	X	X	X														
Weld structure optical microscopy and SEM analysis															H	X	X	X	X	X	X																		
Dynamic mechanical anaylsis														X	H	X	X	X	X	X	X	X			X														
Weld structure X-ray diffraction, FTIR and nano-indentation analysis															H	X	X	X	X	X	X	X	X				X												
Welding trials to verify optimal welding procedure															H							X	X	X															
FEA modelling of stresses in WPTCR test with different weld bead geometries															H						X	X	X																
Weld assesment using analytical techniques and mechanical tests															H									X	X	X	X												
Correlation verification of parameters, performance and structure															H												X	X											
Presentations, publications and reviews									X	X	X		X		H					X	X	X		X									X	X	X	X	X	X	X
Thesis write up, modification, and submission												X	X	X	H							X	X	X									X	X	X	X	X	X	X

200

Appendix B: Material Properties

Table B-1 BorSafe™ HE3490-LS black bimodal PE100 polyethylene for pressure pipe (Borealis Group, 2013)

Physical properties		Typical value*	Unit	Test method
Density	(Base resin)	949	kg/m^3	ISO 1183/ ISO 1872-2B
Density	(Compound)	959	kg/m^3	ISO 1183/ ISO 1872-2B
Melt flow rate	(190 ºC/ 2.16 kg)	<0.1	g/ 10 min	ISO 1133
Melt flow rate	(190 ºC/ 2.16 kg)	0.25	g/ 10 min	ISO 1133
Tensile stress at yield	(50 mm/min)	25	MPa	ISO 527-2
Tensile strain at break		>600	%	ISO 527-2
Tensile modulus	(1 mm/min)	1100	MPa	ISO 527-2
Charpy impact, notched	(0 ºC)	16	kJ/m^2	ISO 179/1eA
Hardness, Shore D		60	-	ISO 868
Carbon black dispersion		<3	-	ISO 18553
Carbon black content		>2	%	ASTN D 1630/ISO 6964
Brittleness temperature		<-70	ºC	ASTM D 746
Resistance to rapid crack propagation, S4 test	(Pc at 0 ºC, test pipe 250 mm SDR11)	>10	bar	ISO 13477
Resistance to SCG	(9.2 bar, 80 ºC)	>1000	h	ISO 13479
Thermal stability	(210 ºC)	>20	min	EN 728
ESCR	(10% IGEPAL), F_{50}	>10000	h	ASTM D 1693-A
* Data should not be used for specification work				

Appendix C: Weld Reports

Table C-1 WP1 and WP2 weld reports provided by Fusion Provida BF-315 printer output

Procedure	WP1						WP2					
Standard	WIS						DVS					
Machine	BF-315						BF-315					
Weld Number	1	2	3	4	5	6	9	10	11	12	13	14
Joint Number (report)	220	221	222	223	224	225	227	228	229	230	231	232
Date	23/01/14						23/01/14					
Bead Pressure (no Drag), Bar	13	13	13	13	13	13	13	13	13	13	13	13
Join Pressure (no Drag), Bar	13	13	13	13	13	13	13	13	13	13	13	13
Dynamic drag, Bar	6.5	7.2	6.3	6.1	6.3	6	5.6	5.8	6.1	5.8	6.1	6.1
Peak drag, Bar	6.6	7.2	6.3	6.2	6.3	6.2	5.6	5.8	6.2	5.8	6.1	6.1
Interfacial pressure, Bar	0.15	0.15	0.15	0.15	0.15	0.15	0.15	0.15	0.15	0.15	0.15	0.15
Bead up pressure, Bar	16.1	17.1	16.1	16.1	16.1	19.3	15.3	15.1	19	19.1	15.8	19.2
Target heat soak pressure, Bar	0	0	0	0	0	0	0	0	0	0	0	0
Heat soak pressure, Bar	0	0	0	0	0	0	0	0	0	0	0	0
Fusion pressure, Bar	19.3	20.3	19.3	19.1	19.1	18.8	18.5	18.7	19	18.7	19	18.6
Target temperature, ^{0}C	233	233	233	233	233	233	220	220	220	220	220	220
Heater temperature, ^{0}C	234	234	234	233	233	233	219	219	218	218	219	218
Bead-up time, seconds	Not measured						Not measured					
Heat soak time, seconds	225	225	225	225	225	225	165	165	165	165	165	165
Dwell time, seconds	1.5	1.5	1.5	1.6	1.5	1.5	1.5	1.5	1.5	1.5	1.5	1.5
Target cool time, seconds	600	600	600	600	600	600	1260	1260	1260	1260	1260	1260
Actual Cooled time, seconds	600	600	600	600	600	600	1260	1260	1260	1260	1260	1260
Bead travel	200	200	200	200	200	200	200	200	200	200	200	200
Notes	Dummy: Weld 7 (Joint 218), Unused: Weld 8						Dummy: Weld 15 (Joint 226), Unused: Weld 16					

Table C-2 WP3 and WP4 weld reports provided by McElroy DynaMc250 EP output

Procedure	WP3							WP4						
Standard	ASTM Ideal							ASTM Acceptable						
Machine	DynaMc250 EP							DynaMc250 EP						
Weld Number	17	18	19	20	21	22	24	25	26	27	28	29	30	32
Joint Number (report)	1	2	3	5	6	7	32	8	9	10	12	13	14	31
Date	07/03/14			10/03/14			14/03/14	10/03/14			12/03/14			14/03/14
Bead Pressure (no Drag), Bar	673	669	670	676	674	675	661	793	791	782	792	786	871	789
Join Pressure (no Drag), Bar	673	669	670	676	674	675	661	793	791	782	792	786	781	789
Dynamic drag, Bar	Not measured							Not measured						
Peak drag, Bar	84	80	81	87	85	86	72	86	84	75	85	79	74	82
Interfacial pressure, Bar	75	75	75	75	75	75	75	90	90	90	90	90	90	90
Bead up pressure, Bar	671	670	669	675	651	675	661	793	792	779	793	787	785	790
Target heat soak pressure, Bar	84	80	81	87	85	86	72	86	84	75	85	79	74	82
Heat soak pressure, Bar	86	80	82	88	85	88	73	87	87	75	85	78	71	83
Fusion pressure, Bar	674	670	672	677	673	676	661	792	792	782	794	788	785	789
Target temperature, ^{0}C	204-232							204-232						
Heater temperature, ^{0}C	219	219	219	219	218	219	217	232	232	232	232	232	232	232
Bead-up time, seconds	29	32	33	33	28	29	29	24	25	25	29	23	21	22
Heat soak time, seconds	430	432	441	444	444	440	436	382	388	371	377	373	383	377
Dwell time, seconds	3	8	9	6	6	4	3	4	4	4	4	6	5	14
Target cool time, seconds	425	425	425	425	425	425	425	425	425	425	425	425	425	425
Actual Cooled time, seconds	432	434	429	451	429	459	429	443	432	466	431	429	437	420
Bead travel	3/16	3/16	3/16	3/16	3/16	3/16	3/16	3/16	3/16	3/16	3/16	3/16	3/16	3/16
Notes	Dummy: Weld 23 (Joint 4)							Dummy: Weld 31 (Joint 11)						

Table C-3 WP5 and WP6 weld reports provided by McElroy DynaMc250 EP output

Procedure	WP5							WP6						
Standard	High pressure low temperature							High pressure high temperature						
Machine	DynaMc250 EP							DynaMc250 EP						
Weld Number	33	34	35	36	37	38	40	41	42	43	44	45	46	48
Joint Number (report)	15	17	18	19	20	21	33	23	24	25	26	27	28	30
Date	12/03/14						14/03/14	13/03/14						14/03/14
Bead Pressure (no Drag), Bar	1024	1013	1027	1013	1021	1012	1018	1249	1263	1259	1262	1257	1256	1256
Join Pressure (no Drag), Bar	1024	1013	1027	1013	1021	1012	1018	1249	1263	1259	1262	1257	1256	1256
Dynamic drag, Bar	Not measured							Not measured						
Peak drag, Bar	81	81	83	70	78	69	75	71	85	81	84	79	78	78
Interfacial pressure, Bar	120	120	120	120	120	120	120	150	150	150	150	150	150	150
Bead up pressure, Bar	1026	1015	1024	1014	1022	1012	1016	1257	1265	1260	1262	1257	1257	1256
Target heat soak pressure, Bar	81	70	84	70	78	69	75	71	85	81	84	79	78	78
Heat soak pressure, Bar	82	70	83	73	83	70	75	75	87	81	85	79	79	78
Fusion pressure, Bar	1023	1015	1025	1016	1023	1016	1015	1249	1260	1257	1261	1253	1258	1257
Target temperature, ^{0}C	175-179							258-260						
Heater temperature, ^{0}C	176	177	177	177	177	177	177	260	260	260	260	260	260	260
Bead-up time, seconds	39	33	41	50	46	40	36	18	18	12	12	14	24	17
Heat soak time, seconds	782	805	805	802	793	822	823	281	245	235	240	245	246	261
Dwell time, seconds	6	4	5	7	10	8	8	7	11	7	11	9	8	5
Target cool time, seconds	431	436	434	438	433	434	417	427	424	427	422	422	426	425
Actual Cooled time, seconds	438	435	437	440	435	436	425	429	424	431	425	424	427	428
Bead travel	3/16	3/16	3/16	3/16	3/16	3/16	3/16	3/16	3/16	3/16	3/16	3/16	3/16	3/16
Notes	Dummy: Weld 39 (Joint 16)							Dummy: Weld 47 (Joint 22 and 29)						

Appendix D: Macrographs

Table D-1 Macrographs of samples listed by position for each of the six welding procedures, pipe outer surface is always at the top for comparison
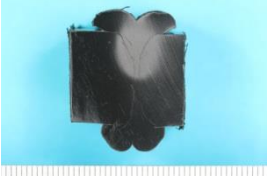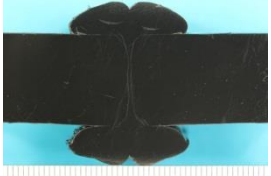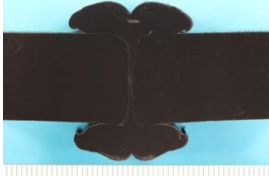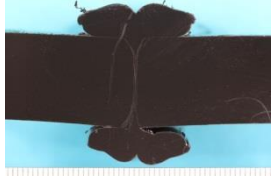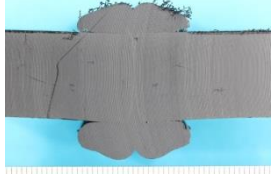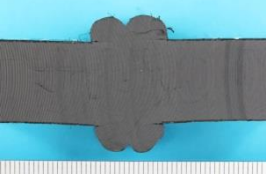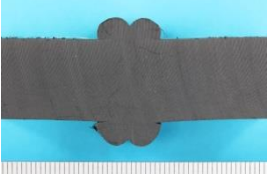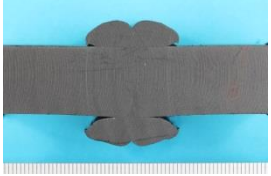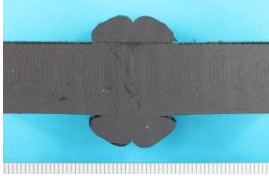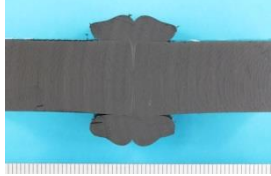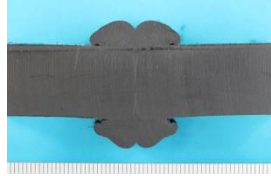
Table D-2 Data of bead parameters for the top bead position in mm

Name	Bead Width		Bead Height		Root length		Central Notch Height	
Bottom	Inside	Outside	Inside	Outside	Inside	Outside	Inside	Outside
22514/4/5A	12.17	16.96	5.76	5.25	4.19	9.11	3.96	3.08
22514/12/5A	11.79	15.55	4.58	4.55	6.61	4.56	3.23	3.65
22514/20/5A	22.61	22.06	7.49	6.04	5.57	8.88	3.81	2.79
22514/28/5A	21.35	23.08	6.97	5.99	7.31	7.42	3.24	2.35
22514/36/5A	19.12	22.02	6.90	6.27	5.87	5.12	2.82	3.26
22514/44/5A	16.89	20.52	6.50	5.91	5.30	7.20	3.44	2.49

Table D-3 Data of bead parameters for the bottom bead position in mm

Name	Bead Width		Bead Height		Root length		Central Notch Height	
Top	Inside	Outside	Inside	Outside	Inside	Outside	Inside	Outside
22514/4/5B	17.65	14.03	6.31	5.33	5.20	4.10	5.44	4.69
22514/12/5B	14.92	11.84	5.05	4.58	3.19	5.27	5.65	4.43
22514/20/5B	22.75	22.46	7.06	6.19	3.42	3.78	5.19	4.49
22514/28/5B	23.00	21.35	6.47	5.88	3.58	4.65	5.41	3.86
22514/36/5B	20.96	20.92	7.29	5.69	4.06	4.32	4.63	4.43
22514/44/5B	22.92	17.04	6.19	5.52	3.43	5.99	5.68	4.38

Table D-4 Data of bead parameters for the side bead position in mm

Name	Bead Width		Bead Height		Root length		Central Notch Height	
Side	Inside	Outside	Inside	Outside	Inside	Outside	Inside	Outside
22514/6/6D	12.92	14.46	5.21	4.90	3.05	4.59	4.88	4.59
22514/14/6D	12.14	11.95	4.67	4.00	3.42	2.65	5.00	4.55
22514/22/6D	17.63	17.51	5.37	4.70	2.87	2.86	5.42	4.63
22514/30/6D	16.14	15.36	5.95	5.13	2.71	5.27	5.15	3.74
22514/38/6D	15.99	16.22	5.91	4.90	4.17	5.78	3.93	4.29
22514/46/6D	15.84	16.97	5.72	4.66	2.83	3.19	5.18	3.80

Table D-5 Minimum, maximum, range and mean for each weld bead parameter for the inside bead, the outside bead and the combined bead position in mm

Name	Bead Width		Bead Height		Root Length		Central Notch Height	
	Inside	Outside	Inside	Outside	Inside	Outside	Inside	Outside
Minimum	11.79	11.84	4.58	4.00	2.71	2.65	2.82	2.35
Maximum	23.00	23.08	7.49	6.27	7.31	9.11	5.68	4.69
Range	11.21	11.24	2.90	2.27	4.59	6.46	2.86	2.34
Mean	17.60	17.79	6.08	5.30	4.27	5.26	4.56	3.86
Minimum	11.79		4.00		2.65		2.35	
Maximum	23.08		7.49		9.11		5.68	
Range	11.29		3.49		6.46		3.33	
Mean	17.70		5.69		4.76		4.21	

Appendix E: Python Scripts

E1 WPTCR

```
# Single file for everything using functions

# All py files have to be in the same folder.

import os
os.chdir(r"C:\AbaqusTemp\WPTCR") # Change work directory

# For Job creation
# -*- coding: mbcs -*-
import math
from part import *
from material import *
from section import *
from optimization import *
from assembly import *
from step import *
from interaction import *
from load import *
from mesh import *
from job import *
from sketch import *
from visualization import *
from connectorBehavior import *

# Defining the basic model

# Drawing the basic shape
OR = 63/2000.0 # Original outer radius
IR = 40/2000.0 # Original inner radius
H = 0.75 # Pipe height is now 1.5 metres

# Part sketch
s = mdb.models['Model-1'].ConstrainedSketch(name='__profile__', sheetSize=1.0)
g, v, d, c = s.geometry, s.vertices, s.dimensions, s.constraints
s.sketchOptions.setValues(viewStyle=AXISYM)
s.setPrimaryObject(option=STANDALONE)
s.ConstructionLine(point1=(0.0, -H), point2=(0.0, H))
s.rectangle(point1=(OR, 0.0), point2=(IR, H))

# Constraints of the sketch
s.FixedConstraint(entity=g[2])
s.HorizontalConstraint(entity=g[6])
s.VerticalConstraint(entity=g[5])
s.VerticalConstraint(entity=g[3])
s.EqualLengthConstraint(entity1=g[6], entity2=g[4])
s.EqualLengthConstraint(entity1=g[3], entity2=g[5])

# Dimensioning the Pipe
s.DistanceDimension(entity1=v[0], entity2=g[2], textPoint=(0.05, -0.05), value=OR)
s.ObliqueDimension(vertex1=v[0], vertex2=v[3], textPoint=(0.07, -0.01), value=(OR-IR))

# Generating the part
p = mdb.models['Model-1'].Part(name='Part-1', dimensionality=AXISYMMETRIC,
type=DEFORMABLE_BODY)
```

```python
p = mdb.models['Model-1'].parts['Part-1']
p.BaseShell(sketch=s)
s.unsetPrimaryObject()
session.viewports['Viewport: 1'].setValues(displayedObject=p)
del mdb.models['Model-1'].sketches['__profile__']

# Partition the pipe using a sketch
p = mdb.models['Model-1'].parts['Part-1']
f, e, d = p.faces, p.edges, p.datums
t = p.MakeSketchTransform(sketchPlane=f[0], sketchPlaneSide=SIDE1, origin=(
    0.0, 0.0, 0.0))
s = mdb.models['Model-1'].ConstrainedSketch(name='__profile__', sheetSize=1.0,
    gridSpacing=0.02, transform=t)
g, v, d, c = s.geometry, s.vertices, s.dimensions, s.constraints
s.setPrimaryObject(option=SUPERIMPOSE)
p = mdb.models['Model-1'].parts['Part-1']
p.projectReferencesOntoSketch(sketch=s, filter=COPLANAR_EDGES)
s.Line(point1=(-0.0, 0.01), point2=(0.5, 0.01))
s.Line(point1=(-0.0, (H-0.065)), point2=(0.5, (H-0.065)))
s.Line(point1=(-0.0, (H-0.015)), point2=(0.5, (H-0.015)))
pickedFaces = f.getSequenceFromMask(mask=('[#1 ]', ), )
p.PartitionFaceBySketch(faces=pickedFaces, sketch=s)
s.unsetPrimaryObject()
del mdb.models['Model-1'].sketches['__profile__']

# Material
f = p.faces # Creating material set
faces = f.getSequenceFromMask(mask=('[#f ]', ), ) # Change f to 1 for full selection
p.Set(faces=faces, name='Mat')
mdb.models['Model-1'].Material(name='HDPE-T5-80')
mdb.models['Model-1'].materials['HDPE-T5-80'].Density(table=((954.0, ), ))
mdb.models['Model-1'].materials['HDPE-T5-80'].Elastic(table=((480000000.0,
    0.5), ))
mdb.models['Model-1'].HomogeneousSolidSection(material='HDPE-T5-80', name=
    'Section-1', thickness=None)
mdb.models['Model-1'].parts['Part-1'].SectionAssignment(offset=0.0,
    offsetField='', offsetType=MIDDLE_SURFACE, region=
    mdb.models['Model-1'].parts['Part-1'].sets['Mat'], sectionName='Section-1',
    thicknessAssignment=FROM_SECTION)

# Assembly
mdb.models['Model-1'].rootAssembly.DatumCsysByThreePoints(coordSysType=
    CYLINDRICAL, origin=(0.0, 0.0, 0.0), point1=(1.0, 0.0, 0.0), point2=(0.0,
    0.0, -1.0))
mdb.models['Model-1'].rootAssembly.Instance(dependent=ON, name='Part-1-1',
    part=mdb.models['Model-1'].parts['Part-1'])

# Step
mdb.models['Model-1'].StaticStep(initialInc=0.001, name='Step-1', previous=
    'Initial')

# Boundary condition
e = p.edges # Creating symmetry set
edges = e.getSequenceFromMask(mask=('[#4 ]', ), )
p.Set(edges=edges, name='Symm')
mdb.models['Model-1'].YsymmBC(createStepName='Initial', localCsys=None, name=
    'HSymm', region=
    mdb.models['Model-1'].rootAssembly.instances['Part-1-1'].sets['Symm'])

# Load
```

```python
DEFLOAD = H/95 # Deformation of 15.789 mm, 1.05%
e = p.edges # Creating symmetry set
edges = e.getSequenceFromMask(mask=('[#1800 ]', ), )
p.Set(edges=edges, name='Clamps')
region = mdb.models['Model-1'].rootAssembly.instances['Part-1-1'].sets['Clamps']
mdb.models['Model-1'].DisplacementBC(name='Displacement', createStepName='Step-1',
    region=region, u1=0.0, u2=DEFLOAD, ur3=UNSET, amplitude=UNSET, fixed=OFF,
    distributionType=UNIFORM, fieldName='', localCsys=None)


# Generating individual input files without the models

def getInputFile(od_element, sdr_element, case_num):
    # Parameters

    OD = float(od_element)
    SDR = float(sdr_element)
    PR = OD/2000.0 # Outer pipe radius
    PW = (math.ceil(OD/SDR))/1000.0 # Pipe wall thickness round to nearest mm
    IW = PR - PW # Inner pipe radius
    NAMED = str(case_num)

    print 'OD=' + str(OD)
    print 'SDR=' + str(SDR)
    print 'H=' + str(H)
    print 'PR=' + str(PR)
    print 'PW=' + str(PW)
    print 'IW=' + str(IW)

    # Redimensioning the Pipe
    p = mdb.models['Model-1'].parts['Part-1']
    s = p.features['Shell planar-1'].sketch
    mdb.models['Model-1'].ConstrainedSketch(name='__edit__', objectToCopy=s)
    s = mdb.models['Model-1'].sketches['__edit__']
    g, v, d, c = s.geometry, s.vertices, s.dimensions, s.constraints
    s.setPrimaryObject(option=SUPERIMPOSE)
    p.projectReferencesOntoSketch(sketch=s,
        upToFeature=p.features['Shell planar-1'], filter=COPLANAR_EDGES)
    d[0].setValues(value=PR, )
    d[1].setValues(value=PW, )
    s.unsetPrimaryObject()
    p.features['Shell planar-1'].setValues(sketch=s)
    del mdb.models['Model-1'].sketches['__edit__']
    p.regenerate()

    # Mesh
    pickedRegions = f.getSequenceFromMask(mask=('[#f ]', ), )
    p.setMeshControls(regions=pickedRegions, elemShape=QUAD, technique=STRUCTURED)
    p = mdb.models['Model-1'].parts['Part-1']
    p.seedPart(size=0.0005, deviationFactor=0.1, minSizeFactor=0.1)
    p = mdb.models['Model-1'].parts['Part-1']
    p.generateMesh()
    mdb.models['Model-1'].parts['Part-1'].generateMesh()
    mdb.models['Model-1'].rootAssembly.regenerate()

    # Input file generation
    mdb.Job(atTime=None, contactPrint=OFF, description=
        'Parametric study of WPTCR test, minimum pipe length', echoPrint=OFF, explicitPrecision=
        SINGLE, getMemoryFromAnalysis=True, historyPrint=OFF, memory=90,
        memoryUnits=PERCENTAGE, model='Model-1', modelPrint=OFF,
        multiprocessingMode=DEFAULT, name=NAMED, nodalOutputPrecision=SINGLE,
```

```python
            numCpus=1, numGPUs=0, queue=None, scratch='', type=ANALYSIS,
            userSubroutine='', waitHours=0, waitMinutes=0)
    mdb.jobs[NAMED].writeInput(consistencyChecking=OFF)

    # Job Submission
    mdb.jobs[NAMED].submit(consistencyChecking=OFF)
    mdb.jobs[NAMED].waitForCompletion()

# For odb readout
from abaqus import *
from abaqusConstants import *
from odbAccess import *
from driverUtils import executeOnCaeStartup
executeOnCaeStartup()

session.Viewport(name='Viewport: 1', origin=(0.0, 0.0), width=268.95, height=154.15)
sv = session.viewports['Viewport: 1'] # Shortens the code
sv.makeCurrent()
sv.maximize()

#odbMaxMises.py from Abaqus Example scripts

def getMaxMises(case_num):
    #""" Print max mises location and value given NAMEDODB
    #   and elset(optional)
    elset = elemset = None
    region = "over the entire model"
    #""" Open the output database """
    case_odb = str(case_num)+'.odb'
    odb = openOdb(case_odb)
    assembly = odb.rootAssembly
    o1 = session.openOdb(name=case_odb)
    sv.setValues(displayedObject=o1)

    #""" Initialize maximum values """
    maxMises = -0.1
    maxElem = 0
    maxStep = "_None_"
    maxFrame = -1
    Stress = 'S'
    isStressPresent = 0
    for step in odb.steps.values():
        print 'Processing Step:', step.name
        for frame in step.frames:
            allFields = frame.fieldOutputs
            if (allFields.has_key(Stress)):
                isStressPresent = 1
                stressSet = allFields[Stress]
                if elemset:
                    stressSet = stressSet.getSubset(
                        region=elemset)
                for stressValue in stressSet.values:
                    if (stressValue.mises > maxMises):
                        maxMises = stressValue.mises
                        maxElem = stressValue.elementLabel
                        maxStep = step.name
                        maxFrame = frame.incrementNumber
    if(isStressPresent):
        print 'Maximum von Mises stress %s is %f in element %d'%(
            region, maxMises, maxElem)
```

211

```python
        print 'Location: frame # %d  step:  %s '%(maxFrame,maxStep)
    f = open('R15.py',"a")
    RESULTS = str(case_num)+'   '+str(maxMises)+'   '+str(maxElem)
    f.write(str(RESULTS)+'\n')
    f.close()
    sv.odbDisplay.display.setValues(plotState=(CONTOURS_ON_UNDEF, ))
    session.viewports['Viewport: 1'].odbDisplay.contourOptions.setValues(
    maxAutoCompute=OFF, maxValue=10000000, showMaxLocation=ON)
    session.viewports['Viewport: 1'].odbDisplay.basicOptions.setValues(
    averageElementOutput=False)
    sv.view.setValues(nearPlane=0.06,
    farPlane=0.1, width=0.07, height=0.03,
    viewOffsetX=0.0, viewOffsetY=-0.0)
    session.printOptions.setValues(vpBackground=ON, reduceColors=OFF)
    session.pngOptions.setValues(imageSize=(1920, 1080))
    session.printToFile(fileName=case_num, format=PNG,
canvasObjects=(session.viewports['Viewport: 1'], ))
    else:
        print 'Stress output is not available in' \
            'the output database : %s\n' %(odb.name)


# Print Report

def getCaseReport(case_num):
    #""" Reports XY data for inner and outer paths, NAMEDODB

    case_odb = str(case_num)+'.odb'

    # """ Define inner and outer paths """
    session.Path(name='Inner', type=NODE_LIST, expression=(('PART-1-1', (3, 8, )), ))
    session.Path(name='Outer', type=NODE_LIST, expression=(('PART-1-1', (4, 7, )), ))
    pth = session.paths['Inner']
    Datainner = 'Inner-' + str(case_num)
    session.XYDataFromPath(name=Datainner, path=pth, includeIntersections=False,
        pathStyle=UNIFORM_SPACING, numIntervals=150, shape=UNDEFORMED,
        labelType=TRUE_DISTANCE_Y)
    pth = session.paths['Outer']
    Dataouter = 'Outer-' + str(case_num)
    session.XYDataFromPath(name=Dataouter, path=pth, includeIntersections=False,
        pathStyle=UNIFORM_SPACING, numIntervals=150, shape=UNDEFORMED,
        labelType=TRUE_DISTANCE_Y)
    plot_name = 'XYPlot-' + str(case_num)
    xyp = session.XYPlot(plot_name)
    chartName = xyp.charts.keys()[0]
    chart = xyp.charts[chartName]
    xy1 = session.xyDataObjects[Dataouter]
    c1 = session.Curve(xyData=xy1)
    xy2 = session.xyDataObjects[Datainner]
    c2 = session.Curve(xyData=xy2)
    session.charts['Chart-1'].axes2[0].axisData.setValues(maxAutoCompute=False)
    session.charts['Chart-1'].axes2[0].axisData.setValues(maxValue=5e+07,
        maxAutoCompute=False)
    session.charts['Chart-1'].axes2[0].axisData.setValues(minAutoCompute=False)
    session.charts['Chart-1'].axes2[0].axisData.setValues(minValue=0,
        minAutoCompute=False)
    chart.setValues(curvesToPlot=(c1, c2, ), appendMode=True)
    session.viewports['Viewport: 1'].setValues(displayedObject=xyp)

    # Save an image of the XY plots
    plot_num = 'p' + str(case_num)
```

```python
    session.pngOptions.setValues(imageSize=(1920, 1080))
    session.printOptions.setValues(reduceColors=True)
    session.printToFile(fileName=plot_num, format=PNG, canvasObjects=(
        session.viewports['Viewport: 1'], ))

    # Save XY data to report file
    x0 = session.xyDataObjects[Datainner]
    x1 = session.xyDataObjects[Dataouter]
    case_report = 'case-' + str(case_num) + '.rpt'
    session.xyReportOptions.setValues(interpolation=ON)
    session.writeXYReport(fileName=case_report, appendMode=OFF, xyData=(x0, x1))

# Provides minimum pipe length for WPTCR for all cases in a single file

def getSTRESSLENGTH(case_num, H):
    case_report = 'case-' + str(case_num) + '.rpt'
    with open(case_report,"r") as f:
        data = f.readlines()

    newdata = data[3:] # Removes the top 3 lines

    a = []
    b = []
    c = []

    x = len(newdata) - 4

    for line in newdata:
        words = line.split()
        a.append(float(words[0]))
        b.append(float(words[1]))
        c.append(float(words[2]))
        x = x-1
        if x == 0:
            break

    stress = (b[0]+c[0])/2 # Average Von Mises stress at the weld interface
    print str(stress) + ' Pa at the weld interface for ' + str(case_num) + '.'

    # Comparing list b and c to report the corresponding a value
    # If the condition is satisfied
    s = 0.01*stress # 1% stress condition for test
    print 'The limiting stress is ' + str(s) + ' Pa.'
    n = 0

    while abs(b[n]-c[n])<s:
        n=n+1
        #print 'd is less than s' # Check

    l = a[n] # The Y value of the point in pipe where the stress diverges
             # over the defined stress value
    # l is calculated from the weld interface
    weld = 0.02 # Maximum weld size
    clamps = 0.1 # Length of both clamps
    free = 0.03 # Free hanging pipe
    minlen = 2*H-2*l
    print 'The minimum length of pipe is ' + str(minlen) + 'metres.'
    g = open('X15.py',"a")
    RESULTS = str(case_num)+'   '+str(minlen)+'   '+str(stress)
    g.write(str(RESULTS)+'\n')
```

```python
    g.close()
    f.close()

# Defining the function elements
od_element=1;
sdr_element=1;

# Variable names
OD = [63, 90, 110, 125, 160, 180, 225, 250, 280, 315, 355, 400, 450, 500, 560, 630] # Outer diameter
SDR = [7.4, 9, 11, 13.6, 17, 21, 26, 33] # Standard dimension ratio
case_num = 0 # 128 original jobs, otherwise 0

# This is the main loop

for od_element in OD:
    for sdr_element in SDR:
        case_num = int(case_num) # Reverts case_num as a integer
        case_num = case_num + 1
        g = open('L15.py',"a") # Append to case file
        input_name = str(case_num)+' '+str(od_element)+' '+str(sdr_element)
        g.write(str(input_name)+'\n')
        g.close()
        # Input file generation
        QUESTION = getInputFile(od_element, sdr_element, case_num)
        # ODB readout
        case_num = str(case_num)
        # Image capture of the odb file with location of max Von Mises stress
        ANSWER = getMaxMises(case_num)
        # Extract Von Mises from inner and outer paths
        REPORT = getCaseReport(case_num)
        # Extract minimum length of WPTCR
        # Extract averaged Von Mises stress at the weld interface
        INSIGHT = getSTRESSLENGTH(case_num, H)
        # Close Abaqus results file
        case_odb = str(case_num)+'.odb'
        session.odbs[case_odb].close()
```

E2 Weld Bead Models

```python
# Single file for everything using functions

# All py files have to be in the same folder.
import os
os.chdir(r"C:\AbaqusTemp\M16") # Change work directory

# For Job creation
# -*- coding: mbcs -*-
import math
from part import *
from material import *
from section import *
from optimization import *
from assembly import *
from step import *
from interaction import *
from load import *
from mesh import *
from job import *
from sketch import *
from visualization import *
from connectorBehavior import *

def getInputFile(od_element, sdr_element, bh_element, bw_element, br_element, case_num):
    # Parameters
    OD = float(od_element)
    SDR = float(sdr_element)
    NH = float(nh_element)/1000.0
    RL = float(rl_element)/2000.0
    BR = float(br_element)/1000.0
    NAMED = str(case_num)

    BH = 10/1000.0 # When defining the shape
    BW = 20/2000.0 # When defining the shape, halved since symm
    #NH = 5/1000.0 # When redimensioning
    #RL = 10/2000.0 # When redimensioning, halved since symm
    #BR = 1/1000.0 # Fillet radius
    H = 0.05 # Pipe height
    PR = OD/2000.0 # Outer pipe radius
    PW = (math.ceil(OD/SDR))/1000.0 # Pipe wall thickness round to nearest mm
    IW = PR - PW # Inner pipe diameter

    print 'OD=' + str(OD)
    print 'SDR=' + str(SDR)
    print 'H=' + str(H)
    print 'PR=' + str(PR)
    print 'PW=' + str(PW)
    print 'IW=' + str(IW)
    print 'BH=' + str(BH)
    print 'BW=' + str(BW)
    print 'NH=' + str(NH)
    print 'RL=' + str(RL)
    print 'BR=' + str(BR)

    # Part sketch
    s = mdb.models['Model-1'].ConstrainedSketch(name='__profile__', sheetSize=1.0)
    g, v, d, c = s.geometry, s.vertices, s.dimensions, s.constraints
```

215

```python
s.sketchOptions.setValues(viewStyle=AXISYM)
s.setPrimaryObject(option=STANDALONE)
s.ConstructionLine(point1=(0.0, -0.5), point2=(0.0, 0.5))

s.Line(point1=(PR-PW/2, 0.0), point2=(PR, 0.0))
s.Line(point1=(PR, 0.0), point2=(PR+BH, 0.0))
s.Line(point1=(PR+BH, 0.0), point2=(PR+BH, BW))
s.Line(point1=(PR+BH, BW), point2=(PR, BW))
s.Line(point1=(PR, BW), point2=(PR, H))
s.Line(point1=(PR, H), point2=(PR-PW/2, H))

# Constraints of the sketch
s.FixedConstraint(entity=g.findAt((PR, 0.0)))
s.HorizontalConstraint(entity=g.findAt((PR+BH, 0.0)), addUndoState=False)
s.ParallelConstraint(entity1=g.findAt((PR, 0.0)), entity2=g.findAt((PR+BH, 0.0)),
addUndoState=False)
s.VerticalConstraint(entity=g.findAt((PR+BH, BW)), addUndoState=False)
s.PerpendicularConstraint(entity1=g.findAt((PR+BH, 0.0)), entity2=g.findAt((PR+BH, BW)),
addUndoState=False)
s.HorizontalConstraint(entity=g.findAt((PR, BW)), addUndoState=False)
s.FixedConstraint(entity=g.findAt((PR-PW/2, H))) # Prevent top from moving
s.EqualLengthConstraint(entity1=g.findAt((PR-PW/2, 0.0)), entity2=g.findAt((PR-PW/2, H))) #
Prevent top from changing length
s.EqualLengthConstraint(entity1=g.findAt((PR+BH/2, 0.0)), entity2=g.findAt((PR+BH/2, BW))) #
Proper change BH to NH
s.HorizontalDimension(vertex1=v.findAt((PR-PW/2, 0.0)), vertex2=v.findAt((PR, 0.0)),
textPoint=(PR+0.01, 0.01), value= PW/2)

# Redimensioning the weld bead
s.VerticalDimension(vertex1=v.findAt((PR+BH, 0.0)), vertex2=v.findAt((PR+BH, BW)),
textPoint=(PR+BH+0.01, BW+0.01), value= RL)
s.FixedConstraint(entity=g.findAt((PR, H/2))) # Allow movement of the bead instead of the outerwall
s.HorizontalDimension(vertex1=v.findAt((PR, 0.0)), vertex2=v.findAt((PR+BH, 0.0)),
textPoint=(PR+RL+0.01, BW+0.01), value= NH)

# Mirroring the half sketch
s.ConstructionLine(point1=(PR-PW/2, 0.0), angle=90.0)
#s.copyMirror(mirrorLine=g.findAt((PR-PW/2, H*10)), objectList=(g.findAt((PR-PW/2, 0.0))))
s.copyMirror(mirrorLine=g.findAt((PR-PW/2, H*10)), objectList=(g.findAt((PR-PW/2, 0.0)),
g.findAt((PR+NH/2, 0.0)), g.findAt((PR+NH, RL/2)), g.findAt((PR+NH/2, RL)), g.findAt((PR, H/2)),
g.findAt((PR-PW/2, H))))

# Fillet radius
s.FilletByRadius(radius=BR, curve1=g.findAt((PR+NH/2, RL)), nearPoint1=(PR+NH/2, RL),
curve2=g.findAt((PR, RL+H/2)),
    nearPoint2=(PR, RL+H/2))
s.FilletByRadius(radius=BR, curve1=g.findAt((IW-NH/2, RL)), nearPoint1=(IW-NH/2, RL),
curve2=g.findAt((IW, RL+H/2)),
    nearPoint2=(IW, RL+H/2))

# Generating the part
p = mdb.models['Model-1'].Part(name='Part-1', dimensionality=AXISYMMETRIC,
type=DEFORMABLE_BODY)
p = mdb.models['Model-1'].parts['Part-1']
p.BaseShell(sketch=s)
s.unsetPrimaryObject()
p = mdb.models['Model-1'].parts['Part-1']
session.viewports['Viewport: 1'].setValues(displayedObject=p)
del mdb.models['Model-1'].sketches['__profile__']
```

```python
# Sets and surfaces
mdb.models['Model-1'].parts['Part-1'].Set(faces=
    mdb.models['Model-1'].parts['Part-1'].faces.findAt(((PR, 0.01, 0.0),
    )), name='Mat')
mdb.models['Model-1'].parts['Part-1'].Set(edges=
    mdb.models['Model-1'].parts['Part-1'].edges.findAt(((IW-RL/4, 0.0, 0.0), ), ((IW+PW/4, 0.0, 0.0), ),
((PR-PW/4, 0.0, 0.0), ), ((PR+RL/4, 0.0, 0.0), )), name='Symm')
mdb.models['Model-1'].parts['Part-1'].Surface(name='Loading', side1Edges= mdb.models['Model-
1'].parts['Part-1'].edges.findAt(((IW+PW/4, H, 0.0), ), ((PR-PW/4, H, 0.0), )))

# Material
mdb.models['Model-1'].Material(name='HDPE-T5-80')
mdb.models['Model-1'].materials['HDPE-T5-80'].Density(table=((954.0, ), ))
mdb.models['Model-1'].materials['HDPE-T5-80'].Elastic(table=((480000000.0,
    0.5), ))
mdb.models['Model-1'].HomogeneousSolidSection(material='HDPE-T5-80', name=
    'Section-1', thickness=None)
mdb.models['Model-1'].parts['Part-1'].SectionAssignment(offset=0.0,
    offsetField='', offsetType=MIDDLE_SURFACE, region=
    mdb.models['Model-1'].parts['Part-1'].sets['Mat'], sectionName='Section-1',
    thicknessAssignment=FROM_SECTION)

# Assembly
mdb.models['Model-1'].rootAssembly.DatumCsysByThreePoints(coordSysType=
    CYLINDRICAL, origin=(0.0, 0.0, 0.0), point1=(1.0, 0.0, 0.0), point2=(0.0,
    0.0, -1.0))
mdb.models['Model-1'].rootAssembly.Instance(dependent=ON, name='Part-1-1',
    part=mdb.models['Model-1'].parts['Part-1'])

# Step
mdb.models['Model-1'].StaticStep(initialInc=0.001, name='Step-1', previous=
    'Initial')

# BC and load
mdb.models['Model-1'].YsymmBC(createStepName='Initial', localCsys=None, name=
    'HSymm', region=
    mdb.models['Model-1'].rootAssembly.instances['Part-1-1'].sets['Symm'])
mdb.models['Model-1'].Pressure(amplitude=UNSET, createStepName='Step-1',
    distributionType=UNIFORM, field='', magnitude=-5500000.0, name='Extension',
    region=
    mdb.models['Model-1'].rootAssembly.instances['Part-1-1'].surfaces['Loading'])

# Mesh
mdb.models['Model-1'].parts['Part-1'].setMeshControls(regions=
    mdb.models['Model-1'].parts['Part-1'].faces.findAt(((PR, 0.01, 0.0),
    )), elemShape=QUAD, technique=FREE) # Quad elements only
mdb.models['Model-1'].parts['Part-1'].seedPart(deviationFactor=0.1,
    minSizeFactor=0.1, size=0.0005)

BRL = ((BR*BR*2)**0.5)/2 # Calculating the point of fillet without SQRT
BRLX = round(PR+BR-BRL, 6) # For finding the fillet
BRLY = round(RL+BR-BRL, 6) # For finding the fillet
OFillet = mdb.models['Model-1'].parts['Part-1'].edges.findAt(((BRLX, BRLY, 0.0), ))
p.seedEdgeByNumber(edges=OFillet, number=20, constraint=FINER)
mdb.models['Model-1'].parts['Part-1'].generateMesh()
mdb.models['Model-1'].rootAssembly.regenerate()

# Input file generation
mdb.Job(atTime=None, contactPrint=OFF, description=
    'Parametric study of nominal cases', echoPrint=OFF, explicitPrecision=
```

```python
            SINGLE, getMemoryFromAnalysis=True, historyPrint=OFF, memory=90,
            memoryUnits=PERCENTAGE, model='Model-1', modelPrint=OFF,
            multiprocessingMode=DEFAULT, name=NAMED, nodalOutputPrecision=SINGLE,
            numCpus=1, numGPUs=0, queue=None, scratch='', type=ANALYSIS,
            userSubroutine='', waitHours=0, waitMinutes=0)
    mdb.jobs[NAMED].writeInput(consistencyChecking=OFF)
    # Job Submission
    mdb.jobs[NAMED].submit(consistencyChecking=OFF)
    mdb.jobs[NAMED].waitForCompletion()


# For odb readout
from abaqus import *
from abaqusConstants import *
from odbAccess import *
from driverUtils import executeOnCaeStartup
executeOnCaeStartup()


session.Viewport(name='Viewport: 1', origin=(0.0, 0.0), width=268.95, height=154.15)
sv = session.viewports['Viewport: 1'] # Shortens the code
sv.makeCurrent()
sv.maximize()


#odbMaxMises.py from Abaqus Example scripts


def getMaxMises(case_num):
    #""" Print max mises location and value given NAMEDODB
    #   and elset(optional)
    elset = elemset = None
    region = "over the entire model"
    #""" Open the output database """
    case_odb = str(case_num)+'.odb'
    odb = openOdb(case_odb)
    assembly = odb.rootAssembly
    o1 = session.openOdb(name=case_odb)
    sv.setValues(displayedObject=o1)

    #""" Initialize maximum values """
    maxMises = -0.1
    maxElem = 0
    maxStep = "_None_"
    maxFrame = -1
    Stress = 'S'
    isStressPresent = 0
    for step in odb.steps.values():
        print 'Processing Step:', step.name
        for frame in step.frames:
            allFields = frame.fieldOutputs
            if (allFields.has_key(Stress)):
                isStressPresent = 1
                stressSet = allFields[Stress]
                if elemset:
                    stressSet = stressSet.getSubset(
                        region=elemset)
                for stressValue in stressSet.values:
                    if (stressValue.mises > maxMises):
                        maxMises = stressValue.mises
                        maxElem = stressValue.elementLabel
                        maxStep = step.name
                        maxFrame = frame.incrementNumber
    if(isStressPresent):
```

218

```python
            print 'Maximum von Mises stress %s is %f in element %d'%(
                region, maxMises, maxElem)
            print 'Location: frame # %d  step:  %s '%(maxFrame,maxStep)
        f = open('R16.py',"a")
        RESULTS = str(case_num)+'   '+str(maxMises)+'   '+str(maxElem)
        f.write(str(RESULTS)+'\n')
        f.close()
        sv.odbDisplay.display.setValues(plotState=(CONTOURS_ON_UNDEF, ))
        session.viewports['Viewport: 1'].odbDisplay.contourOptions.setValues(
        maxAutoCompute=OFF, maxValue=1E+007, minAutoCompute=OFF, minValue=1E+006,
        showMaxLocation=ON, numIntervals=9)
        session.viewports['Viewport: 1'].odbDisplay.basicOptions.setValues(
        averageElementOutput=False)
        sv.view.setValues(nearPlane=0.0636722,
        farPlane=0.10535, width=0.0661007, height=0.0286001,
        viewOffsetX=0.00171196, viewOffsetY=-0.00298077)
        session.printOptions.setValues(vpBackground=ON, reduceColors=OFF)
        session.pngOptions.setValues(imageSize=(1920, 1080))
        session.printToFile(fileName=case_num, format=PNG,
canvasObjects=(session.viewports['Viewport: 1'], ))
    else:
        print 'Stress output is not available in' \
            'the output database : %s\n' %(odb.name)

    session.odbs[case_odb].close()

# Defining the function elements
od_element=1;
sdr_element=1;
nh_element=1;
rl_element=1;
br_element=1;

# Variable names
OD = [180]
SDR = [11]
NH = [4]
# NH = 4 in all models
#NH = [2,2.5,3,3.5,4,4.5,5,5.5,6]
# NH_max = 6, NH_min = 2, NH_ave = 4
# BH_max = 9, BH_min = 4, BH_ave = 6.5
RL = [6.5]
# RL = 6.5 in all models
#RL = [2,2.5,3,3.5,4,4.5,5,5.5,6,6.5,7,7.5,8,8.5,9,9.5,10]
# RL_max = 10, RL_min = 2, RL_ave = 6
# BW_max = 26, BW_min = 13, BW_ave = 19.5
BR = [1]
# BR = 1 in all models
#BR = [0.1,0.2,0.3,0.4,0.5,0.6,0.7,0.8,0.9,1,1.2,1.4,1.6,1.8,2,2.5,3]
case_num = 0 #Used to be 0

# This is the main loop
for od_element in OD:
    for sdr_element in SDR:
        for nh_element in NH:
            for rl_element in RL:
                for br_element in BR:
                    case_num = int(case_num) # Reverts case_num as a integer
                    case_num = case_num + 1
                    g = open('L16.py',"a") # Append to case file
```

```python
        input_name = str(case_num)+' '+str(od_element)+' '+str(sdr_element)+'
'+str(nh_element)+' '+str(rl_element)+' '+str(br_element)
        g.write(str(input_name)+'\n')
        g.close()
        # Input file generation
        QUESTION = getInputFile(od_element, sdr_element, nh_element, rl_element,
br_element, case_num)
        # ODB readout
        case_num = str(case_num)
        ANSWER = getMaxMises(case_num)
        case_odb = str(case_num)+'.odb'
        session.odbs[case_odb].close()
```

Appendix F: FEA of Realistic Weld Bead Models

The FEA results of realistic weld beads models are shown for the corresponding welding procedures below:

- WP1: Figure F-1 (a-c)
- WP2: Figure F-1 (d-f)
- WP3: Figure F-2 (a-c)
- WP4: Figure F-2 (d-f)
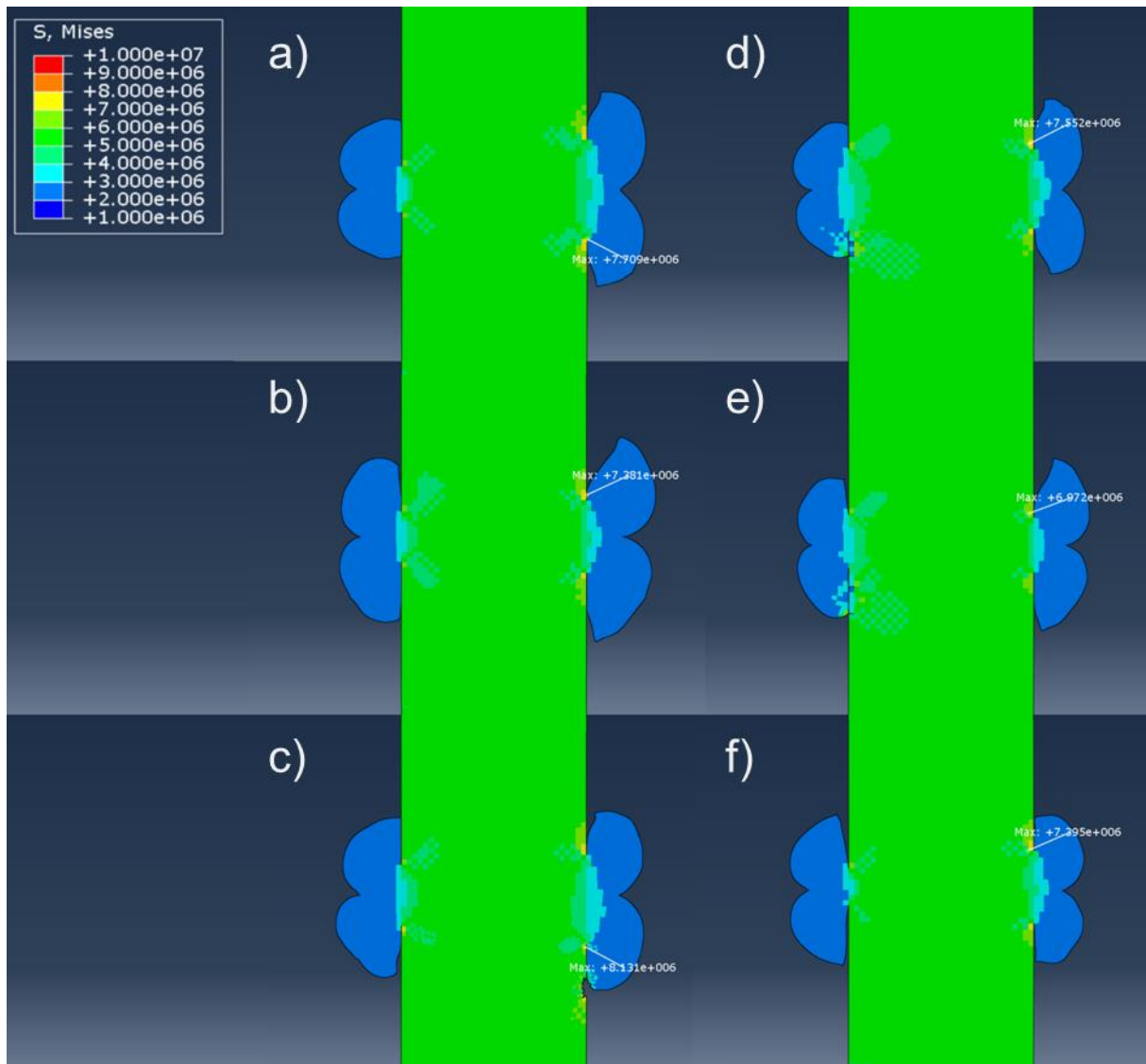- WP5: Figure F-3 (a-c)
- WP6: Figure F-3 (d-f)

Figure F-1 FEA results of realistic weld bead shape models of WP1 and WP2 for three circumferential positions: bottom (a and d), top (b and e), and side (c and f)
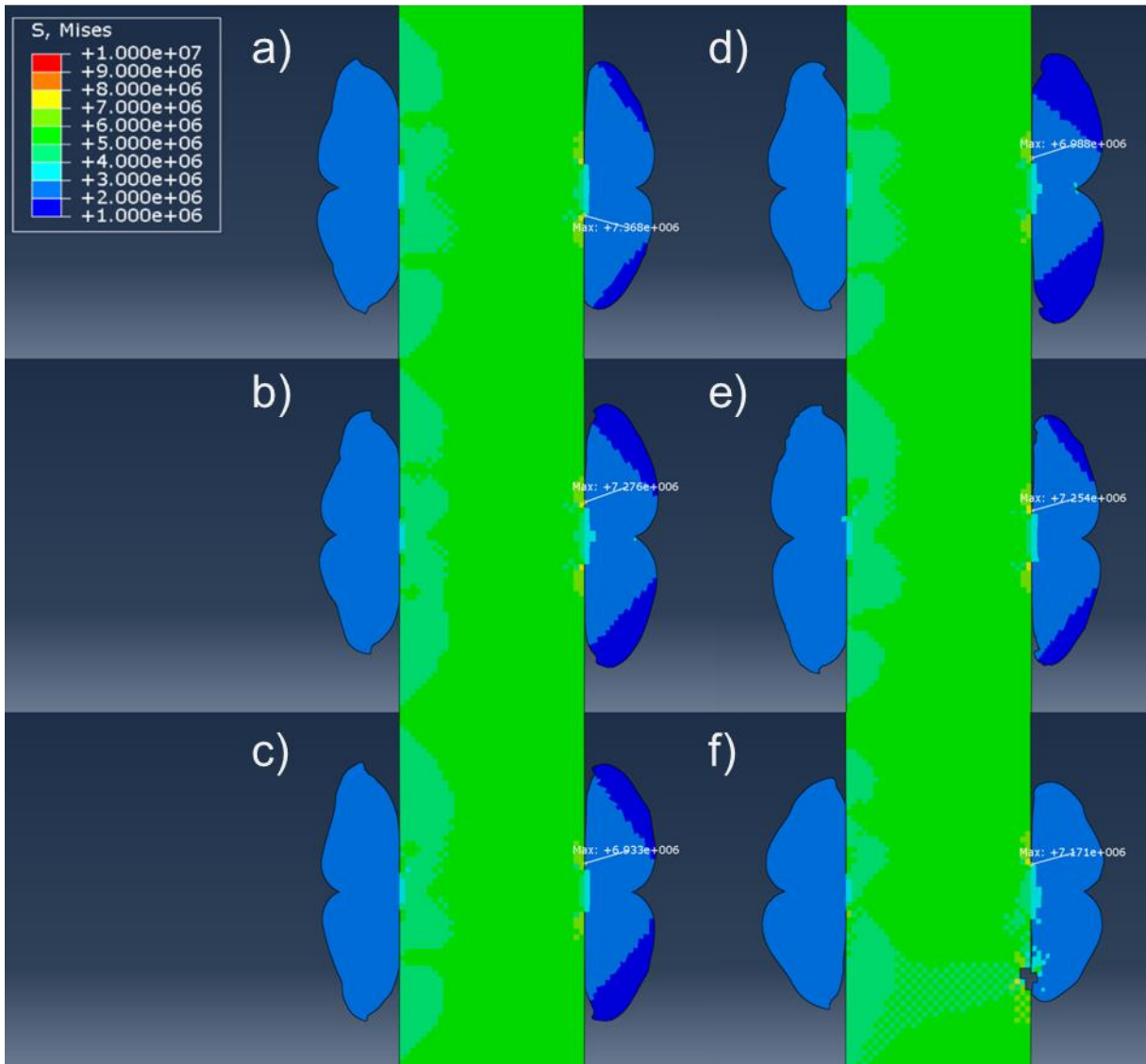
Figure F-2 FEA results of realistic weld bead shape models of WP3 and WP4 for three circumferential positions: bottom (a and d), top (b and e), and side (c and f)
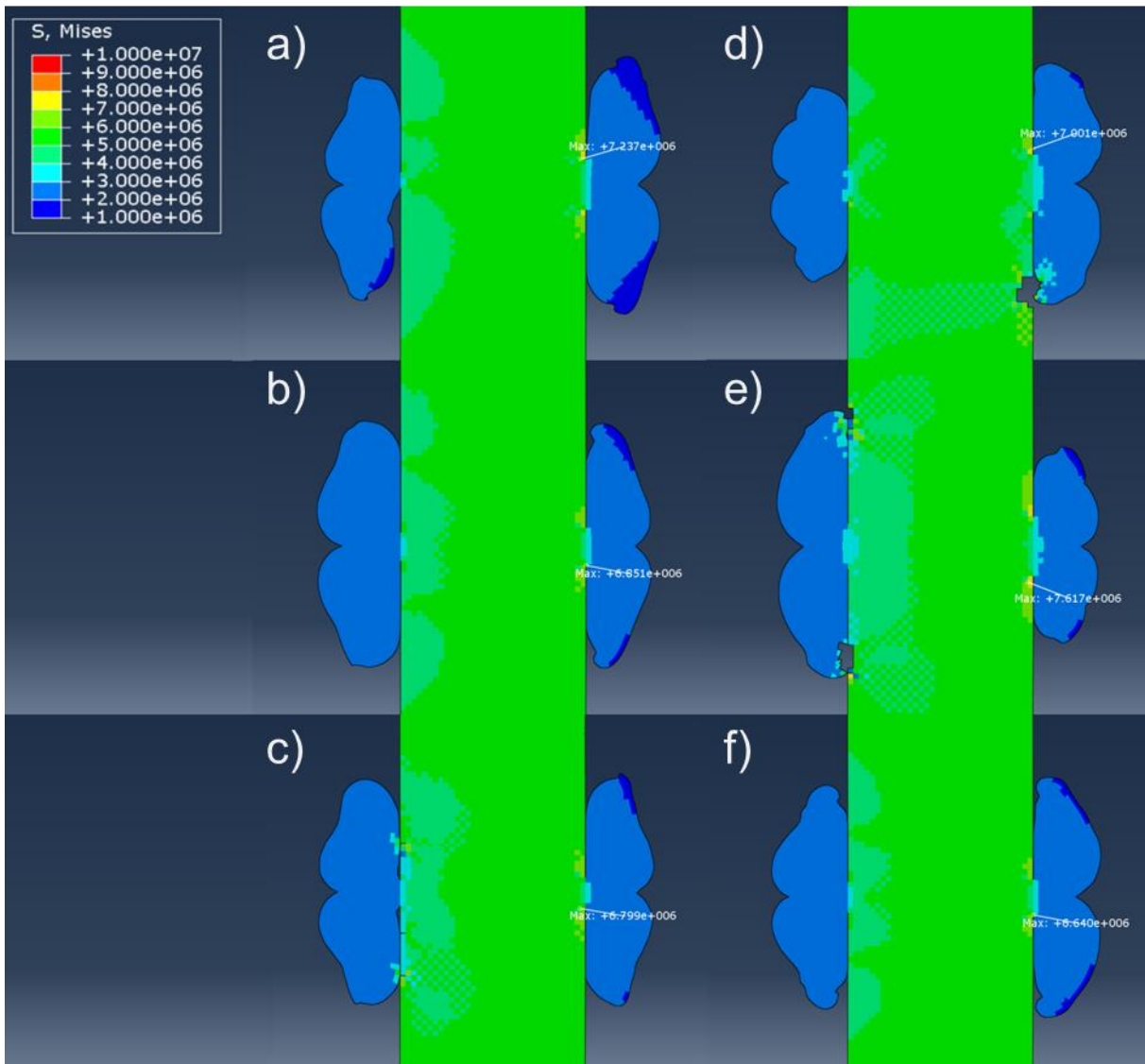
Figure F-3 FEA results of realistic weld bead shape models of WP5 and WP6 for three circumferential positions: bottom (a and d), top (b and e), and side (c and f)

The FEA models that required removal of collapsed elements due to limiting geometry are listed below:

- WP1: Figure F-1 (c)
- WP4: Figure F-2 (f)
- WP6: Figure F-3 (e)
- WP6: Figure F-3 (f)

Appendix G: Post-Nanoindentation Microscopy Images

The nanoindentation at TWI was carried out on all welding procedures using 60 indentations across the weld interface with the exception of WP1 and WP2. WP1 had a test grid of 40 indents and WP2 utilised a grid of 120 indentations across.
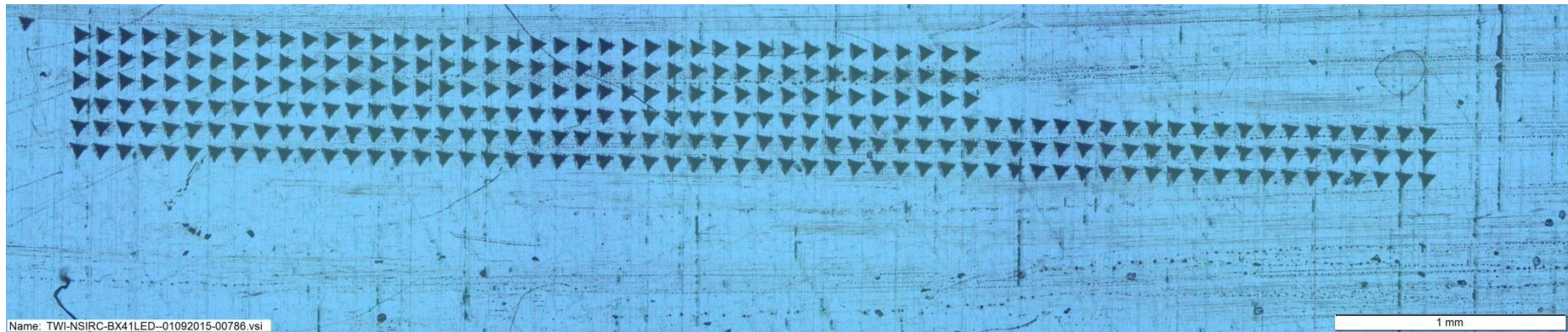
G1 TWI Nanoindentation

Name: TWI-NSIRC-BX41LED--01092015-00786.vsi

1 mm

Figure G-1 Microscopy image of WP1 post-nanoindentation, Olympus BX41 LED at 2.5X resolution
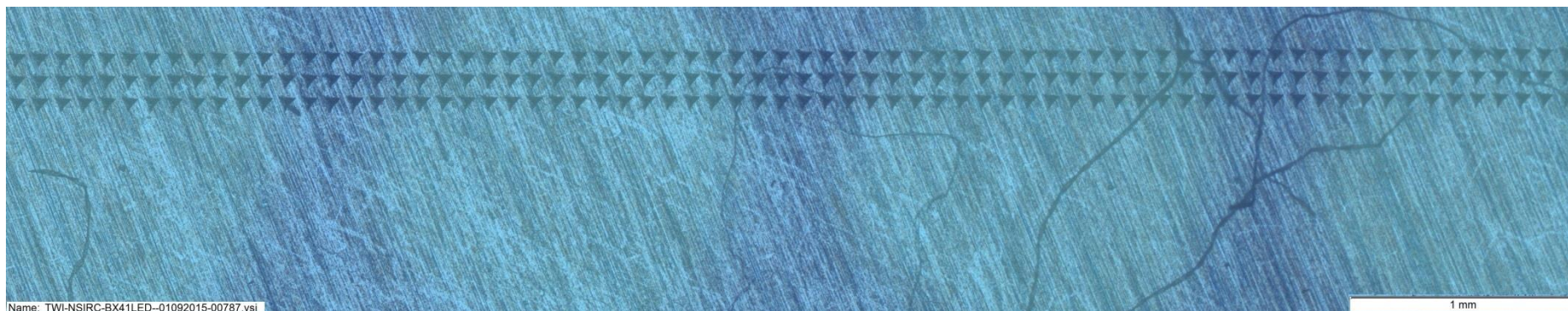
Name: TWI-NSIRC-BX41LED--01092015-00787.vsi

1 mm

Figure G-2 Microscopy image of WP2 post-nanoindentation showing the 60 indentations across the weld interface, Olympus BX41 LED at 2.5X resolution
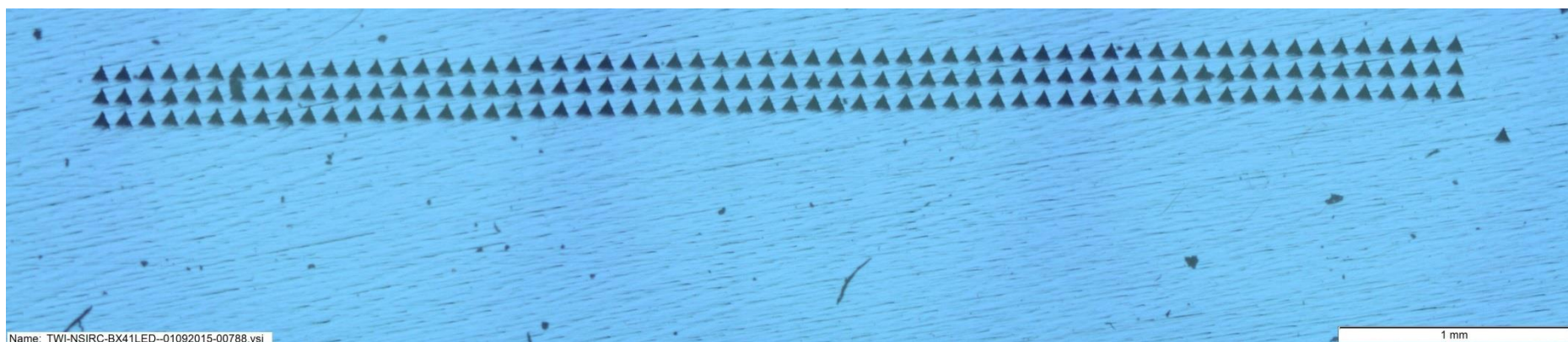

Name: TWI-NSIRC-BX41LED--01092015-00788.vsi

1 mm

Figure G-3 Microscopy image of WP3 post-nanoindentation, Olympus BX41 LED at 2.5X resolution

Name: TWI-NSIRC-BX41LED--01092015-00790

1 mm

Figure G-4 Microscopy image of WP4 post-nanoindentation, Olympus BX41 LED at 2.5X resolution

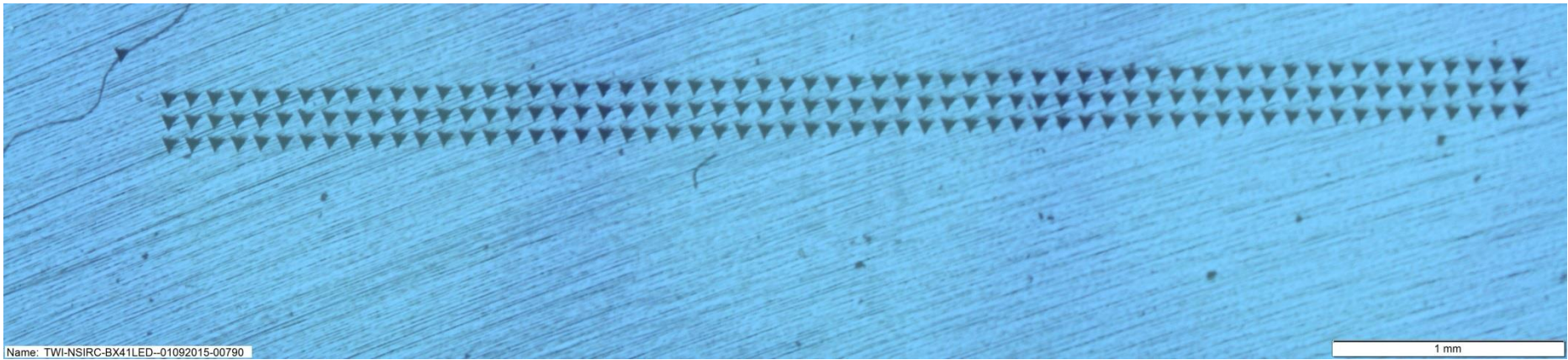Name: TWI-NSIRC-BX41LED--01092015-00791.vsi
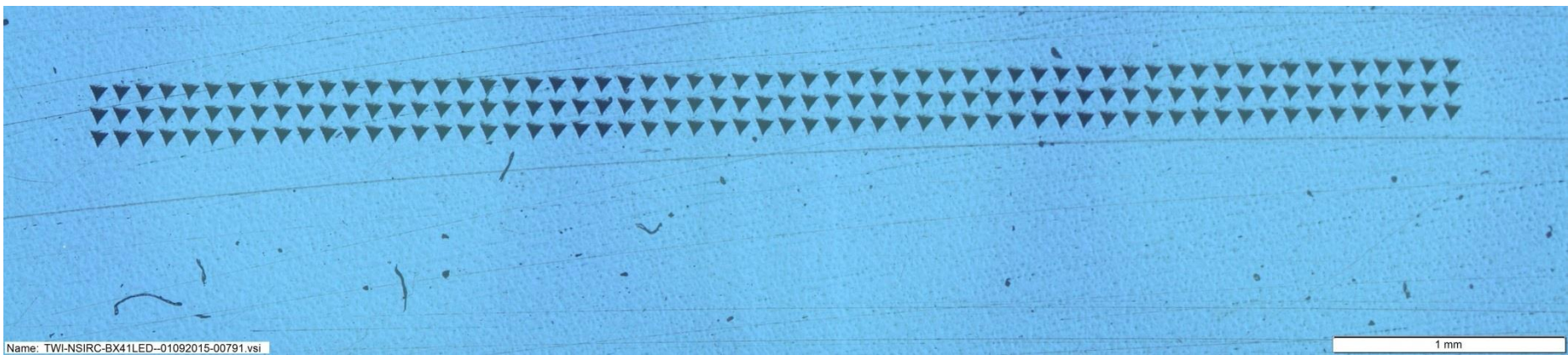
1 mm

Figure G-5 Microscopy image of WP5 post-nanoindentation, Olympus BX41 LED at 2.5X resolution
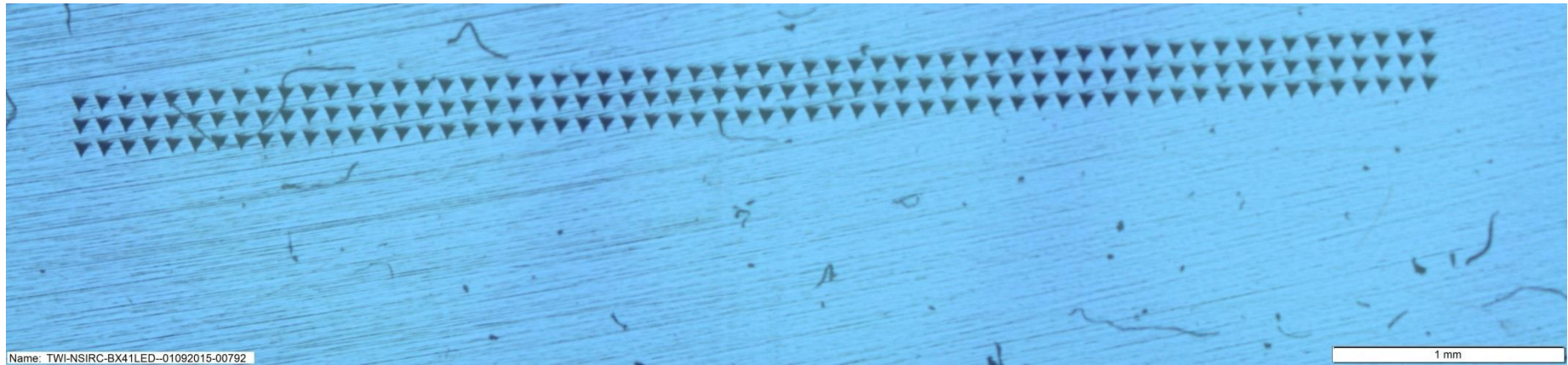
226

Figure G-6 Microscopy image of WP6 post-nanoindentation, Olympus BX41 LED at 2.5X resolution

Figure G-7 Microscopy image of WP2 post-nanoindentation showing the full 120 indent grid, Olympus BX41 LED at 2.5X resolution

G2 Dates of Nanoindentation Tests

Table G-1 Completion dates of nanoindentation tests for respective welding procedures, listed in chronological order for TWI

Dates	Procedure
16/07/2015	WP1*
17/07/2015	WP1
24/07/2015	WP3
27/07/2015	WP4
28/07/2015	WP5
29/07/2015	WP6
03/08/2015	WP2
* the test was interrupted unexpectedly	